PHOTOABSORPTION OF ULTRAVIOLET LIGHT BY MOLECULAR OXYGEN : THE SCHUMANN-RUNGE BANDS AND THE LYMAN-α WINDOW.

By

H.P.F. GIES B.Sc.(Hons)

Department of Physics

A Thesis submitted for the Degree of
Doctor of Philosophy
at the
University of Adelaide

January, 1979.

Awarded July 1979

SUMMARY

This thesis describes the measurement of oscillator strengths and linewidths of rotational lines in the Schumann-Runge bands of molecular oxygen, for the wavelength range 1750-2000Å . A study of the variation of absorption coefficient of molecular oxygen with pressure and temperature was also done near the H Lyman-α emission line at 1215.6Å . The absorption coefficient here varies rapidly, and the form of the variation is important, as it determines to what depth into the atmosphere the incident Lyman-α radiation penetrates.

The dispersing instrument used was a 6.65 m vacuum ultraviolet scanning monochromator with off-plane Eagle mount, operated in first order with a resolution of 0.04-0.06Å . Light was provided by a thyratron triggered hydrogen discharge in the case of the Schumann-Runge bands, and by an argon discharge in the case of the Lyman-α work.

The cross-section measurements in the Lyman-α window were made at 0.2Å intervals in the wavelength region 1214.0Å to 1218.6Å with a path length of 1.1 metres at temperatures of 294 °K, 195 °K and 82 °K using respectively, ambient room temperature, a solid CO_2 methanol slush coolant, and liquid air. The minimum value of absorption was found to decrease with a decrease in temperature, and this minimum also shifted slightly to longer wavelengths as the temperature decreased. The pressure dependence of the cross-section was found to be in agreement with earlier measurements, but the room temperature observations were found to disagree somewhat from the previous observations.

Rotational lines in the (1-0) to (15-0) Schumann-Runge bands were scanned, and the integrated line areas at two different pressures recorded. After taking into account adjacent lines, Herzberg and Schumann-Runge continua and O_4 continua (in the case of lower bands and higher pressures), this integrated absorption area was simulated by computer using curve of growth techniques to extract oscillator strengths and linewidths. The (2-0) to (15-0) bands were observed at room temperature and pressures in the range 0.02 torr to 850 torr. The measurements for bands above (15-0) were made at liquid air temperatures to reduce spectrum complexity.

The results of these Schumann-Runge band investigations show previous measurements to be in error. A measure of the rotational dependence of band strength was obtained for each vibrational band, and a straight line fitted to the points where possible, and these were compared with theoretical predictions.

P R E F A C E

This thesis contains no material which has been accepted for the award of any other degree or diploma in any University. To the best of the author's knowledge and belief, no material previously published or written by another person has been included, except where due reference is made in the text.

Peter Gies
JANUARY, 1979.

ACKNOWLEDGEMENTS

With the exception of the 1-0 to 3-0 Schumann-Runge bands described in Chapter 6 (Section 6.6.1), most of the experimental absorption work described in this thesis was carried out in association with Mr Trevor Hobbs.

The author would like to thank his supervisor, Dr A.J. Blake, for his valuable assistance and guidance during the course of this work, and for his helpful comments during the writing of this thesis. Thanks are due as well to Dr D.G. McCoy for the many helpful discussions with him, and for the co-operation received on many aspects of this work.

The author would also like to thank Dr B.H. Horton, Dr B.R. Lewis and Professor J.H. Carver for their assistance. Mr P. Schebella and the workshop staff must also be thanked for their part in the construction of the absorption cell. Finally, thanks to Mr F.A. Smith and Mr J. Wright for their technical assistance on many occasions.

I would also like to express my appreciation to both my parents, and my wife, Kathy, for their help in producing this thesis. Thanks must also go to my typist, Pat Coe.

The author was the holder of a Commonwealth Postgraduate Award during the greater part of his study.

C O N T E N T S

Contents continued..... Page

Contents continued.... Page

Contents continued....

Contents continued..... Page

Contents continued....

CHAPTER 1

1.1 Introduction

The absorption of ultra-violet light by oxygen in the wavelength region of the Schumann-Runge bands (1750 - 2000Å) has been the subject of numerous investigations (described later in this chapter), mostly with the view to applying the newly devised experimental results to atmospheric problems. The Schumann-Runge bands provide all the atomic oxygen dissociated from the molecular form in the height range near 80 kms in the atmosphere, as well as having important consequences for the dissociation of water vapour. Any models of the atmosphere requiring the transmission of radiation downwards to the surface, or the production rate of oxygen atoms, therefore requires accurate measurements of absorption coefficients, and the Schumann-Runge results are difficult to obtain, due to the large number of lines present, and to their small widths preventing their direct resolution by present instruments.

Also of atmospheric interest, is the penetration of the intense solar Lyman-α line into the atmosphere. Accurate measurements of the absorption coefficient of oxygen in this region are vital, since this coefficient is varying rapidly there, to determine to what depth this radiation will penetrate, and thus remain active at dissociating various molecular species.

Oxygen is also the classic case of predissociation, the Schumann-Runge bands providing quantities of data on the predissociation process. The linewidths obtained experimentally can be used to estimate crossing points of various potential curves of states of the molecule (this will be discussed more fully in Chapter 6).

This thesis presents both the line strengths of absorption lines in the Schumann-Runge bands, in the form of band oscillator strengths, and linewidths obtained indirectly from the measurements. Also presented are the absorption coefficients of the Lyman-α absorption window of molecular oxygen, and their temperature dependence.

1.2 Previous Experimental Work - The Schumann-Runge Bands

The Schumann-Runge band system of molecular oxygen ($B^3\Sigma_u^- - X^3\Sigma_g^-$) has been studied extensively. The first significant measurements were made by Curry and Herzberg (1934) and Knauss and Ballard (1935) who identified the various lines, assigned these lines to bands and obtained rotational constants for the upper states, as well as a measurement of the dissociation limit. Watanabe et al (1953) obtained values of the absorption intensities of the bands, as well as an improved value for the dissociation limit of the $B^3\Sigma_u^-$ state. Brix and Herzberg (1954) published high resolution data for the 12-0 to 18-0 bands, with accurate values for line positions, rotational constants and a definitive value for the $B^3\Sigma_g^-$ dissociation limit. The first values of oscillator strength for the bands were obtained photographically by Ditchburn and Heddle (1954) assuming a Doppler line shape, but these results were later shown to be in error by Bethke (1959), who used a pressure broadening effect to overcome the problem of low instrumental resolution. Oscillator strengths were also obtained by Farmer et al (1968) using a curve of growth technique for the 2-0 to 20-0 bands, and by Hasson et al (1970) using high resolution direct photography for the 0-0 to 3-0 bands. Halmann (1965) used a pressure broadening effect and measured values for the 2-0 to 10-0 bands while Ackermann et al (1970)

calculated oscillator strengths from absorption measurements at the wavelength of various narrow silicon emission lines. The experimental results of Hudson and Carter (1968) were analysed and oscillator strengths extracted by Hudson and Mahle (1972) using a fitting procedure on the high resolution data. Huebner et al (1975) published oscillator strengths for the 1-0 to 20-0 bands using electron impact studies. The numerous oscillator strength results will be discussed fully in Chapter 6.

Predissociation in oxygen was first suggested by Flory (1935) as being responsible for the rotational line broadening. Wilkinson and Mulliken (1956) and Carroll (1958) obtained qualitative evidence of line broadening, and gave an estimate of the crossing point of the potential curves near $v' = 4$. Hudson and Carter (1969) confirmed the predissociation of the $v' = 3$ to $v' = 17$ bands, and Ackerman et al (1969) also confirmed that the lines were broadened from that of the Doppler case, using spot measurements of absorption at the wavelengths of numerous silicon emission lines. Murrell and Taylor (1969) performed theoretical calculations on potential curves, and showed that the observed predissociation could be explained by a single crossing of the potential curves of the ground and upper state near $v' = 4$ of the ground state, confirming the previous work. Ackerman and Biaume (1970) made photographic estimates of the linewidths for the 0-0 to the 19-0 bands, as well as measuring accurately the line positions for the 0-0 to 13-0 bands and obtaining rotational constants. Their results confirmed that the maximum of the linewidths occurred in the 4-0 band, with a further maximum at $v' = 11$ and a minimum at $v' = 9$, Schaeffer and Miller (1970) however suggested that the curve crossing was not as previously put forward. Julienne and Krauss (1975) and Julienne (1976) discuss the

predissociation problem, as well as presenting theoretical linewidths. Hudson and Mahle (1972) also present linewidths along with their values of oscillator strength. The discrepancies in the linewidths are discussed fully in Chapter 6.

Once line positions, strengths and widths for the rotational lines in the Schumann-Runge bands have been obtained accurately, then it will be possible to calculate transmission through the atmosphere and to build up atmospheric models. These atmospheric models depend critically on the absorption coefficients and on the predissociation. Hudson et al (1969) discuss the predissociation and its atmospheric effects, while Kockarts (1970) presents a theoretical analysis of the absorption of the Schumann-Runge bands in the atmosphere. Blake et al (1966) present low resolution absorption cross-sections and discuss the validity of Beer's law for transmission through the Schumann-Runge bands. Thompson et al (1963) also present low resolution data for oxygen and many other gases of atmospheric interest, as does Huffman (1968). Creek and Nicholls (1975) re-analyse the Schumann-Runge bands, and re-assess the molecular constants previously derived. Fang et al (1974) present a theoretical attempt to describe transmission through the bands using opacity distribution functions, while Blake (1978) presents a model using effective absorption over 10Å and 2.0Å wavelength intervals. Hudson et al (1966) investigate the effect of temperature on the absorption coefficient.

1.3 Previous Experimental Work

Lyman-α Photoabsorption by O_2

Laboratory measurements of the absorption cross-section of molecular oxygen at H Lyman-α were first done by Watanabe (1958) and

Metzger and Cook (1963), and somewhat more comprehensively by Ogawa (1968). Ogawa and Yamawaki (1970) obtained values for the pressure dependence in reasonable agreement with Watanabe, and the more recent results of Dose et al (1975) confirm the pressure dependence of the absorption coefficient. Use of the laboratory measurements to extract molecular oxygen densities was done by Carver et al (1964). Knowledge of the solar hydrogen Lyman-α line profile allowed refinements to be made to the calculations of the extinction of Lyman-α radiation as it passes through the atmosphere. Purcell and Toussey (1960) and Quessette (1970) presented their results for the line profile. Hall (1972) took account of the variation in the cross-section with wavelength in his calculations of extinction. The realization that the absorption cross-section could not be assumed to be constant soon led to the conclusion, that laboratory room temperature measurements were inapplicable to the atmosphere [Thrane and Johannessen (1975), Smith and Miller (1974), Weeks (1975) and Prinz and Brueckner (1977)]. The temperature dependence of the absorption coefficient was thought to be responsible for the discrepancy between the O_2 densities derived using Lyman-α extinction and other methods. It is noted that rotational lines of the $\alpha'\Sigma_u^+ - X^3\Sigma_g^-$ of high rotational number coincide with the long wavelength side of the minimum of the absorption coefficient [Alberti et al (1967), Ogawa and Yamawaki (1970)].

CHAPTER 2

ELECTRONIC TRANSITIONS IN DIATOMIC MOLECULES

2.1 Introduction

This chapter is a brief summary of the various energy levels of diatomic molecules and the spectra resulting from transitions between those energy levels, with particular reference to oxygen. A more comprehensive treatment is given in "Spectra of Diatomic Molecules" by G. Herzberg (1950). This chapter will concentrate mainly on basic quantities and concepts necessary to discussions in later chapters.

Molecules, like atoms, have electronic energy levels between which transitions may occur. However, molecules have the additional complexity of possible rotational and vibrational motions, and these result in vibrational and rotational energy levels. The total energy of the molecules can be resolved into electronic, vibrational and rotational parts, so that each electronic level may be considered to have vibrational fine structure, and each vibrational level as having rotational fine structure. The resulting spectrum can then be a complex series of bands, as for example, in the Schumann-Runge bands.

The absorption or emission of radiation corresponds to a transition between two different energy states, the frequency of the transition given by

$$h\nu = \Delta E \qquad (2.1)$$

where ΔE is the energy difference between the states, and h is Planck's constant. In general, there will be a simultaneous change in electronic, vibrational and rotational energy. Differences in energy between vibrational energy levels are much smaller than those for electronic levels,

while rotational energy level differences are smaller still.

2.2.1 Rotational Energy

The simplest model for a rotating diatomic molecule would be that of a rigid rotator, having solutions to the appropriate Schroedinger equation of

$$E_J = \frac{h^2 J (J+1)}{8\pi^2 I} \qquad (2.2)$$

where $I = \mu r^2$ and $\mu = \frac{m_1 m_2}{m_1+m_2}$ is the reduced mass and I is the moment of inertia. Here E_J is the energy of the Jth rotational level, and J is the rotational number. The appropriate rotational wavefunctions Ψ_R are

$$\Psi_R = N_R P_J^{|M|}(\cos\theta) e^{M\phi}$$

where $P_J^{|M|}(\cos\theta)$ is the associated Legendre function, N_R is a normalization constant, and M is a second quantum number representing the component of the angular momentum $\underline{J}$ in the direction of the z-axis in terms of $\hbar$. Equation 2.2 shows the rotational energy to be quantized, there being only certain allowed solutions, when J is integer.

Transitions between the various energy levels can occur when the transition matrix elements

$$R_x = \int \Psi_u^* M_x \Psi_l \, dr$$

$$R_y = \int \Psi_u^* M_y \Psi_l \, dr$$

$$R_z = \int \Psi_u^* M_z \Psi_l \, dr$$

are non-zero. Here M_x, M_y and M_z are the components of the rotator dipole moments in the x, y and z directions respectively, and Ψ_u and Ψ_l are the wavefunctions of the upper and lower states respectively.

The selection rules satisfying the condition $R_x = R_y = R_z = 0$ are $\Delta J = \pm 1$, and then only when the dipole moment of the molecule is non-zero. For a transition, the rotational level in the lower state is denoted by J'' , while the level in the upper state is denoted by J' (similarly for N', N'' and for vibrational number v', v''). This rules out pure rotation spectra for homonuclear molecules like O_2 , where both atoms have the same charge configuration and the dipole moment is thus zero. However, when an electronic transition takes place, rotational transitions may then be possible. This is found to be the case in oxygen, which has no pure rotational spectrum, but electronic transitions are accompanied by rotational transitions.

Using equation 2.2 and $J'' = J' + 1$ $(\Delta J = \pm 1)$ then

$$\Delta E_R = \frac{2\hbar^2}{2I}(J + 1) = 2B(J + 1) \qquad (2.3)$$

where $B = \frac{\hbar^2}{2I}$ is the rotational constant, and ΔE_R is the energy separation of two adjacent rotational levels for a given electronic vibrational state. The rotational spectrum consists of a number of equally spaced lines in frequency ν , so the variation with wavelength will be slightly non-linear. For $J \sim 10$, the rotational energy difference

$$\Delta E_R \approx 10^{-22} \text{ Joules } (.0006 \text{ eV})$$

for oxygen.

Approximating diatomic molecules with rigid rotators shows the basic properties of the spectra one would expect to see. However, considering a molecule as a rigid object can only be an approximation. Some account of the centrifugal stretching of the chemical bond as the molecule rotates faster must be taken into account. This centrifugal

force tending to stretch the bond holding the molecule together increases with increasing rotation, so the internuclear distance and therefore the moment of inertia, increase with increasing rotation. That is, the quantity B is dependent upon J. The non-rigid rotator model takes these factors into account. The rotational energy levels of the non-rigid rotator are given by

$$E_J = B\,J(J+1) - DJ^2\,(J+1)^2 \qquad (2.4)$$

where D depends on the sharpness of the potential curve and therefore on the vibrational frequency ω, and is very much smaller than B. The selection rule is still $\Delta J = \pm 1$ which gives for the energy difference

$$\Delta E_R = 2B(J+1) - 4D(J+1)^3 \qquad (2.5)$$

That is, the levels are no longer equidistant with frequency, but their separation decreases slightly for increasing J. It is found that $D < 10^{-4}B$, so the rigid rotator model is often accurate enough.

2.2.2 Vibrational Energy

The simplest model for vibration of a diatomic molecule is the simple harmonic oscillator, since for small amplitudes, the restoring force exerted by the atoms on each other is approximately proportional to the change in internuclear distance. This will mean a parabolic potential energy curve, as is the case for the simple harmonic oscillator. The energy levels of the simple harmonic oscillator are

$$E_v = h\nu_{osc}\,(v + \tfrac{1}{2}) = w\,(v + \tfrac{1}{2}) \qquad (2.6)$$

That is, a series of equidistant levels. Note $v = 0$ does not correspond to $E = 0$, but to $E = \tfrac{1}{2}h\nu_{osc}$, the zero point energy. The vibrational

wave functions are found to be

$$\Psi_v = N_v \exp(- \tfrac{1}{2} \alpha x^2). \; H_v(\sqrt{\alpha}\, x) \qquad (2.6)$$

where $\alpha = \dfrac{4\pi^2 \mu \nu_{osc}}{h}$, and H_v are the Hermite polynomials. These have maximum amplitudes close to where the energy level meets the potential curve. The selection rule for vibration is $\Delta v = \pm 1$.

Again for molecules consisting of like atoms, such as O_2 , no pure vibrational spectrum results, but electronic transitions are accompanied by vibrational transitions.

Comparison of observed potential curves with the parabolic assumptions of the linear harmonic oscillator show large discrepancies as the displacement increases. The addition of a cubic term to the potential e.g.

$$U = f(r - r_e)^2 - g(r - r_e)^3$$

gives an anharmonic oscillator showing better agreement over a wider range.

The new energy levels can be written as

$$E_v = \omega_e(v + \tfrac{1}{2}) - \omega_e x_e(v + \tfrac{1}{2})^2 \qquad (2.7)$$

where $\omega_e x_e$ is the anharmonicity constant, and ω_e is a measure of the curvature of the potential well near the minimum. The selection rules for the anharmonic oscillator give $\Delta v = \pm 1$ for the most intense transitions, but $\Delta v = \pm 2, \pm 3$ etc., are also possible, although the intensities fall off very rapidly.

The vibrational wavefunctions for the anharmonic oscillator are very similar to those of the harmonic oscillator, with the exception that they are no longer symmetrical. Due to the asymmetry of the potential well,

the molecule spends longer on the shallow right hand side of the potential well, and therefore the probability density there will be higher.

The energy difference between transitions can be found quite simply from the harmonic oscillator energy levels

$$E_v = \omega_e(v + \tfrac{1}{2})$$

and $$\Delta E_v = \Delta n\hbar\omega \approx 10^{-20} \text{Joules } (.06 \text{ eV}) .$$

2.2.3 Interaction between Energy Modes

A simultaneous vibration and rotation will mean that there will be some interaction between the two modes of motion. A molecular vibration means that the internuclear distance, and thus the moment of inertia is changing, and this leads to a vibrational dependence of the rotational constant B. The period of a rotation is considerably larger than the period of a vibration, so during the course of a single rotation, the molecule undergoes many vibrations, with consequent change of internuclear distance. Therefore in the presence of vibration, some sort of mean value of B must be used. Pauling and Wilson (1935) have shown that in a vibrational state v, B can be written as

$$B(v) = B_e - \alpha_e(v + \tfrac{1}{2})$$

to a first approximation, while the mean centrifugal stretching constant D can be expressed as

$$D(v) = D_e + \beta_e(v + \tfrac{1}{2})$$

The suffix e denotes values taken at the equilibrium nuclear separation r_e in the appropriate electronic state. The energy levels of a vibrating symmetric top can be written

$$E = E_{VIB} + E_{ROT}$$

or

$$E(V, J, \Lambda) = \sum_{n=1}^{\infty} A_n(v + \tfrac{1}{2})^n + B(v)\, J(J + 1)$$

$$+ (A - B(v))\Lambda^2 - D(v)J^2 (J + 1)^2$$

where A is dependent upon the moment of inertia about the internuclear axis and is unaffected by vibration and where $|\Lambda|$ is the electronic angular momentum neglecting spin, and Λ is the quantum number of the angular momentum of the electrons about the internuclear axis. Choosing A_n to suit the potential curves takes the electronic-vibration interaction into account.

2.3 The Diatomic Molecule as a Symmetric Top

The model of the rotation of a diatomic molecule described earlier was based on the assumption that the moment of inertia about the internuclear axis is zero. This is not the case, because of the electrons revolving about the two nuclei, which produce a small moment of inertia about the line joining the two nuclei. The resultant can be thought of as a symmetric top. The moment of inertia I_A about the internuclear axis is very much smaller than I_B, but the angular momentum is comparable, since the electrons rotate much more rapidly. The total angular momentum $\underset{\sim}{J}$ is then the sum of the angular momenta $\underset{\sim}{R}$ and $\underset{\sim}{\Lambda}$ perpendicular to and along the internuclear axis respectively (see Figure

2.1). Here $\underset{\sim}{R}$ represents essentially the rotation of the nuclei alone. That is

$$\underset{\sim}{J} = \underset{\sim}{R} + \underset{\sim}{\Lambda}$$

and $\underset{\sim}{J}$ is constant in magnitude and direction. The component along the internuclear axis is constant in magnitude, but not in direction, and is due to the revolution of the electrons. The magnitude is

$$|\underset{\sim}{J}| = \sqrt{J(J+1)}\,\hbar$$

and also $$|\Lambda| = \Lambda\hbar$$

Since $\underset{\sim}{\Lambda}$ and $\underset{\sim}{J}$ have integral values, $\underset{\sim}{R}$ cannot have an integral value, and there is no quantum number associated with $\underset{\sim}{R}$. $\underset{\sim}{J}$ is always larger than $\underset{\sim}{\Lambda}$, and can be written

$$J = \Lambda,\ \Lambda+1,\ \Lambda+2,\ \ldots\ldots$$

The wave equation for the symmetric top was solved by Reiche and Rademacher (1926, 1927) (see also Pauling and Wilson (1935)) and the resulting energy levels are given by

$$E(J, \Lambda) = B\,J(J+1) + (A - B)\,\Lambda^2$$

where $$B = \frac{\hbar^2}{2I_B} \quad \text{and} \quad A = \frac{\hbar^2}{2I_A}$$

and where $I_B = \mu r^2$ and I_A is the moment of inertia of the electrons about the internuclear axis. Since I_A is small, A is very much larger than B. The energy levels are very similar to those for a simple rotator except for the shift in magnitude $(A-B)\Lambda^2$, which is constant for a given electronic state. Levels with $J < \Lambda$ are absent. The non-rigid symmetric top has energy levels given by

$$E_v(J, \Lambda) = B_v\,J(J+1) + (A - B_v)\Lambda^2 - D_v\,J^2(J+1)^2$$

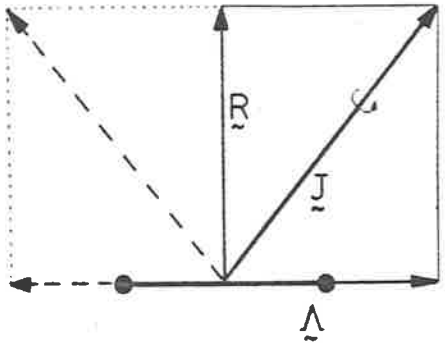

FIG 2.1 Rotation of the symmetric top about $\underset{\sim}{J}$, the total angular momentum vector. The dotted part of the Figure gives the vector diagram when the direction of $\underset{\sim}{\Lambda}$ is reversed.

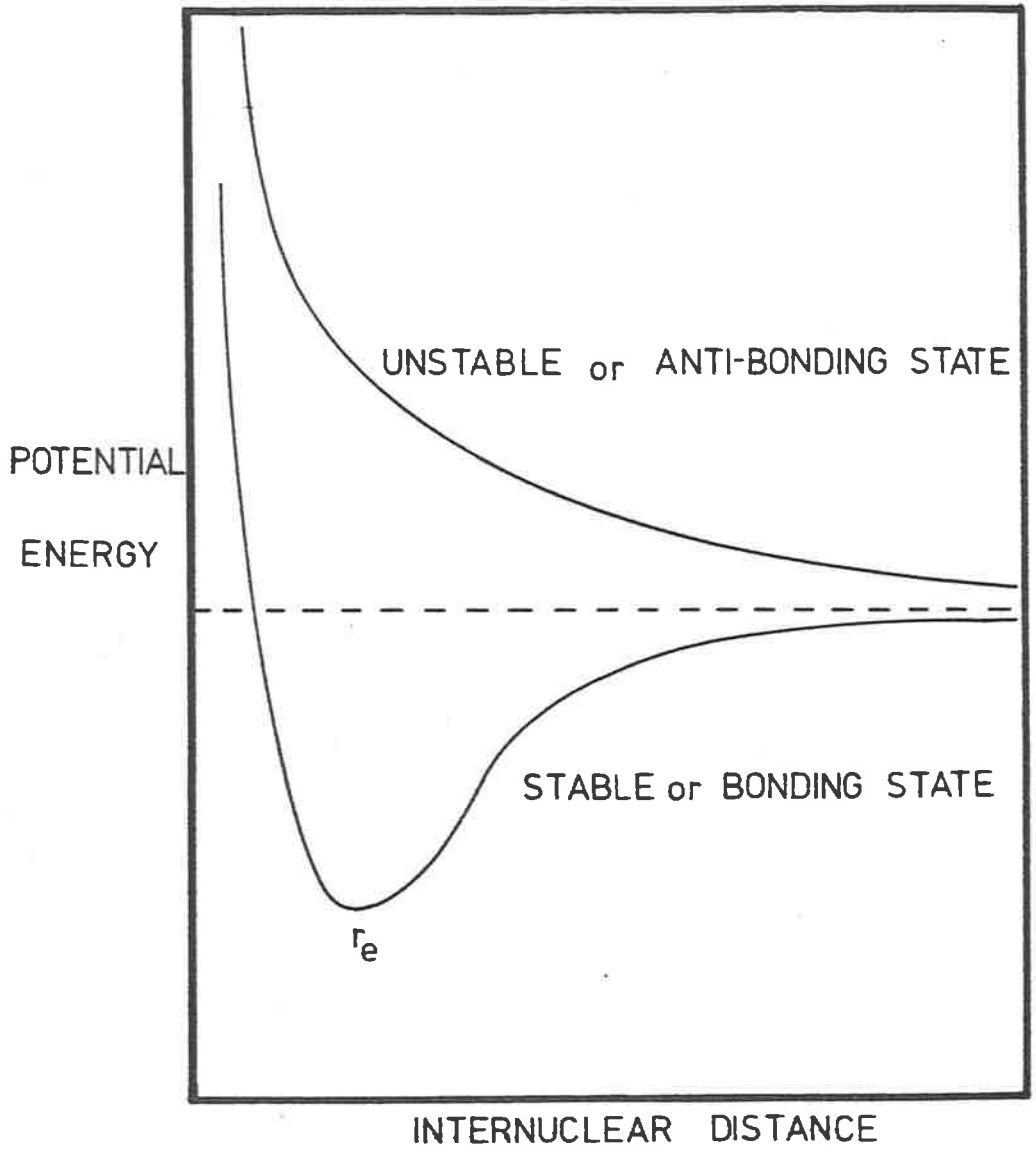

FIG 2.2 A plot of the potential energy dependence upon internuclear distance, showing a stable and an unstable molecular state.

where B_v and D_v are effective values of the rotational constants which differ for different vibrational levels.

The energy levels will be degenerate, since for each value of J, there are two values of $M_L = \pm \Lambda$. Also, M, the magnetic quantum number giving the component of J along a given axis is

$$M = J,\ J - 1,\ \ldots\ldots,\ -J$$

that is, $2J + 1$ values of M are possible, giving $(2J + 1)$ independent eigenfunctions. Energy levels with $\Lambda=0$ will be non degenerate, while levels with $\Lambda \neq 0$ will have degeneracy $2(2J + 1)$.

2.4 Electronic Energy and Total Energy

Molecules, like atoms, have different possible electronic states, depending upon which orbitals are occupied by electrons. The differences in electronic energy levels in molecules are similar to those in atoms, given by

$$\Delta E = \frac{-m e^4}{8\varepsilon_0^2 h^2} \cdot \Delta n \left(\frac{n_1 + n_2}{n_1^2 n_2^2} \right)$$

and this is approximately equal to 10^{-18} Joules (6 eV) with $n = 1$, $\Delta n = 1$ for oxygen. That is, the ratio of electronic energy to vibrational energy to rotational energy is $10^4 : 10^2 : 1$.

The molecule is held together by the attractions between nuclei and electrons of the opposing atoms being greater than the repulsive forces acting between the two nuclei and the two sets of electrons. The total energy of the molecule consists of the potential and kinetic energy of the electrons, and the potential and kinetic energy of the nuclei. Because the electrons move so much faster than the nuclei, the electronic energy when the nuclei are free to move takes up the value corresponding to the

instantaneous positions of the nuclei. The sum of the electronic energy and the Coulomb potential of the nuclei acts as the potential energy under whose influence the nuclei carry out their vibrations. If the potential energy's dependence on internuclear distance has a minimum, and only then, will the state in question be stable. No minimum means the state is unstable, and the molecule will break apart (see Figure 2.2).

The Schroedinger equation for a molecular system may be resolved into two separate equations. One describes the behaviour of electrons in the field of fixed nuclei, and the wavefunctions of this equation Ψ_e are functions of the electronic coordinates and the internuclear separation. The second equation is for the nuclei in a potential field $(E_{el} + V_N)$, where E_{el} is the total electronic energy and V_N is the nuclear Coulomb potential. Here the wavefunctions Ψ_{VR} are dependent only upon the internuclear separation.

Born and Oppenheimer (1927) showed that to a good approximation, the total eigenfunction Ψ could be split into Ψ_e and Ψ_{VR}, because the variation of Ψ_e with internuclear distance r is slow enough to make its first and second order derivatives with respect to r negligible, so we can write

$$\Psi = \Psi_e \Psi_{VR}$$

Pauling and Wilson (1935) show that Ψ_{VR} can be divided into $\frac{1}{r} \Psi_V$ and Ψ_R, so the total wavefunction can be written

$$\Psi = \Psi_e \frac{1}{r} \Psi_V \Psi_R$$

The total energy of the molecule can be considered as the sum of electronic, vibrational and rotational energies, $E = E_e + E_V + E_R$.

2.5 Symmetry Properties of the Electronic Eigenfunctions

In a diatomic molecule, any plane through the internuclear axis is a plane of symmetry. Therefore the electronic eigenfunction of a non-degenerate state (Σ state with $\Lambda = 0$) remains either unchanged or changes sign when reflected at any plane passing through both nuclei. If the eigenfunction remains unchanged it is called a Σ^+ state, if it changes sign, it is a Σ^- state. Herzberg (1950) shows that this classification is redundant for states with $\Lambda > 0$.

In diatomic molecules, where the nuclei have the same charge, as in oxygen, the field in which the electrons move has a centre of symmetry. That is, the field remains unchanged by a reflection of the nuclei about this centre (the mid-point of the internuclear axis). The electronic eigenfunctions remain either unchanged or change sign when reflected about this centre. Remaining unchanged, the state is called an even state, changing sign makes it an odd state, and these are denoted by the subscripts g and u for even and odd respectively.

For Σ states, the selection rules are

$$\Sigma^+ \longleftrightarrow \Sigma^+ , \quad \Sigma^- \longleftrightarrow \Sigma^- , \quad \Sigma^+ \not\longleftrightarrow \Sigma^-$$

The selection for even and odd states is

$$g \longleftrightarrow u , \quad g \not\longleftrightarrow g , \quad u \not\longleftrightarrow u .$$

2.6 Symmetry Properties of the Rotational Levels

2.6.1 Positive and Negative Rotational Levels

Inspection of the rotator eigenfunctions (see Section 2.2.1) shows that for a reflection about the origin the eigenfunctions either remain unchanged or simply change sign. For even values of J they remain unchanged, while for odd values of J, they change to $-\Psi_R$. A rotational level is called positive or negative depending on whether the total eigenfunction remains unchanged or changes sign upon reflection. We have

$$\Psi = \Psi_e \frac{1}{r} \Psi_v \Psi_R$$

and the vibrational component $\frac{1}{r}\Psi_v$ always remains unchanged upon reflection. If $\Lambda = 0$ and Ψ_e remain unchanged, the parity of the rotational levels is positive or negative if J is even or odd.

If $\Lambda \neq 0$, we have a symmetric top, and therefore for each value of J there is a positive and a negative rotational level of equal energy. For dipole radiation, the selection rules are positive levels combine only with negative and vice versa, that is

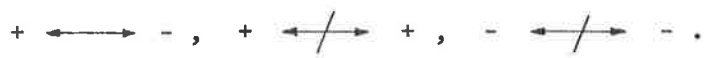

2.6.2 Symmetric and Antisymmetric Rotational Levels for Homonuclear Molecules

For homonuclear molecules, the wave equation of the system remains unchanged if the two nuclei are exchanged. So, for an exchange of nuclei, the total eigenfunction either remains unchanged or simply changes its sign. If they remain unchanged, the eigenfunctions are symmetric, if not,

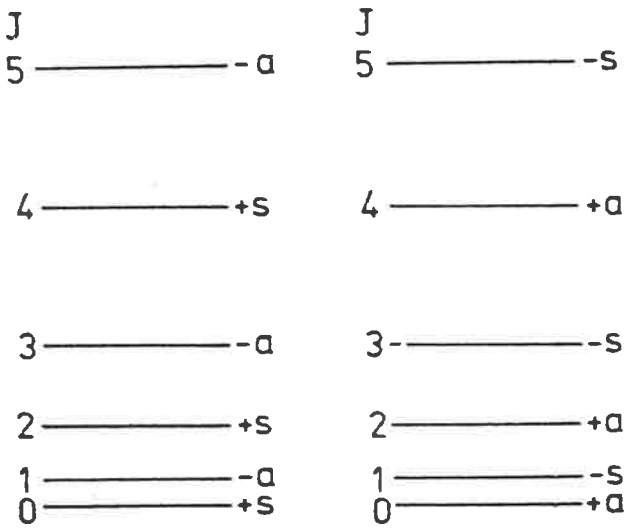

FIG 2.3 Symmetry properties of the rotational levels of homonuclear molecules with $\Lambda = 0$. The levels on the left have the positive levels symmetric and the negative antisymmetric, while the reverse is the case for the levels on the right.

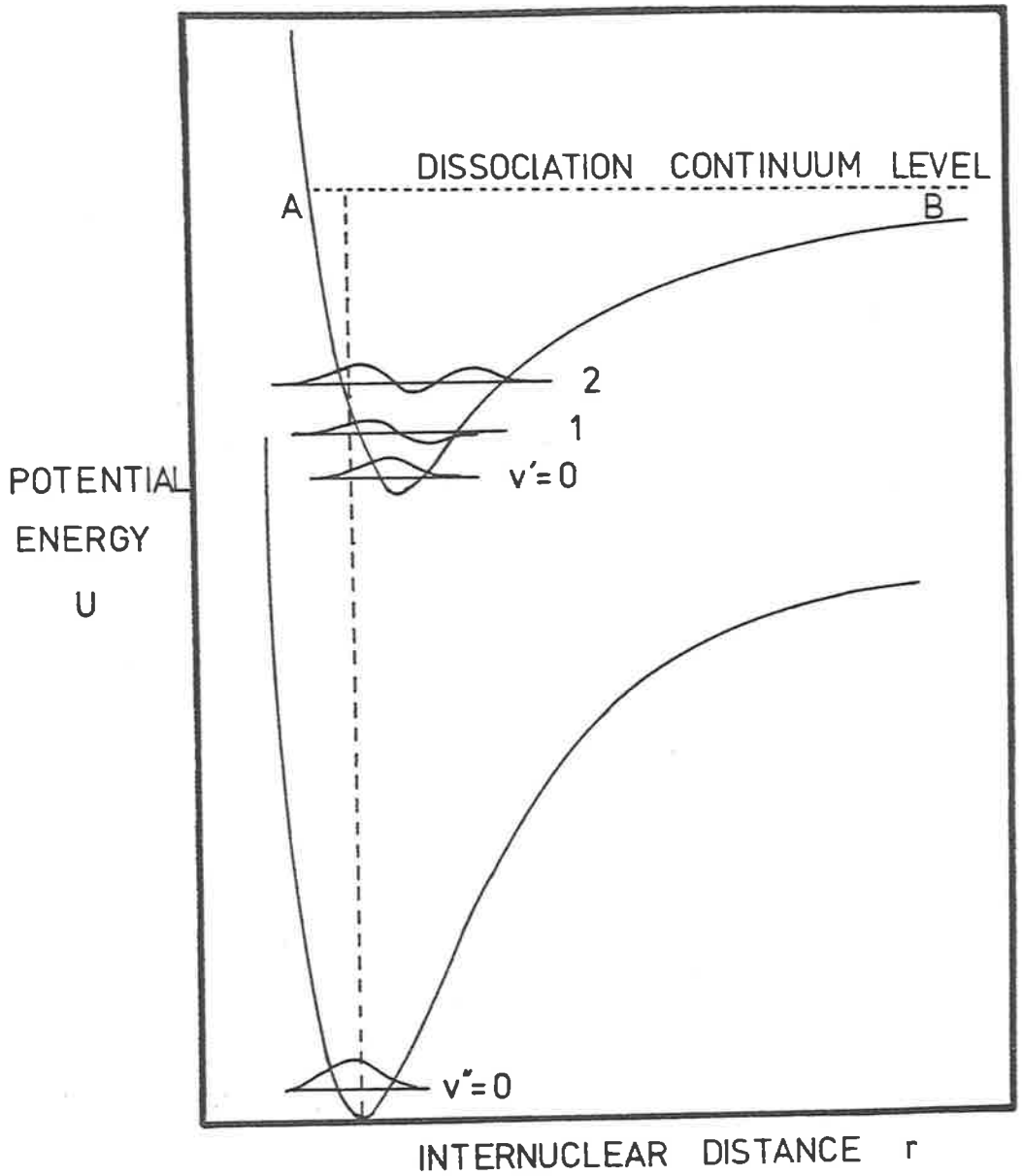

FIG 2.5 The Franck-Condon principle, illustrated for two stable states with potential curves slightly displaced. The best overlapping occurs for v''=0, v'=2, when the transition is vertically upwards.

antisymmetric. For a given electronic state, either the positive rotational levels are all symmetric, and the negative all antisymmetric or vice versa. The levels are labelled s and a depending upon whether they are symmetric or antisymmetric, and the selection rules are

$$s \longleftrightarrow s\,, \quad a \longleftrightarrow a\,, \quad s \not\longleftrightarrow a\,.$$

In a given electronic state of a molecule, either the positive rotational levels are symmetric and the negative are anti-symmetric throughout, or vice versa. For the case with $\Lambda = 0$, either the even-numbered levels are symmetric (s) and the odd are antisymmetric (a), or the reverse is the case. Figure 2.3 shows the two alternatives for electronic states whose Ψ_e remains unchanged upon reflection at a plane through the internuclear axis. For electronic states where Ψ_e changes sign, both designations -, + and s, a must be reversed.

2.7 The Influence of Nuclear Spin

The nuclear spin may be non-zero, giving an angular momentum $\underset{\sim}{I}$, and this produces an alternation in intensity, where every second line is weaker. There is a contribution to the statistical weights of the various levels (Tatum (1967)), and for homonuclear molecules, can be written

I	integral	$(2I + 1) \cdot (I + 1)$	for a levels
		$(2I + 1) \cdot I$	for a levels
I	odd-half integral	$(2I + 1)\ I$	for s levels
		$(2I + 1) \cdot (I + 1)$	for a levels .

If the nuclear spin is zero, as is the case for O_2, then every alternate line will be completely missing.

2.8 Classification of Electronic States

In diatomic molecules, only the component of the orbital angular momentum of the electrons about the internuclear axis is a constant of the motion. This component along the axis of $\underset{\sim}{L}$ is M_L, and M_L can take the values

$$M_L = L,\ L-1,\ \ldots,\ -L$$

In diatomic molecules, states differing only in the sign of M_L have the same energy. States with different $|M_L|$ have widely different energies. Accordingly we define

$$\Lambda = |M_L|$$

where Λ represents the component of the electronic orbital angular momentum along the internuclear axis, of magnitude $\Lambda\hbar$. Λ can take the values $\Lambda = 0, 1, 2, \ldots L$, and the states are designated Σ, π, Δ, ϕ, etc., where the π, Δ, ϕ, ... states are doubly degenerate.

In molecules, as in atoms, the spins of the electrons form a resultant $\underset{\sim}{S}$, the corresponding quantum number S being integral or half integral as the number of electrons is even or odd. M_s is the component along the internuclear axis, and is denoted by Σ, where

$$\Sigma = S,\ S-1,\ S-2,\ \ldots,\ -S$$

That is, there are $2S+1$ values. Σ can be positive or negative, and is undefined for states with $\Lambda = 0$ (Σ states).

The total angular momentum of the electrons, denoted by $\underset{\sim}{\Omega}$ is the sum of $\underset{\sim}{\Lambda}$ and $\underset{\sim}{\Sigma}$. Since both $\underset{\sim}{\Lambda}$ and $\underset{\sim}{\Sigma}$ are along the internuclear axis, algebraic summing is sufficient. The total quantum number is then

$$\Omega = |\Lambda + \Sigma|$$

Therefore an electronic term with $\Lambda \neq 0$ splits into $2S + 1$ components. If $\Lambda = 0$, in the absence of rotation, no splitting occurs. The quantity of $2S + 1$ is called the multiplicity. A full electronic state may then be written as, adding the symmetry properties

$$^{2S+1}\Lambda_{\Lambda + \Sigma}$$

and in the case of Σ states are written

$$^{2S+1}\Sigma^{+,-}_{g,u}$$

2.9 Coupling of Electronic and Rotational Motion

The influence of rotational and vibrational motions upon each other has already been discussed, as has the coupling of vibrational and electronic motions, where the vibrational levels are chosen to fit the potential curve of the electronic state. All that remains to consider, is the influence of rotational and electronic motion on each other.

The different angular momenta in the molecule such as electron spin, electronic orbital angular momentum and angular momentum of nuclear rotation form a resultant $\underline{J}$, the total angular momentum. If the spin $\underline{S}$ and orbital angular momentum $\underline{\Lambda}$ of the electrons are zero, that is a $^1\Sigma$ state, then the angular momentum of nuclear rotation is identical with the total angular momentum $\underline{J}$, and we have the simple rotator case. In all other cases, there are different modes of coupling, first investigated by Hund.

2.9.1 Hund's case (a)

Here the interaction of the nuclear rotation with the electronic motion (spin as well as orbital) is weak, but the electronic motion is coupled very strongly to the line joining the two nuclei. The electronic angular momentum $\underset{\sim}{\Omega}$ is well defined, and with $\underset{\sim}{R}$, the angular momentum of nuclear rotation, forms the resultant $\underset{\sim}{J}$. We have

$$J = \Omega, \quad \Omega + 1, \quad \Omega + 2, \ldots.$$

that is, levels with $J < \Omega$ do not occur.

2.9.2 Hund's case (b)

When $\Lambda = 0$, and $S \neq o$, the spin vector $\underset{\sim}{S}$ is not coupled to the internuclear axis at all, or for light atoms with $\Lambda \neq 0$, the coupling may be weak, and therefore $\underset{\sim}{\Omega}$ is not defined. In this case the angular moments $\underset{\sim}{\Lambda}$ (when $\Lambda \neq 0$) and $\underset{\sim}{R}$ form a resultant $\underset{\sim}{N}$ (as did $\underset{\sim}{\Omega}$ and $\underset{\sim}{R}$ in case (a)) and where

$$N = \Lambda, \quad \Lambda + 1, \quad \Lambda + 2, \ldots.$$

where $\underset{\sim}{N}$ is the total angular momentum apart from spin. If $\Lambda = 0$ then $\underset{\sim}{N} \equiv \underset{\sim}{R}$, and is therefore perpendicular to the internuclear axis, $\underset{\sim}{N}$ and $\underset{\sim}{S}$ form a resultant $\underset{\sim}{J}$, the total angular momentum. Possible values for the quantum number J are

$$J = N + S, \quad N + S - 1, \quad N + S - 2, \ldots.|N-S|$$

Therefore in general (except when $N < S$) each level with a given N consists of $2S + 1$ components. Again J is half-integral for an odd number of electrons, and integral for an even number of electrons. A slight coupling of $\underset{\sim}{S}$ and $\underset{\sim}{N}$ produces a small splitting of the levels with different J and equal N, which increases with increasing N.

Other coupling cases are also possible, and are dealt with more

fully in Herzberg. Hund's coupling cases (a) and (b) are the ones most often encountered.

N.B. The quantities $\underset{\sim}{N}$ and $\underset{\sim}{R}$ and the quantum number for $\underset{\sim}{N}$, N are referred to in Herzberg as $\underset{\sim}{K}$ and $\underset{\sim}{N}$ respectively, with the quantum number of $\underset{\sim}{K}$ being K . This change was made in 1953 by the International Astronomical Union.

2.10 Selection Rules

Whether a transition will take place between two particular levels of a diatomic molecule depends on the quantum numbers and symmetry properties of the two levels concerned. These selection rules are obtained by calculating the matrix elements R_{12} of the electric dipole moment of equation 2.8. This matrix element may turn out to be zero, in which case the transition strength is zero, and the transition is denoted as forbidden (at least for electronic dipole radiation). If the matrix element is non-zero, then the transition is allowed. There are selection rules that always apply, regardless of the two states involved, and there are selection rules which apply to particular energy levels.

2.10.1 General Selection Rules

These selection rules apply to all states.

(1) The selection rule for the total angular momentum quantum number J is

$$\Delta J = 0, \pm 1 \quad \text{with} \quad J = 0 \not\longleftrightarrow J = 0$$

That is $\Delta J = 0$ is not allowed for Σ-Σ transitions.

(2) Parity must change. Positive terms combine only with negative and vice versa. This is written as

$$+ \longleftrightarrow - \qquad + \not\longleftrightarrow + \qquad - \not\longleftrightarrow -$$

(3) Nuclear symmetry must not change. That is, symmetric states combine only with symmetric and antisymmetric only with antisymmetric, and this is denoted as

$$s \longleftrightarrow s, \quad a \longleftrightarrow a, \quad s \not\longleftrightarrow a$$

(4) Finally, for molecules with equal nuclear charge, even electronic states combine only with odd, and this is written as

$$g \longleftrightarrow u, \qquad u \not\longleftrightarrow u, \qquad g \not\longleftrightarrow g$$

2.10.2 Selection Rules holding in case (a) and case (b)

Some selection rules hold in Hund's case (a) and Hund's case (b), but not in other coupling cases. These are the cases that occur most frequently, so these selection rules are significant.

(5) $\Delta \Lambda = 0, \pm 1$

(6) reflection symmetry does not change, that is

$$\Sigma^+ \longleftrightarrow \Sigma^+ , \quad \Sigma^- \longleftrightarrow \Sigma^-, \quad \Sigma^+ \not\longleftrightarrow \Sigma^-$$

and both Σ^+ and Σ^- can combine with π states.

(7) $\Delta S = 0$, so only states of the same multiplicity can combine with each other.

2.10.3 Selection Rules holding for case (a)

Σ, the quantum number of the component of spin along the internuclear axis is defined, so for both states belonging to case (a) $\Delta \Sigma = 0$ that is, the component of spin along the internuclear axis does not alter. Also applying are $\Delta \Omega = 0, \pm 1$ and $\Delta J = 0$ is forbidden for $\Omega = 0 \longleftrightarrow \Omega = 0$.

2.10.4 Selection Rules holding for case (b)

$\mathcal{N}$, the total angular momentum apart from spin, is bound by the rule on its quantum number N of

$$\Delta N = 0, \pm 1$$

but $\Delta N = 0$ is forbidden for Σ-Σ transitions.

2.11 Selection Rules Applied to the Schumann-Runge Bands

The selection rules discussed in the previous section can be applied to the Schumann-Runge bands. The electronic transition in question is

$$X^3\ \Sigma_g^- \longrightarrow B^3\ \Sigma_u^-$$

so the selection rules

$$\Delta\Lambda = 0, \pm 1,\quad \Sigma^- \longleftrightarrow \Sigma^-,\quad g \longleftrightarrow u \quad \text{and} \quad \Delta S = 0$$

are obviously obeyed. The selection rules still remaining are

$\Delta J = 0, \pm 1$ and can be denoted as follows

$$\begin{aligned}
\Delta J = +1 &= F_{v'}(J+1) \longrightarrow F_{v''}(J) && \text{R branch}\\
\Delta J = 0 &= F_{v'}(J) \longrightarrow F_{v''}(J) && \text{Q branch} \qquad (2.8)\\
\Delta J = -1 &= F_{v'}(J-1) \longrightarrow F_{v''}(J) && \text{P branch}
\end{aligned}$$

Figure 2.4 shows the possible transitions for the 15-0 band of the Schumann-Runge bands, with levels of alternate N values missing in both the ground state and the upper state (the even-numbered N missing in the ground state, the odd-numbered N levels missing in the upper state) due to zero nuclear spin (see Section 2.7). This results in only symmetric levels (s) occurring in both states, and only positive levels (+) occurring in the ground state, and only negative levels (-) in the upper state, so the last two selection rules $s \longleftrightarrow a$, $+ \longleftrightarrow -$ are automatically fulfilled. This also means there is no Q branch for the Schumann-Runge bands.

It should now be possible to discuss the terminology used in later chapters. For example, the oscillator strength of the $R_{13}(2\text{-}0)$ may be discussed, and this terminology contains the quantum numbers used above.

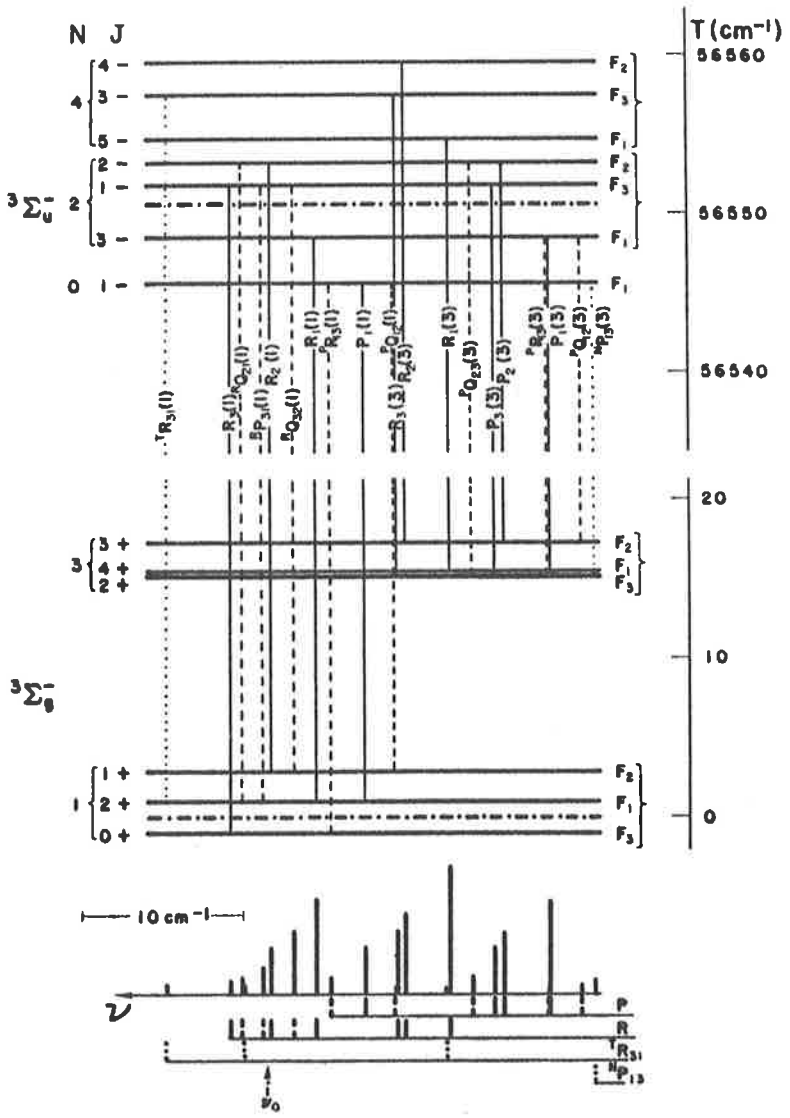

FIG 2.4 Energy level diagram of a $^3\Sigma_u^- - {}^3\Sigma_g^-$ band.

The figure is drawn to scale for the 15–0 band of the Schumann-Runge system. The vertical lines representing the transitions are drawn in such a way that their projections below give a representation of the spectrum. The main branches are indicated by full lines, the satellite branches by broken lines, and the "forbidden" branches (with $\Delta N = \pm 3$) by dotted lines. The (nonexisting) $N = 0$, $J = 0$ levels and, correspondingly, the band origin ν_0 are marked by dot-dash lines. Estimated intensities are indicated by different heights of the "lines" in the schematic spectrum. The lines $^TR_{31}(3)$ and $^TR_{31}(5)$ originating from higher rotational levels of the upper state could not be shown in the energy level diagram. Their positions have, however, been marked in the schematic spectrum below because they fall into the region of the band head. The lines $^PQ_{12}(1)$ and $^PR_{13}(3)$ as well as the satellite lines for the $R(3)$ transition (not drawn) have not been observed in any of the bands under investigation.

(Reproduced from Brix and Herzberg (1954))

That is, (2-0) means $v' = 2$, $v'' = 0$. R_{13} means $\Delta J = +1$, $N'' = 13 \longrightarrow N' = 14$. The R_{13} line actually consists of a triplet of lines, the $R_1(13)$, $R_2(13)$ and $R_3(13)$, where $J'' = N'' + 1$, N'', $N'' - 1$ respectively. Similarly, the $P_{11}(5-0)$ line, means $v' = 5$, $v'' = 0$, $\Delta J = -1$, $N' = 11 \longrightarrow N'' = 10$, and this line is also composed of a triplet of lines, the $P_1(11)$, $P_2(11)$ and $P_3(11)$ lines with $N'' = 11$, $J'' = N'' + 1$, N'', $N'' - 1$ respectively, there are six main branches between any two levels, and they are P_1, P_2, P_3 and R_1, R_2, R_3 There are also six allowed satellite branches, denoted by $^{P}Q_{12}$, $^{P}Q_{23}$, $^{P}R_{13}$, $^{R}Q_{21}$, $^{R}Q_{32}$, $^{R}Q_{31}$ (shown in Figure 2.4). The strengths of these satellite branches fall off very rapidly with N, and they only play a significant role near the band head ($N \leqslant 7$). The selection rule $\Delta N = \pm 1$ is not as rigorous as the other selection rules, and lines with $\Delta N = \pm 3$ have been observed, denoted by $^{T}R_{31}$ and $^{N}P_{13}$, but they only occur weakly, for low N values.

2.12 Transition and Transition Strength

The strengths of transitions between the various molecular states described previously vary greatly. As shown by the previous section, many transitions are completely forbidden. The interaction of an electromagnetic wave with electric vector $\underset{\sim}{E}$ with a molecule of electric dipole moment $\underset{\sim}{M}$ has been done by Pauling and Wilson (1935), and for a molecule in state 1 undergoing a transition to a higher state 2 when exposed to radiation of energy $h\nu = \Delta E$, the energy difference between the states, it is found that

$$B_{12} = \frac{8\pi^3 \left|R_{12}\right|^2}{3h^2 \; 4\pi \; \varepsilon_o}$$

where B_{12} is the Einstein transition probability of absorption, and R_{12} is the transition moment, written

$$R_{12}(r) = \int \Psi_1 \; \underset{\sim}{M} \; \Psi_2 \; \alpha \; \tau \qquad (2.9)$$

where Ψ_1 and Ψ_2 are the total wave functions.

It is often useful to consider the components of R , where

$$\left|R_{12}(r)\right|^2 = \left|R_{12}(x)\right|^2 + \left|R_{12}(y)\right|^2 + \left|R_{12}(z)\right|^2$$

and it is to these transitions to which all quantities referring to line strength eventually relate. The electric dipole line strength S is defined by

$$S_{12} = \left|R_{12}\right|^2 = \left|R_{12}(x)\right|^2 + \left|R_{12}(y)\right|^2 + \left|R_{12}(z)\right|^2$$

$$= e^2 \left(\left|x_{12}\right|^2 + \left|y_{12}\right|^2 + \left|z_{12}\right|^2\right)$$

where x_{12}, y_{12} and z_{12} are the electric dipole moment matrix elements.

The strengths of transitions between states depends primarily on the overlap integral between the two wavefunctions, given by equation 2.8. If the matrix element is non-zero, and therefore an allowed transition, then this matrix element or transition moment can take a range of values, the larger the value, the greater the transition strength. Wavefunctions which maximize this overlap, will therefore be accompanied by the strongest transitions.

2.13 Population Numbers and the Boltzmann Distribution

The strength of a line depends not only on the transition probability, but also upon the population of the state from which the transition arises.

Boltzmann's formula for the ratio of the populations of two energy levels E_1 and E_2 in thermal equilibrium at temperature T is

$$\frac{N_2}{N_1} = \frac{g_2}{g_1} \exp\left[- \left(\frac{E_2 - E_1}{K_B T} \right) \right]$$

where g_1 and g_2 are the statistical weights of the respective states, N_1 and N_2 are their populations and K_B is Boltzmann's constant. This can be written as

$$\frac{N_1}{N} = \frac{g_1}{Q_{int}} \exp\left(- \frac{E_1}{K_B T} \right) \qquad (2.10)$$

where N is the total number of particles, $\exp(- E_1/K_B T)$ is the Boltzmann factor and Q_{int} is the partition function given by

$$Q_{int} = \sum_{j=o}^{\infty} g_j \exp(- E_j/K_B T)$$

and is the sum of all the weighted Boltzmann factors. At room temperature only the ground state vibrational level is populated to a significant extent, although the 1st excited vibrational level has a small fraction of

the population. The rotational levels in the ground vibrational state are populated, since the energy available at room temperature ($\sim 300\ ^{\circ}K$) is $300 \times 1.38 \times 10^{-23} = 4.2 \times 10^{-21}$ Joules and $G(v) = \Delta E_{VIB} \sim 10^{-20}$ Joules while $F(J) = \Delta E_{ROT} \sim 5.7 \times 10^{-23}$ Joules. That is the thermal energy available at $300\ ^{\circ}K$ is sufficient to excite some of the molecules to the first vibrational level, and to a large number of rotational levels.

Tatum (1967) gives a detailed analysis of population number for all the different types of energy levels. Since the Schumann-Runge bands consist of transitions between states, the following equations are specifically for such states.

Consider a sample consisting of N molecules. The fraction of these molecules in a particular electronic state n is given by

$$\frac{N(n)}{N} = \frac{g_e \exp[- (hc/K_B T)T_e]}{\sum_{\text{all states}} g_e \exp[- (hc/K_B T)T_e]} \qquad (2.11)$$

where $N(n)$ is the number of molecules in electronic state n, N is the total number of molecules, T_e is the electronic energy, and g_e is the electronic statistical weight, given by $g_e = (2 - \delta_{o,\Lambda})(2S + 1) = (2S + 1)$ for Σ states.

The denominator in equation 2.10 is the electronic partition function, Q_{el}.

Of the $N(n)$ molecules in the electronic state n, the fraction in the vibrational level v of that state is

$$\frac{N(nv)}{N(n)} = \exp[- \frac{hc}{K_B T} G(v)] \Big/ \sum_{v=o}^{v\ max} \exp[- \frac{hc}{K_B T} G(v)] \qquad (2.12)$$

where $G(v)$, the vibrational energy should be referred to the lowest vibrational level, and not the potential minimum. The statistical weight of vibrational levels is 1 . The denominator of equation 2.12 is the vibrational partition function, Q_{VIB} .

Of the molecules in that vibrational state, the fraction in the Nth rotational level is

$$\frac{N(nvN)}{N(nv)} = \frac{2\phi\ hc\ B_v}{K_B T}\ (2N + 1)\ \exp\left[- \frac{hc}{K_B T}\ F(N) \right] \qquad (2.13)$$

where $\phi = \frac{I+1}{2I+1}$ for s levels, and $\frac{I}{2I+1}$ for a levels (see section 2.7), and B_v is the rotational constant for the vth vibrational level. The rotational partition function in equation 2.12 has been replaced by

$$\frac{K_B T}{B_v hc}$$

a good enough approximation at temperatures above $273\ ^\circ K$.

The number of molecules in sub-level J is $N(nvN\ J)$ and is given by

$$\frac{N(nvN\ J)}{N(nvN)} = \frac{2J + 1}{(2S+1)(2N+1)} \qquad (2.14)$$

except for the $N = 0$ state of a Σ state, in which case $N(nvNJ) = N(nvN)$, and where $(2J + 1)$ is the rotational statistical weight.

Transitions involving Σ states are always single, and states are always of the Hund's case (b) coupling type. The population of a single level is then, using all the above interrelations is

$$\frac{N(nvNJ)}{N} = 2\phi\ \frac{(2J + 1)\ \exp\left[- \frac{hc}{K_B T}\ (T_e + G(v) + F(J)) \right]}{Q_{el}\ Q_{VIB}\ Q_{ROT}} \qquad (2.15)$$

and where the electronic statistical weight g_e is 1, since only one state is under discussion.

The above section allows the populations of levels to be calculated, but what is also needed, is the transition strengths of the various allowed transitions.

2.14 Line Strengths

For a molecular line within a band, the line strength S can be written as

$$S = \mathcal{S}(N' J' , N'' J'') \quad R_{ev}^2 \ (n', v', n'' v'')$$

or $$S = \mathcal{S}(N' J' , N'' J'') \ . \ \mathcal{S}(n' v' , n'' v'') \qquad (2.16)$$

where $\mathcal{S}(n'v', n''v'')$ is the band strength (usually denoted $p'v'v''$) and is the square of the transition moment of the band. The n', n'' are the upper and lower molecular states, and the v', v'' are the vibrational levels in these states. The $\mathcal{S}(N' J', N'' J'')$ are related to the Hönl-London factors. The justification for the above factorization is the Born-Oppenheimer approximation, which regards the effects of nuclear motion as perturbations to the electronic wavefunctions. It is possible to write the total wave function as the product

$$\Psi = \Psi_{el}(r) \ \Psi_{VIB}(r) \ \Psi_{ROT}$$

where the first two terms depend on the internuclear separation r, and the last term only has angular dependence. The radial part of the transition moment can be written

$$S(n'v', n''v'') = \left| \int \Psi_{v'} R_e(r) \ \Psi_{v''} dr \right|^2$$

where $R_e = \int \Psi_e^* \ \underset{\sim}{M} \ \Psi_e \ d\tau$ and $\underset{\sim}{M}$ is the dipole moment of the

molecule. Since both the vibrational and electronic wavefunctions are functions of r, the integral cannot be separated exactly into two factors. However, if R_e is assumed to vary slowly with r over the range in question, the approximation

$$S(n'v', n''v'') = \mathcal{S}(v',v'') . \; R_e^{\,2}(n',n'')$$

may be made. Here $\mathcal{S}(v',v'')$ is the Franck-Condon factor (usually written $q_{v',v''}$), and is a measure of the overlap integral between two vibrational wave functions. That is

$$\mathcal{S}(v',v'') = \left| \int \Psi_{v'} \, \Psi_{v''} \, dr \right|^2$$

and these factors satisfy the sum rules

$$\sum_{v'} \mathcal{S}(v',v'') = \sum_{v''} \mathcal{S}(v',v'') = 1$$

It would appear that the band strength $S(n'v',n''v'')$ could be determined from the Franck-Condon factors, and a knowledge of $R_e^{\,2}$. However, $R_e^{\,2}$ has a dependence upon v' and v'' (that is, the Born-Oppenheimer approximation is inadequate), and the $R_e^{\,2}$ term has been replaced by a mean $< R_e^{\,2} >$ for the whole system, which is independent of v' and v''. This quantity is called the r-centroid, and is defined as

$$< r_{v'\,v''} > = \frac{\int \Psi_{v'} \, \Psi_{v''} \, r dr}{\int \Psi_{v'} \, \Psi_{v''} \, dr} \qquad (2.17)$$

An electronic transition, in a homonuclear molecule such as oxygen, is accompanied by vibrational and rotational changes of state. The strengths of the vibrational and rotational transitions are given by the Franck-Condon factors and the Hönl-London factors, respectively.

2.14.1 The Franck-Condon Principle

The variations in the vibrational intensity distribution can be explained briefly as due to a maximizing of the overlap of vibrational

wavefunctions. Franck's postulate was that an electron jump in a molecule takes place so rapidly in comparison to the vibrational motion that immediately after the transition the nuclei still have very nearly the same relative positions and velocities as before. Condon showed that this corresponds to transitions vertically upwards or downwards in the potential energy diagram (see Figure 2.5). Since the ground state vibrational wavefunction has its maximum at the centre of the potential curve, whenever this centre lines up with the maximum of some other vibrational state in the upper state, the transition with the greatest strength will occur. Thus, Franck-Condon factors are a measure of the overlap, and thus the strength of various vibrational transitions.

2.14.2 Hönl-London Factors

The Hönl-London factors determine the relative intensities of the branches within a band, in the case of the Schumann-Runge bands, the rotational line strengths for a given vibrational transition.

The Hönl-London factors $S(N'J', N''J'')$ are often normalized so that

$$\sum_{J' \text{or} J''} S(N'J', N''J'') = 2J' + 1 \quad \text{or} \quad 2J'' + 1$$

respectively.

A table of Hönl-London factors for the Hund's case (b) coupling is given in Table 2.1. (see also Tatum (1966).

Tatum and Watson (1971) present Hönl-London factors for intermediate coupling cases, pointing out that departures from Hund's coupling case (b) have been observed in the Schumann-Runge bands. However, a comparison of the two types of Hönl-London factors shows virtually exact

TABLE 2.1

Hönl-London Factors for $^3\Sigma^{\pm} - {}^3\Sigma^{\pm}$ Transitions.

P_1	$\frac{N''(2N'' + 3)}{2N'' + 1}$	$\frac{(J'' - 1)(2J'' + 1)}{2J'' - 1}$
R_1	$\frac{(N'' + 1)(2N'' + 5)}{2N'' + 3}$	$\frac{J''(2J'' + 3)}{2J'' + 1}$
PQ_{12}	$\frac{1}{N''}$	$\frac{1}{J''}$
P_2	$\frac{(N'' - 1)(N'' + 1)}{N''}$	$\frac{(J'' - 1)(J'' + 1)}{N''}$
R_2	$\frac{N''(N'' + 2)}{N'' + 1}$	$\frac{J''(J'' + 2)}{J'' + 1}$
PQ_{23}	$\frac{1}{N''}$	$\frac{1}{J'' + 1}$
RQ_{21}	$\frac{1}{N'' + 1}$	$\frac{1}{J''}$
P_3	$\frac{N''(2N'' - 3)}{2N'' - 1}$	$\frac{(J'' + 1)(2J'' - 1)}{2J'' + 1}$
R_3	$\frac{(N'' + 1)(2N'' - 1)}{2N'' + 1}$	$\frac{(J'' + 2)(2J'' + 1)}{2J'' + 3}$
RQ_{32}	$\frac{1}{(N'' + 1)(2N'' + 1)(2N'' + 3)}$	$\frac{1}{J''(2J'' - 1)(2J'' + 1)}$

(Reproduced from Tatum (1966))

agreement for rotational levels above $N'' = 5$, with only slight departures below this level, so the original factors of Tatum (1966) were used in the results analysis.

2.15 Oscillator Strength

When the Hönl-London factors have been correctly normalized, then the line strength S can be written

$$S = \frac{\delta(N'J', N''J'')}{(2S + 1)} \cdot \frac{S(n'v', n''v'')}{(2J + 1)} \qquad (2.18)$$

for a Σ state. The designation J in $(2J + 1)$ should be changed to J' or J'' depending upon whether emission or absorption is being discussed. The quantity, oscillator strength is defined as the ratio of the number of classical oscillators N to the number of molecules N which absorb the same amount of energy, that is

$$N = N f$$

where f is the oscillator strength. The oscillator strength of a line is related to the line strength S by (Thorne (1974))

$$f(v'J', v''J'') = \frac{8\pi^2 m\nu_J S}{3he^2} = \frac{8\pi^2 m\nu_J}{3he^2} \frac{\delta(N'J', N''J'')}{(2S + 1)} \frac{S(n'v', n''v'')}{(2J + 1)} \qquad (2.19)$$

where ν_J is the frequency corresponding to the energy difference between the states.

A band oscillator strength can be defined by summing $f(v'J', v''J'')$ over all branches of the J'' sub-levels, that is

$$f(v', v'') = \sum_{J'} f(v'J', v''J'') = \frac{8\pi^2 m\nu_v}{3he^2} \frac{S(n'v', n''v'')}{(2S + 1)}$$

where ν_v is the frequency corresponding to the energy difference between the two vibrational levels. We can write

$$f\ (v',v'') = \frac{f\,(v'J',\ v''J'')\,(2J+1)}{\delta(N'J',N''J'')}\ \frac{\nu_v}{\nu_J}$$

or as $f\ (v'J',v''J'') = f\ (v',v'')\ \frac{\delta(N'J',N''J'')}{(2J+1)}\ \frac{\lambda_v}{\lambda_J}$

That is, there is a wavelength dependence in the summing procedure. Only if the extent of the vibrational band is small, that is $\lambda_v \sim \lambda_J$, can it be said that

$$f\ (v'J',\ v''J'') = \frac{f\ (v',v'')\ \ \delta(N'J',\ N''J'')}{(2J+1)} \qquad (2.20)$$

and also that

$$f\ (v',v'') = \sum_J f\,(v'J',\ v''J'').$$

That is the band f-value can be obtained from the line f-values by summing over all transitions of lines comprising the band.

2.16 Predissociation

Predissociation is discussed comprehensively in Herzberg (1950), and only a short introduction, sufficient for understanding later sections of this thesis, is given here. Transitions between different states were discussed previously in the section on the Franck-Condon principle. The states shown in Figure 2.5 were all bound states. If a transition should occur between the lower state $v'' = 0$ and a state v' above the level A-B (of Figure 2.5), then dissociation of the molecule would take place, since A-B designates the dissociation continuum level.

If the situation in Figure 2.6 is now considered, then it can be seen that the bound states of the upper potential curve have dissociation levels of other states below them. This means that vibrational and rotational states of the upper electronic state, given by the upper potential curve, can make radiationless transitions to states belonging to the lower electronic level, and when this lower level is an unbound state, or corresponds to a vibrational or rotational state above the dissociation level if it is a bound, stable state, then predissociation occurs for the molecule. The predissociation, illustrated more clearly in Figure 2.7, does not necessarily occur immediately the molecule is in the region of the intersection point of the two curves, but occurs with a probability that depends on the types of states in question. The larger the overlap of wavefunctions, as shown in Figure 2.7, the more likely is the transition and the shorter is the predissociation lifetime τ_p. This gives a relation to the predissociated linewidth α_p, using the uncertainty principle, and is discussed further in Section 3.3.3. The predissociation lifetime τ_p is usually much larger than the natural lifetime τ_N, and so the lines appear to be broadened, as is the case in the Schumann-Runge bands.

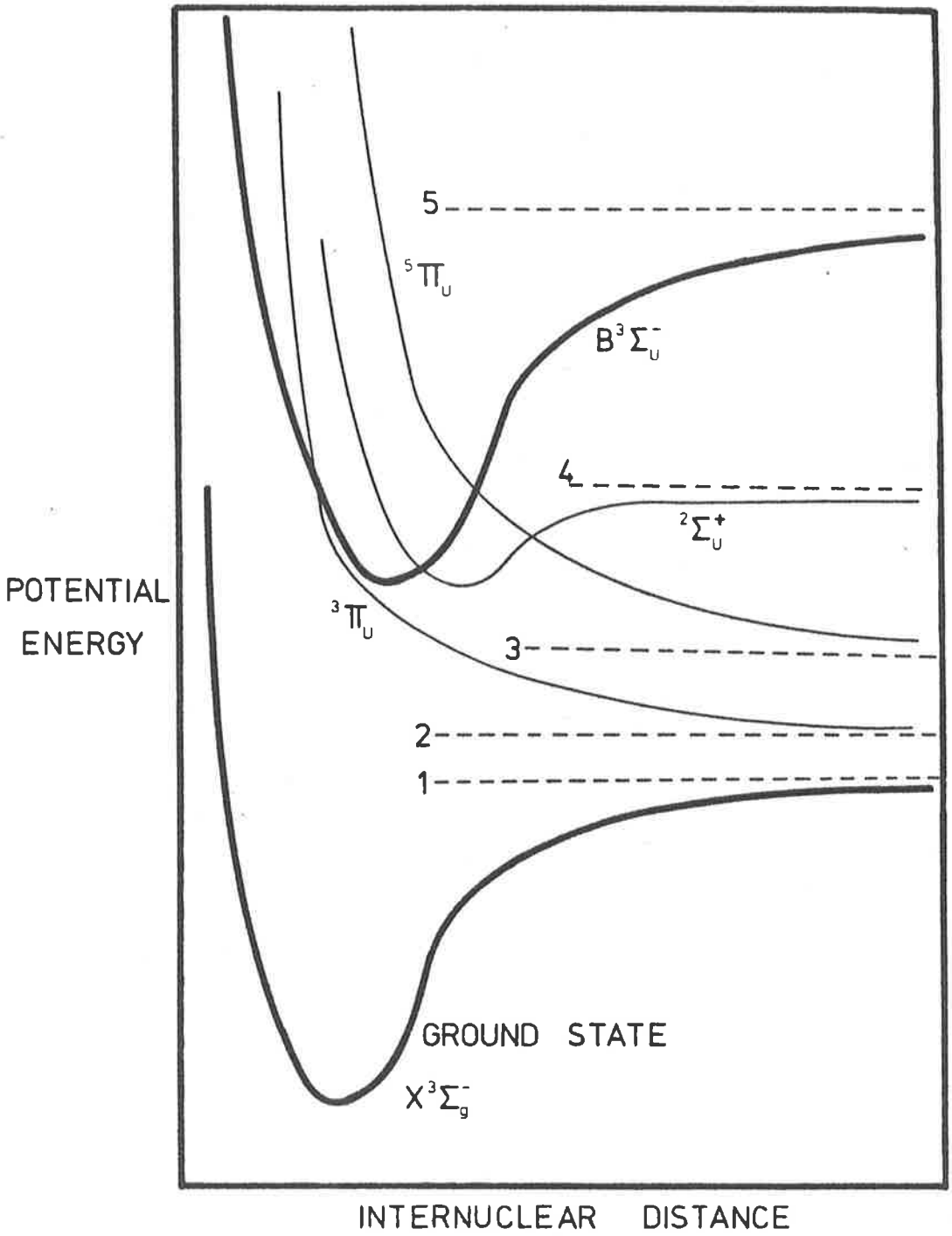

FIG 2.6 A hypothetical example of a molecule which would undergo predissociation. This case is very similar to oxygen, and the upper state $B^3\Sigma_u^-$ can predissociate to the $^3\pi_u$, $^5\pi_u$ or $^2\Sigma_u^+$ states, since all these states have dissociation levels below the stable occupied levels of the $B^3\Sigma_u^-$ state. The various dissociation levels are denoted by the numbers 1 - 5 .

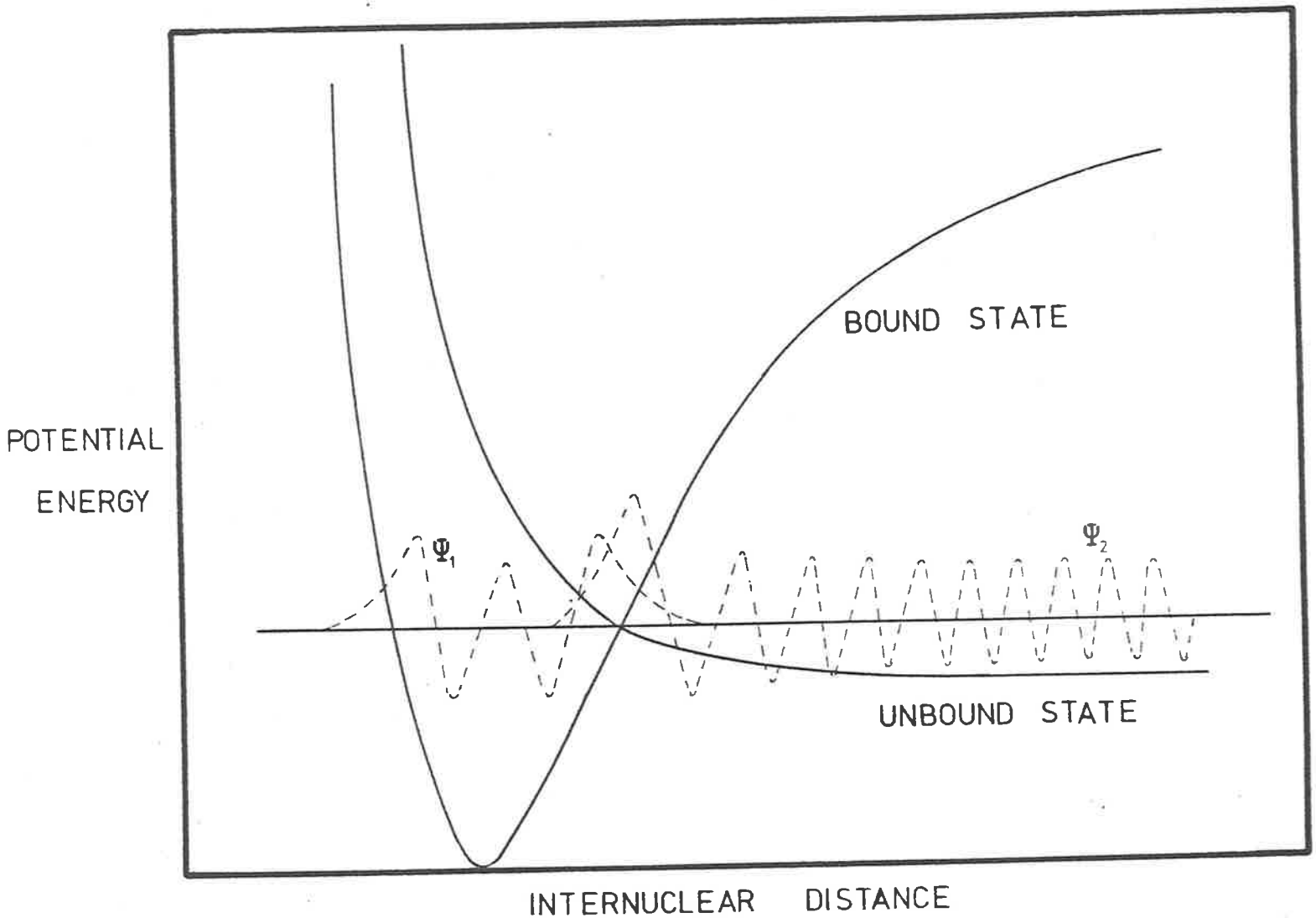

FIG 2.7 The Franck-Condon principle in predissociation. The larger the overlap of the eigenfunctions Ψ_1 and Ψ_2, the greater the probability of predissociation.

CHAPTER 3

3.1 Absorption of Radiation by a Gas

As monochromatic radiation passes through an absorbing gas, the intensity is attenuated in such a way that the fractional decrease in intensity dI/I (here dI is the actual decrease in intensity, and I is the incident intensity) is the same for each small path length dx. This can be written as

$$dI = -I\,k\,dx \tag{3.1}$$

where k is the absorption coefficient. The way the intensity varies over a path length x comprising a whole series of dx's is found by integrating equation 3.1 over the path length,

$$\int_{o}^{F} \frac{dI}{I} = \int_{o}^{x} -k\,dx$$

to give $$\ell n\, I_F - \ell n\, I_o = -kx\ .$$

Taking exponentials of both sides, the well known Beer's Law is obtained

$$I_F = I_o \exp(-kx) \tag{3.2}$$

The above derivation applied to monochromatic radiation, but a case of more experimental interest is when the intensity is not constant with wavelength, and it is then necessary to write $I(\lambda)$. Consider radiation incident over a wavelength interval $\Delta\lambda$. The total intensity I is then

$$I = \int_{\Delta\lambda} I(\lambda)\,d\lambda$$

and it may also be that the absorption coefficient has some wavelength dependence, and $k(\lambda)$ is the absorption coefficient at wavelength λ. The intensity after passing through a length of absorber x can then be

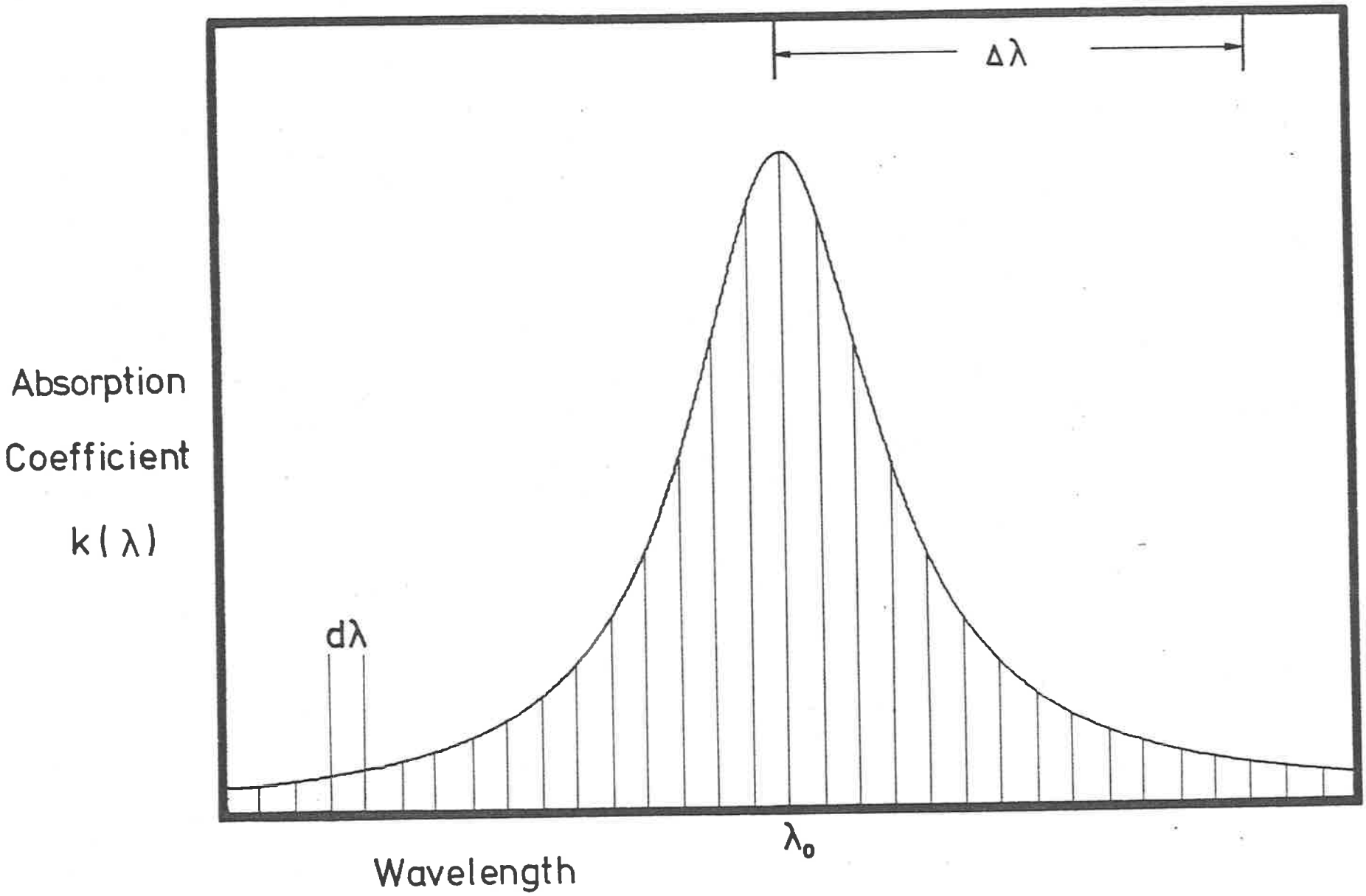

FIG 3.1 : The variation in absorption coefficient with wavelength λ for an absorption line centred at λ_o. Beer's Law would be obeyed for the wavelength intervals $d\lambda$, but not for the interval $\Delta\lambda$.

written

$$I = \int_{\Delta\lambda} I(\lambda)\, d\lambda = \int_{\Delta\lambda} I_o(\lambda)\, \exp[\, -k(\lambda)x\,]\, d\lambda \qquad (3.3)$$

If $k(\lambda) = k$, that is, is constant with wavelength then equation 3.3 again reduced to Beer's Law, that is

$$I = \exp(\, -kx\,) \int I_o(\lambda)\, d\lambda = I_o \exp(\, -kx\,)$$

Otherwise, if absorption coefficient varies with wavelength, then Beer's Law is not valid over the wavelength interval $\Delta\lambda$, and the intensity is a more complex function of the path length. For example, in Figure 3.1, Beer's Law would not be obeyed over the wavelength interval $\Delta\lambda$, but would be obeyed to a good approximation over the interval $d\lambda$.

If the wavelength region $\lambda_o \pm \Delta\lambda$ of Figure 3.1 is considered again, then for small absorber thickness x, radiation will be absorbed at all wavelengths, and the effective absorption over the wavelength interval will be as if due to some constant absorption coefficient k_{eff}, where $k_{eff} \simeq k_{average}$.

For larger absorber thicknesses however, the central regions near λ_o will be completely absorbed out, and will thus no longer contribute to continuing absorption. Only the radiation in the wings near $\lambda_o \pm \Delta\lambda$ will be absorbed, and the effective absorption coefficient k_{eff} will be approximately equal to k_{wings} (this process is called radiation hardening). Figure 3.6 shows an example of absorption occurring at different wavelengths within a wavelength region as the absorption path length changes.

Experimentally, Beer's Law is obeyed when the incident wavelength is monochromatic, that is when extremely high resolution is used (for example

a narrow emission line of a hollow cathode lamp), or when the absorption coefficient $k(\lambda)$ is constant (a continuum). Beer's Law fails when $k(\lambda)$ varies rapidly over the finite instrumental resolution wavelength interval $\Delta\lambda$, and this is the case encountered in this thesis for the work done on the Schumann-Runge bands.

The departures from Beer's Law occur because light detectors looking at the incident light, measure how much light there is in the wavelength band under inspection, and take no account of the distribution of intensity with wavelength. Wavelength distribution of the light changes as the beam passes through the absorber, because of the effects of the varying absorption coefficient, and a detector looking at this final intensity again does so independently of the wavelength distribution.

In many experiments, the absorption coefficient varies over the small range of wavelengths given by the instrument resolution. In such a case the intensity is made as near as is possible constant over the region of interest, by choosing the lamp, and the lamp gas to provide a continuum of fairly constant intensity with wavelength. This is not always possible, and care should be taken if there are emission lines present.

Absorption lines, the principal source of rapid variations of absorption coefficient with wavelength, are due to atoms or molecules of the gas absorbing radiation and undergoing transitions from one energy state to another. In the case of molecules, electronic, vibrational and rotational transitions are all possible, and each peak in the absorption coefficient corresponds to radiation at that wavelength being absorbed, and the energy used for a transition to another state. What the experiment seeks to find is a measure of absorption coefficient at each wavelength, and this can be accomplished if the strength and line-shape

parameters of each transition are measured. This would be simple if the monochromator had instrument width much less than the line widths. In this ideal case, a scan across a certain wavelength region would exactly reproduce the absorption coefficient of that region. However, as the monochromator always has some finite resolution, the absorption coefficient will be greatly modified.

3.2 The Effect of Instrument Resolution

Consider an ideal experimental case, where an absorption line of some undetermined shape is to be measured. The shape of the absorption line can be described by some function $k(\lambda)$. A scan across the line, with very high resolution (a delta-function perhaps), will simply reproduce the line shape. As the resolution is reduced, the delta-function scan function broadens out, and this function can be denoted by $g(\lambda)$. Now each point on the experimentally measured absorption curve is given by area under the convolution of the resolution function $g(\lambda)$ and the absorption of the line function $k(\lambda)$. It is possible to define $A(\lambda)$ as the absorption at wavelength λ, where

$$A(\lambda_i) = \exp [- k_p X \, k(\lambda_i)] \tag{3.4}$$

and where $k_p X$ is a path length factor.

The convolution function $C(\lambda_i)$ is then

$$C(\lambda_i) = \int_{\lambda_A}^{\lambda_B} g(\lambda_j - \lambda_i) \, A(\lambda_j) \, d\lambda_j \tag{3.5}$$

Ideally, the integration range should be $-\infty$ to ∞, but experimental limitations preclude this. This convolution, representing the experimentally measured absorption curve will now be different from the actual absorption coefficient, and the effect is to smear out the absorption line, by reducing its peak height and increasing its width.

This is illustrated in Figure 3.2 for three different values of instrument resolution α_g, where α_g is the half-width of the resolution function (full-width at half height), taken to be a Gaussian function. If both functions $g(\lambda)$ and $A(\lambda)$ were Gaussian, then the resultant would also be a Gaussian with width

$$\alpha_T = \sqrt{\alpha_g^2 + \alpha_A^2}$$

where α_A is the half width of the absorption function. This expression is only accurate for the case where both functions are Gaussian, though it can be applied to other cases to obtain qualitative results.

Irrespective of the form of $A(\lambda)$, if $g(\lambda)$ is much narrower, the resultant function $C(\lambda)$ will have a width comparable to $A(\lambda)$, while if $g(\lambda)$ is much wider (as in case (c) of Figure 3.2) then the resultant will have a width comparable to $g(\lambda)$. Figure 3.2 shows the effect of blending of two individual lines by the poor instrumental resolution to produce an apparent single line, something which happens often in the Schumann-Runge bands.

The area under the resolution function should be unity, since this function should neither reduce nor add to the area of the absorption line, but only affect its distribution. That is

$$\int C(\lambda)\, d\lambda = \int A(\lambda)\, d\lambda \qquad (3.6)$$

and the above integral is independent of the width of the resolution function (see Appendix 1).

3.3 The Width and Shape of Spectral Lines

In considering a spectral absorption line, there are three basic quantities which completely define the line. These quantities are the position of the line centre λ_o, the width of the line α_v, and the

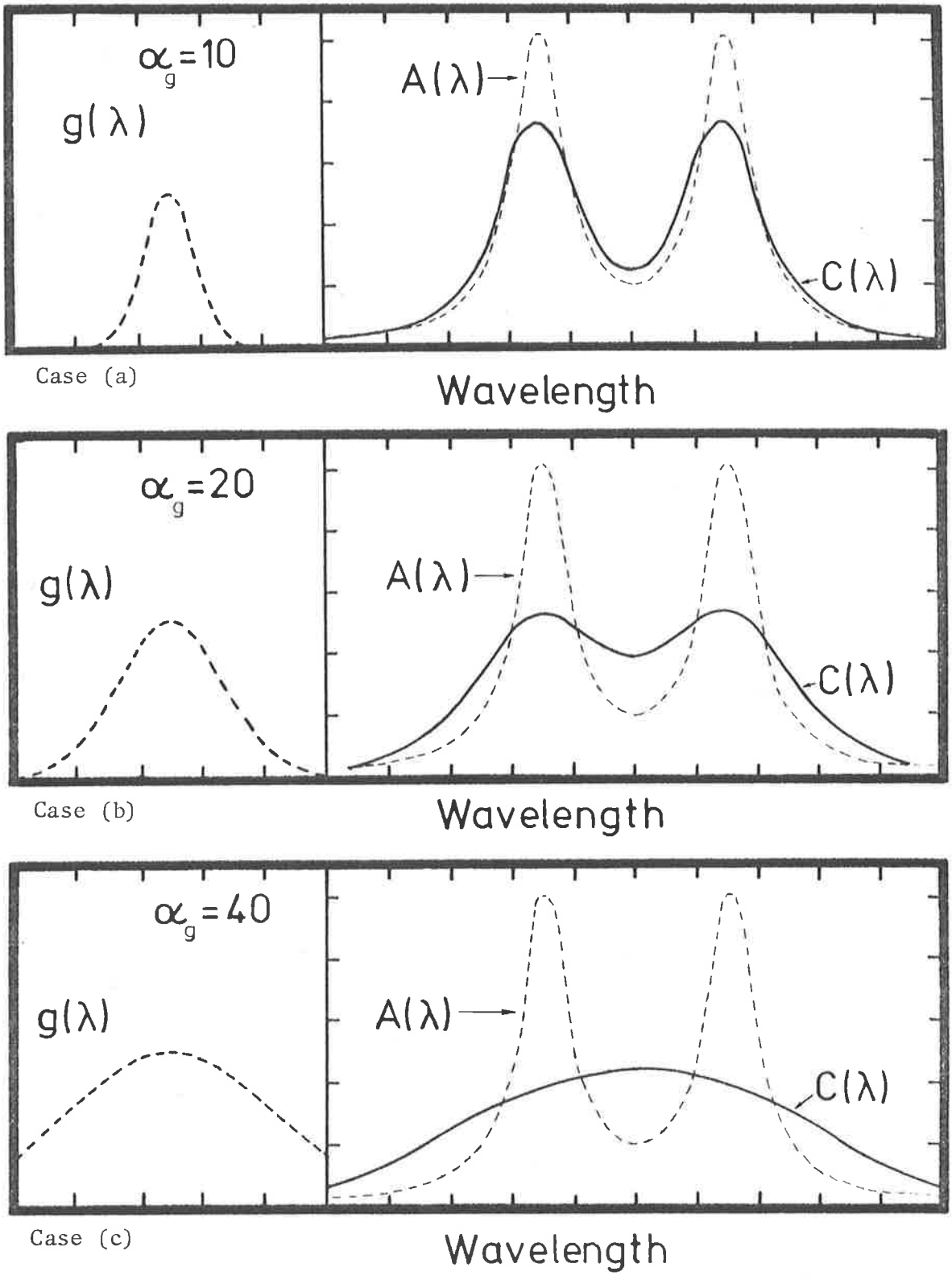

FIG 3.2 The effect of resolution function $g(\lambda)$ upon observed absorption $C(\lambda)$ for a given absorption $A(\lambda)$, plotted as intensity versus wavelength. The peak height of apparent absorption decreases as the resolution function broadens out, and the two absorption lines are no longer resolved. The total area beneath the function $C(\lambda)$ remains constant.

line strength S . Each line is characterized by a function $k(\lambda)$ which completely determines the way in which the absorption will behave as optical depth or absorption path length is increased. Common examples of the type of function $k(\lambda)$ are the Gaussian or Doppler function.

$$k(\lambda) = \exp\left[- \left(\frac{\lambda - \lambda_o}{\alpha_D} \right)^2 4 \ln 2 \right] \qquad (3.7)$$

and the Lorentz or Natural broadening function

$$k(\lambda) = \frac{1}{1 + 4 \left(\frac{\lambda - \lambda_o}{\alpha_N} \right)^2} \qquad (3.8)$$

There are other possible parameters, such as peak height k_p (the height at the line centre) and the integrated absorption coefficient $\int k(\lambda)\, d\lambda$, but knowledge of any three parameters allows the others to be determined.

3.3.1 Doppler Broadening.

Absorption lines have a Doppler profile when the major contribution to the width is due to random thermal motion of the atoms or molecules under consideration. The formula for the Doppler width is

$$\alpha_e = \frac{\lambda_o}{C} \left(2 \frac{K_B T}{M} \right)^{\frac{1}{2}} \qquad (3.9)$$

where α_e is the 1/e half width (see Figure 3.3) and T is temperature in $^\circ K$.

K_B is Boltzmann's constant

M is the mass of the molecule, and

C is the speed of light.

Equation 3.9 is derived as follows.

The Doppler effect, where there is an apparent shift in wavelength of signal from a moving source, applies to the molecules in random motion.

The observer will see molecules moving towards as well as away from himself, with wavelength shift given by

$$\lambda \simeq \lambda_o \left(1 + v/c \right) \tag{3.10}$$

or $\Delta\lambda = v/c$ where $\Delta\lambda$ is positive when v is negative (away from observer) and negative when v is positive (towards observer). There will be a distribution of velocities given by the Maxwell distribution, and thus a distribution of observed wavelengths, resulting in a broadened line.

The Maxwell distribution gives

$$dn_v = \frac{n}{u\sqrt{\pi}} e^{-v^2/u^2} dV \tag{3.11}$$

where $\frac{dn_v}{n}$ is the fraction of molecules having velocity between v and $v + dv$ along an axis, and u is the most probable velocity

$$u = \sqrt{\frac{2kT}{M}} \tag{3.12}$$

(Thorne (1974) page 259).

This gives

$$\frac{dn_\lambda}{n} = \frac{1}{u\sqrt{\pi}} e^{-c^2 \Delta\lambda^2/\lambda_o^2 u^2} \frac{C}{\lambda_o} d\lambda \tag{3.13}$$

Since the absorption coefficient at λ is proportional to dn_λ, the line profile can be written in terms of the peak value at the line centre k_p as

$$k(\lambda) = k_p \exp \left[- c^2 (\lambda_o - \lambda)^2 / \lambda_o^2 \alpha^2 \right] \tag{3.14}$$

The full width at half-maximum of the Doppler line α_D, is given by

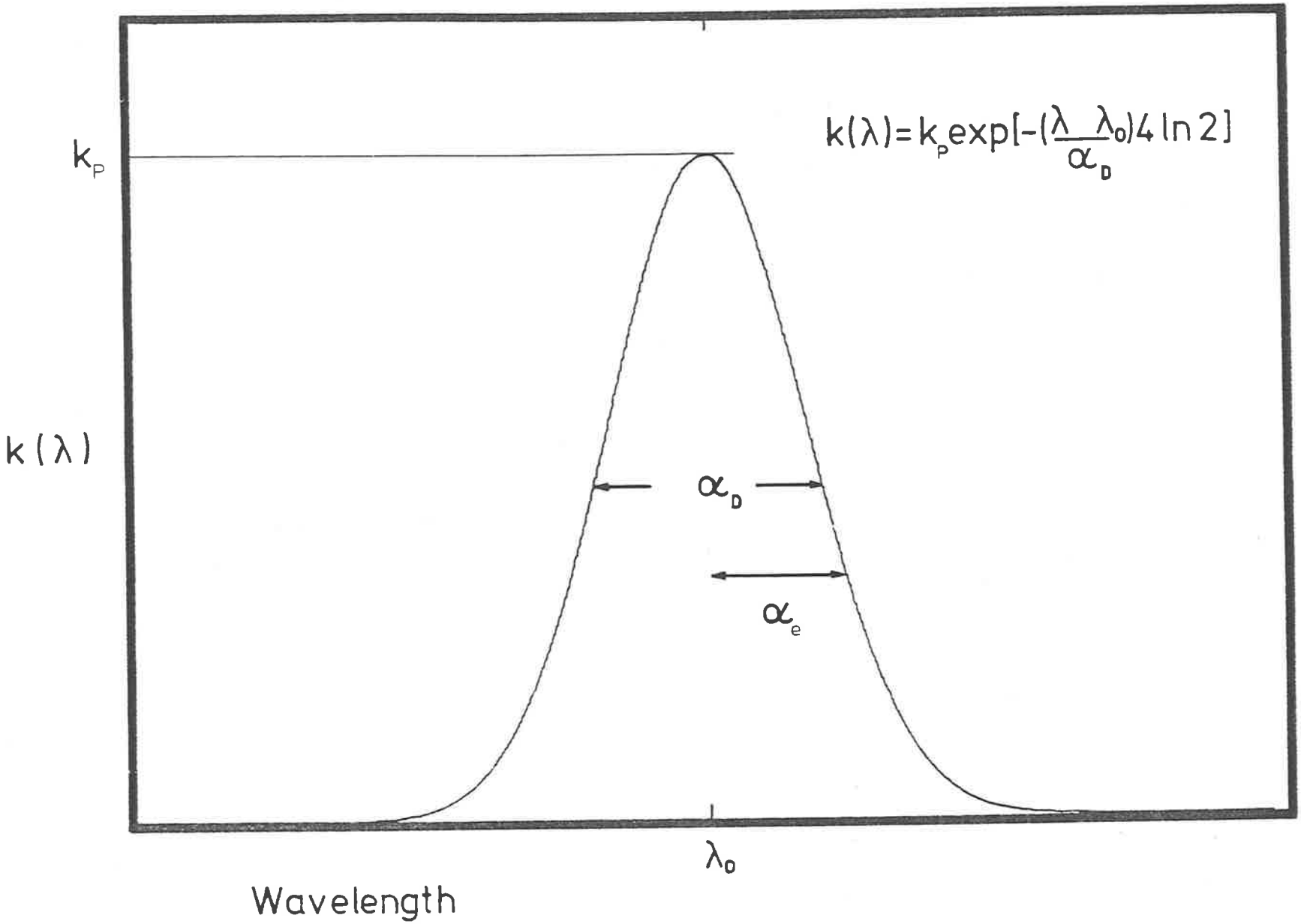

FIG 3.3 A Doppler absorption line with half-width α_D and 1/e width α_e, plotted as absorption coefficient versus wavelength. Note the rapid decrease in amplitude with wavelength.

$$\alpha_D = 2\sqrt{\ell n 2}\ \ \alpha_e = 2\sqrt{\frac{\ell n 2\ 2K_B T}{M}}\ \frac{\lambda_o}{c} \qquad (3.15)$$

and the area under a Doppler line is given by (see Appendix 2).

$$\int k(\lambda)\ d\lambda = \frac{k_p\ \alpha_D \sqrt{\pi}}{2\sqrt{\ell n 2}} = k_p\ \alpha_e\ \sqrt{\pi} \qquad (3.16)$$

That is, the area under the line varies linearly with width, a not unsurprising result. It is a property of the Doppler line, that the intensity of the line wings falls off in a very rapid manner, and is virtually zero beyond 2 to 3 αe . Typical Doppler widths at room temperature in the Schumann-Runge bands were of the order of 0.004Å (0.13 cm^{-1}) or 4.0 mÅ , there being a small variation with wavelength over the range 1750Å to 2000Å .

3.3.2 Natural Broadening

Associated with each energy level in an atom or molecule, is a lifetime, which is the time the energy level is in existence or is occupied, before decaying to a lower level. From the uncertainty principal, such a lifetime must have associated with it a spread in energy ΔE , where

$$\Delta E\ \Delta t \simeq \hbar \qquad (3.17)$$

so that the shorter the lifetime, the larger the energy spread. Since the ground state is a stable state, with infinite lifetime, its energy is uniquely and accurately defined. However upper states, with varying lifetimes have varying energy spreads, and it is these energy uncertainties which give the finite width to the transitions. Natural widths are usually much smaller than Doppler widths (by several orders of magnitude) at room temperature, and can only be observed with low

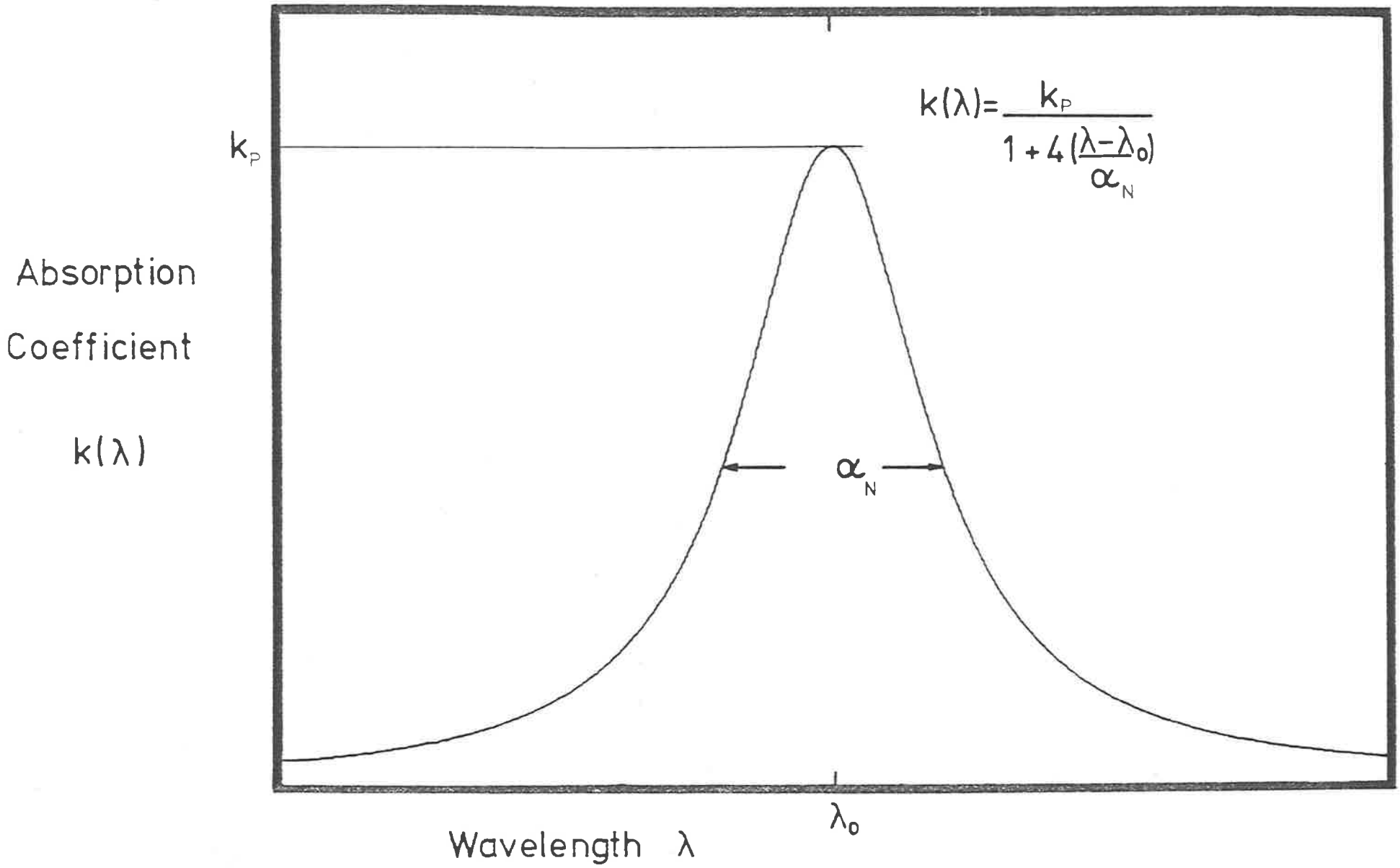

FIG 3.4 A Lorentz absorption line, with half-width α_N, plotted as absorption coefficient versus wavelength. Note the slow amplitude decay in the wings of the line.

temperature gas samples with small Doppler widths.

The Lorentz or Natural Broadening function is

$$k(\lambda) = \frac{1}{1 + 4\left(\frac{\lambda - \lambda_o}{\alpha_N}\right)^2}$$

where the natural width $\alpha_N = \frac{\lambda_o^2}{4\pi c \tau_N}$ (3.18)

is the full width at half maximum (see Figure 3.4) and τ_N is the lifetime of the state.

The area under a Lorentz line is given by (see Appendix 3)

$$\int k(\lambda)\, d\lambda = k_p\, \alpha_N\, \pi/2 \qquad (3.19)$$

That is, for the same peak height (say $k_p = 1$) and the same width ($\alpha_N = \alpha_D$), the area under a Lorentz line-shape function is greater than that under a Doppler line-shape function. This must be taken into account later when a mixed function is used as an approximation to the Voigt profile.

3.3.3 Predissociation Broadening

Predissociation broadening can be considered to be a special case of Natural broadening. In Natural broadening, the distribution of lifetimes results in a distribution of energy levels (because of the uncertainty principle) and this distribution gives rise to the Natural or Lorentz line profile. For predissociation broadening, the natural lifetime is replaced by the predissociation lifetime τ_p , which is a measure of how long the molecule will exist in a certain state before making a radiationless transition through dissociation to an unbound state. This dependence on state lifetime gives predissociation broadening a line profile of the same form as the Natural or Lorentzian shape. It is

no longer possible, if a state is predissociated, to talk of a natural lifetime, because the lifetime of the state is completely determined by τ_p . In almost all cases $\tau_p \ll \tau_N$ thus giving line widths for predissociation broadening which are much greater than the natural line-widths would have been. The predissociation linewidth α_p is related to the predissociation lifetime by

$$\alpha_p = \frac{\lambda_o^2}{4\pi C \tau_p} \tag{3.20}$$

and in the Schumann-Runge bands was found to vary from 2.0 mÅ (0.06 cm^{-1}) to 150 mÅ (4.1 cm^{-1}).

3.3.4 Pressure Broadening

This is a broadening phenomenon due to the effects produced by pressure on the transition taking place in molecules. These effects can be of different types, and there is no one theory which completely describes all the effects and produces a single formula for the pressure contribution to the linewidth. The simplification that is made is that only actual collisions are considered. That is, if an absorption process is taking place in a molecule, when it collides with another molecule, thus terminating the process, then the wavelength of that process will be altered, a situation analogous to natural broadening. The lifetime however, must now be replaced by the mean time between collisions, and the line width for such a pressure broadened line is given by

$$\bar{\ell} = \frac{1}{\sqrt{2\, n\, \pi\, d^2}} \tag{3.22}$$

where n is the number density, and d is the diameter of the molecule. The value that should be assigned to the diameter is uncertain, the actual diameter of the outer electron shell being inappropriate in this case. For this order of magnitude calculation, a diameter of 2 to 4 times

the electron shell radius is assumed. From the ideal gas equation

$$PV = N K_B T \tag{3.23}$$

an expression relating pressure to number density can be obtained, for example

$$P = \frac{N}{V} K_B T = n K_B T \tag{3.24}$$

Substitution into equation 3.23 gives

$$\bar{\ell} = \frac{1}{\sqrt{2}} \frac{K_B T}{p \pi d^2} \tag{3.25}$$

The most probable speed of the molecule, v_p is given by equation

$$v_p = \sqrt{\frac{2 K_B T}{M}} \tag{3.26}$$

and the collision time τ_c is

$$\tau_c = \frac{\bar{\ell}}{v_p} = \frac{1}{\sqrt{2}} \frac{K_B T}{P \pi d^2} \left(\frac{M}{2 K_B T} \right)^{\frac{1}{2}} \tag{3.27}$$

Substitution into equation 3.21 gives

$$\alpha_c = \frac{\lambda_o^2}{4\pi c} P\pi d^2 \frac{\sqrt{2}}{K_B T} \left(\frac{2 K_B T}{M} \right)^{\frac{1}{2}}$$

which reduces to

$$\alpha_c = \frac{\lambda_o^2}{2c} P d^2 \left(\frac{1}{K_B T M} \right)^{\frac{1}{2}} \tag{3.28}$$

Using a value of $d = 5$ Å to $d = 10$ Å for O_2

the above equation becomes

$$\alpha_c = Z \lambda_o^2 P \tag{3.29}$$

where Z lies between the values 2.9 and 11.5 , and where λ_o is in metres and P in atmospheres.

The maximum pressure used during the present measurements in the Schumann-Runge bands is 850 torr or 1.12 atmospheres (in the 1-0 and 2-0 bands near λ = 2000Å) so the maximum pressure width would be of the order of

$$\alpha_c = (1.3 \text{ to } 5) \times 10^{-13} \text{ metres or } 1.3 \text{ to } 5 \text{ mÅ} .$$

Collision broadening gives a line with a Lorentz core, so the total Lorentz width α_L, due to natural broadening α_N and collision broadening α_C would be

$$\alpha_L = \alpha_N + \alpha_C \tag{3.30}$$

where both processes simply combine to give a total Lorentz shape. It must be remembered however, that only collision induced broadening has been taken into account. Close encounters and perturbations of surrounding molecules, which have been neglected, produce broadened wings. The presence of a foreign gas will increase the number of collisions and will broaden the line-shape as well as shifting the actual position of the line.

3.4 The Mixed Line Profile

To produce realistic line shapes in the Schumann-Runge bands, it is necessary to use a function with a parameter which changes the line shape from pure Doppler to pure Lorentz, since the lines in these bands may vary in such a fashion. This parameter is called the mixing parameter a, and is defined

$$a = \frac{\alpha_L}{\alpha_D} \sqrt{\ell n 2} \tag{3.31}$$

where α_L and α_D are the Lorentz and Doppler full-widths at half maximum respectively.

A line in the Schumann-Runge bands will have a certain shape and width, due to mixing of the Doppler effect due to temperature, and the natural and predissociation broadening effects which produce a Lorentz line shape. Lines will therefore be a combination of all these effects, and can be described by a Voigt width α_V, and a mixing parameter a, detailing the ratio of Lorentz to Doppler width. A line with $a = 0$ will be a pure Doppler line and will have $\alpha_V = \alpha_D$, whereas a line with $a = \infty$ is a pure Lorentz line, with $\alpha_V = \alpha_N$.

The Voigt profile is given by (see Appendix 4)

$$k(\lambda) = k_o \frac{a}{\pi} \int_{-\infty}^{\infty} \frac{\exp(-x^2)}{a^2 + (v - x)^2} \, dx \qquad (3.32)$$

where $v = 2\left(\frac{\lambda - \lambda_o}{\alpha_N}\right)\sqrt{\ln 2}$. That is, each point on the Voigt profile requires the calculation of an integral. Therefore a calculation of an equivalent width requiring the integration across an absorption line profile, first requires n integrations to obtain n $k(\lambda)$ points. To speed up computing, the empirical approximations of Whiting (1968) were used. Whiting's second approximation basically consists of a weighted sum of the two limiting cases, the Doppler function and the Lorentz function, with the addition of a correction term so that the final function is in close agreement with the Voigt function. Errors in the line profile are very small (always less than 5%, and usually less than 3%), and errors in the equivalent width are within 1% of those given by the Voigt profile. Whiting's second approximation can be written as

$$k(\lambda) = k_p\left(1 - \frac{\alpha_L}{\alpha_V}\right)\exp\left[-2.772\left(\frac{\lambda - \lambda_O}{\alpha_V}\right)^2\right] + \frac{\alpha_L}{\alpha_V} - \frac{1}{1 + 4\left(\frac{\lambda - \lambda_O}{\alpha_V}\right)^2} + E \quad (3.33)$$

where

$$E = 0.016\left(\frac{\alpha_L}{\alpha_V}\right)\left(1 - \frac{\alpha_L}{\alpha_V}\right)\left(\exp\left[-0.4\left(\frac{\lambda - \lambda_O}{\alpha_V}\right)^{2.25}\right] - \frac{10}{10 + \left(\frac{\lambda - \lambda_O}{\alpha_V}\right)^{2.25}}\right) \quad (3.34)$$

and

$$k_p = \frac{\int k(\lambda)\, d\lambda}{\alpha_V\left(1.065 + 0.447\,\frac{\alpha_L}{\alpha_V} + 0.058\left(\frac{\alpha_L}{\alpha_V}\right)^2\right)} \quad (3.35)$$

is the peak height at the line centre λ_O .

$$\alpha_V = \frac{\alpha\,\alpha_D}{2\sqrt{\ln 2}}\left[1 + \left(\frac{1 + 4\ln 2}{\alpha^2}\right)^{\frac{1}{2}}\right] \quad (3.36)$$

is the Voigt width (total width of the final line). This width can also be written as

$$\alpha_V = \frac{\alpha_L}{2} + \sqrt{\frac{\alpha_L}{4} + \alpha_D^2} \quad (3.37)$$

There are many other approximations to the Voigt profile, which give varying degrees of accuracy, and they are listed in Penner (1959) and also by Armstrong (1967). Some of the properties of the second approximation of Whiting are discussed in Appendix 5 .

3.5 Equivalent Width

In considering an absorption line and the passage of radiation of a wavelength coincident with this line through a gas, an interesting result is obtained. Although the measured absorption at any one wavelength point in the vicinity of the line depends upon the resolution of the system making the measurement, the total integrated absorption across the line is independent of system resolution (if the limits of integration are extended far enough). The limit is reached if the resolution of the system is so poor in comparison to the linewidth that the intensity of the line is dispersed over such a wide region, that it becomes very difficult to measure.

In the case of an isolated absorption line, it would be possible to integrate right out along the wings, and a total integrated absorption independent of instrumental resolution would be found. However in the real case, as in the Schumann-Runge bands, the experimental conditions are far from ideal. Lines are crowded together, so the above condition is not satisfied. In many cases though, it still holds to a good approximation. The further out onto the wings of a line the integration is taken, the more closely the result approximates that for the ideal case.

For example, in the case of a Doppler line, integration onto the line wings beyond $3\alpha_D$ from the line centre is unnecessary, as adequate accuracy has been obtained by then. This is much less true of Lorentz lines, but if the integration is taken out onto the wings far enough to include most of the area under the line, then it is true to a good approximation. The total integrated area under an absorbed line is called the equivalent width (not to be confused with the total integrated area under an absorption coefficient $\int k(\lambda)\, d\lambda$), and is the width of a

rectangular line with the same integrated absorption. In Figure 3.5 this is illustrated by the shaded rectangle with a given width being equivalent to the area of absorption for the absorption line centred at λ_o .

The intensity transmitted through a gas is

$$I = I_o \exp(- k_p \, k(\lambda) \, x) \tag{3.38}$$

where I_o is the incident intensity, $k_p \, k(\lambda)$ is the absorption coefficient at wavelength λ , and x is the path length. The absorption is

$$\frac{I_o - I}{I_o} = 1 - \exp(- k_p \, k(\lambda) \, x)$$

while the equivalent width is defined as

$$W = \int_o^\infty (1 - \exp[- k_p \, k(\lambda) \, x]) \, d\lambda \tag{3.39}$$

and is thus the integrated sum of the absorption. The equivalent width at low optical densities is linear with pressure or path length x (see Appendix 6), and can be written

$$W \simeq k_p X \int_o^\infty k(\lambda) \, d\lambda \tag{3.40}$$

In equation 3.40, the only unknown is k_p so this can be determined, to give a value for line strength. In the linear limit, the equivalent width is independent of α-value , and depends only upon the oscillator strength, and the normalized path length X . Equation 3.39 represents the ideal case for infinite integration range. In practice this is not possible and the measured equivalent width is given by

$$W' = \int_{\lambda_A}^{\lambda_B} [1 - \exp(- k_p \, k(\lambda) \, x)] \, d\lambda \tag{3.41}$$

FIG 3.5(a)

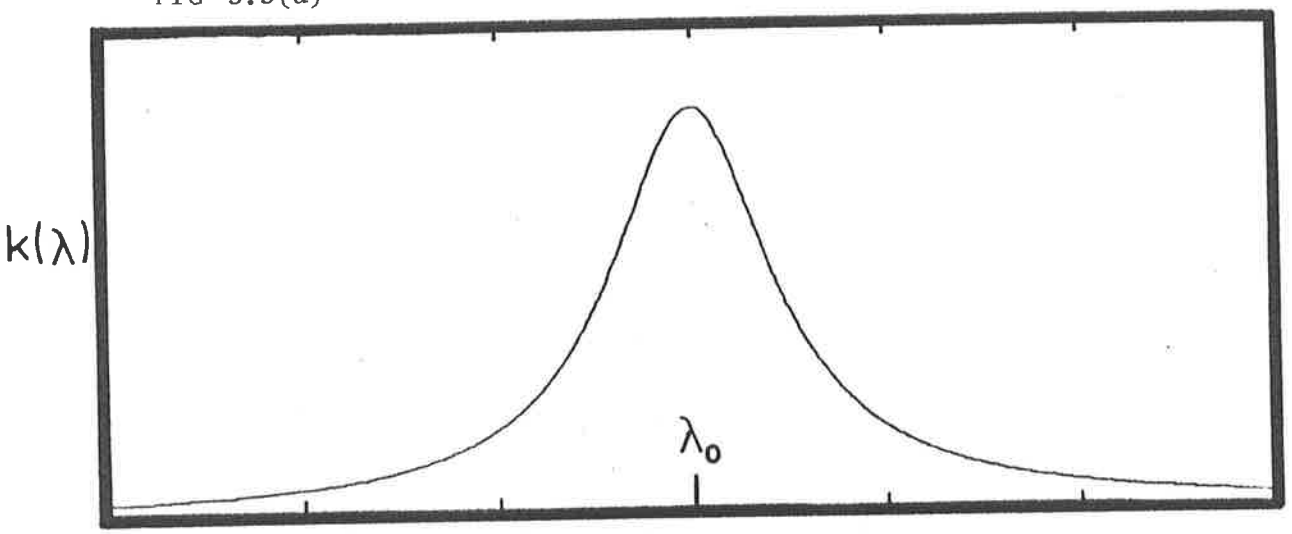

Wavelength λ

FIG 3.5(b)

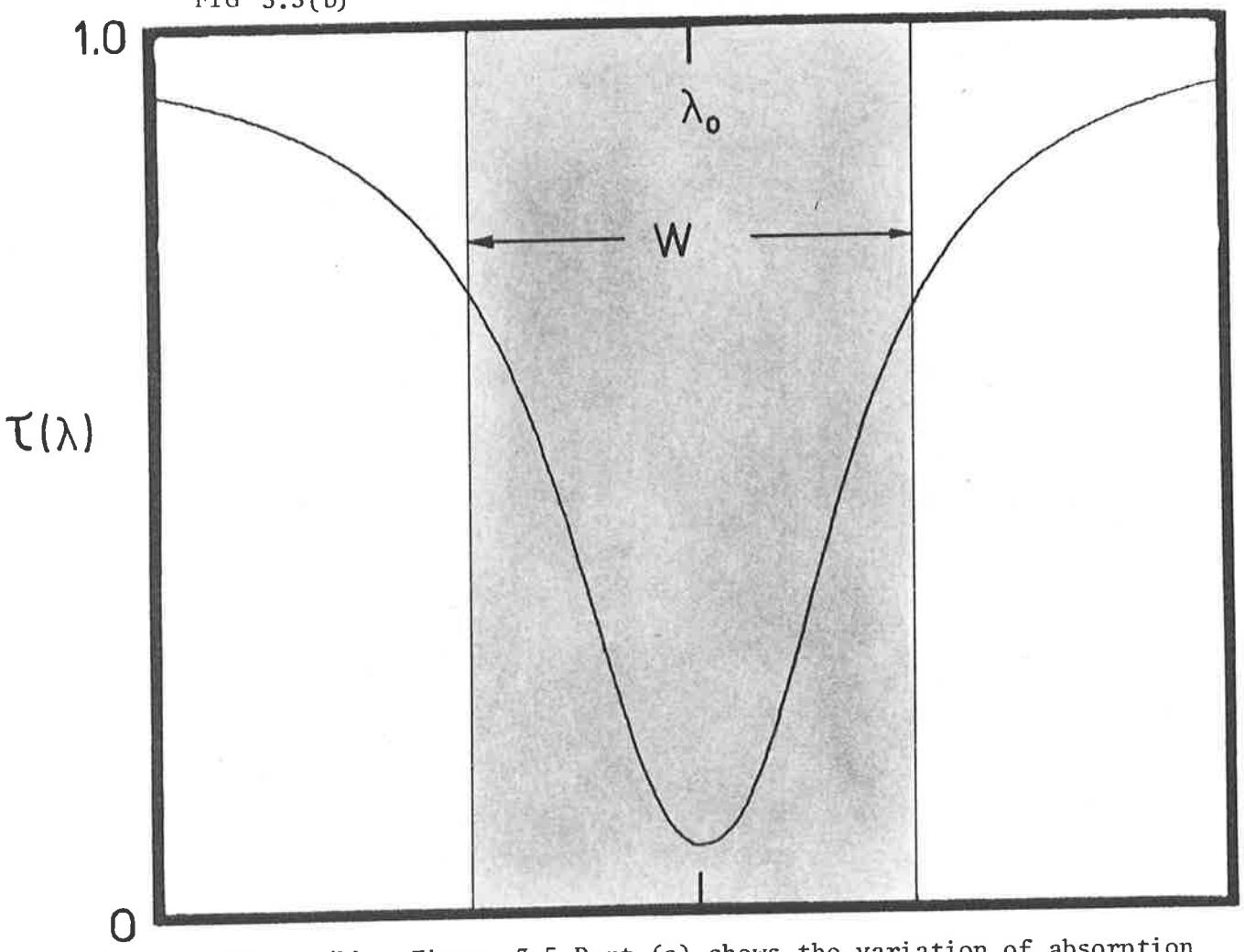

FIG 3.5(b). Figure 3.5 Part (a) shows the variation of absorption coefficient with wavelength while Part (b) shows the variation in transmission τ with wavelength for a particular value of optical depth. The total area of absorption (the area between the curve and τ=1) is equivalent to the shaded area of the rectangle which is the equivalent width of a completely absorbed rectangular line.

where the further out onto the line wings λ_A and λ_B are the closer W' approximates W (see Appendix 7).

3.6 Curves of Growth

The behaviour of absorption as the path length through the absorbing gas increases is not immediately obvious. If a smoothly varying absorption coefficient is considered, such as a continuum, then Beer's Law is obeyed. However, different behaviour is noted when the absorption coefficient consists of an absorption line and its associated wings. The variation in equivalent width as either the path length is increased, or as pressure is increased is of great importance. Equation 3.41 for equivalent width can be written as

$$W' = \int_{\lambda_A}^{\lambda_B} [\, 1 - \exp(- \frac{N}{No} \frac{P}{760} \frac{273}{T} \times k_p \, k(\lambda) \,) \,] \, d\lambda \qquad (3.42)$$

where N is the number density, No is Loschmidt's number and is the number density at standard pressure and temperature (2.687×10^{25} molecules/m^3), P is the pressure in torr, x is the actual path length in cms. and T the temperature in $^\circ K$. The term k_p is introduced to fix the values of $k(\lambda)$ on an absolute scale, and is simply the peak height at the line centre. Equation 3.42 reduces to 3.41 at standard temperature and pressure, and it is possible to re-write equation 3.42 as

$$W' = \int_{\lambda_A}^{\lambda_B} [\, 1 - \exp(- k_p X \, k(\lambda) \,] \, d\lambda \qquad (3.43)$$

by defining X as the optical depth where

$$X = \frac{N}{No} \frac{P}{760} \frac{273}{T} \, x \qquad (3.44)$$

and is a normalized number density, path length term.

There is no analytical expression for W' (or W), in terms of $k(\lambda)$ or $k_p X$ unless simplifications are made (as in the small optical depth case in Appendix 6). A curve of growth can be defined as

the growth of equivalent width as a function of optical depth $k_p X$. The variations of equivalent width W with $k_p X$ are plotted in Figures 3.10 and 3.11 for the pure Doppler case, and the pure Lorentz case, as well as for intermediate cases with a-values between 0 and 100,000.

A numerical study has been made of curves of growth and the characteristics of different a-values and widths, and is described in Appendix 8 . A summary of the properties for the two important limiting cases, an isolated Doppler line, and an isolated Lorentz line follows.

For the Doppler case, equation 3.43 becomes

$$W' = \int_{\lambda_A}^{\lambda_B} \left(1 - \exp\left[- k_p X \exp\left(- \left(\frac{\lambda - \lambda_o}{\alpha_D} \right)^2 4\ell n 2 \right) \right] \right) d\lambda \qquad (3.45)$$

For small optical paths, the equivalent width increases linearly with number density. However, when the optical density (or path length) reaches a high enough value (> 0.1) the growth in the absorption area starts to slow down, and departures from the straight line begin (cases two and three of Figures 3.6 and 3.7). As more and more absorption takes place, the departures from the linear become even greater (case 4 of Figure 3.6). By the time the transmission at the line centre λ_o nears zero, the increase in equivalent width with number density has become very small, and is rapidly approaching a new constant value of increase (cases 6 and 7 of Figures 3.6 and 3.7).

The residual increase is due entirely to the Doppler wings of the line, which fall off very rapidly with increasing wavelength from the

FIG 3.6(a)

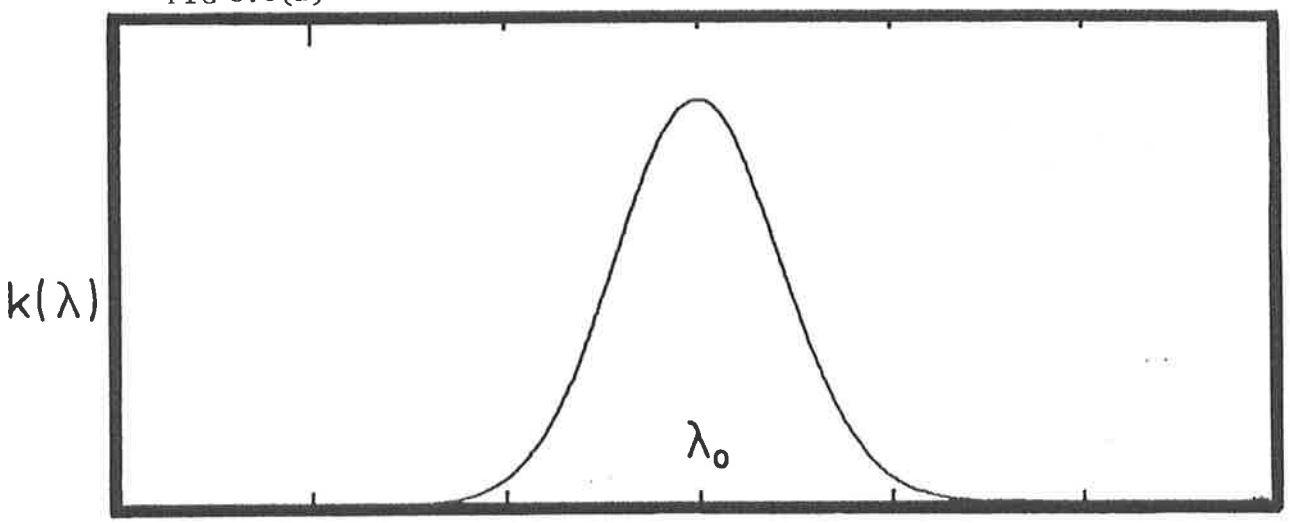

FIG 3.6(b)

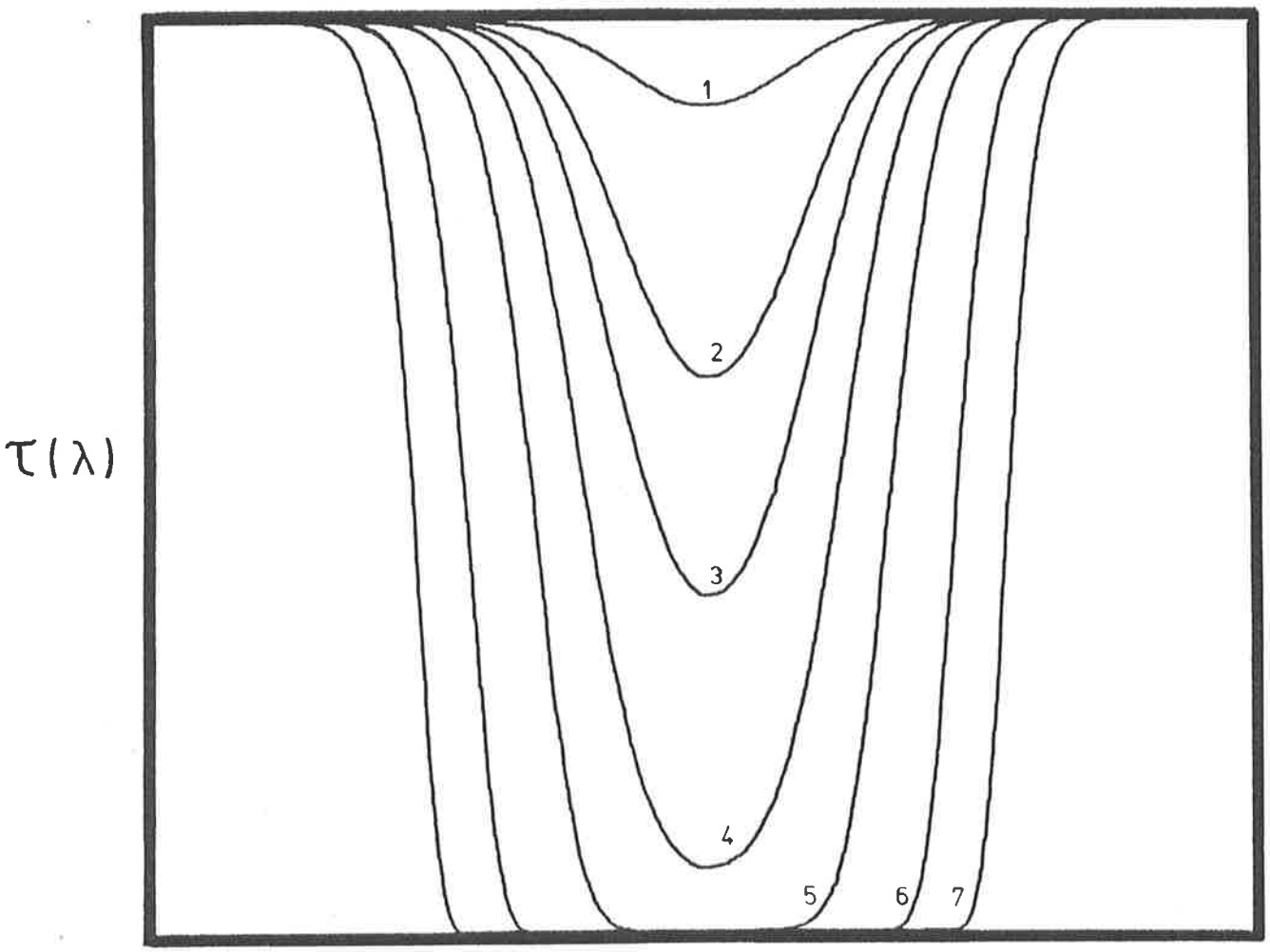

FIG 3.6. Part (a) shows the variation of absorption coefficient with wavelength for an absorption line (in this case a Doppler line) while Part (b) shows the variation in absorption due to the line at different values of optical depth.
The numbers on the various absorption curves correspond to the various $k_p X$ values shown in Figure 3.7 . It should be noted that Curve 1 is identical in shape and form to the curve for absorption coefficient, since this is in the region of low absorption.

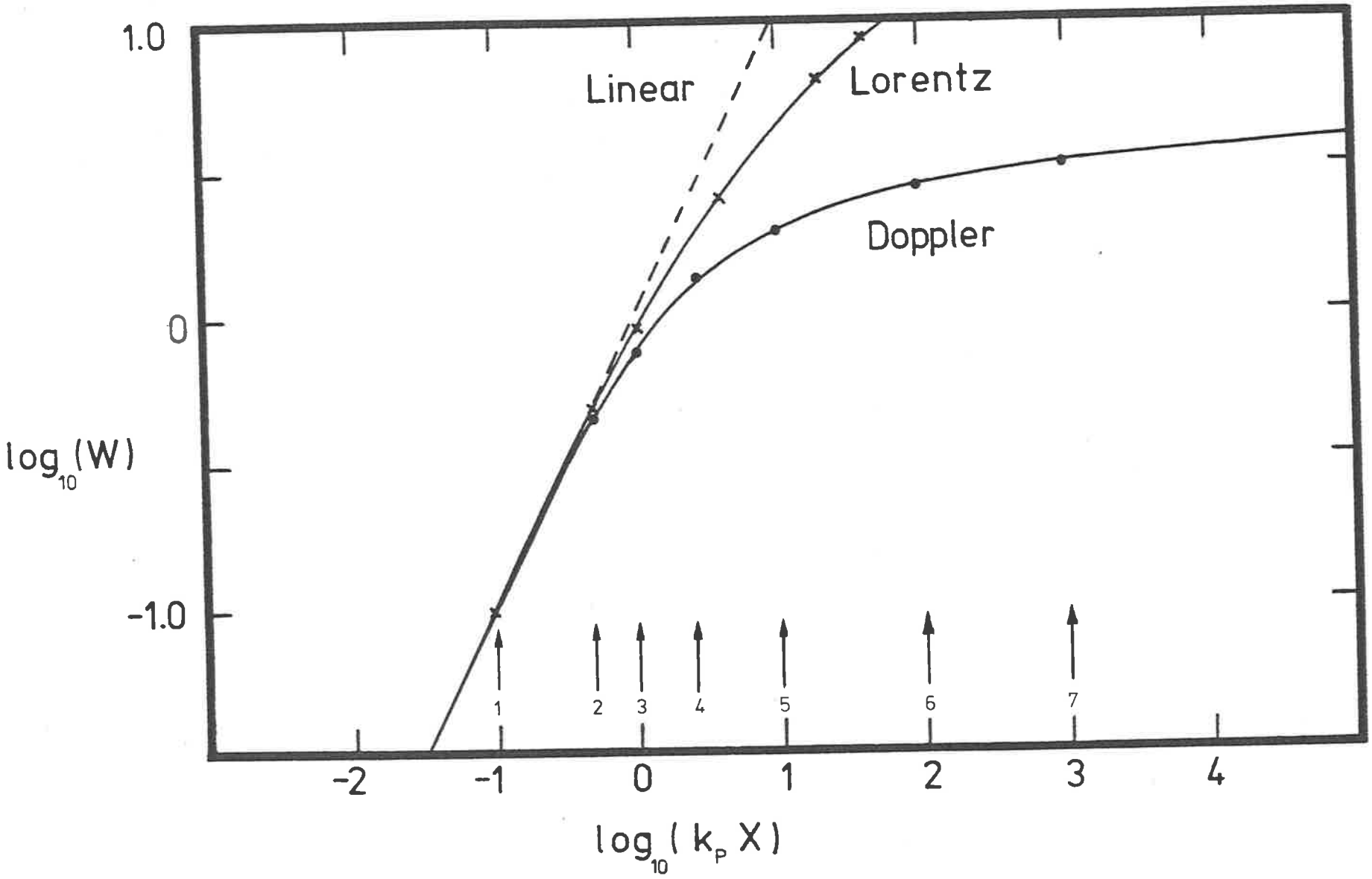

FIG 3.7 A plot at the curves of growth of the Doppler and Lorentz absorption cases shown in Figures 3.6 and 3.9 with the values of $k_p X$, corresponding to the numbered absorption curves, shown by arrows above.

line centre, and thus contribute little. The line centre has by now been virtually absorbed out, and has already contributed a very large absorption area. The small values of absorption coefficient in the wings can produce only insignificant absorption, and the small section of the line-shape absorption coefficient which is currently providing the increase in equivalent width at that value of optical thickness (that is with a transmission value neither too near zero or unity) is very narrow. The transmission curves for the Doppler line pass from values near zero (that is, completely absorbed) to unity (hardly absorbed) very quickly due to the rapid decrease of the line wings (see Figure 3.6). Once the transmission curve has bottomed out at $\lambda = \lambda_o$, then for a 10-fold increase in $k_p X$, only a small fraction is added to the equivalent width area (cases 6 and 7 in Figure 3.6). Consequently curves of growth of Doppler lines flatten off quickly, once the line centre has been absorbed.

A comparison of the Lorentz and Doppler line profiles (Figure 3.8) shows that with the same area beneath each curve, the Doppler line (with $\alpha_D = 1.0$, $k_p = 1.0$) has almost all of its area within $3\alpha_D$ of the line centre, while the Lorentz line (with $\alpha_L = 1.0$, $k_p = \frac{1}{\sqrt{\pi \ln 2}}$) has a significant proportion of its area in the line wings.

This difference in the wings of the two lines produce differences in the curves of growth. The Lorentz line also has its linear region. For $k_p X < 0.1$, the absorption curve is proportional to the curve for absorption coefficient at the same wavelength (that is, case 1 of Figure 3.9(b) is of the same type and shape as the absorption coefficient curve

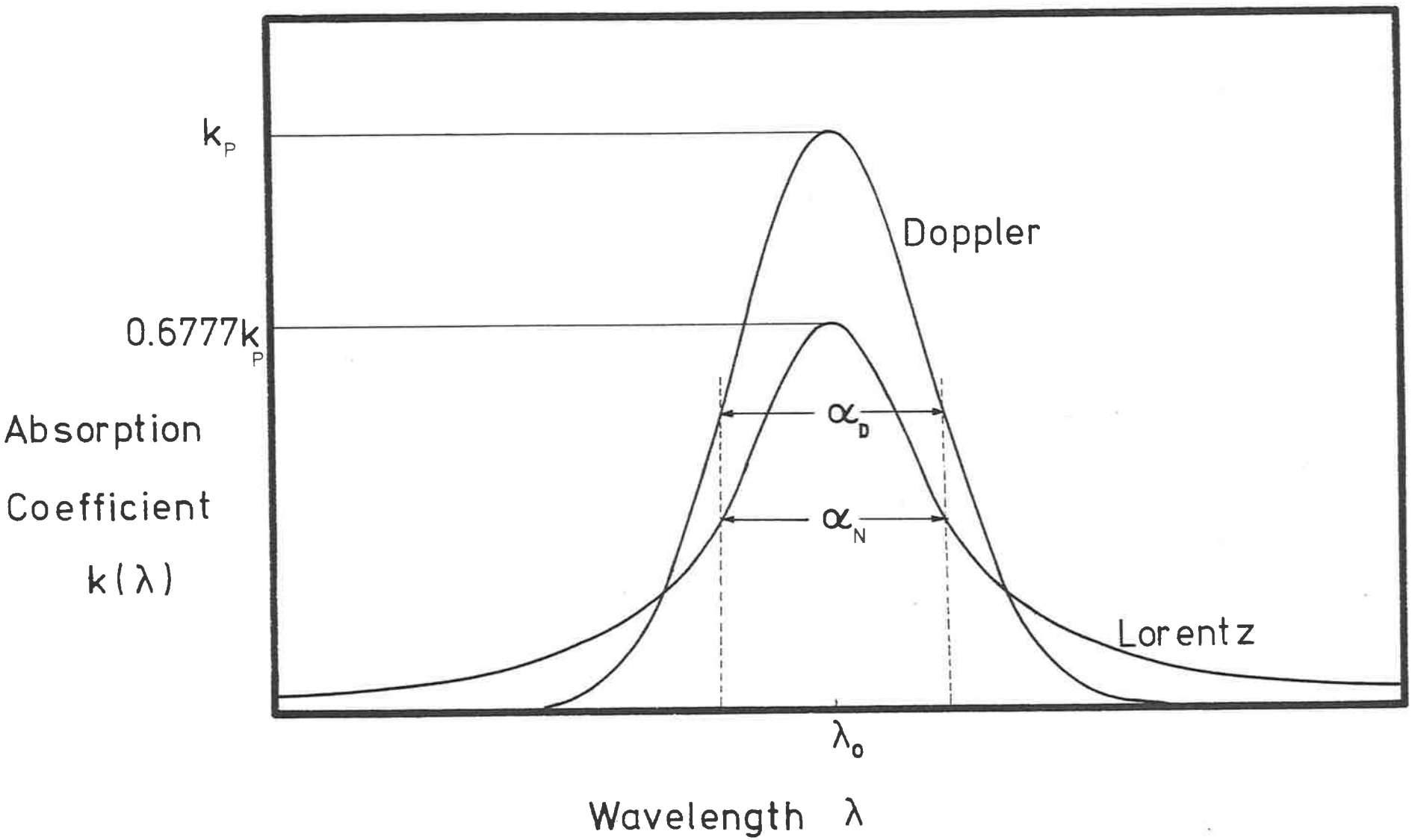

FIG 3.8. A comparison of Doppler and Lorentz line profiles. The area beneath both curves $\int k(\lambda)\, d\lambda$ is the same, achieved by setting k_p for the Lorentz line to be $0.6777\, k_p$ for the Doppler line. Both profiles have the same half width i.e. $\alpha_D = \alpha_N$.

FIG 3.9(a)

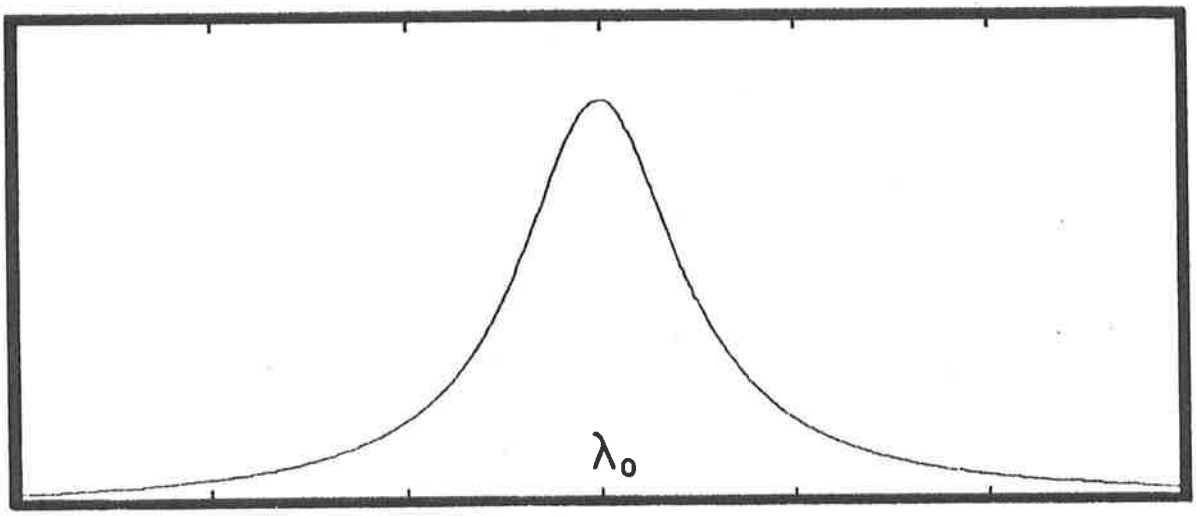

Wavelength λ

FIG 3.9(b)

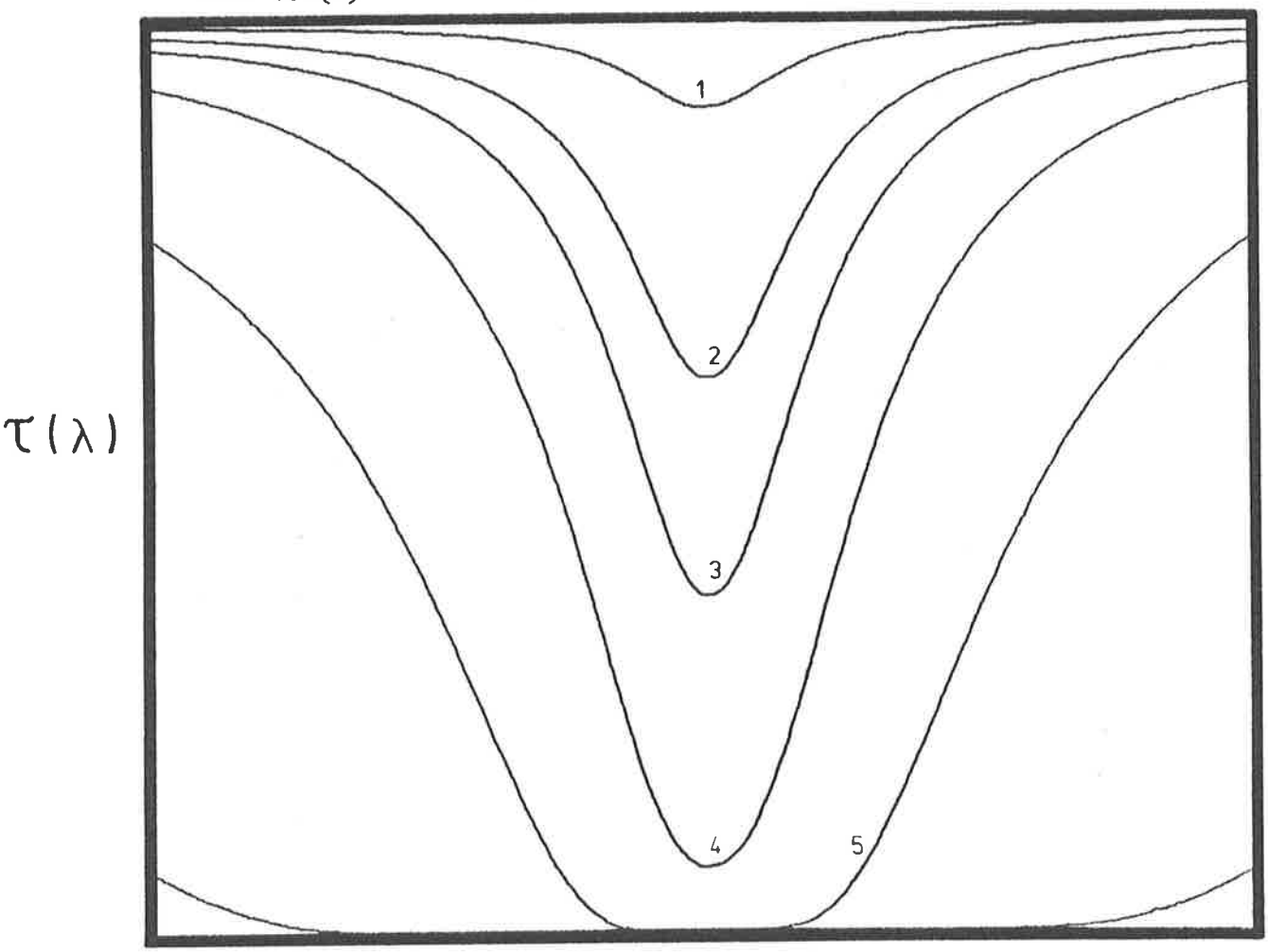

FIG 3.9 Part (a) shows the variation in absorption coefficient $k(\lambda)$ with wavelength, while Part (b) shows the variation in transmission τ with wavelength for a Lorentz absorption line. The numbers on the various absorption curves correspond to the $k_p X$ values arrowed in Figure 3.7.

in Figure 3.9(a)) as in the Doppler case for low $k_p X$. Once $k_p X > 0.1$ however, the curve of growth of a Lorentz line begins to depart from that of the Doppler case. It remains linear for slightly longer, since its peak height is slightly less, and therefore the zero transmission will be reached at a slightly higher value of $k_p X$. The fact that the wings extend out from the line centre and decrease at a slower rate than the Doppler case, means that even a long way from the line centre there will be values of absorption coefficient which are significant. Once the line centre has been absorbed out, the equivalent width can still grow because the wings start to contribute. This can be seen in Figure 3.9, where increasing $k_p X$ increases the equivalent width area of the absorption curve. The Lorentz line does not flatten off as does the Doppler case, but continues increasing in such a way that (see Appendix 8).

$$W \propto \sqrt{k_p X} \tag{3.46}$$

when $k_p X$ becomes large (that is following a square root law, with slope $\frac{1}{2}$ as in Figures 3.10 and 3.11).

It is the curves of growth shown in Figure 3.10 with constant Voigt width α_v , and constant area beneath each line profile ($\int k(\lambda)\, d\lambda$ = constant), which more clearly show the effect of line shape upon curve of growth. The variation in these curves is due entirely to shape factor, denoted by a where

$$a = \frac{\alpha_L}{\alpha_D} \sqrt{\ell n 2}$$

The curves are for constant α_v , achieved only at the expense of varying both α_L and α_D . Figure 3.11 shows curves of growth for varying values of a , but with α_D = constant (that is at constant temperature). They were first plotted by Van der Held (1931), copied ever since

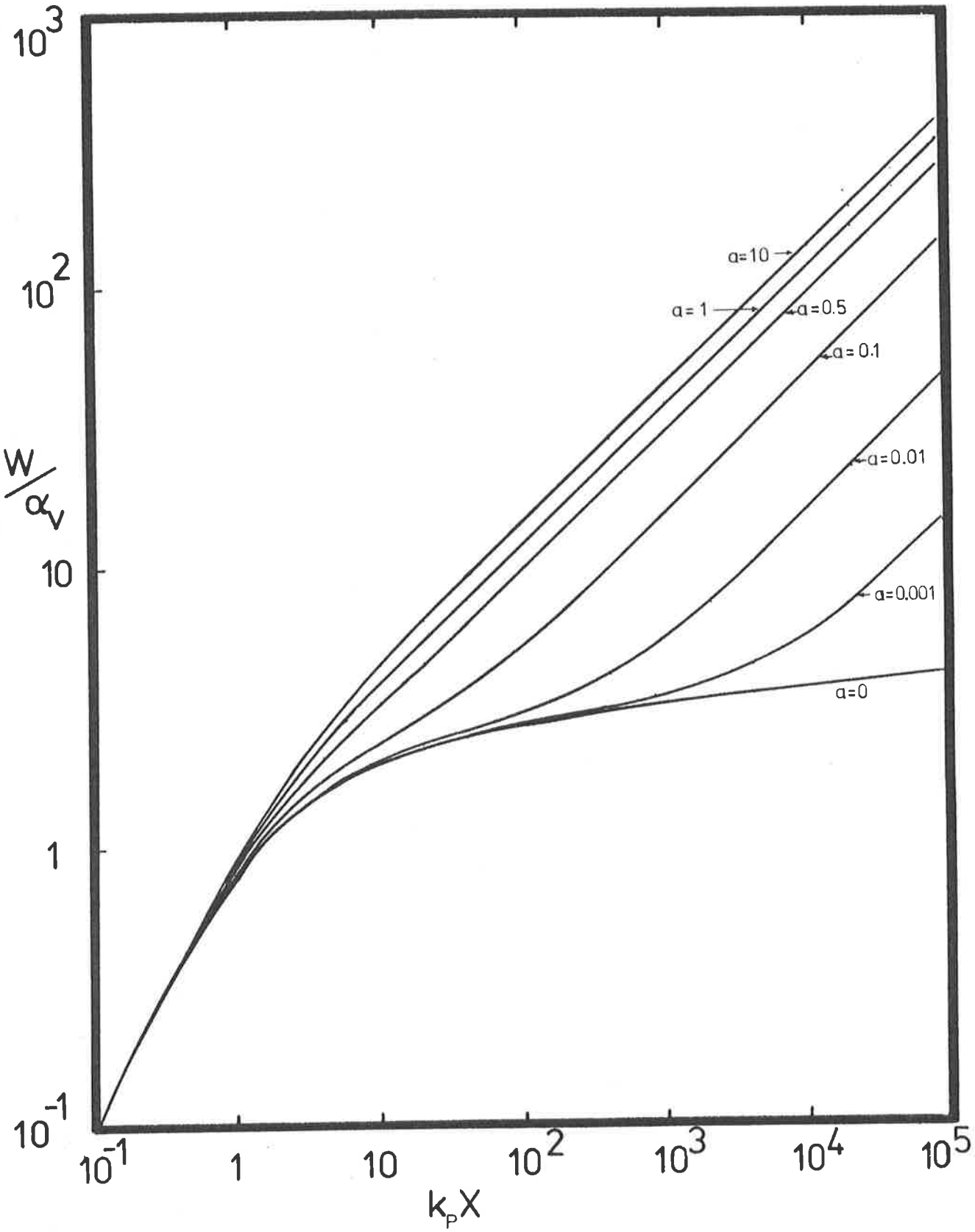

FIG 3.10. Curves of growth for various α - values plotted for constant line width α_v.

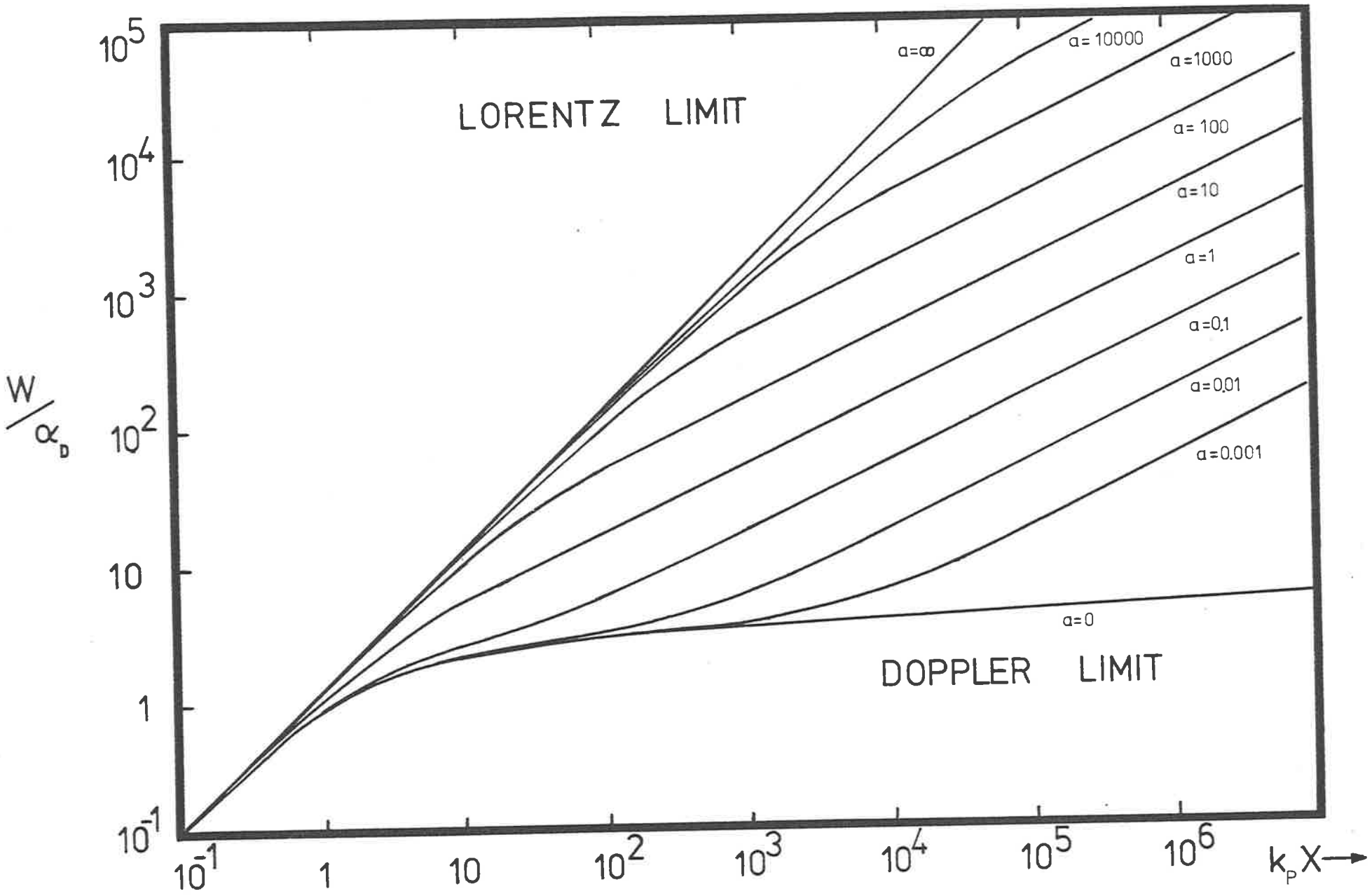

FIG 3.11. Curves of growth plotted for constant Doppler width α_D for various a-values.

(for example Goody (1964)). These curves are slightly misleading in that they seem to suggest that the curve of growth for the Lorentz case ($a = \infty$) is a straight line of slope 1, which it is not. The curves of growth in Figure 3.11 are for lines of equal area, and for constant Doppler width (as in the experimental case), but the Voigt width is allowed to vary with a-value. To compensate for this increasing width, the peak height k_p must be reduced. For example, a line with $a = 1000$ has $\alpha_v = 1000\ \alpha_D$, so the height must be $1/1000$ of the Doppler peak height. This low peak height means the line will not be absorbed out (saturated) until approximately 1000 times the value of X than if it had $k_p = 1.0$ (the Doppler case). That is saturation for both cases occurs at the same value of k_pX, but $k_p' = 1/1000k_p$ so X' is $1000X$. In this way, a line with $a = \infty$ (and therefore $k_p = 0$) will have an infinitely long linear region.

Very rarely in practice are either pure Doppler or Lorentz lines encountered. Lines are usually a mixture of both, so their curves of growth will have features of both ideal cases. The exact behaviour is determined by mixing ratio a , since this determined how much of each type of line is present. A line with $a = 0.001$ will fairly closely follow the Doppler case (for most of the curve) while a line with $a = 100$ will closely follow the Lorentz case. In general, the behaviour of all cases is as follows.

All lines, whatever their a-value, have equivalent widths that increase linearly for low number densities. Above $k_pX > 0.1$ they begin to diverge, the Doppler case diverging first, the most Lorentz case last, and all other cases at some stage in between, cases with lower a-value first. This is because a higher a-value means that the line has

more Lorentz component than Doppler, and the Doppler line centre is absorbed first, at low and medium optical depths. The Lorentz wings do play some part, at first insignificant, but rapidly becoming greater. Then as the number density increases, and the Doppler component has been virtually absorbed out (leaving only the Lorentz component), the line starts to behave like a Lorentz line, and its curve of growth starts to follow the Lorentzian again. At very high k_pX values, the wings of the line are now the only part still absorbing, and these wings, with their Lorentz shape, increase the equivalent width quite rapidly with k_pX (Figure 3.11).

The curves of growth in Figure 3.10 are plotted as $\log_{10} W/\alpha_v$ against $\log_{10} k_pX$ and are for various values of the mixing parameter a. Figure 3.11 shows curves of growth of various a-values plotted as $\log_{10} W/\alpha_D$ against $\log_{10} k_pX$. The division of W by α_v in Figure 3.10 will change α_v, and thus line area. For instance, the curves of growth of two pure Doppler lines could be compared only with difficulty, if one line had twice the width of the other (and thus twice the area). This would give two similar curves displaced by a small amount. The curves can be made coincident by dividing W by the Doppler half-widths α_D, thus making the curves of growth of all Doppler lines coincident.

To summarize, this experiment seeks to find a curve of growth, satisfying the conditions of equivalent width and k_pX, passing through both measured values of W, W_L and W_u at the correct values of k_pX_L and k_pX_u. Only one curve of growth can pass through the required points, and is denoted in Figure 3.12 by a solution for the a-value of a_f.

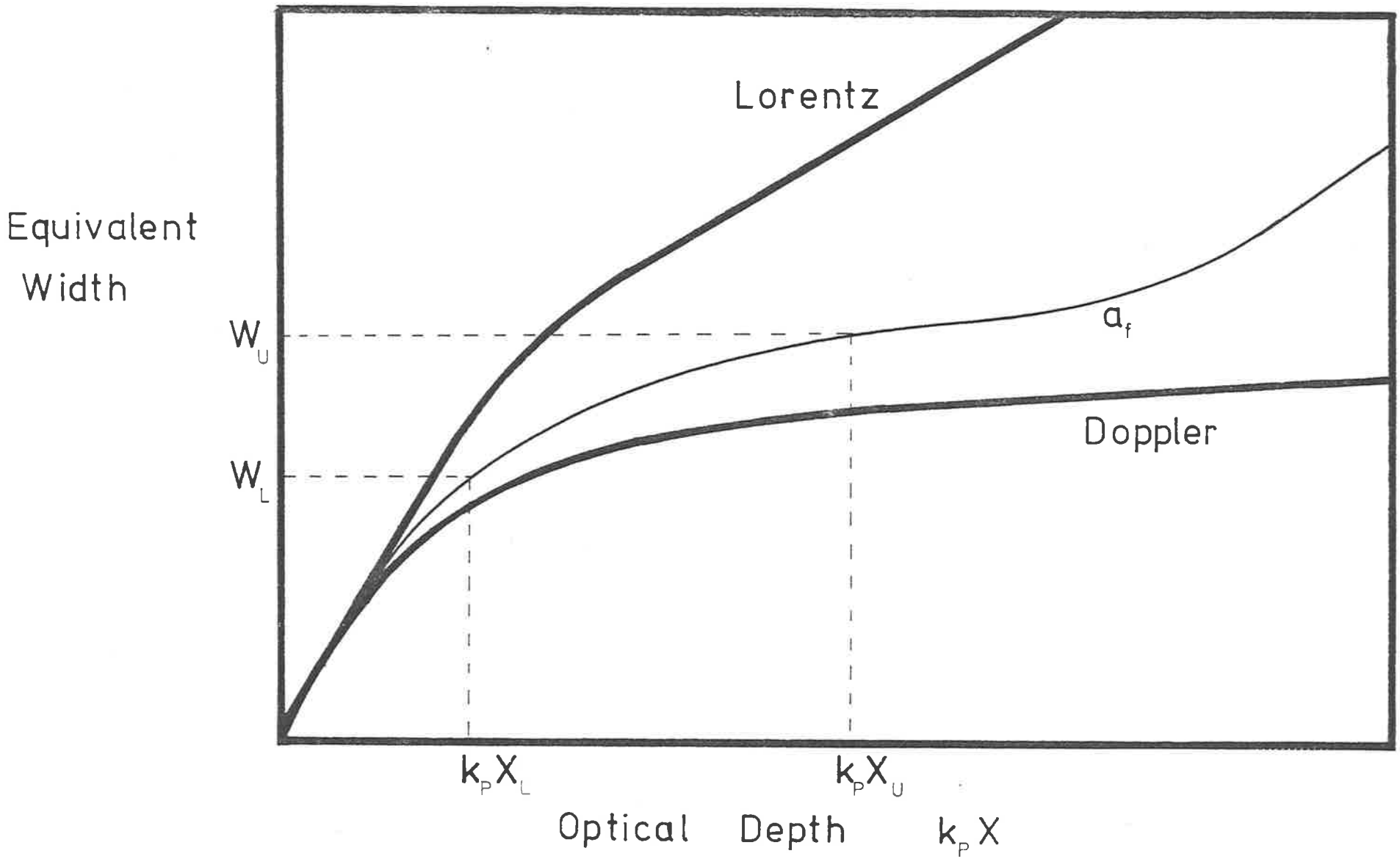

FIG 3.12 Curves of growth of equivalent width W versus optical depth $k_p X$. The solution curve through the two measured equivalent width values W_L and W_u, is denoted by a_f and is unique.

CHAPTER 4

EXPERIMENTAL APPARATUS

4.1 General Description

The various components comprising the experimental apparatus will be described in more detail later, but the basic system consists of an absorption cell containing the target gas, in this case oxygen, a monochromator providing radiation of approximately one wavelength and detectors to measure the incident and transmitted flux of radiation through the gas (see Figure 4.1). Radiation from the discharge lamp emerges from the exit slit of the monochromator and is incident onto a very fine wire grid which partially transmits and partially samples the beam. The grid has a sodium salicylate coating which absorbs the ultraviolet light and fluoresces in the visible and this light is then passed along a light-pipe to the monitor photomultiplier, and is thus a measure of the flux of light incident on the cell. The light transmitted through the grid passes into the absorption cell through an end window, usually lithium fluoride, and then through the target gas. Radiation which reaches the other end of the cell is incident onto another window, and then onto a perspex light-pipe which also has a thin coating of sodium salicylate deposited on the face nearest the exit window. Fluorescent radiation from the phosphor then passes through this short light-pipe to the detector photomultiplier. The outputs from the two photomultiplier detectors are used to measure a relative transmission. This relative transmission value can be normalized to a maximum of unity, by measuring the ratio of outputs with the cell empty of any absorbing gas. The empty cell pressure was usually several orders of magnitude less than the case with the cell "full", and thus introduced very little error. The pressure in the cell was kept at a

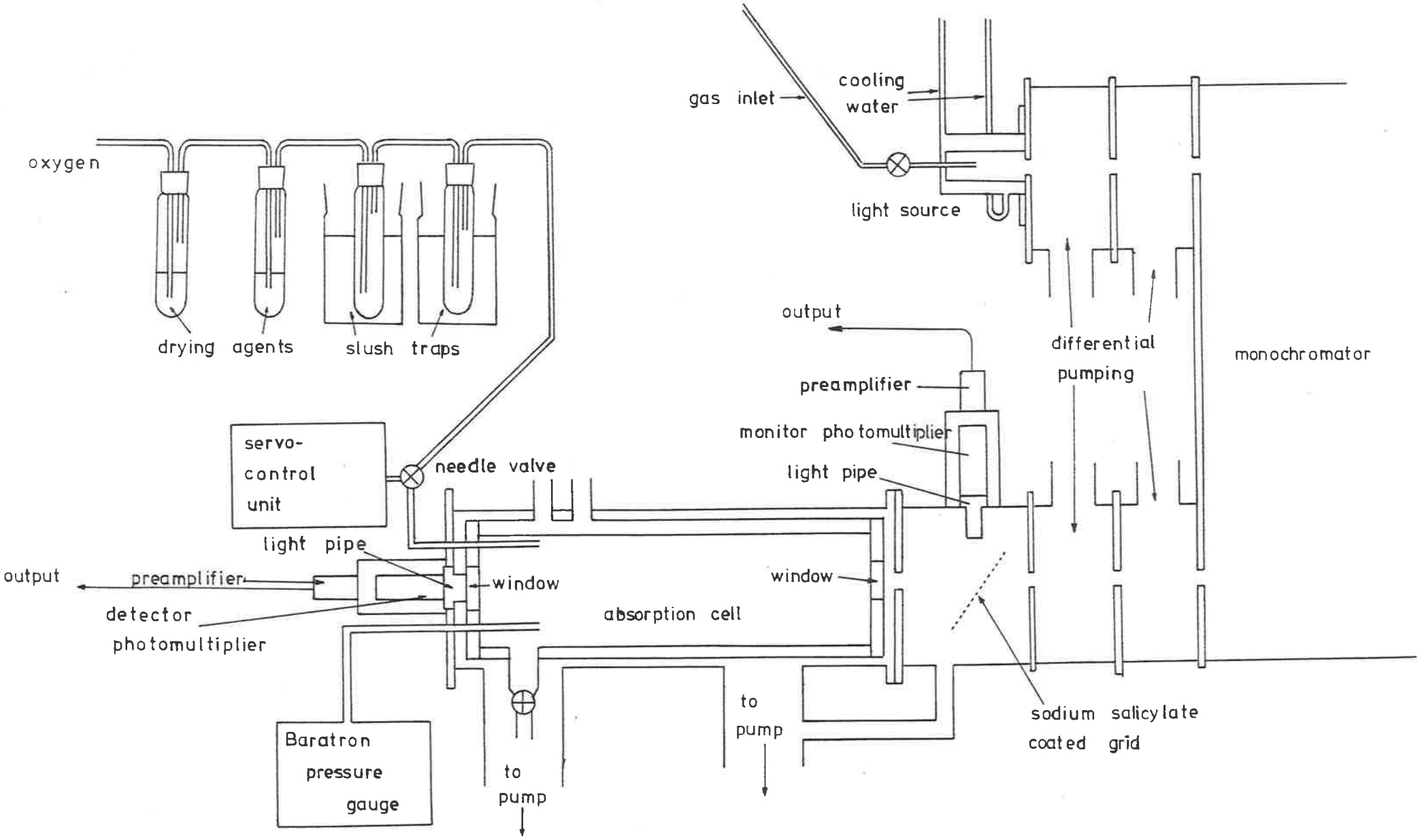

FIG 4.1 A diagrammatic view of the experimental system.

constant value by an M.K.S. Baratron gauge and a Granville-Phillips servo-controlled needle valve. The target gas was fed in through the needle valve after being purified by passing through cold traps and drying agents. The photomultiplier outputs in pulse counting mode were fed through pre-amplifiers back to the multi-channel store-calculator unit, where the results were accordingly plotted, printed or put into visual display.

4.2 The Light Source

The light source was a thyratron triggered hydrogen, helium or argon discharge, depending on the wavelength region required. The repetition rate of the discharge was 1-2 KHz and pulse voltage up to 10 KV, with an average current of between 30 to 40 mA . It consisted of a water-cooled, rectangular cross-section, capillary discharge tube operated as a windowless system with two stage differential pumping consisting of a high speed Roots blower and high speed oil booster pump backed by rotary pumps.

4.3 Lamp Spectra

The experimental results obtained for the Schumann-Runge continuum were done with hydrogen as the lamp gas, at a pressure of 2-4 Torr, giving a continuum in the wavelength range 1600-5000Å . For the Lyman-α work, argon at 40 Torr was used, giving a continuum in the wavelength range 1066-1300Å . A sketch of the various possible lamp gases and their useful wavelength ranges for continuum light are shown in Figure 4.2.

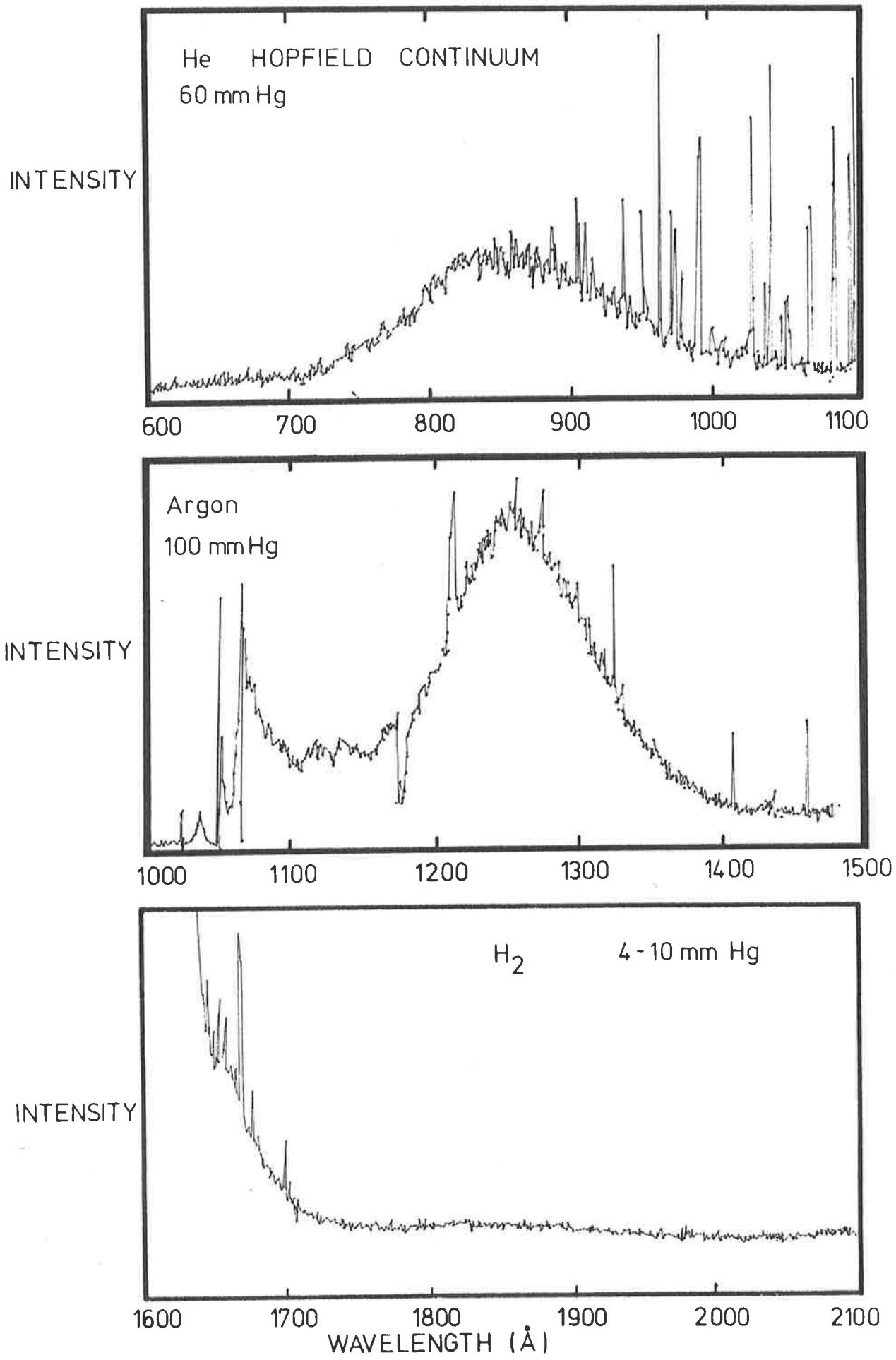

FIG 4.2 Discharge lamp outputs versus wavelength for the three gases used, helium, argon and hydrogen. The usual pressure of gas in the lamp is indicated in the Figures.

4.4 The Monochromator

The Adelaide University 6.65 metre monochromator was used as the dispersing instrument, and a full description of its construction and use is given by Carver et al (1978). This monochromator uses an "off-plane Eagle" mounting in first order and has fixed entrance and exit slits which always remain on the Rowland cylinder as the grating is tilted, and are placed a small distance either side of the Rowland plane. The Rowland circle is in the vertical plane so that the two sets of entrance and exit slits are horizontally placed, an arrangement which is more practical experimentally. The wavelength is scanned by rotating and translating the grating so that the Rowland circle always passes through the point bisecting the line joining the entrance and exit slits.

The monochromator is fitted with a 1200 lines per mm grating blazed for 1500Å and with a radius of curvature of 6.65 metres. It has a ruled area of 175 mm wide and 100 mm long . The monochromator was operated with a resolution of 0.06Å with an entrance and exit slit width of between 24 and 30 microns (10^{-6} m) . The grating mount and slit system as well as the main vacuum tank are supported on a massive (30 tonne) reinforced concrete pier acting as an optical bench, 10 metres in length and providing a rigid experimental platform. The concrete pier is isolated from building vibrations and other disturbances by nine servo-controlled air supports (see Figure 4.3).

Wavelength selection and increments were all controlled from the HP 9810-A calculator, which calculates focus positions simultaneously. Scans covering more than 4Å used the coarse scan system, where the grating is rotated and translated using electric motors. The motors were

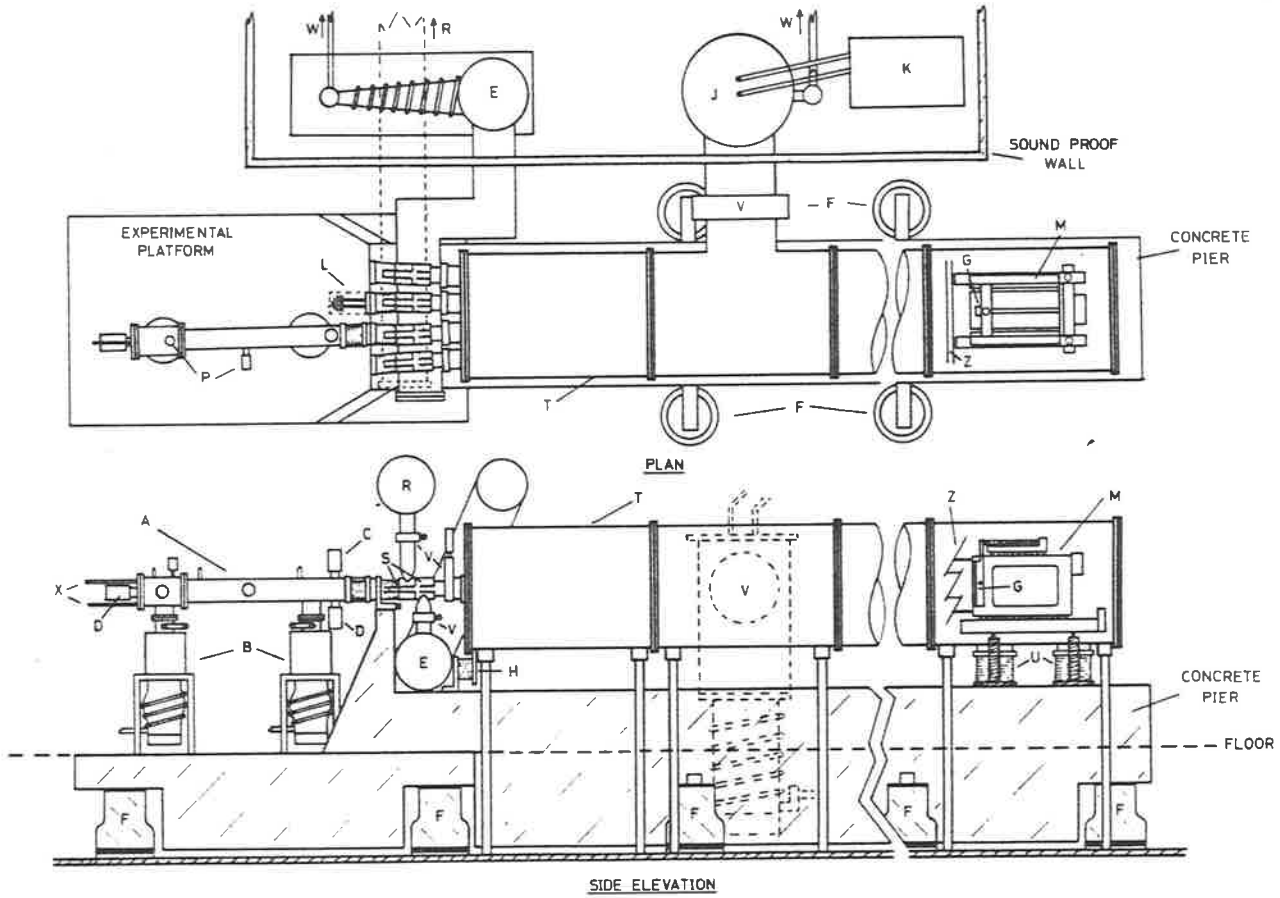

FIG 4.3 Schematic layout of 6.65-m monochromator showing mechanical arrangements, vacuum systems, and experimental platform. *A*, photoabsorption gas cell with temperature jacket; *B*, diffusion pumps and liquid nitrogen traps; *C,D*, light monitors and detectors; *E*, differential pumping, oil booster; *F*, antivibration air support cylinders; *G*, grating; *H*, pressure compensation bellows; *J*, refrigerated cold trap; *K*, two-stage refrigerator; *L*, lamp; *M*, grating mount; *P*, cell pressure gauges; *R*, differential pumping, Rootes Blower; *S*, isolation bellows and differential pumping slits; *T*, main vacuum tank; *U*, vibration isolation bellows; *V*, gate and butterfly valves; *W*, to mechanical backing pumps; *X*, gas inlet and absorption cell pressure monitor; *Z*, light baffle.

(Reproduced from Carver et al (1978)

driven to a position near the wavelength required, and a 10-15Å scan covering a whole vibrational band could then be done. Once the position of the line of interest has been determined, a fine detail, high resolution scan could be done at the correct position. The fine scans were always done using the piezo-electric crystal stack, since this system allows wavelength increments as small as 1 mÅ . This piezo-electric system allowed a scan range of approximately 4Å , using 4095 steps of 1 mÅ , though increments of 10 to 20 mÅ were almost always used. With the piezo number on 2000, that is in the centre of its range, the wavelength passing through the exit slit was equal to that given by the setting of the coarse wavelength control.

4.5 The Absorption Cell

The absorption cell is shown in Figure 4.4. It consisted of an outer vacuum chamber, enclosing a double walled cell with end-plates, all made from stainless steel. The radiation entered through windows mounted in the end-plates, and both windows and end-plates were interchangeable, so that different window materials could be used. Due to beam divergence from the monochromator, the end exit window was necessarily larger than the entrance window (40 mm to 25 mm). The volume between the walls of the inner cell could be filled with a cooling liquid, such as liquid air, so that absorption by cooled gas samples could be measured. This necessitated the use of vacuum seals which would not fail at low temperatures. Neoprene '0' rings become hard and brittle at such low temperatures, and no longer make good contact to form vacuum seals. The end-plates were sealed with annealled copper gaskets pinched between metal to metal fittings, and these provided excellent vacuum sealing for very long time periods. The gaskets were re-usable, but

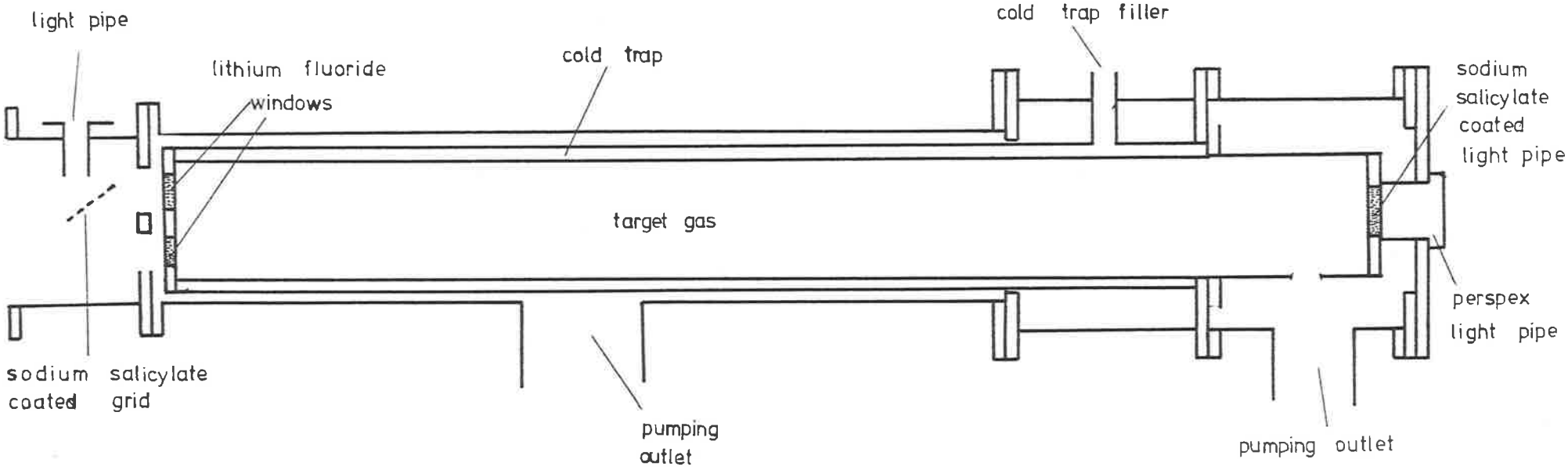

FIG 4.4 A diagrammatic view of the absorption cell used in this work.

after about three or four compressions were no longer useful. The windows were attached to the end plate, and used 'O' rings made from extruded indium wire. These worked satisfactorily, but generally degraded with age, and had to be renewed. The continual changing of pressure in the cell worked the malleable indium down, so that the windows were held less and less tightly. Except for their finite lifetime, these indium seals worked well.

Two end-plates with different window materials in place were used, and these could be interchanged to allow work in a different wavelength region. Quartz and lithium fluoride were the only window types used, the advantage of quartz being that it was much more resistant to thermal shock than was lithium fluoride, a definite advantage at liquid air temperatures. The constant changing of temperature as the cell jacket was filled in the morning and emptied at night eventually produced cleavage lines in the lithium fluoride crystal which shattered the window when the gas pressure was re-applied. The Lyman-α results necessitated using lithium fluoride windows, and working at low temperatures, so window failures were inevitable.

Gas was leaked in through an inlet pipe at the rear of the cell, and the pressure monitored at another inlet pipe. A large screw-turn plunger valve allowed pumping access to the cell. A small line running from the inside of the cell to the pumping region allowed some of the target gas to be bled off, and thus allowed gas cycling, new gas entering to replenish the cell.

4.6 The Light Detectors

The light detectors used were both EMI 9514S photomultipliers. The incident ultraviolet light was converted to visible by sodium salicylate, deposited on a partially transparent wire grid for the monitor, and a coating on the perspex light-pipe for the detector. The wires on the grid were set vertically, each one sampling the radiation passing through the horizontal exit slit of the monochromator.

Some of the preliminary measurements made at Lyman-α were made using a quartz exit window, which was replaced by a lithium fluoride window when one of sufficient size became available. This had the advantages that it transmitted more light, and that the salicylate coating could be moved from the inside of the exit window to a position external to the absorption cell, on the perspex light pipe, to minimize effects due to interaction between the target gas and the salicylate. The transmission of quartz at 1216Å is virtually zero, so the incident light must first be converted to visible to exit the cell if a quartz window is used. This problem does not arise with lithium fluoride, which has a wavelength transmission down to 1050Å . Visible light produced by the salicylate passed down 25 mm diameter light pipes to the photomultipliers.

The photomultipliers were cooled to approximately $-20^{\circ}C$ using a small refrigerator. Considerable care was necessary to maintain both the light sealing of the photomultiplier housing as well as the moisture sealing. Any moisture condensing inside the housing tended to produce discharges and increase the dark current. Cooling the photomultipliers reduces the noise and dark current by a factor of between 15 and 20 .

The photomultipliers were operated in pulse counting mode, the output passing through a preamplifier to the ORTEC counters. These had

a discriminator set to reject the low level noise and to accept only pulses. The counters were 'gated' to the discharge lamp, and only counted when there was a pulse of light emitted by the lamp. The dark current was monitored for both detectors for a length of time equal to their count time, and this was then subtracted from the total counts, leaving only the counts due to incident light. The detectors were shielded with aluminium foil, and the outputs taken along co-axial cable to prevent pickup of stray signals from the lamp power supply.

The light detectors were carefully checked for stray light, scattered light and noise pickup from the lamp. The lamp was shielded carefully, as was the lamp power supply, with earthed wire-mesh, and co-axial cables with sufficient shielding were used. Precautions for interference effects and noise pickup were considered adequate when the dark current measured by the counters remained unchanged with the lamp on or off. Stray light was checked by noting that, with either of the monochromator valves shut, all incident light was removed, there being no light counts registered on the counters. Stray light was also eliminated from other sources, by carefully checking that all joins near the photomultipliers were light tight, and noting no difference on the counters with the room darkened.

Scattered light was corrected for by observing an absorption line, and then increasing the pressure 10 to 20 times. This means that the line will have saturated (case 5 of Figure 3.6), and that there should then no longer be any light of wavelength λ_o, the wavelength of the line centre, incident onto the detector photomultiplier, all light of this wavelength having been absorbed on passing through the cell. However, some light, apparently of this wavelength, but actually consisting of scattered light

from the monochromator grating, was getting through. Measurements of this residual light allowed corrections for scattered light to be made, and these corrections were usually minimal, of the order of 0.3% or less. The response curve of sodium salicylate with wavelength can be considered as flat for all the wavelength intervals considered for this work (see Samson (1967) p. 214).

It was found necessary to add a third lithium fluoride window to the experimental system, between the monochromator exit slit, and the first photomultiplier. This was due to the monitor photomultiplier observing second order lines of wavelength less than 1050Å of large intensity, and moving to a non-linear region of its response curve. The photomultiplier output became non-linear when the input light flux became large, as was the case near intense emission lines. The second photomultiplier, screened by the two windows thus remained linear, but the ratio of the two detectors then became meaningless. The addition of the third lithium fluoride window meant that the monitor photomultiplier could then only observe light of wavelength greater than 1050Å , and thus behaved in a manner similar to the detector photomultiplier. When an emission line of wavelength greater than 1050Å was encountered, and was thus visible to both photomultipliers, the ratio of detector counts remained fairly stable.

CHAPTER 5

PROCEDURE AND DATA ANALYSIS

5.1 Experimental Quantities

As will be shown in this chapter, the experimentally derived quantities such as equivalent width, pressure, temperature, path length and wavelength are all used in the calculation of oscillator strengths. Each of these quantities has an associated error, and the combination of these various errors gives a measure of the uncertainty in the final value for oscillator strength. The two other terms in the expression, the Hönl-London factors and the Boltzmann factors can be considered to be known exactly, although the Hönl-London factors will have to be carefully considered at some other stage (see Section 2.14.2). Each quantity is dealt with individually, its method of measurement, and the error associated with each measurement.

5.1.1 Wavelength

The values of wavelength assigned to the various lines studied were taken from the published values of Ackerman and Biaume (1970) for $v' < 12$ and from Brix and Herzberg (1954) for $v' \geqslant 12$. The accuracy quoted on these figures is 0.0002% for Ackerman and Biaume and approximately 0.0004% for Brix and Herzberg. These figures apply to the main lines in each scan i.e. either the P_{123} or R_{123} lines under consideration. It will be shown later that in the theoretical analysis of the equivalent width, weak lines of neighbouring bands lying close to the lines under analysis, had to be accounted for, and wavelengths assigned to these lines. The worst possible case error for these lines occurred when a calculated value of wavelength, that is, a value using the known molecular constants to calculate energy levels and transitions, was used,

and was never more than .05 A° in error, that is a maximum error of .003% . Since these lines only make minor contributions to the equivalent width, it can be seen that wavelength errors are negligible in comparison to other sources.

5.1.2 Temperature

The entire experiment was performed in a room in which the temperature is controlled so that the variation in the ambient temperature is less than 8°C over the course of the year. The variation over any one day would be less than 1-2°C. For room temperature results, the target gas was assumed to be in thermal equilibrium with its surroundings, and over any one equivalent width measurement, this temperature never varied by more than ± 1°C or ± 0.3% . Some equivalent width measurements were made with the cell cooled by liquid air, giving a temperature of about 82°K. Uncertainty in the cell temperature results from variations in the nitrogen-oxygen mixture of the liquid air, the effects of topping up the coolant container and non-uniform cooling of the cell. The error in the temperature for this case was estimated to be ± 3% .

5.1.3 Absorption Path Length

The absorption path length, the distance between the inside faces of the entrance and exit windows along the interior of the absorption cell, was measured to an accuracy of 1-2 mm, giving an error of 0.1% or less. This error is so small that it can be neglected in the calculation of oscillator strength.

5.1.4 Pressure

Most of the pressure measurements were made with a capacitance manometer (MKS Baratron) gauge. This gauge was first calibrated against a

McLeod gauge, over the range 10^{-3} to 2 torr. Over this range, agreement was found to be very good, errors being no larger than ± 1%. The reference side of the Baratron gauge was always kept at a pressure of 5×10^{-6} torr or less, so that this contributed at maximum, an error of ± 0.025% (when the cell pressure was 0.02 torr, the minimum used).

For very high pressures, in the range 30-700 torr, a mercury manometer was used to measure a reference pressure for the Baratron gauge, the height of the mercury column being measured to 0.1 mms using a telescope with attached vernier. This was necessary because the maximum pressure difference the Baratron gauge could measure was 30 torr . The pressure in the cell was then put equal to the Baratron gauge reading plus the reference pressure. Typical errors in this range would therefore be of the order of 0.1% or less. The servo-controlled needle valve maintained a constant cell pressure to within an accuracy of ± 0.002 torr. The maximum pressure error was ± 1%, and occurred for very low pressure measurements.

The oxygen pressure in the cell was assumed to be the cell full pressure P_F minus the cell empty pressure P_E , or

$$P_{oxygen} = P_F - P_E$$

Since $P_E \leqslant 5 \times 10^{-6}$ torr, this could safety be neglected, and the oxygen pressure put equal to the measured pressures or $P_{oxygen} \simeq P_F$.

5.2 Experimental Procedure

Introduction

The equivalent width of a line or group of lines is measured by observing the transmission of the gas as a function of wavelength over a region containing the lines. Beginning at a wavelength to one side of the region of interest, transmission is measured at a set of wavelengths separated by small steps of wavelength $\Delta\lambda$. Each value of wavelength λ_i will thus have a measured value of transmission τ_i associated with it, and this procedure is called a scan, some terminology which will be used frequently. Each scan produces a value of equivalent width.

Measurements of equivalent width thus require the ability to increment wavelength by regular, fixed amounts. As discussed previously in Chapter 4, the Adelaide 6-metre monochromator has two wavelength stepping procedures, a coarse wavelength shift using electric motors, and a fine wavelength shift using a Piezo-electric grating drive. All measurements of equivalent width used the Piezo-electric fine wavelength control, since only this had sufficient precision to make the necessary very small wavelength steps. The limitations of the Piezo-electric wavelength control was its narrow wavelength range of only $4A^{\circ}$. This only accommodated 3 to 4 rotational lines, so that if it was desired to scan across more than this, such as a whole vibrational band, then it was necessary to use the coarse wavelength stepping motors, since these have unlimited range.

5.3 Equivalent Width

5.3.1 Line selection and Scan Range

Before an accurate scan was done on a line doublet, the entire band under discussion, or a section of it, was inspected first. This consisted of doing a very quick scan, at high pressure to achieve substantial absorption, and with sufficient counting time to allow lines to be reasonably resolved (about 200-500 counts). The lines were then identified by their line spacing, or by position in reference to the band head. A comparison of line spacing of the rotational lines with those given by Brix and Herzberg (1954) for $v' \geqslant 12$ and Ackerman and Biaume (1970) for $v' < 12$ allowed positive identification.

With the coarse wavelength drive motors set at a fixed position at a wavelength close to the line of interest, an accurate locating scan was done with the Piezo-electric grating drive to position the line within the $4A^{\circ}$ range of the Piezo-scan system. The scan range of the equivalent width measurement was selected to completely enclose the line, and as much of the wings of the line as possible. This was done by choosing limits where the absorption due to the line was negligible, that is where the transmission was close to the value for the background. The equivalent width is not invariant with scan range unless the integration is taken well out onto the wings of the lines (see Appendix 7), but it is true to a good approximation if most of the area of the line is taken into account, as is the case once the transmission value in the line wing approaches the background or zero pressure value. When the lines were close together, the scan range was set up so that the beginning and end of the scan coincided with maxima in transmission between lines. If the scan range was increased from these values, then the measurement of

equivalent width would begin to include significant absorption from neighbouring strong lines, which it is desirable to minimize. Decreasing the scan range means reducing the integration limits for the equivalent width, a quantity which should be maximized (see Figure 5.1).

5.3.2 Scan Procedure

Before each equivalent width measurement scan was made, a pre-scan to accurately locate the rotational line was done. Care must be taken to ensure that the line is inside the scan-range of wavelengths, and this was accomplished by beginning the experimental run at a wavelength below λ_A (of Figure 5.1), and continuing on past λ_B, the final wavelength setting. Only the transmission values measured at points between λ_A and λ_B will be used to calculate the equivalent width, but the above precaution was found to be necessary to allow for slight apparent wavelength shifts of the line with time, and for different apparent linewidths at different pressures (lines appear wider at high pressure than at low, so the scan range must be increased at high pressure), to be sure of completely enclosing the line.

The wavelength increment $\Delta\lambda$ was chosen to give sufficient points across the apparent half-width of the line to allow accurate determination of the equivalent width (usually never less than 10 points). The increment was usually 20 mA° for a high pressure scan, and usually 10-20 mA° for a low pressure scan (though sometimes as small as 5 mA°). This gave between 50-100 points per scan. The monitor-detector signal ratio γ_i (measured at wavelength λ_i), was stored away in the multi-channel store. A typical scan is shown in Figure 5.1.

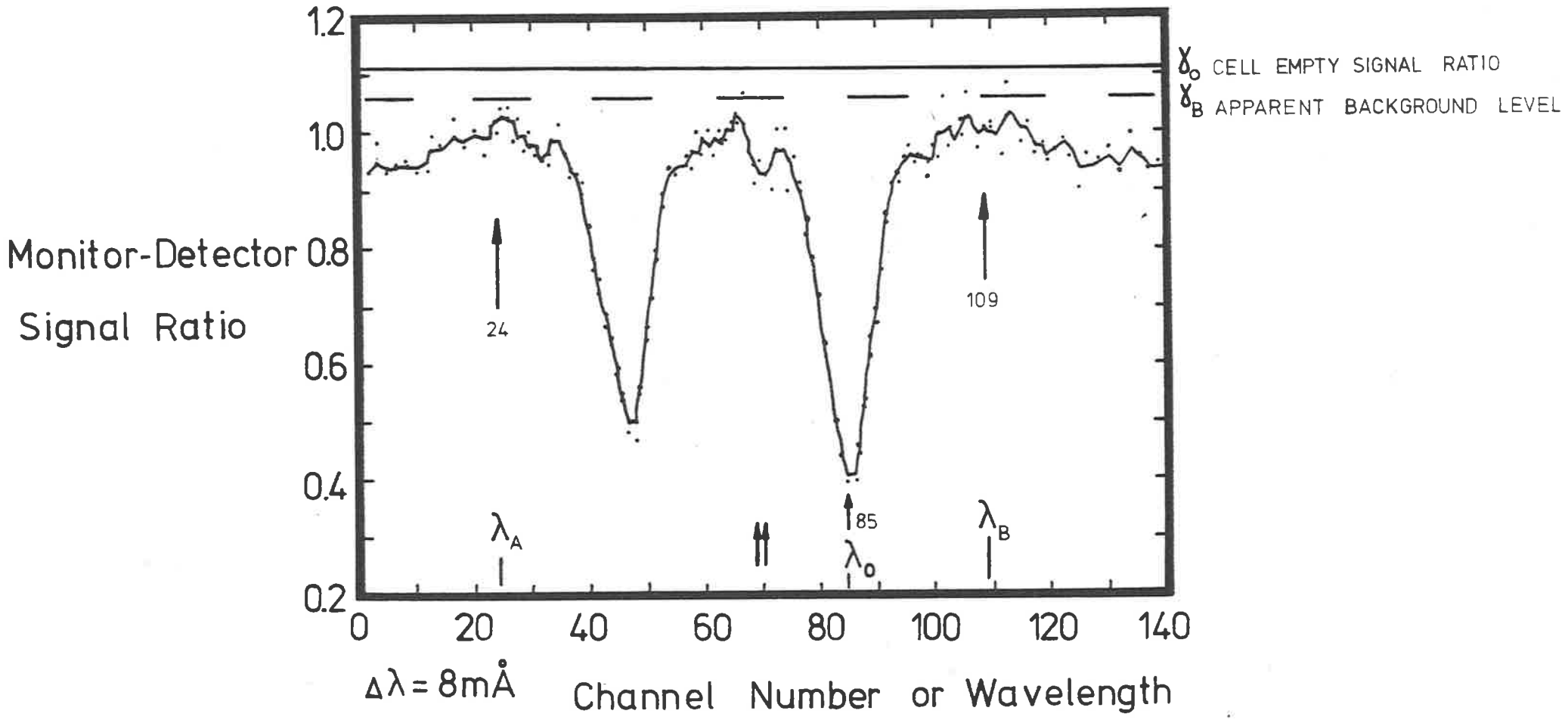

FIG 5.1 A typical scan used for an equivalent width measurement. The wavelength limits λ_A and λ_B, denoted by channel numbers 24 and 109 respectively, are the integration limits.

5.4 Background Corrections and Background Factor.

Once the monitor-detector signal ratios γ_i at the various wavelengths λ_i have been recorded and stored in the multi-channel store, values of transmission τ_i may be extracted. To do this, knowledge of the background, or cell empty signal ratio γ_o must be obtained. The transmission value with the cell empty is unity (by definition), but due to different collecting efficiencies of the light gathering systems supplying each photomultiplier, then it will almost never be the case, that the cell empty, monitor-detector signal ratio, γ_o, will be unity. The differences due to grid transmission at the monitor photomultiplier not being equal to the transmission of the cell end-window near the detector photomultiplier, different salicylate thicknesses at each detector, different light pipe arrangements and lengths, and intrinsic differences between the photomultipliers will ensure that γ_o is not unity. The values can be converted to true transmission values by

$$\tau_i = \gamma_i/\gamma_o \qquad (5.1)$$

where τ_i is now the transmission at wavelength λ_i.

The empty cell ratio of signals, γ_o, was measured at a wavelength inside the scan range $\lambda_A - \lambda_B$, but away from the line centre (to minimize any absorption due to gas remaining in the cell, usually several orders of magnitude less than the pressure at which the scan was done). The total number of counts used for γ_o was made equal to the total number of counts comprising the equivalent width measurement. If the equivalent width was measured over 50 channels, and each channel had a monitor count of 2000, then the equivalent width was composed of 100,000 counts, and the total number of counts used for the background, zero

pressure ratio γ_o would also be 100K (10 channels of 10K counts). In this way each contributes equally to the total error.

It is assumed here, that the cell empty signal ratio γ_o is invariant with wavelength over a scan (found to be the case in numerous checks). τ_i is now the transmission value through the absorbing gas due to absorption in the gas, and thus consists of absorption due to all processes which may have a contribution to make at wavelength λ_i. The quantity of direct interest is the equivalent width due to absorption by the rotational absorption line alone, and the contributions to the absorption of any underlying continuum, and due to neighbouring lines must be subtracted from the measured equivalent width value. The equivalent width is given by

$$W = \int_{-\infty}^{\infty} (1 - \tau_T) \, d\lambda \qquad (5.2)$$

where τ_T is the transmission inside the scan range. The above integral should actually be written

$$W'' = \int_{\lambda_A}^{\lambda_B} (1 - \tau_T) \, d\lambda \qquad (5.3)$$

since the integration never extends to infinity in the experimental case. Here W'' is approximately equal to W, the approximation becoming better the more of the line is included inside the integration limits (see Appendix 7). An integral can be approximated by a summation, especially if the function being integrated does not vary too rapidly between measured points (the reason for choosing sufficient points across the line half-width by choosing small enough $\Delta\lambda$). Equation 5.3 can therefore be approximated by

$$W'' = \int_{\lambda_A}^{\lambda_B} (1 - \tau_T) \, d\lambda \simeq \sum_{i=1}^{n} (1 - \tau_i) \, \Delta\lambda$$

$$W'' = \sum_{i=1}^{n} (1 - \frac{\gamma_i}{\gamma_o}) \, \Delta\lambda \qquad (5.4)$$

Since γ_o is a constant, equation 5.4 reduces further to

$$W'' = n\Delta\lambda - \frac{\Delta\lambda}{\gamma_o} \sum_{i=1}^{n} \gamma_i \qquad (5.5)$$

Here γ_i and γ_o are measured experimental quantities. What is needed is to isolate the equivalent width due to the rotational line alone. The procedure is as follows. Other absorption lines nearby usually have wings which contribute significant absorption inside the scan range. A computer programme was used to calculate the absorption coefficient due to neighbouring lines, by summing contributions from all lines within 100 cm^{-1} (3 to 4 A°) of the reference line (inside the scan range), at the wavelength of the reference line, λ_o . That is, a value of the absorption coefficient k_E , due to external lines was computed. To this was added the value for the continuum absorption coefficient at that wavelength, k_c . The total absorption coefficient inside the scan range is the sum of the three values.

$$k_T = k_L + k_E + k_c \qquad (5.6)$$

where k_L is the absorption coefficient due to lines inside the scan range. The values used for k_c are some extrapolated values for the Herzberg continuum of Shardanad and Prasad Rao (1977) for the Schumann-Runge continuum (see Section 5.8).

The transmission τ is related to the absorption coefficient by Beer's Law,

$$\tau_T \quad \exp\ (\ -\ k_T\ x\ ) \tag{5.7}$$

where x is the path length. That is, τ can be written

$$\tau_T = \exp\ [\ -\ (k_L + k_C + k_E)\ x\ ] \tag{5.8}$$

or $$\tau_T = \exp\ [\ -\ (k_E + k_C)\ x\ ] \exp\ (\ -\ k_L\ x\ ). \tag{5.9}$$

This reduces to

$$\tau_T = \tau_B . \tau_L \quad \text{where} \quad \tau_B = \exp\ [\ -\ (k_E + k_C)\ x\ ]$$

Here τ_T is τ_i at wavelength λ_i, so equation 5.3 reduces to

$$W' = \sum_{i=1}^{n} (1 - \tau_L)\ \Delta\lambda = \sum_{i=1}^{n} (1 - \frac{\tau_i}{\tau_B})\ \Delta\lambda$$

$$W' = (1 - \frac{\gamma_i}{\gamma_o} . \frac{1}{\tau_B})\ \Delta\lambda = \sum_{i=1}^{n} (\frac{\tau_o - \tau_i}{\tau_B})\ \Delta\lambda \tag{5.10}$$

where $\tau_L = \tau_i/\tau_B$ and τ_B is computed by the background factor programme. Division by this factor τ_B is equivalent to subtracting the continuum and external line contributions from the τ_i values.

5.4.1 Analysis of Data

The equivalent width due to lines under consideration is given by the area enclosed between the background transmission and the total transmission values of Figure 5.2. The expression for equivalent width is

$$W' = n\Delta\lambda - \Delta\lambda \sum_{i=1}^{n} \tau_i/\tau_B \tag{5.11}$$

The values of equivalent width were calculated from the values for γ_i stored in the multi-channel store, and the cell empty monitor detector signal ratio γ_o, measured either immediately before or after the

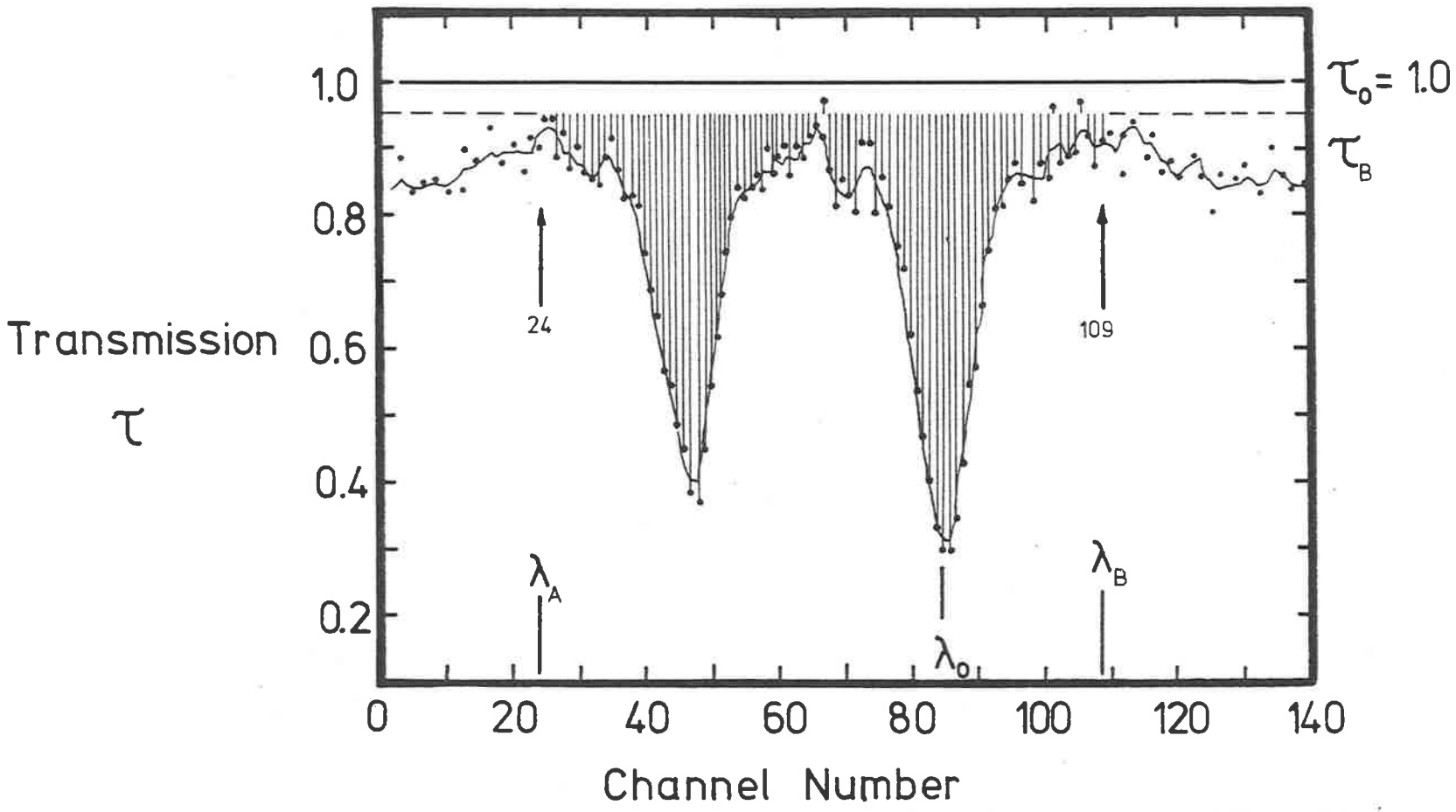

FIG 5.2 A typical scan used to determine equivalent width. This is a normalized version of Figure 5.1., with signal ratios converted to transmission values. The equivalent width is the ruled area, the length of the lines corresponding to $\tau_B - \tau_i$ in equation 5.10.

equivalent width scan. At the same time, the HP 9810 A calculator computed the statistical errors associated with each equivalent width measurement, based on the number of counts (see Section 5.5).

5.5 Statistical Errors for Equivalent Width Measurements.

Each measured value of equivalent width W has an error ΔW associated with it, and this error quantity has contributions from two main sources (see equation 5.11). Neglecting the minute consequences from n and $\Delta\lambda$, these two sources are τ_B, the background transmission values, and the transmission values τ_i.

From Figure 5.2, the equivalent width is the sum of all $(\tau_B - \tau_i)$ points, corresponding to the area between the τ_B line and the various τ_i points. Errors in the background value correspond to displacing the background line τ_B of Figure 5.2, and thus changing the area (and the equivalent width value), while errors in the τ_i values result in changes to the contributing area of those points to the equivalent width.

The contribution from the individual points τ_i consists of statistical errors due to counting statistics of the monitor and detector for the signal ratios γ_i and γ_o. Defining the monitor counts as M, and the detector counts as D, the signal ratio γ_i is

$$\gamma_i = D_i/M_i \tag{5.12}$$

where M_i and D_i are the monitor and detector counts of the ith point respectively. The counts comprise that due to the light source, and that due to the dark current of the detector. That is, we have

$$M_L = M_{L+D} - M_D \quad \text{and} \quad D_L = D_{L+D} - D_D$$

where the subscripts L and D refer to counts due to the light source, and those due to dark counts respectively. The quantities of direct interest are M_L and D_L and the errors in those quantities.

The signal counters are gated for a short time period synchronised

with the pulsed light source. The counts recorded in this interval are M_{L+D} and D_{L+D}. The dark current counters are gated for an equal time period between lamp pulses, giving counts M_D and D_D which are subtracted from the former counts to give M_L and D_L. The counts M_{L+D} are much greater than M_D, so the ratio M_D/M_{L+D} is very small (a fraction of a percent) since the dark currents are kept to a minimum. The error in $M_L = M_{L+D} - M_D$ can then be written

$$\delta M_L = \sqrt{\delta M^2_{L+D} + \delta M^2_D} \tag{5.13}$$

where δM_{L+D} and δM_D are the errors in M_{L+D} and M_D respectively, and are equal to $\sqrt{M_{L+D}}$ and $\sqrt{M_D}$. Equation 5.13 can then be written

$$\delta M_L = \sqrt{\delta M_{L+D}^{\,2} \left(1 + \delta M_D^{\,2}/\delta M_{L+D}^{\,2}\right)}$$

or

$$\delta M_L \simeq \delta M_{L+D} \simeq \sqrt{M_L} \tag{5.14}$$

The errors in M_L and D_L are therefore $\sqrt{M_L}$ and $\sqrt{D_L}$.

Using equation 5.14, the expression for the error in γ_i, $\delta\gamma_i$ can be written as

$$\frac{\delta\gamma_i}{\gamma_i} = \sqrt{\left(\frac{\delta D_i}{D_i}\right)^2 + \left(\frac{\delta M_i}{M_i}\right)^2}$$

which reduces to

$$\frac{\delta\gamma_i}{\gamma_i} = \sqrt{1/D_i + 1/M_i} = \sqrt{\frac{1 + \gamma_i}{\gamma_i M_i}} \tag{5.15}$$

Since in almost every case, the number of monitor counts used for each point was held constant, the M_i in equation 5.15 can be replaced by M to give

$$\frac{\delta\gamma_i}{\gamma_i} = \sqrt{\frac{1 + \gamma_i}{M\gamma_i}} \tag{5.16}$$

and this term gives the dependence of the equivalent width upon the number of counts M used for each point.

The statistical error associated with the measurement of cell empty signal ratio γ_o takes the same form as equation 5.16 , and can be written

$$\frac{\delta\gamma_o}{\gamma_o} = \sqrt{\frac{1 + \gamma_o}{M_o \gamma_o}} \tag{5.17}$$

γ_o is measured for a total number of counts equal to M_o (usually 100,000, or put equal to $n\,M$, where n is the number of channels comprising the equivalent width, and M is the number of counts per channel). τ_B has no statistical error to contribute, although it does have an error (usually small). For example, an error of 10-20% in the value for the continuum background absorption coefficient value would only have an 0.2-0.4% change in the value of τ_o for a low pressure equivalent width measurement, and an 0.6-1.0% change for a high pressure equivalent width measurement. The value of τ_B is calculated from theoretical line spacings, strengths and continuum values.

The error in W' , written $\delta W'$ can then be obtained as follows,

$$(\delta W')^2 = \sum_{i=1}^{n} \left(\frac{\partial W'}{\partial \gamma_i} \right)^2 \delta\gamma_i^{\,2} + \left(\frac{\partial W'}{\partial \gamma_o} \right)^2 \partial\gamma_o^{\,2} + \left(\frac{\partial W'}{\partial \tau_B} \right)^2 \delta\tau_B^{\,2} \tag{5.18}$$

where $\frac{\partial W}{\partial \gamma_i}$ is the partial derivative of the equivalent width with respect to the various signal ratios, $\frac{\partial W'}{\partial \gamma_o}$ is the partial derivative of the equivalent width with respect to the zero pressure signal ratio and $\frac{\partial W'}{\partial \tau_B}$ is the partial derivative with respect to the background transmission due to continuum and external lines. The quantities $\frac{\partial W'}{\partial \gamma_i}$, $\frac{\partial W'}{\partial \gamma_o}$, and

$\frac{\partial W'}{\partial \tau_B}$ are a measure of the rate of change of equivalent width W' with change in signal ratio γ_i, zero pressure signal ratio γ_o and background contribution respectively.

The terms $\frac{\partial W}{\partial \gamma_i}$ and $\frac{\partial W}{\partial \gamma_o}$ are used in preference to $\frac{\partial W}{\partial \tau_i}$ to eliminate cross-product derivatives in equation 5.18 and simplify the calculation. Since the expression for equivalent width is

$$W' = n\,\Delta\lambda - \frac{\Delta\lambda}{\gamma_o \tau_B} \sum_{i=1}^{n} \gamma_i$$

then

$$\frac{\partial W'}{\partial \gamma_o} = \frac{\Delta\lambda}{\gamma_o^2\, \tau_B} \sum_{i=1}^{n} \gamma_i \qquad (5.19)$$

$$\frac{\partial W'}{\partial \gamma_i} = -\frac{\Delta\lambda}{\gamma_o\, \tau_B} \qquad (5.20)$$

and

$$\frac{\partial W'}{\partial \tau_B} = \frac{\Delta\lambda}{\gamma_o\, \tau_B^2} \sum_{i=1}^{n} \gamma_i \qquad (5.21)$$

Substitution of equations 5.19 to 5.21 into 5.18 yields

$$(\delta W')^2 = \sum_{i=1}^{n} \left(-\frac{\Delta\lambda}{\tau_B\, \gamma_o} \right)^2 \gamma_i^2 \left(\frac{1+\gamma_i}{M\gamma_i} \right) + \left(\frac{\Delta\lambda}{\gamma_o\, \tau_B^2} \right)^2 \left(\sum_{i=1}^{n} \gamma_i \right)^2 \delta\tau_B^2$$

$$+ \left(\frac{1+\gamma_o}{M_o \gamma_o} \right) \left(\frac{\Delta\lambda}{\gamma_o^2\, \tau_B} \right)^2 \left(\sum_{i=1}^{n} \gamma_i \right)^2 \gamma_o^2$$

and this reduces further to

$$(\delta W')^2 = \frac{\Delta\lambda^2}{\gamma_o^2 \tau_B^2} \left(\sum_{i=1}^{n} \gamma_i \right)^2 \left[\frac{\sum_{i=1}^{n} \gamma_i (1+\gamma_i)}{M \left(\sum_{i=1}^{n} \gamma_i \right)^2} + \left(\frac{1+\gamma_o}{M_o \gamma_o} \right) + \frac{\delta\tau_B^2}{\tau_B^2} \right]$$

The above expression may be written as

$$\delta W' = \frac{\Delta\lambda}{\gamma_o\, \tau_B} \sum_{i=1}^{n} \gamma_i \sqrt{\frac{1+\gamma_o}{M_o \gamma_o} + \frac{\sum_{i=1}^{n} \gamma_i (1+\gamma_i)}{M \left(\sum_{i=1}^{n} \gamma_i \right)^2} + \frac{\delta\tau_B^2}{\tau_B^2}}$$

and this gives a final result for $\delta W'$ of

$$\delta W' = \frac{\Delta\lambda}{\tau_B} \sum_{i=1}^{n} \tau_i \sqrt{\frac{1+\gamma_o}{M_o\gamma_o} + \frac{\sum_{i=1}^{n} \tau_i (1+\gamma_o\tau_i)}{M\gamma_o \left(\sum_{i=1}^{n} \tau_i\right)^2} + \frac{\delta\tau_B^2}{\tau_B^2}} \qquad (5.22)$$

5.6 Computer Simulation of Experiment

An important part of the results analysis is the theoretical simulation of the experimentally measured equivalent widths. A computer programme first built up a theoretical total absorption coefficient using line positions, strengths and widths, and this was then used to compute the absorption at all the different wavelengths across the scan using a small increment $\delta\lambda$ (usually 1 or 2 mÅ). This computed absorption (a function of wavelength denoted by $A(\lambda)$) was then convoluted with the instrument resolution function, $g(\lambda)$, and the area of this new absorption function, $C(\lambda)$ was summed and compared with the measured experimental equivalent width values W_L (the value measured at low pressure) and W_u (the value measured at high pressure). This process was repeated with varying values of the optical density until the theoretical equivalent width absorption areas agreed with the experimentally determined equivalent widths W_L and W_u at the correct value of pressure ratio Y , where

$$Y = P_u/P_L \qquad (5.23)$$

and where P_L and P_u are the pressures used to measure W_L and W_u respectively. The line broadening parameter a is varied during the computation, to obtain the best fit to the two measured equivalent widths.

5.6.1 The Theoretical Absorption Coefficient

To build up a model of the absorption coefficient in a

certain wavelength region, three basic parameters are required. These are the wavelengths of the lines λ_m , line strengths S_m , and a_m , where a_m is the ratio of Lorentz to Doppler broadening of line m . The line width is related to this a-value by equation 3.38. The absorption coefficient at wavelength λ_i inside the scan range is the sum of all the contributions from the various lines at that wavelength. This coefficient is stored in a matrix used by the computer programme, and may be used a number of times during the course of a calculation. Each scan usually contained a P and an R branch rotational line, each consisting of a triplet of lines (P_1 , P_2 and P_3 , and R_1, R_2 and R_3), as well as a number of weaker lines, usually from neighbouring bands or from bands of the first vibrational level. If it is not possible to resolve the individual triplet components, as is often the case in the lower bands, the three triplet components were combined to form one line of approximately 3 times the strength at the wavelength given by Ackerman and Biaume (1970). When separate wavelengths are given for the components, these are then used in the programme. The wavelengths of lines from $v' = 1$, and forbidden transitions, and from neighbouring bands were calculated by a computer programme using level constants and splitting parameters of Bergeman and Wofsy (1972) to calculate energy levels and wavenumbers of transitions.

The strengths of the individual triplet components are calculated using Boltzmann factors, Hönl-London factors, and theoretical oscillator strengths of Allison, which are used as initial starting values.

Line strength S'_m is given by

$$S'_m = \alpha_J \, \delta_J f \qquad (5.24)$$

where α_J is the weighted Boltzmann factor, S_J is the Hönl-London factor and f is the oscillator strength. One line was chosen as the reference line (usually the P_1 component) and assigned a strength of 1.0 , and the other lines were adjusted so that their strengths were

$$S_m = \frac{S_m'}{S_R'} \qquad (5.25)$$

where S_m' is the strength of line m , and S_R' is the calculated strength of the reference line. After this normalization, an oscillator strength is obtained from the computed value of $k_p X$ for this reference line. The variation in a-value during the computation produces a solution a_f , the final value of a , which produces a curve of growth passing through both W_L and W_u . As a first estimate for the values of a_m , linewidths of Hudson and Mahle (1972) were used. An example of a theoretical absorption coefficient built up using known parameters is shown in Figure 5.3.

5.6.2 Instrument Resolution Function

The absorption coefficient at wavelength λ_i is used to calculate the absorption at this wavelength by using the variable $k_p X$ which is a measure of the absorption path length. Beer's Law gives

$$I = I_o \exp [- k_p X \, k(\lambda_i)]$$

where I is the final intensity after passing through an amount of absorber length X , and $k(\lambda_i)$ is a function representing the absorption coefficient at wavelength λ_i . The actual value of absorption coefficient at any wavelength λ_i is $k_p k(\lambda_i)$, where k_p is the peak height at the line centre. It is usual to write I_o as independent of wavelength, as the lamp provides a continuum, which

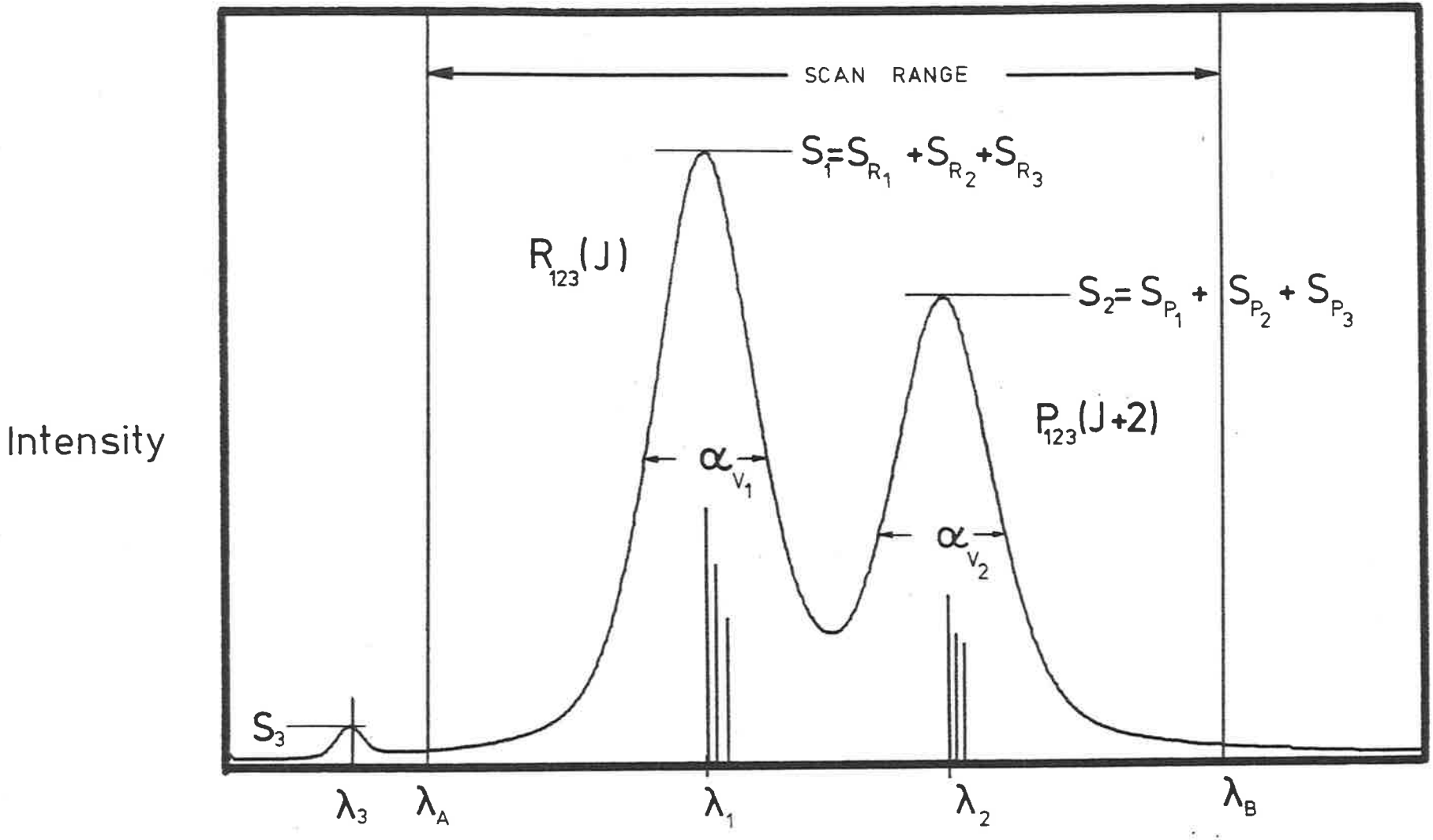

FIG 5.3. An example of a theoretical absorption coefficient built up by computer simulation. The three triplet components near λ_1 and λ_2 are combined to form a single line, of strength S_1 and S_2. The width of the combined lines are α_{v_1} and α_{v_2}, where α_{v_1} and α_{v_2} are the widths of each of the triplet components.

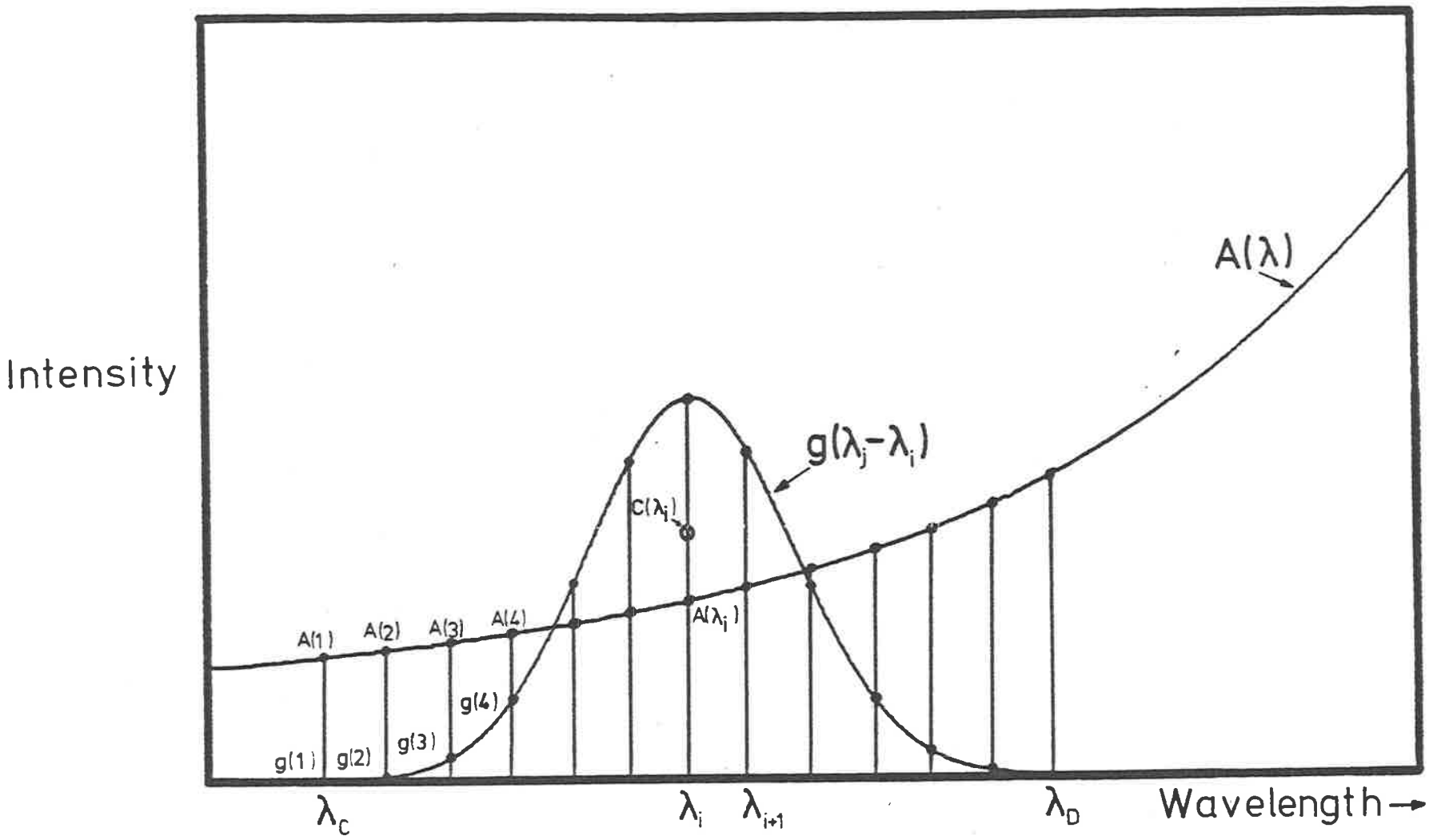

FIG 5.4. A plot of the instrument resolution function $g(\lambda_j - \lambda_i)$, and the convolution with the absorption function $A(\lambda)$, to produce the convolution point $C(\lambda_i)$, where $C(\lambda_i) = \sum_{j=1}^{n} A(\lambda_j)\, g(\lambda_j - \lambda_i)\, \Delta\lambda$.

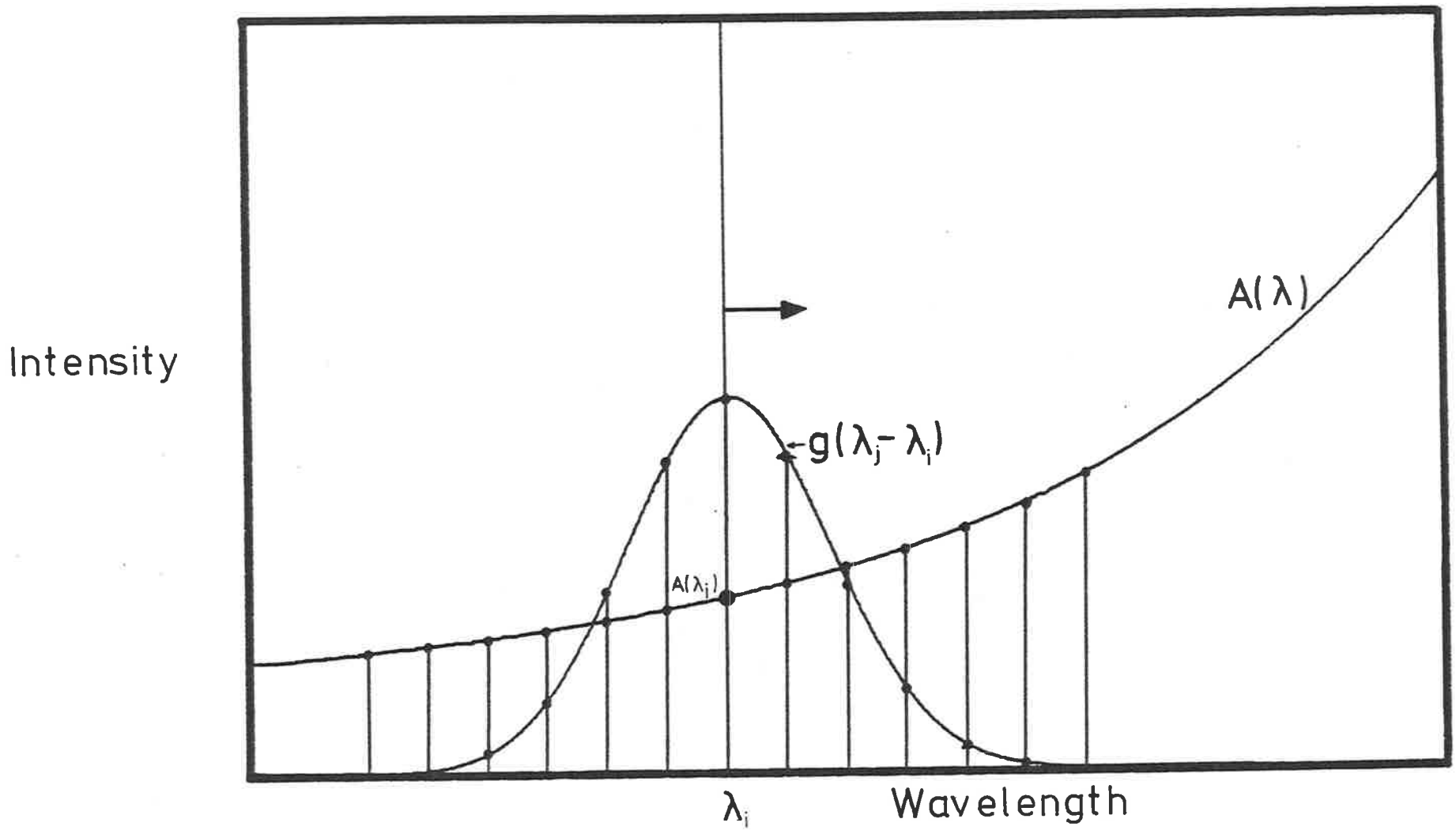

FIG. 5.5 The alternate convolution process. The point $A(\lambda_i)$ is multiplied in turn by all the $g(\lambda_j-\lambda_i)$ points to the left of λ_i as $g(\lambda_j-\lambda_i)$ sweeps past.

has a relatively constant value over wavelength intervals which are larger than any used to scan equivalent widths. However, some wavelength dependence will be introduced by the instrument resolution function $g(\lambda)$. This instrument resolution function was assumed to be a Gaussian function, of the form

$$g(\lambda) = g_o \exp \left[- \left(\frac{\lambda - \lambda_o}{\alpha_g} \right)^2 4 \ln 2 \right] \qquad (5.26)$$

where the half-width (full width at half height) α_g was 0.05Å . Before the equivalent width can be calculated, the theoretical absorption must be convoluted with the instrument function. This then produces an absorption spectrum, which should closely resemble the one obtained experimentally. Convolution of the absorption $A(\lambda)$ with the instrument function $g(\lambda)$ produces a convoluted absorption spectrum, $C(\lambda)$ where

$$C(\lambda_i) = \int_a^b A(\lambda_j) \cdot g(\lambda_j - \lambda_i) \, d\lambda_j \qquad (5.27)$$

and this can be written as

$$C(\lambda_i) = \sum_{j=1}^{m} A(\lambda_j) \cdot g(\lambda_j - \lambda_i) \, \Delta\lambda \qquad (5.28)$$

Here $A(\lambda_j) = \exp \left[- k(\lambda_j) \, k_p X \right]$ and $C(\lambda_i)$ is the value of the convolution at wavelength λ_i, $A(\lambda_j)$ is the value of the absorption at wavelength λ_j , and $g(\lambda_j - \lambda_i)$ is the value of the instrument function at λ_j (see Figure 5.4). The instrument function $g(\lambda)$ is normalized so that

$$\int g(\lambda) \, d\lambda = 1.0 \qquad (5.29)$$

which can be written $\sum_{j=1}^{\infty} g(\lambda_j - \lambda_i) \, \Delta\lambda = 1.0.$

This is simply a statement of fact that all light incident on the slit

area passes through the slit, and the only effect of the resolution function is to redistribute some of the light to different wavelengths. The equivalent width W' is now given by

$$W' = \int_{\lambda_A}^{\lambda_B} C(\lambda_i)\, d\lambda_i \qquad (5.30)$$

or more relevantly by $W' = \sum_{i=K}^{L} C(\lambda_i)\,\Delta\lambda$, where K and L are integers corresponding to λ_A and λ_B in Figures 5.2 and 5.3 .

The convolution method consists of centring the resolution function at wavelength λ_i , and convoluting with the absorption $A(\lambda_j)$ using (see Figure 5.4)

$$C(\lambda_i) = \sum_{j=1}^{m} A(\lambda_j) \cdot g(\lambda_j - \lambda_i)\,\Delta\lambda$$

Here the variable is j (or λ_j) , the computer programme multiplies the various different values of $A(\lambda_j)$ by the value of the resolution function at that wavelength $g(\lambda_j - \lambda_i)$ when it is centred at λ_i , and then takes the sum over all values of λ_j for which the resolution function has a significant value. The resolution function is then moved to λ_{i+1} , and the process repeated. In this way, the values of the convolution function $C(\lambda_i)$ are obtained, and the equivalent width is then the sum of all these values. That is

$$W' = \sum_{i=1}^{n} C(\lambda_i)\Delta\lambda = \sum_{i=1}^{n}\sum_{j=1}^{m} A(\lambda_j)\; g(\lambda_j - \lambda_i)\Delta\lambda \qquad (5.31)$$

and this value will be a good approximation to the ideal case of infinite scan and the true value W , if the scan encloses most of the line. Here

$$W = \sum_{i=1}^{\infty}\sum_{j=1}^{\infty} A(\lambda_j)\; g(\lambda_j - \lambda_i)\Delta\lambda \qquad (5.32)$$

and the above expression is independent of $g(\lambda_j - \lambda_i)$, since the summation signs can be interchanged as follows

$$W = \sum_{j=1}^{\infty} A(\lambda_j) \sum_{i=1}^{\infty} g(\lambda_j - \lambda_i)\Delta\lambda = \sum_{j=1}^{\infty} A(\lambda_j)\Delta\lambda \text{ using}$$

$$\sum_{i=1}^{\infty} g(\lambda_i - \lambda_j) = \sum_{j=1}^{\infty} g(\lambda_j - \lambda_i) = 1.0.$$

In a typical computation, the above method would involve about 800 wavelength points λ_i across the entire scan range, with $\Delta\lambda$ of 1 or 2 mÅ, and 200 points across the resolution function $g(\lambda - \lambda_0)$. This means at each wavelength λ_i, 200 multiplications of $A(\lambda_j) \cdot g(\lambda_j - \lambda_i)$ must be done, and this must be repeated 800 times across the scan range from λ_A to λ_B, giving a total of 160,000 multiplications for each value of $k_p X$. The above procedure can be visualized as sliding the resolution function across the absorption function to produce the convolution function, the convolution being done at each point λ_i between λ_A and λ_B.

The reason a number as small as 200 can be used for the number of data points comprising the resolution function is because it is Gaussian, and a property of Gaussian functions is that the amplitudes fall to zero very quickly. If the half-width α_g is 50 mÅ, then by 100 steps of 1 mÅ out onto the line wings, the amplitude will be negligible. Thus a Gaussian curve of 50 mÅ half-width can be adequately represented by 200 data points separated by 1 mÅ.

There is an alternative convolution method, which uses this very rapid amplitude decay property of the Gaussian function to greatly reduce computing time. If the half-width of the Gaussian α_g is 50 mÅ, then the 1/e half-width α_e is 30 mÅ. If λ_A and λ_B are the limits of the scan range, then the interval $\lambda_A - 3\alpha_e$ to $\lambda_B + 3\alpha_e$ encloses virtually all of the contribution to the measured equivalent width.

In the ideal case of equation 5.32 we have

$$W = \sum_{j=1}^{\infty} A(\lambda_j) \sum_{i=1}^{\infty} g(\lambda_j - \lambda_i)\Delta\lambda \qquad (5.33)$$

and this is identical to choosing a fixed value of the absorption function $A(\lambda_j)$ and multiplying it in turn by the various values of $g(\lambda_j - \lambda_i)$ as the resolution function sweeps across that wavelength λ_i (see Figure 5.5). This is equivalent to multiplying this absorption value by the area beneath a Gaussian function, or by part of that area if the entire resolution function does not sweep across that wavelength, as is the case near the edges of a scan. This has the advantage that the area required is given simply by the error function, $erf(x)$, where

$$erf(x) = \frac{2}{\sqrt{\pi}} \int_0^x e^{-t^2}\, dt \qquad (5.34)$$

Some of the properties of this function are described in Appendix 9. The term $\sum_{i=1}^{n} g(\lambda_j - \lambda_i)$ in the expression for equivalent width can then be replaced by $erf(x)$, where x is a variable depending upon where in the scan range the wavelength λ_j is. If λ_j is equal to λ_A or λ_B, then that value of absorption function $A(\lambda_j)$ will be multiplied by $\frac{1}{2}$, since one-half of the points $g(\lambda_j - \lambda_i)$ will be multiplied by $A(\lambda_j)$ as the function $g(\lambda)$ sweeps past (half the area contributes). Values of $A(\lambda_j)$ well inside the scan range (between D and E in Figure 5.6) will be multiplied by 1.0, since this value of $A(\lambda_j)$ will be multiplied by each and every value of $g(\lambda_j - \lambda_i)$ in turn as $g(\lambda)$ sweeps past (see Figure 5.5). Any point more than $3\alpha_e$ inside the edges of the scan, λ_A, λ_B, will have this multiplication value of 1.0, and any point more than $3\alpha_e$ outside the scan range will have the multiplication value zero, since the amplitude of $g(\lambda)$ outside these

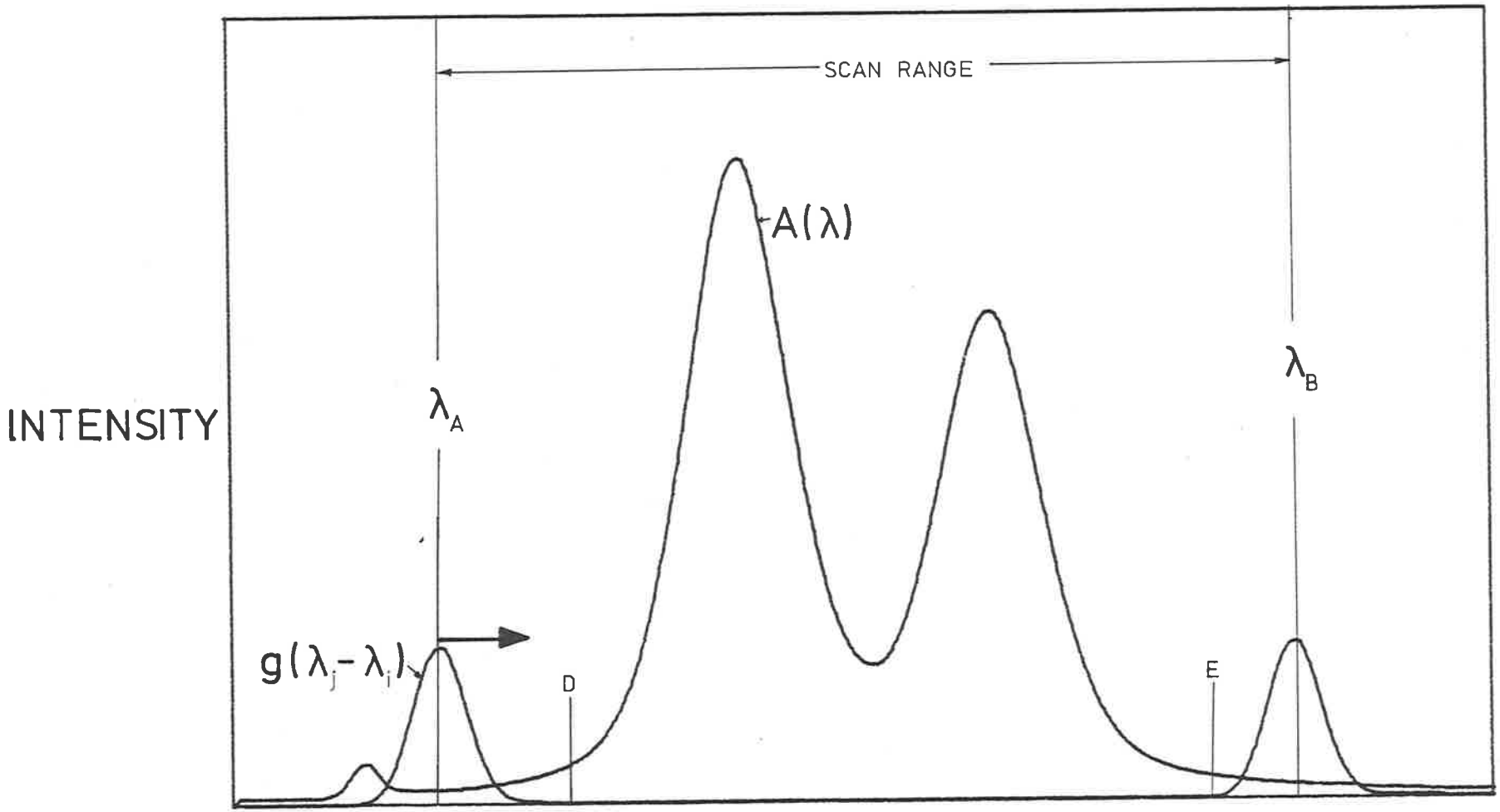

FIG 5.6. $g(\lambda_j - \lambda_i)$, the instrument resolution function sweeps across $A(\lambda)$ from λ_A to λ_B. Any wavelength between D and E will be multiplied by every value of $g(\lambda j - \lambda_i)$, in other words by the full area. Points outside D and E will be multiplied by some function of the area given by the relationship between distance from the scan edge λ_A or λ_B, α_g (where α_g is the half-width of the resolution function) and the error function.

limits is negligible. In this way, a scan function $S(\lambda_i)$ can be built up, showing the effect on spectral intensity across the scan range. The rate of rise and fall of this scan function (shown in Figure 5.7) at the integration limit edges λ_A , λ_B is a characteristic of instrument resolution. If the resolution function was not Gaussian, but instead consisted of a delta function (the infinite resolution case), the scan function would then consist of a rectangular block between λ_A and λ_B , with value 1.0 between those limits and zero outside them. The more precise the resolution, the faster the scan function rises to the value 1.0 from 0 at λ_A , λ_B (see Figure 5.7).

Some approximations are made in this analysis, such as the assumption that $g(\lambda - \lambda_o)$ is negligible when $|\lambda - \lambda_o| > 3\alpha_e$ and that the measured equivalent width

$$W' = \sum_{j=1}^{m} A(\lambda_j) \sum_{i=1}^{n} g(\lambda_j - \lambda_i)\Delta\lambda \text{ is equal to}$$

$$W = \sum_{j=1}^{\infty} A(\lambda_j) \sum_{i=1}^{\infty} g(\lambda_j - \lambda_i)\Delta\lambda$$

or more explicitly

$$C(\lambda_i) = \sum_{j=1}^{m} A(\lambda_j) \cdot g(\lambda_j - \lambda_i)\Delta\lambda \simeq \sum_{j=1}^{\infty} A(\lambda_j \cdot g(\lambda_j - \lambda_i)\Delta\lambda$$

which is true to a good approximation, since the scan range encloses most of the line. The area obtained using this error function approximation, is equal to that obtained using the convolution process, so both will give the same answer for theoretical equivalent width. However, only the convolution process produces a picture of what the real absorption spectrum would look like. The use of the error function approximation cuts the number of multiplications needed to calculate a

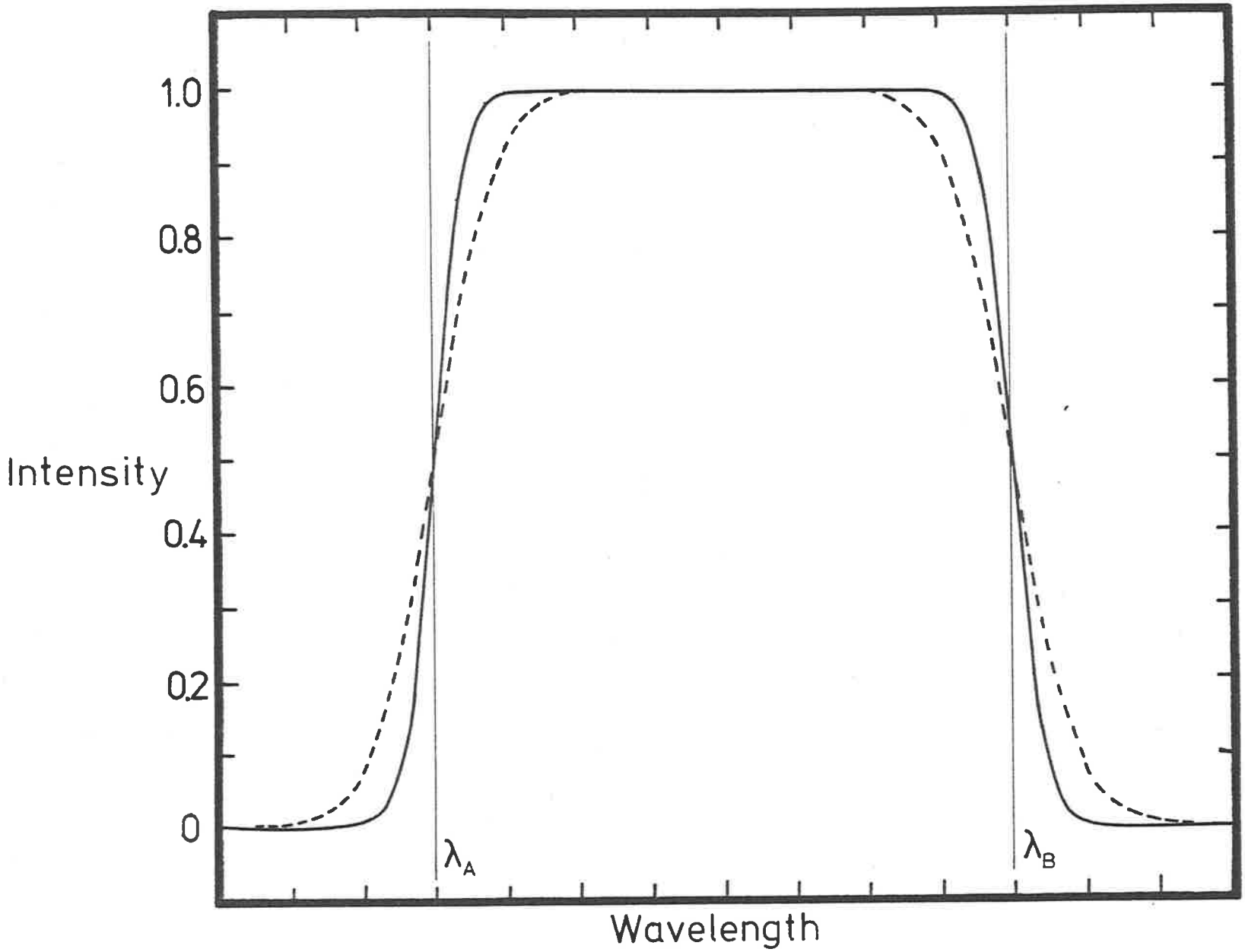

FIG 5.7 Examples of scan functions $S(\lambda)$. The solid line corresponds to a scan function of twice the resolution of the dashed line, and consequently rises and falls faster near λ_A and λ_B.

theoretical equivalent width from 160,000 to 800, and thereby considerably improves computing time, with no real loss of accuracy. This was checked by comparing answers obtained using both methods.

5.6.3 Calculation of Oscillator Strengths and Linewidths

The oscillator strength was extracted from the measured results as follows. After the equivalent widths had been adjusted to take account of the continuum contribution, they were used as input data for a computer programme, which varied the optical depth $k_p X$ for the lower pressure case until the theoretical equivalent width produced by the programme

$$W'_L = \int_{\lambda_A}^{\lambda_B} (1 - \exp [- k_p X \; k(\lambda,\alpha)]) \, d\lambda \qquad (5.35)$$

agreed with the experimental quantity, W_L . The notation $k(\lambda,\alpha)$ is used here because the absorption coefficient, as well as being a function of wavelength, is also a function of α-value, which is allowed to vary in an effort to find a solution. The value of $k_p X$ which produced this agreement, denoted by $k_p X_L$, was then multiplied by the pressure ratio of the two scans, Y, to give $k_p X_u$, where

$$Y = P_u / P_L \qquad (5.36)$$

where P_u is the pressure used for the upper equivalent width measurement, and P_L is the pressure used for the lower equivalent width measurement, $k_p X_L$ was found to be almost independent of α-value , since the equivalent width was deliberately chosen in this region of the curve of growth. The α-value parameter was then varied so that the

value of equivalent width obtained at this new value $k_p X_u$

$$W'_u = \int_{\lambda_A}^{\lambda_B} [\, 1 - \exp (- k_p X_u \, k(\lambda,\alpha)) \,] \, d\lambda \qquad (5.37)$$

agreed with the experimental quantity, W_u . A new value of $k_p X_L$ was then calculated for this new α-value and the cycle repeated until a curve of growth was obtained that passed through both equivalent width values and with $k_p X_u = Y \, k_p X_L$. That is, a curve of growth is fitted to the pair of points $(k_p X_L, W_L)$ and $(Y \, k_p X_L, W_u)$, as discussed previously in Chapter 3 (see Section 3.6 and Figure 3.12).

The two experimentally measured quantities W_L and W_u are thus used to give two quantities of direct theoretical interest, the oscillator strength f and the linewidth, given indirectly by α . These two quantities completely describe the rotational line at a given temperature. The oscillator strength is calculated from the equation (see Thorne (1974). (Sections 9.5 to 9.6)).

$$f = \frac{\varepsilon_o \; mc^2}{\alpha_J \; Ne^2 \; \lambda^2} \int k(\lambda) \, d\lambda \qquad (5.38)$$

where in all cases, $k(\lambda)$ has been normalized so that

$$\int k(\lambda) \, d\lambda = k_p \sqrt{\pi} \; \alpha_e \qquad (5.39)$$

and where

$$\alpha_e = \frac{\lambda_o}{c} \sqrt{\frac{2 \, K_B \, T}{M}} \qquad (5.40)$$

is the 1/e Doppler half-width, $N = P/K_B T$ is the number of molecules per unit volume, λ_o is the wavelength of the line maximum, c is the velocity of light, K_B is Boltzmann's constant, M is the mass of the O_2

molecule, T is the temperature in °K , ε_o is the free space permittivity constant, m is the mass of an electron, e is the electronic charge and α_J is the Boltzmann factor of the state in question, so that $\alpha_J N$ gives the total number of molecules in that state. The above equation reduces to (see Appendix 10)

$$f\ (v',\ v''\ ,\ N''\ ,\ J''\ ) \ = \ \frac{1.577 \times 10^{-3}\ \ k_p X\ T^{3/2}}{P(\mu)\ \lambda_o(A^\circ)\ \ell(cms)\ \alpha_J''}$$

and is the line oscillator strength, and where $P(\mu)$ is the pressure of O_2 in microns, $\lambda^\circ(A^\circ)$ is the wavelength of the line centre in Å , and $\ell(cms)$ is the path length in cms.

A more useful quantity is the band oscillator strength $f\ (v',\ v''\ ,\ N''\ )$, and this is related to the line oscillator strength by

$$f\ (v',\ v''\ ,\ N''\ ) \ = \ f\ \frac{(v',\ v''\ ,\ N''\ ,\ J''\ )\ \ (2J''\ +1)}{\delta_J''} \qquad (5.41)$$

where δ_J'' is the Hönl-London factor of the line. We can therefore write

$$f\ (v',\ v''\ ,\ N''\ ) \ = \ \frac{1.577 \times 10^{-3}\ \ k_p X\ T^{3/2}}{P(\mu)\ \lambda(A^\circ)\ \ell(cms)\ \alpha_J''\ \ \delta_J''} \qquad (5.42)$$

5.7 Errors

The expression for the oscillator strength given by equation 5.42 shows which quantities (and thus their associated errors) will contribute to the error of the oscillator strength. The contribution to the error from the wavelength would be very small, as discussed in Section 5.1.1. This wavelength dependence of the oscillator strength shows itself in the final equation because of the dependence of Doppler

width upon wavelength, there being a small, steady change of Doppler width with wavelength over the range of the Schumann-Runge bands. At constant temperature (near room temperature) the Doppler width varied from 4.4 mÅ near 2000Å to 3.8 mÅ near 1750Å .

As a check on the uncertainties in wavelength of the neighbouring lines which are included during a calculation of $k_p X$, these wavelengths were allowed to vary by 10 - 20 mÅ to observe the effect on values of $k_p X$ and α . The errors associated with these lines would certainly be less than 10 mÅ , and as the effects produced by shifts of this magnitude were very small (fractions of a percent), they can be neglected. The errors in pressure and path length have already been discussed previously (see Sections 5.1.3 and 5.1.4).

The contribution of temperature error to the error in oscillator strength was carefully examined. A rotational line and its associated experimental equivalent widths were chosen at random, and the results analysed at different values of temperature. The final values for the oscillator strength and line broadening parameter α were compared at different values of temperature, and were found to vary by only small amounts (see Figure 5.8 and 5.9). The variation of $k_p X$ for a 1% change in temperature (about $\pm 3^\circ K$) was only $\pm 0.6\%$, while at the same time, the line-broadening parameter α changed by about $\pm 0.5\%$. The effect at liquid air temperature would be more marked, and would begin to become significant for higher rotational states. However, at room temperature, the temperature error would not introduce much error.

The worst possible case error would occur when the temperature of the low pressure result was in error in one direction (too large or too small), while that for the high pressure result was in the opposite direction (too small or too large). Since the oscillator strength

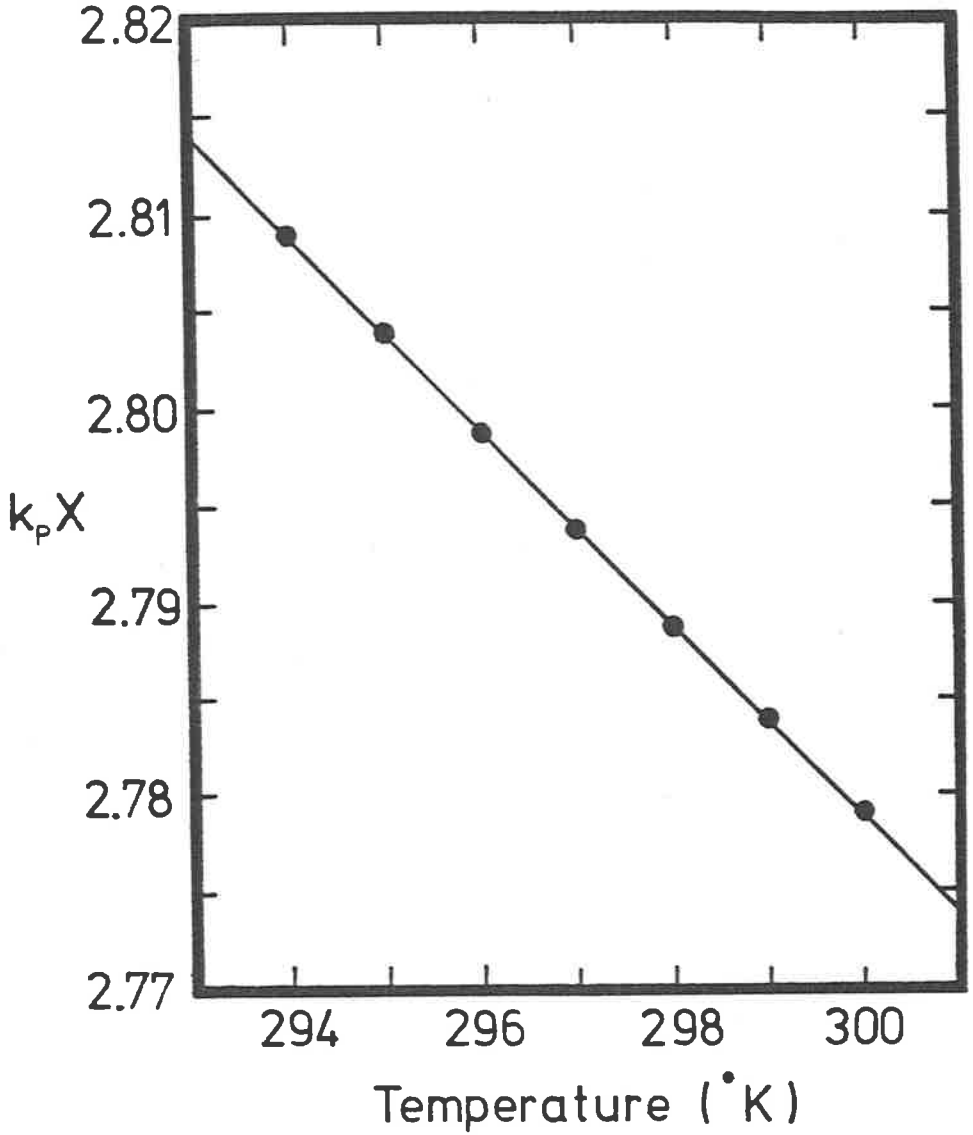

FIG 5.8. The variation in the final value of k_pX with temperature for an equivalent width scan.

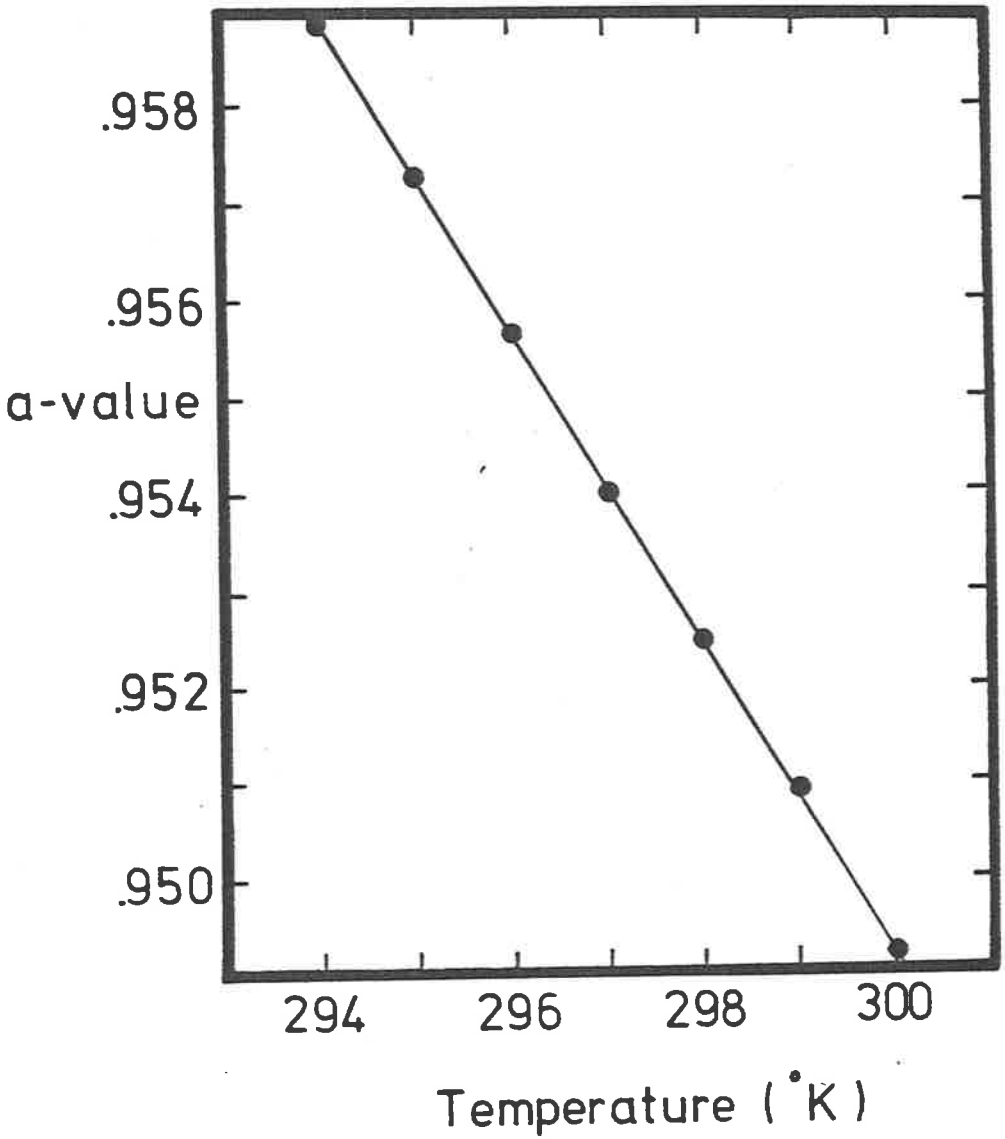

FIG 5.9. The variation in a-value with temperature for an equivalent width scan.

determination is only dependent upon the low pressure equivalent width measurement, this worst possible case error would only affect the a-value . The very slight dependence upon a-value that the oscillator strength determination usually has is negligible. The result is a maximum uncertainty in the oscillator strength of $\pm$ 0.2% due to temperature (accurate to $\pm$ 1°K), but the a-value, dependent as it is upon both measured values of equivalent width, will have a maximum possible error of approximately $\pm$ 0.4% .

The temperature error will also have some effect upon the Boltzmann factor α_J . Although each factor is known to a high degree of accuracy as a function of temperature, the temperature has an uncertainty, and may be in error by $\pm$ 1°K , meaning that a slightly different Boltzmann factor α_J should have been used in the analysis. A 1% change in temperature, will produce different percentage changes in Boltzmann factor, depending upon the rotational number. In almost all cases, J(or N'') was 21 or less, and at this value of 21, a 2.2% error would be introduced by a 1% change in temperature. However, for lines with between 7 and 15 (as was usually the case), a 1% change produces a change of 0.6% or less (see Figure 5.10). The rapid rise in error for the high rotational numbers is due to the fact that these levels are sparsely populated, and even a small temperature change will add a significant amount to the population, and thus produce a relatively large change. The Boltzmann distribution has maxima near J = 9, 11 or 13, and this means a population change for these levels is relatively small, as can be seen from Figure 5.10.

The most significant contribution to the error in oscillator strength is the error in k_pX . The error in k_pX , δk_pX can be written as

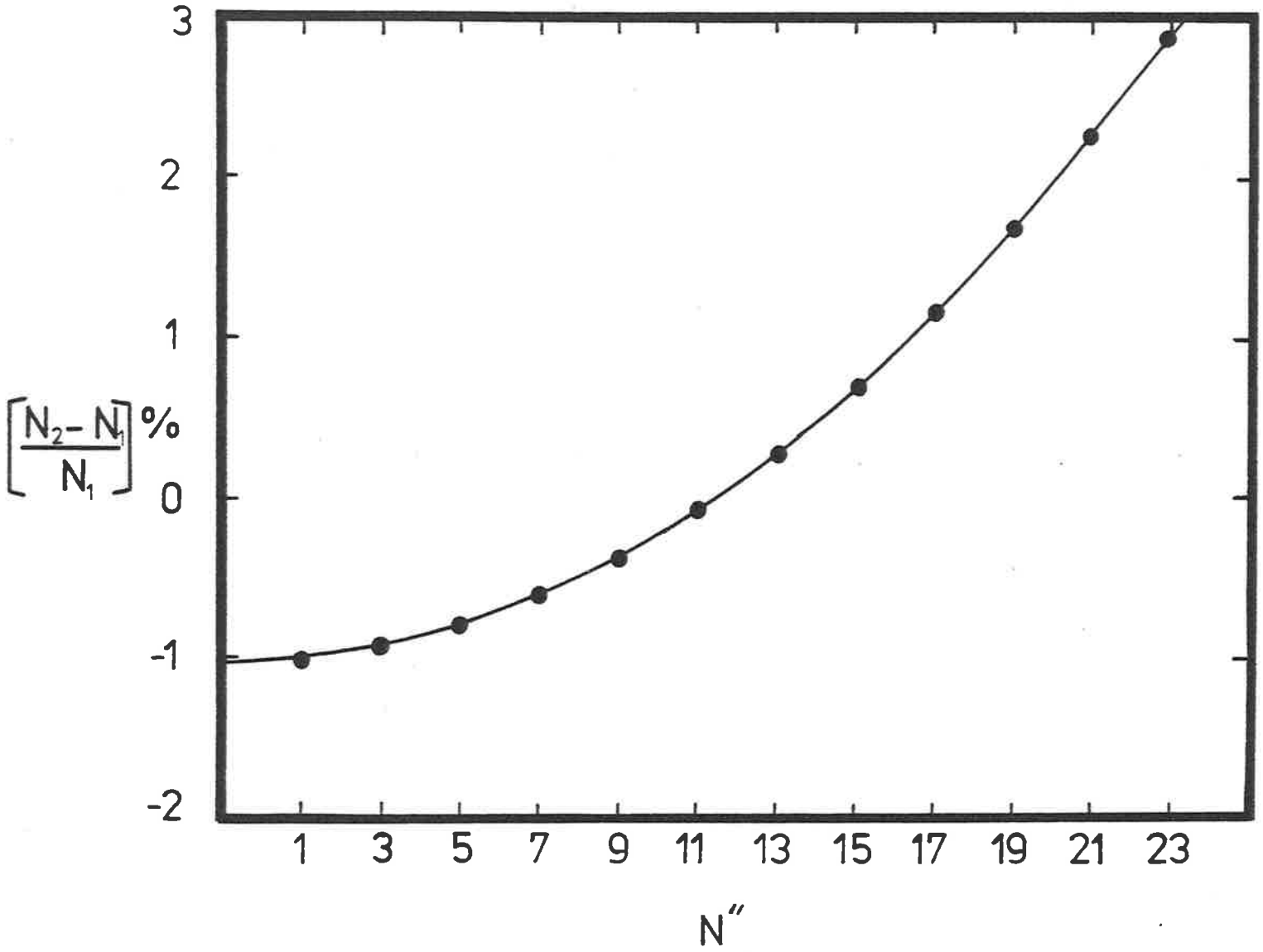

FIG 5.10. The variation in population of a rotational level with rotational number, plotted as percentage change of population in the level versus rotational number N'' .

$$(\delta k_p X)^2 = (\frac{\partial k_p X}{\partial W})^2 \delta W^2 + (\frac{\partial k_p X}{\partial a})^2 \delta a^2 \qquad (5.43)$$

$$\text{or} \qquad (\delta k_p X) = \sqrt{(\frac{\partial k_p X}{\partial W})^2 \delta W^2 + (\frac{\partial k_p X}{\partial a})^2 \delta a^2} \qquad (5.44)$$

where $\frac{\partial k_p X}{\partial W}$ is the rate of change of $k_p X$ with equivalent width W, $\frac{\partial k_p X}{\partial a}$ is the rate of change of $k_p X$ with a-value, δW is the error in W (also written as ΔW), and δa is the error in a. For almost all bands (the exceptions are the 1-0 and 2-0 bands), $\frac{\delta a}{a}$ is a variation of 10% or less, and this coupled with a very small value of $\frac{\partial k_p X}{\partial a}$, since the oscillator strength determination is deliberately done in a region where the a-value dependence of $k_p X$ is small, produces an error which is small compared to that due to equivalent width. It was found that a 10-20% change in a-value produced a change of 1% or less in the value of $k_p X$. Thus, the term

$$(\frac{\partial k_p X}{\partial a})^2 \partial a^2 \quad \text{in equation 5.44}$$

can be neglected, since the term

$$(\frac{\partial k_p X}{\partial W})^2 \delta W^2$$

is of the order of 6-10%, and this outweighs the other term. Equation 5.44 can safely be reduced to

$$k_p X \approx \frac{\partial k_p X}{\partial W} \delta W \simeq \frac{1}{\frac{dW}{dk_p X}} \Delta W \qquad (5.45)$$

where $\frac{dW}{dk_p X}$ is the slope of the tangent to the curve of growth at $k_p X$.

Thus, the error in $k_p X$ is basically due to the error ΔW_L in W_L, the lower value of equivalent width. A value of $\delta k_p X$ is

obtained using the results of iterations towards the solution for k_pX to extract the value of the slope to the curve of growth. In Figure 5.11, the curve of growth near the low pressure equivalent width is plotted (that is, near the linear region of the curve of growth). The measured equivalent width is $W_L \pm \Delta W_L$, and the corresponding value of k_pX_L is obtained from the computer simulation. The error δk_pX (or Δk_pX), is related to ΔW and the slope of the tangent to the curve of growth $\frac{dW}{dk_pX}$ by

$$\frac{dW}{dk_pX} \simeq \frac{\Delta W}{\Delta k_pX} \qquad (5.46)$$

Use of the iteration points (k_pX, W), in particular, a point falling near the value $W_L - \Delta W_L$ (in this case, W_1 of Figure 5.12) allows an estimate of the slope to be calculated. This slope $\frac{W_L - W_1}{k_pX_L - k_pX_1}$ can be used as $\frac{dW}{dk_pX}$ and can thus give value for Δk_pX. Because of the curvature of the curve of growth, the error Δk_pX is slightly asymmetric, there tending to be a slightly larger Δk_pX on the upper side of k_pX. However, the difference was usually negligible when compared to the size of Δk_pX for most of the lines analysed, so it was neglected.

Since $\frac{\Delta W_L}{W_L}$ was of the order of 5%, and since $\frac{dW}{dk_pX}$ had values between 1 and 2, the error $\frac{\Delta k_pX_L}{k_pX_L}$ was between 5-10%, and was thus the major contribution to error in the oscillator strength.

One error quantity which is not apparent from equation 5.42, but which may play a significant role is that of instrumental resolution. For all the lines analysed, an instrumental half-width of either 50 or 60 mÅ was used. The uncertainties in this quantity would be no greater than

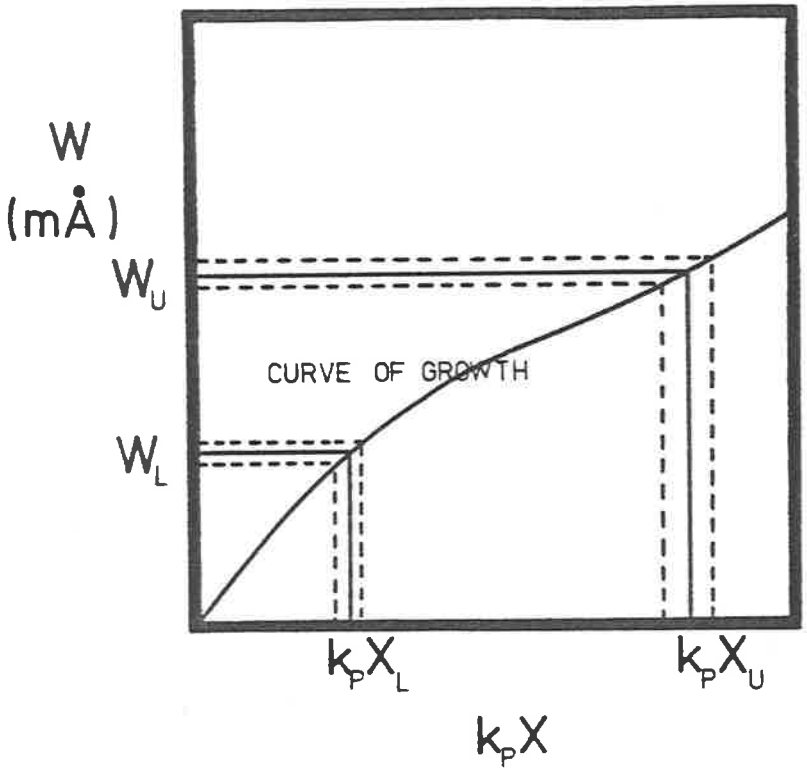

FIG 5.11. The two measured equivalent widths W_L and W_u are shown, with their associated errors, and their corresponding values of k_pX. A curve of growth passing through both required points is found.

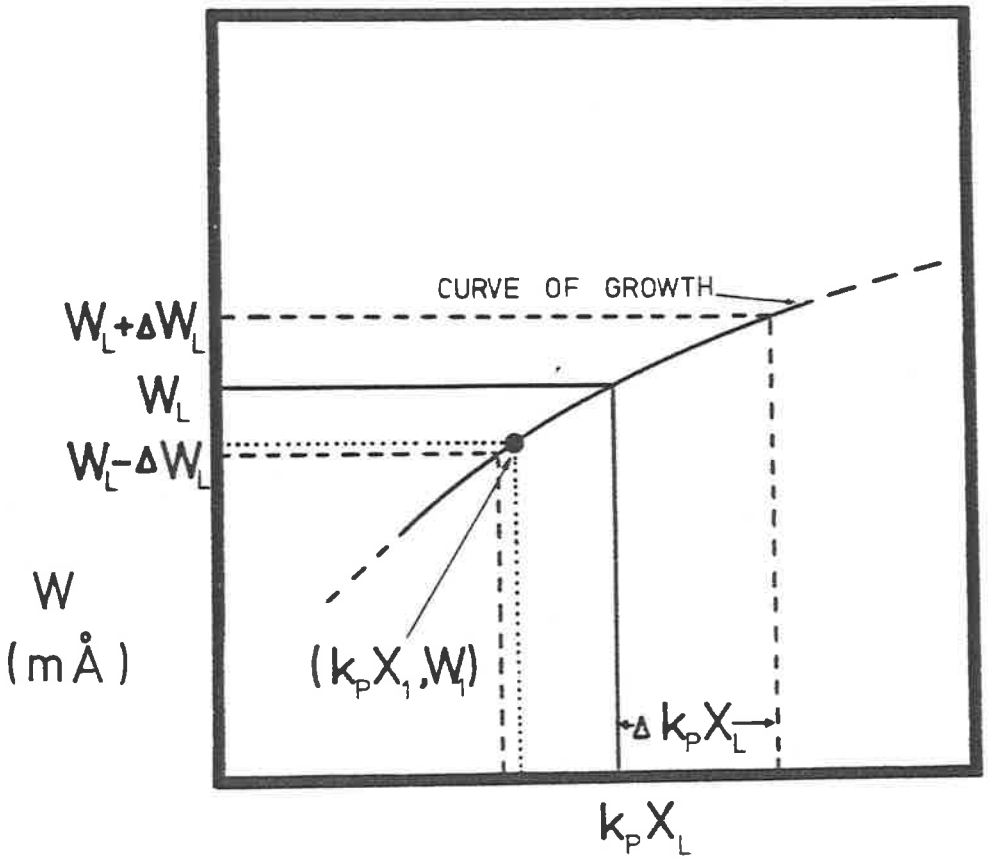

FIG 5.12. The low pressure equivalent width W_L and its corresponding value of optical depth, and the errors in both are shown. The slope of the tangent to the curve of growth at k_pX_L is calculated from the iteration point (k_pX_1, W_1). The error Δk_pX_L is slightly asymmetric.

10 mÅ , and Figure 5.13 shows the variation in k_pX with resolution. A large change in resolution (25%) produces only a 0.18% change in the value of k_pX . Similarly for the line-broadening parameter a , shown in Figure 5.14. Here a 25% change in resolution, produces only an 0.07% change in a .

The error in a-value requires a little more calculation. Figure 5.15 shows a series of curves of growth with different a-values passing through the allowed range of equivalent widths. The two basic errors important in the a-value determination are ΔW_u and Δk_pX_u . Δk_pX_u is directly proportional to Δk_pX_L , being related by the ratio of the two pressures at which the two equivalent widths W_L and W_u were measured. We have therefore that $\Delta k_pX_u = Y\Delta k_pX_L$ (from equation 5.23).

The line-broadening parameter is dependent upon only two quantities, the equivalent width and the index of absorption, k_pX . Holding the equivalent width constant, and varying k_pX (by an amount Δk_pX_u say) will allow a variation in a-value . Similarly, holding k_pX_u constant, and varying the allowed equivalent width, also allows a variation in a . The total variation in a due to both quantities varying simultaneously can be written

$$\left(\delta(a)\right)^2 = \left(\frac{\partial a}{\partial W}\right)^2_{k_pX} \delta W^2 + \left(\frac{\partial a}{\partial k_pX}\right)^2_{W} \delta(k_pX)^2 \qquad (5.47)$$

where $\left(\frac{\partial(a)}{\partial W_{k_pX}}\right)$ is the variation in a-value with equivalent width for a fixed value of k_pX , and $\left(\frac{\partial a}{\partial k_pX_w}\right)$ is the variation of a -value with k_pX for a fixed equivalent width. Equation 5.47 can be approximated by

$$\left(\delta(a)\right)^2 = \left(\frac{\Delta a}{\Delta W}\right)^2 \Delta W_u^2 + \left(\frac{\Delta a}{\Delta k_pX}\right)^2 \left(\Delta k_pX_u\right)^2$$

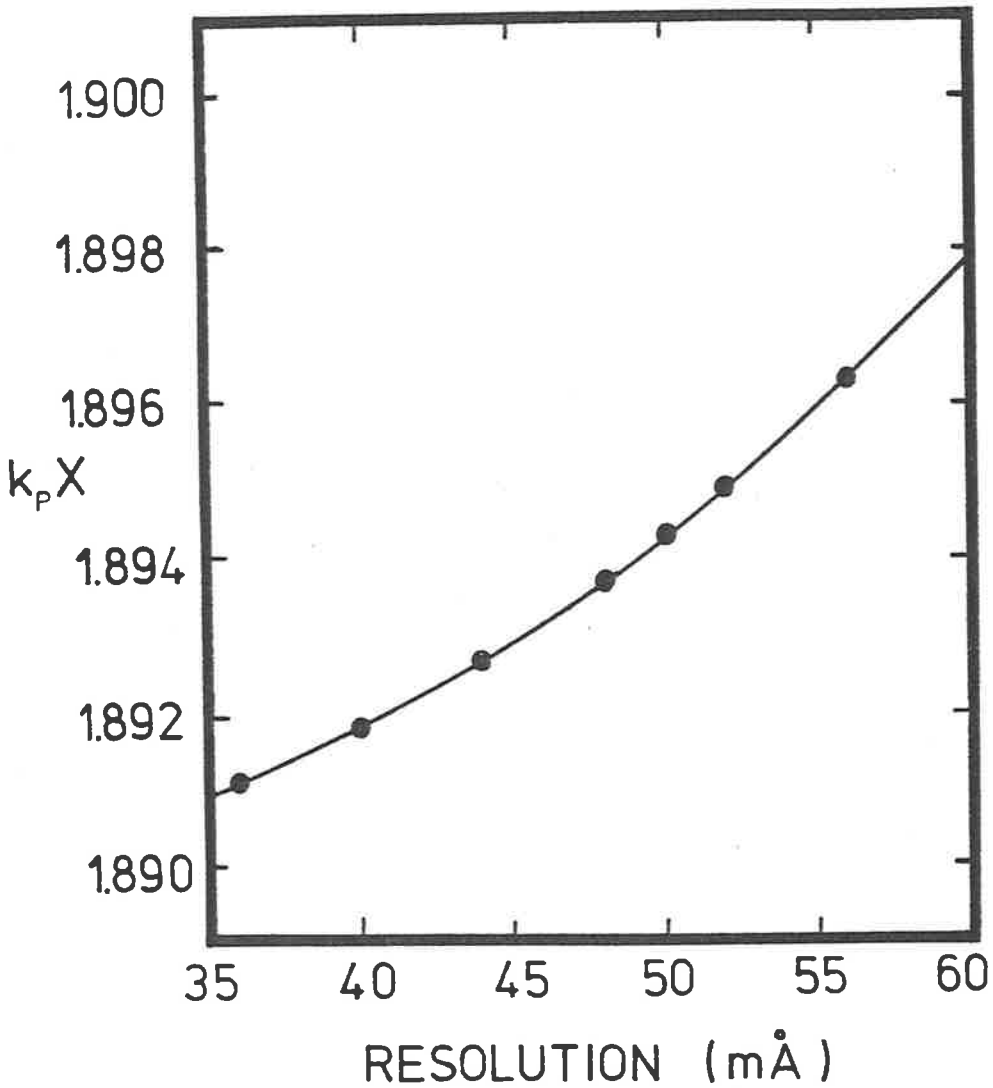

FIG 5.13. The variation of optical depth k_pX with instrumental resolution α_g. A large charge in α_g produces a small change in k_pX and thus oscillator strength.

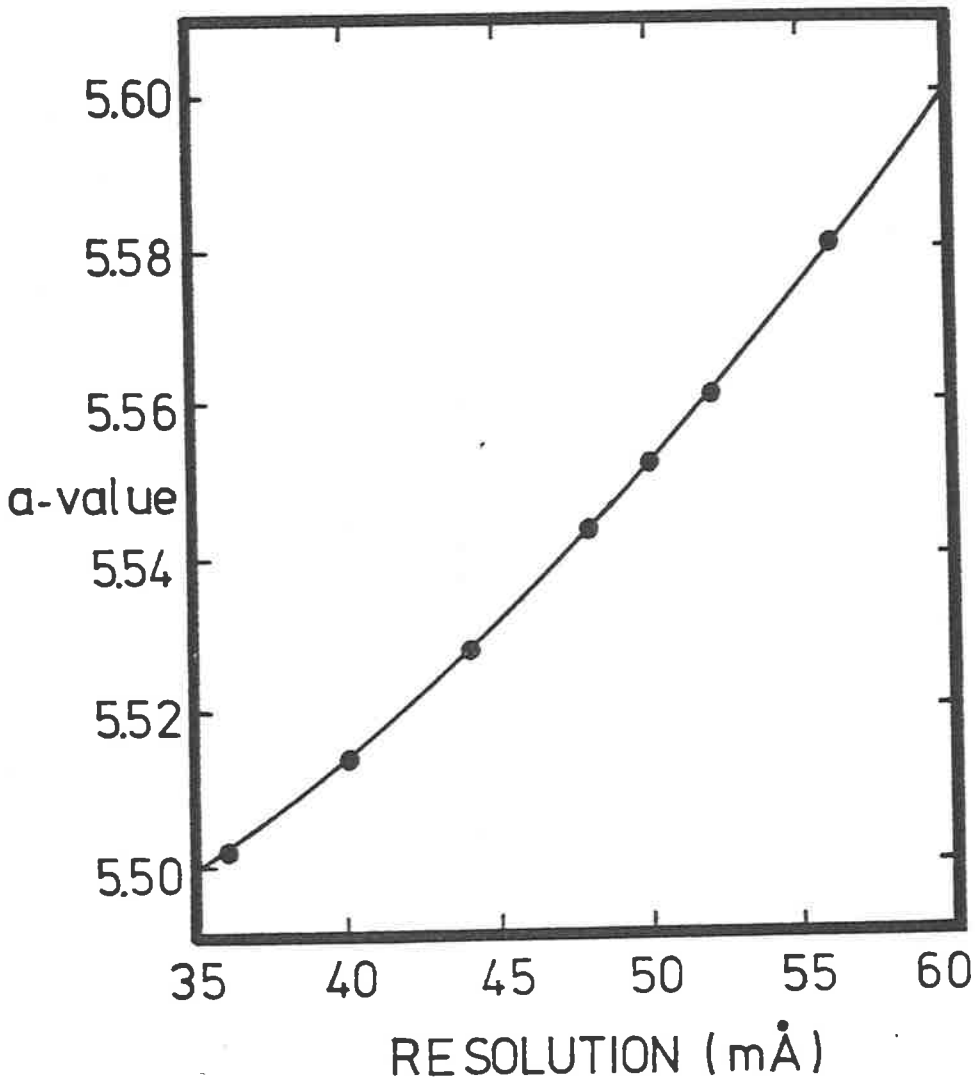

FIG 5.14. The variation in α-value with instrumental resolution α_g produces a small change in α-value.

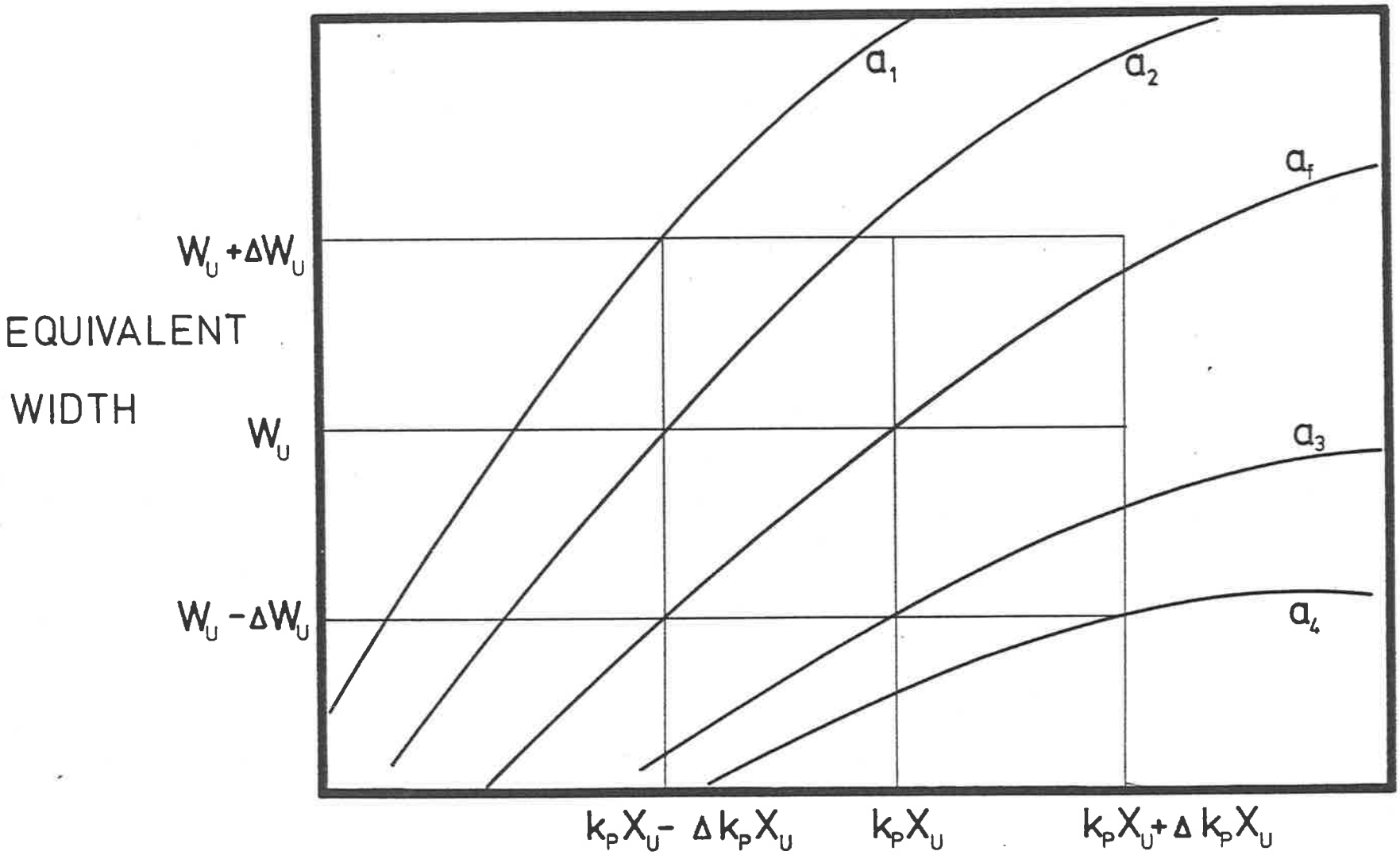

FIG 5.15. The range of possible values of a which fit the upper equivalent width W_u and its associated error, and corresponding $k_p X_u$ value. The value a_f is the first solution given by the computer iterations.

where $\delta(a)$ is the error in a, Δa and ΔW are obtained from the computer printout of iterations towards a final solution, as are Δa and $\Delta k_p X$. Values of δa were calculated for each line analysed, since $\frac{\partial a}{\partial W}$ and $\frac{\partial a}{\partial k_p X}$ will vary from line to line depending upon pressure, number of background lines and scan range.

A further complication to the uncertainty in a-value determination was caused by a combination of factors which became important in the 1-0 and 2-0 bands. Firstly, the rotational lines become weaker as rotational number increases, requiring a gradual increase in pressure at which the lower value of equivalent width W_L was measured. Near the band head, this pressure was 161 torr (for the 2-0 band), and it increased to 500 torr for the $R_{21}P_{19}$ (2-0) line group. Since the maximum pressure attainable in the cell was 850 torr, this meant a gradual decrease in the pressure ratio along the band, declining from $Y = 5.28$ near the band head to $Y = 1.70$ for the higher lines. The pressure ratio was almost always 10.0 for the other bands, although this may not have been quite the optimum value in many cases. As shown in Figure 5.16, two equivalent width measurements with the same error bars, but separated by different ratios Y, will produce widely differing errors in a-value. These errors are usually taken into account by the terms

$$\left(\frac{\partial a}{\partial W}\right)^2_{k_p X} \quad \text{and} \quad \left(\frac{\partial a}{\partial k_p X}\right)^2_{W} \quad \text{in equation 5.47,}$$

and in case 1 of Figure 5.16, the error δa will be extremely large, while case 2 will have a much smaller error δa.

A simultaneous effect, which coupled with the above pressure ratio behaviour, makes the determination of a-values for higher

rotational lines in the 1-0 and 2-0 bands unreliable is that due to the underlying continuum. As mentioned above, the rotational line strength decreases with increasing rotational number (for N'' >9), the higher numbered lines producing progressively smaller amounts of absorption, at the maximum pressure of 850 torr. The amount of absorption produced by the lines under examination becomes comparable to that produced by the continuum for high rotational number (N'' >13). It thus becomes very important to set the amount of absorption due to the continuum accurately, so that the amount actually due to the absorption lines can be determined.

The valuesof the absorption coefficient of the underlying continuum, in this case the Herzberg continuum, have not been measured accurately in this wavelength region inside the bands. Experimental measurements of the Herzberg continuum extend down to 2000Å , the beginning of the Schumann-Runge bands. To overcome this problem a theoretical extrapolation of these experimental results was used, extending down to 1750Å . These continuum cross-sections, and those of the Schumann-Runge continuum (as shown in Figure 5.17) were used to calculate background contributions for all lines in each band, and were found to work satisfactorily. This was because, with the exception of the 1-0, 2-0 and 3-0 bands, all the results were taken at relatively low pressures. However, for the 1-0 and 2-0 bands, taken at higher pressures, the Herzberg continuum values failed to give solutions when applied to line analyses.

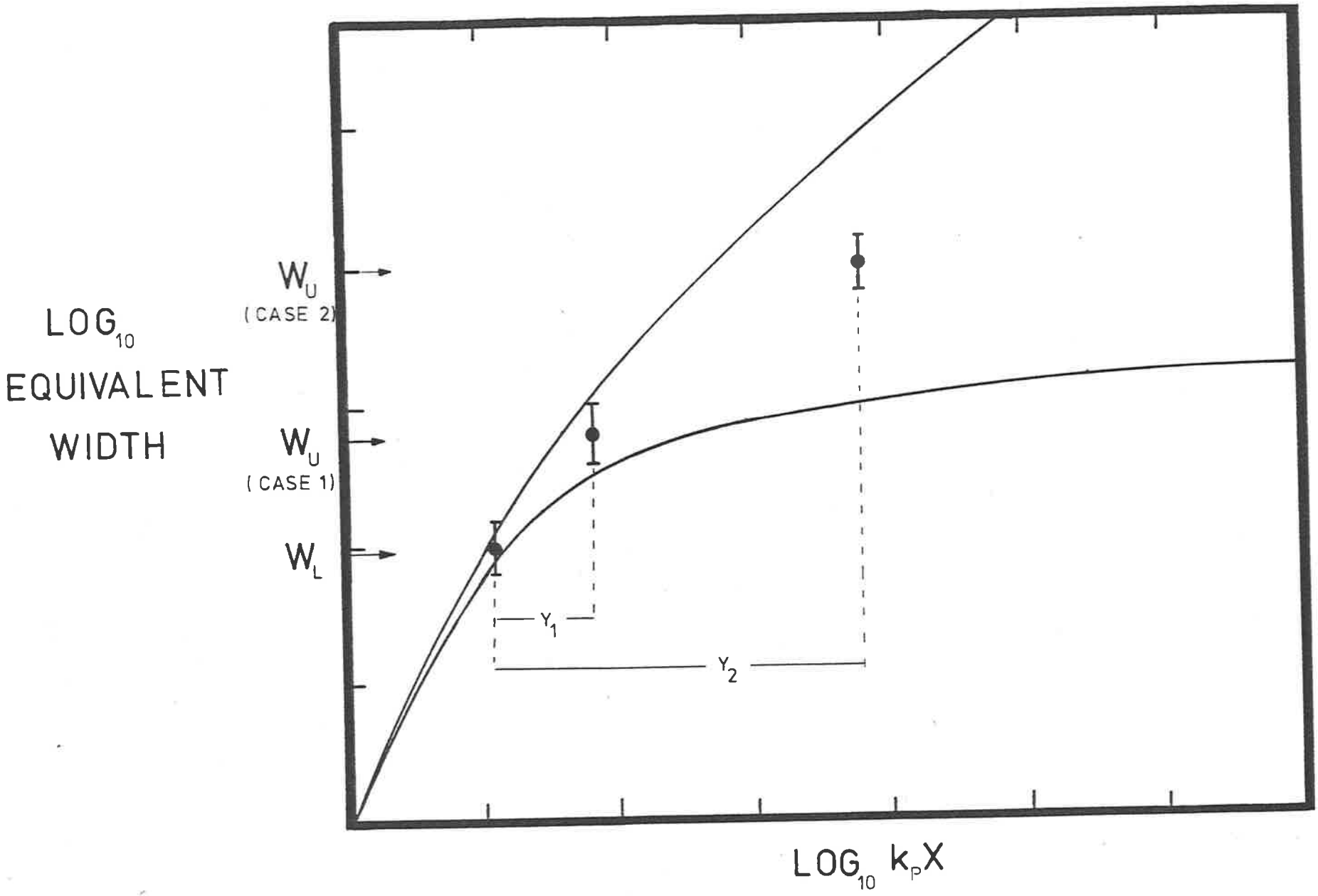

FIG 5.16 A comparison of the effects of pressure ratio, Y, on the α-value error range. Case 2 is the case normally applying to most experimental results, and has only a limited number of curves of growth which can pass through W_u and its associated error bar. Case 1, with an equivalent width with error equal to Case 2, has a much larger range of possible α-values which can pass through W_u. In fact almost all α-values are a possible solution.

5.8 The Pressure Dependent Absorption Continuum

The failure of the Herzberg continuum values to provide solutions in the 1-0 and 2-0 bands was due to the fact, that these bands had their high pressure equivalent width values, W_u, measured at pressures of 1 atmosphere or greater. The absorption cross-section in the Herzberg continuum has been observed to be pressure dependent, and at pressures of 850 torr, this can have the effect of more than doubling the effective continuum cross-section (in comparison to pressures near zero). This dependence has been measured by Shardanand and Prasad Rao (1977) for the wavelength range 2000-2500Å. They interpret the increase in absorption coefficient as due to the formation of O_4 at high pressure, and list their values of the continuum absorption of O_4 at 50Å intervals, and these results closely parallel the results of the O_2 continuum cross-section in the same wavelength region (see Figure 5.17).

The ratio of σ_{O4}/σ_{O2} does not vary much in the wavelength range 2000-2500Å, and use is made of this fact to extrapolate the O_4 continuum cross-section to lower wavelengths. The continuum absorption values of Jarmain & Nicholls (1967) for the Herzberg continuum have been renormalized to bring them into agreement with the more recent measurements of Shardanand and Prasad Rao (1977), and the shape of the curve of their values in the range 1750-2000Å was used to extrapolate a similar curve for O_4 continuum cross-sections by using the relation $\sigma_{O4}/\sigma_{O2} \approx$ constant. The results are plotted in Figure 5.17. The extrapolated results for O_4 continuum cross-section can then be combined with the O_2 continuum cross-section to give a total effective cross-section using the equation of Shardanand and Prasad Rao

$$\sigma_T(\lambda) = \sigma_{O2}(\lambda) + kn\sigma_{O4}(\lambda) \qquad (5.48)$$

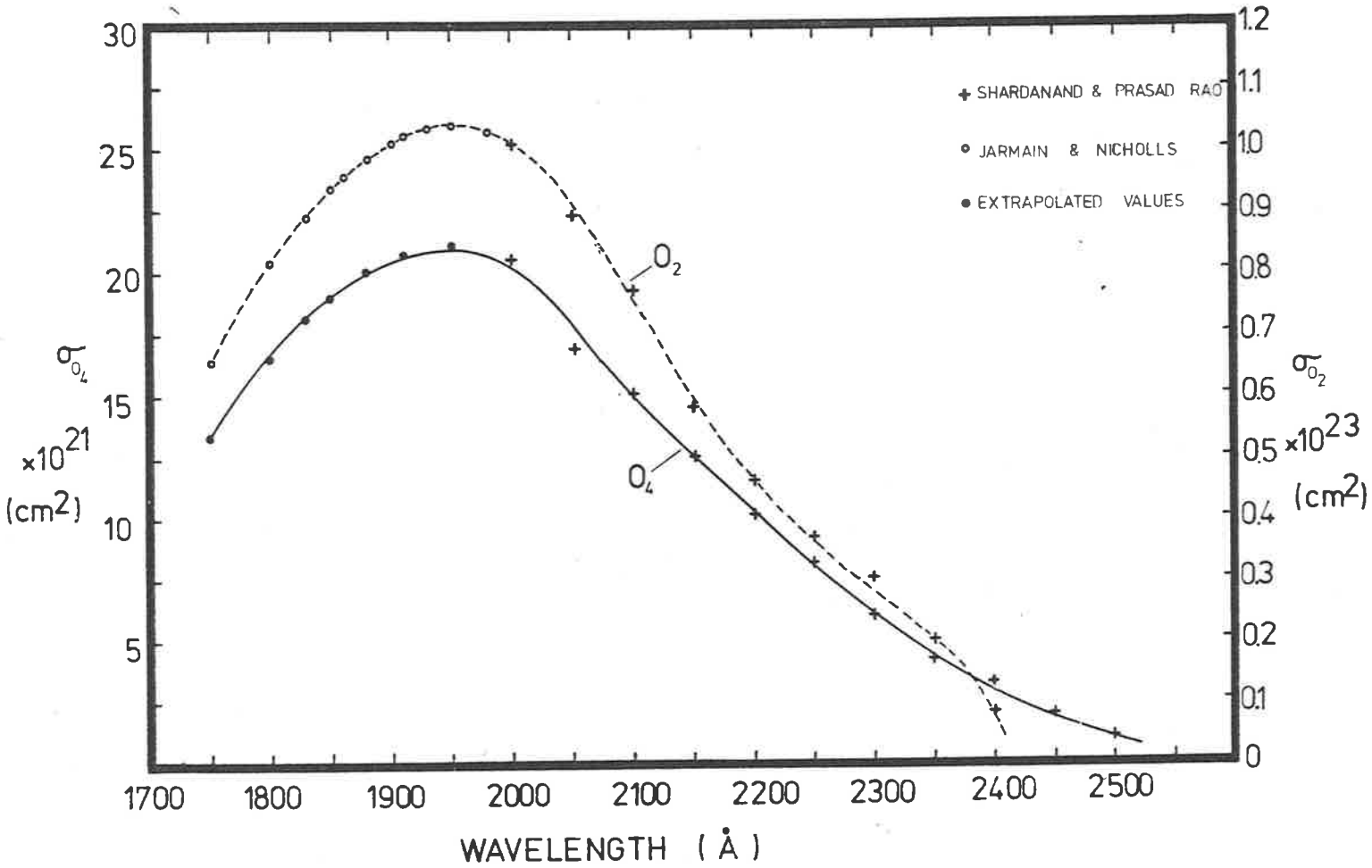

FIG 5.17 The absorption measurements of Shardanand and Prasad Rao (1977) extrapolated to lower wavelengths. The values of Jarmain and Nicholls (1967) have been scaled to fit those of Shardanand and Prasad Rao at 2000Å.

where $\sigma_{O2}(\lambda)$ and $\sigma_{O4}(\lambda)$ are the continuum cross-section of O_2 and O_4 at wavelength λ respectively, and n is the number density of O_2. The constant k was found by Shardanand and Prasad Rao to be 2.6×10^{-23} cm^3/molecule, and this value was adopted for this work.

Irrespective of whether Shardanand and Prasad Rao are correct in their assumption of the formation of an O_4 dimer , their experimental results can be assumed to be correct, and thus

$$\sigma_T(\lambda) = \sigma_{O2}(\lambda) + n A \qquad (5.49)$$

is a correct description of the total effective cross-section. Here $A = k\sigma_{O4}(\lambda)$ is a directly measured quantity, and neither k nor $\sigma_{O4}(\lambda)$ need to be known separately, to use the results.

This new value of total effective continuum cross-section was then used to calculate a background contribution. In the case of the 1-0 and 2-0 bands this had the effect of reducing the amount of high pressure equivalent width attributed to the absorption lines. The a-value iteration was then able to find a solution, which had previously eluded it, due to the W_u values being too large, and falling outside the range of allowed values.

The 3-0 results were also re-analysed using the new O_4 corrected, continuum background contribution, and there was some effect, the new values of oscillator strength and line-broadening differing slightly from the previous values derived using only the O_2 Herzberg continuum background correction. Compared with the 2-0 and 1-0 bands, the effect in the 3-0 is smaller, and it becomes negligible in the 4-0 and 5-0 bands. This is because, in moving from the 2-0 band through to the 5-0 , the lines become stronger when compared to the continuum, and thus less dependent upon the continuum corrections, and because the pressures

at which the measurements are made become lower, and thus the pressure dependent contribution decreases, and also because the actual value of the O_4 continuum cross-section begins to fall off with wavelength, again resulting in a less significant contribution.

The effect of O_4 continuum is to change equivalent width values, and since the errors in the O_4 continuum cross-section values will be substantial, due to the approximations made (that σ_{O4}/σ_{O2} is constant in the wavelength range 1750-2000Å , and σ_{O2} are only extrapolated theoretical values), this will introduce substantial uncertainties to the values W_L and W_u (more importantly W_u). In addition to the statistical uncertainties, there will be uncertainties of 10-20% in the value of W_u, and the effects of these uncertainties will be greater, the smaller the pressure factor (that is, the closer to case 1 in Figure 5.16 the situation becomes). The net effect is to make α-value determinations of high numbered rotational lines unreliable in the 1-0 and 2-0 bands.

5.9 Rotational Dependence of Oscillator Strength - Calculation of Slopes and Intercepts.

The least squares fit formula for a straight line of the form

$$f = f_0 + \beta x$$

to describe the form of the rotational variation of the oscillator strength f, where x is related to the rotational number (c.f. equation 6.1), can be derived as follows. The points (x_i, f_i) are to be fitted to the line of slope β and intercept f_0, and the errors in f_0, δf_0, and β, $\delta \beta$ are required from the errors in x_i and f_i. The error in f_i, δf_i, is simply the statistical error in the oscillator strength f, and the error in x_i, δx_i is assumed to be zero, since the number of a rotational line is a known integer.

The sum square deviation of the f_i from the straight line $f = f_0 + \beta x$ is

$$Q = \sum_{i=1}^{n} [f_i - (\beta x_i + f_0)]^2$$

$$= \sum_{i=1}^{n} [(f_i - f_0) - \beta x_i]^2$$

Solving $\frac{dQ}{d\beta} = 0$ and $\frac{dQ}{df_0} = 0$ gives

$$\beta(\Sigma x_i^2) + f_0(\Sigma x_i) = \Sigma x_i y_i$$

and $$\beta(\Sigma x_i) + f_0(n) = \Sigma y_i$$

Solving for β and f_0 gives

$$\beta = n\left[\frac{\Sigma x_i y_i - \Sigma x_i \Sigma y_i}{n \Sigma x_i^2 - (\Sigma x_i)^2}\right] \qquad (5.50)$$

and

$$f_0 = \left[\frac{\Sigma x_i^2 \, \Sigma y_i - \Sigma x_i \, \Sigma x_i y_i}{n \, \Sigma x_i^2 - (\Sigma x_i)^2} \right] \tag{5.51}$$

Since $\delta x_i = 0$, then the errors in β and f_0 are dependent only upon δf_i and are

$$(\delta\beta)^2 = \Sigma \left(\frac{\delta\beta}{\delta f_i} \right)^2 (\delta f_i)^2$$

$$(\delta f_0)^2 = \Sigma \left(\frac{\delta f_0}{\delta f_i} \right)^2 (\delta f_i)^2$$

$\frac{\delta\beta}{\delta f_i}$ and $\frac{\delta f_0}{\delta f_i}$ can be obtained from equations 5.50 and 5.51

and so

$$(\delta\beta)^2 = \sum_{i=1}^{n} \left[\frac{n x_i - \Sigma x_j}{n\Sigma x_j^2 - (\Sigma x_j)^2} \right]^2 (\delta f_i)^2 \tag{5.52}$$

$$(\delta f_0)^2 = \sum_{i=1}^{n} \left[\frac{\Sigma x_j - x_i \, \Sigma x_j}{n\Sigma x_j^2 - (\Sigma x_j)^2} \right]^2 (\delta f_i)^2 \tag{5.53}$$

CHAPTER 6

RESULTS — SCHUMANN-RUNGE BANDS

6.1 Introduction

The results presented in this chapter are split into two main parts, the first covering oscillator strengths, the second covering line width measurements. Oscillator strengths for the same vibrational band were often calculated at slightly different values of α , the line broadening parameter. This occurred because the experimental results used in the computations almost invariably produced a slight difference in the value of α_f for each line, and the oscillator strength quoted is for this value of α_f . The α-value was allowed to vary in this manner because it was hoped to present results for the variation of linewidth with rotational number, and the quantity α_f is required if this is to be done. However, the error associated with each measurement of linewidth was usually larger than any differences noticed between the various rotational lines, so no real width dependence on rotational number could be determined. The individual linewidths and α-values for each rotational line, and their accompanying oscillator strength are listed in Appendix 11.

N.B. For Figures in this thesis, a point corresponding to, for example, 1.0 on a vertical axis labelled $f \times 10^5$ is actually a value $f = 1.0 \times 10^{-5}$. The term $\times 10^5$ means values in the Figure are multiplied by 10^5 and then plotted. Some of the Figures reproduced from other works use the alternative notation $\times 10^5$ to mean that all points plotted in the Figure are of the order of magnitude 10^5 .

6.2 Previous Experimental Results

The first oscillator strength measurements for the Schumann-Runge bands of molecular oxygen were obtained by Ditchburn and Heddle (1954) for the (0-0) to (20-0) bands using photographic techniques. They used an indirect analysis technique, combining line broadening, spectrograph parameters and observed line intensities. However, their results were shown to be in error by Bethke (1959), and subsequently by other investigators. Bethke overcame the problem of low instrumental resolution by pressure broadening the absorption lines with argon. Allowance for O_4 continuum was made by subtracting the pressure dependent continuum from the integrated area. From Table 6.1, it can be seen that Bethke's results (2-0) to (17-0) compare reasonably with other more recent investigators.

Oscillator strengths were also obtained by Halmann (1966) for the (2-0) to (10-0) bands, again using a pressure broadening technique with argon to overcome the instrument resolution problem. Farmer et al (1968) used curve of growth techniques similar to the present work to obtain oscillator strengths for the (2-0) to (20-0) bands. Absorption measurements were made at low values of absorption (in the linear region of the curve of growth), so that the integrated areas were directly proportional to the oscillator strengths.

Hasson et al (1970) obtained oscillator strengths for the (0-0) to (3-0) bands, as well as the (2-1) to (5-1) bands, by measuring absorption in air. Ackerman et al (1970) present a comprehensive list of oscillator strengths for (0-0) to the (19-0) bands obtained

BAND	DITCHBURN & HEDDLE	BETHKE	FARMER *et al*	HASSON *et al*	HALMAN	HUDSON & MAHLE	ACKERMAN *et al*	HUEBNER *et al*	THIS WORK
0-0	1.55×10^{-8}			3.3×10^{-10}		2.62×10^{-10}	3.44×10^{-10}		
1-0	1.89×10^{-7}			3.5×10^{-9}		3.05×10^{-9}	3.897×10^{-9}	2.7×10^{-8}	$(8.75 \pm 0.73) \times 10^{-9}$
2-0	1.18×10^{-6}	2.3×10^{-8}	2.69×10^{-8}	1.99×10^{-8}	2.6×10^{-8}	2.7×10^{-8}	2.37×10^{-8}	6.2×10^{-8}	$(2.45 \pm 0.09 \times 10^{-8}$
3-0	8.35×10^{-6}	7.4×10^{-8}	1.54×10^{-7}	6.8×10^{-8}	8.2×10^{-8}	7.1×10^{-8}	9.88×10^{-8}	5.6×10^{-8}	$(1.01 \pm 0.037) \times 10^{-7}$
4-0	2.76×10^{-5}	2.74×10^{-7}	7.11×10^{-7}		2.4×10^{-7}	2.5×10^{-7}	3.21×10^{-7}	2.97×10^{-7}	$(2.70 \pm 0.12) \times 10^{-7}$
5-0	6.65×10^{-5}	7.28×10^{-7}	2.80×10^{-6}		7.48×10^{-7}	6.1×10^{-7}	8.51×10^{-7}	7.39×10^{-7}	$(7.72 \pm 0.19) \times 10^{-7}$
6-0	1.37×10^{-4}	1.73×10^{-6}	4.40×10^{-6}		1.77×10^{-6}	1.7×10^{-6}	1.91×10^{-6}	1.70×10^{-6}	$(1.75 \pm 0.07) \times 10^{-6}$
7-0	3.53×10^{-4}	3.56×10^{-6}	8.15×10^{-6}		4.24×10^{-6}	3.5×10^{-6}	3.81×10^{-6}	3.50×10^{-6}	$(3.85 \pm 0.16) \times 10^{-6}$
8-0	5.94×10^{-4}	6.75×10^{-6}	1.22×10^{-5}		6.59×10^{-6}	6.0×10^{-6}	6.68×10^{-6}	6.85×10^{-6}	$(7.53 \pm 0.31) \times 10^{-6}$
9-0	6.40×10^{-4}	1.07×10^{-5}	1.50×10^{-5}		1.13×10^{-5}	1.0×10^{-5}	1.06×10^{-5}	1.05×10^{-5}	$(1.32 \pm 0.07) \times 10^{-5}$
10-0	9.45×10^{-4}	1.56×10^{-5}	2.05×10^{-5}		1.42×10^{-5}	1.6×10^{-5}	1.57×10^{-5}	1.60×10^{-5}	$(1.84 \pm 0.05) \times 10^{-5}$
11-0	1.44×10^{-3}	2.16×10^{-5}	2.74×10^{-5}			1.7×10^{-5}	2.09×10^{-5}	2.26×10^{-5}	$(2.60 \pm 0.16) \times 10^{-5}$
12-0	1.31×10^{-3}	2.81×10^{-5}	3.58×10^{-5}			2.5×10^{-5}	2.53×10^{-5}	2.88×10^{-5}	$(3.21 \pm 0.10) \times 10^{-5}$
13-0	4.04×10^{-4}	3.17×10^{-5}	3.66×10^{-5}			4.5×10^{-5}	2.88×10^{-5}	3.41×10^{-5}	$(3.65 \pm 0.15) \times 10^{-5}$
14-0	8.12×10^{-4}	3.24×10^{-5}	3.69×10^{-5}			5.0×10^{-5}	3.03×10^{-5}	3.77×10^{-5}	$(4.46 \pm 0.10) \times 10^{-5}$
15-0	2.79×10^{-3}	3.26×10^{-5}	3.77×10^{-5}			3.1×10^{-5}	2.91×10^{-5}	3.73×10^{-5}	$(3.45 \pm 0.10) \times 10^{-5}$
16-0	5.55×10^{-3}	3.16×10^{-5}	3.31×10^{-5}			2.5×10^{-5}	2.59×10^{-5}	3.53×10^{-5}	$(3.4 \pm 0.15) \times 10^{-5}$
17-0	6.63×10^{-3}	2.95×10^{-5}	3.16×10^{-5}			2.94×10^{-5}	2.23×10^{-5}	3.03×10^{-5}	$(2.58 \pm 0.13) \times 10^{-5}$
18-0	6.93×10^{-3}		2.03×10^{-5}			2.57×10^{-5}	1.83×10^{-5}	2.72×10^{-5}	$(1.69 \pm 0.19) \times 10^{-5}$
19-0	7.58×10^{-3}		1.74×10^{-5}			1.96×10^{-5}	1.43×10^{-5}	1.98×10^{-5}	
20-0	8.25×10^{-3}		1.35×10^{-5}					1.64×10^{-5}	

TABLE 6.1 A comparison of the results of this work with those of previous experimenters.

photographically. Hudson and Mahle (1975) used a fitting procedure on their photometrically obtained results, to deduce oscillator strengths for the (0-0) to the (19-0) bands. Their results were used as a first estimate in the present work. All the results mentioned above are compared with those obtained by electron impact studies of Huebner et al (1975) and the present results for band oscillator strength in Table 6.1.

Allison (1975) has theoretically calculated the variation in band oscillator strength across a band as the rotational number N'' is varied. His theoretical estimates will be compared with the present results for the 1-0 to 15-0 bands. A typical example of the rotational dependence of the band oscillator strength from the theoretical calculations of Allison is shown in Figure 6.1 for the 9-0 band of the Schumann-Runge bands. The present experiment attempts to find the values of f_0, the oscillator strength for zero rotational number, and the rate of rotational dependence β, by fitting the measured oscillator strengths to a straight line of the form

$$f(v',v'',N'') = f_0(v',v'') - \beta(v')(N'' + 1)N'' \qquad (6.1)$$

where $f(v',v'',N'')$ is the oscillator strength of the N'' rotational line of the v' vibrational band, and where the subscript v' for f_0 and β refers to those quantities for the v' vibrational band.

It should be noted that Allison's theoretical predictions are not exactly straight lines. The P branch rotational dependence departs from the linear at very low N'' values, flattening off somewhat, while the R branch rotational dependence has an ever increasing value of slope towards lower N'' values, rising away from the linear towards the value for the P branch f_0 value. The accuracy of the results obtained in this experiment allow estimates of the f_0 oscillator strength values, and the

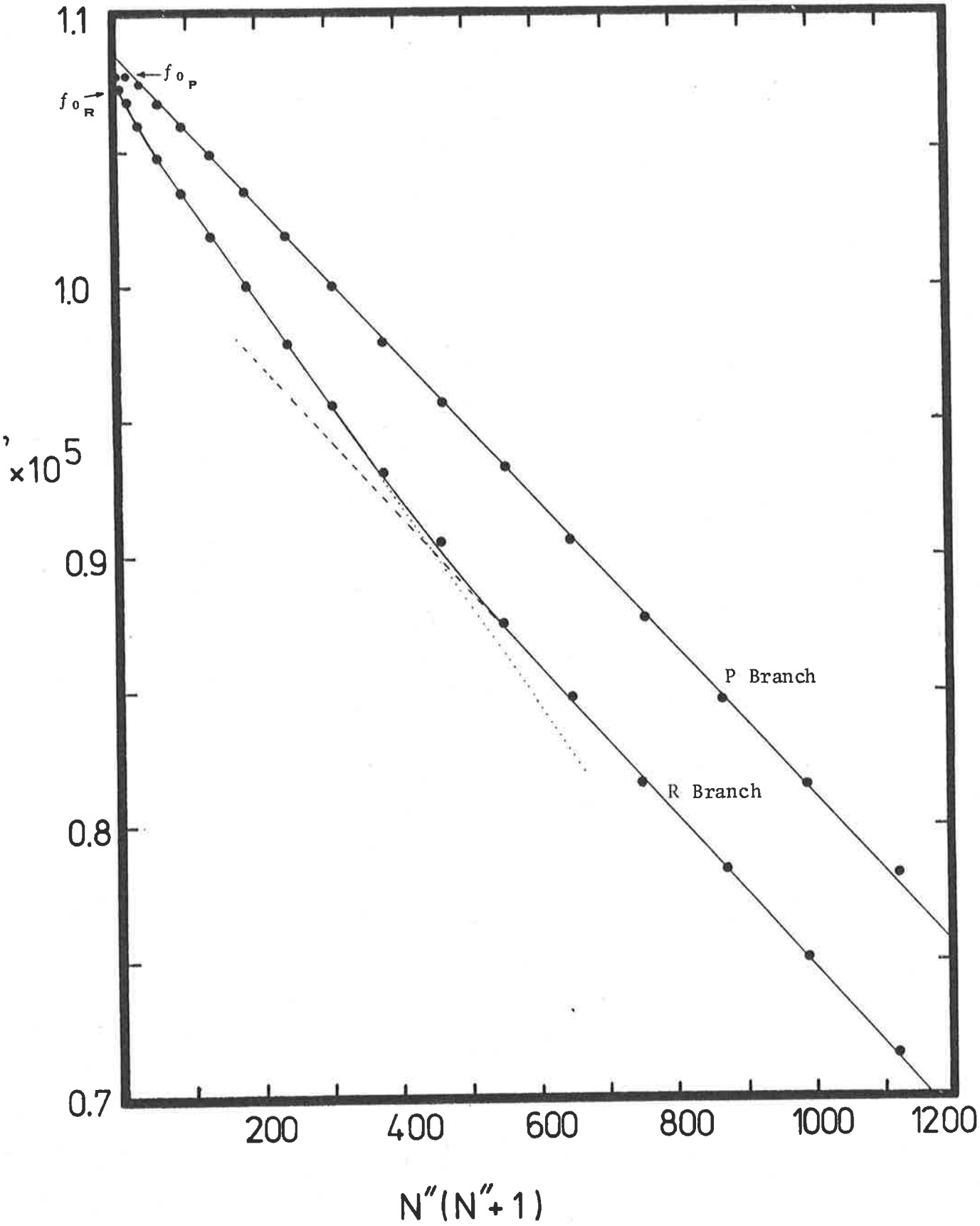

FIG. 6.1 A plot of Allison's predicted variation of oscillator strength with rotational number, N'' , in this case for the 9-0 band. The intercepts for zero rotational number are denoted by f_{0_P} and f_{0_R} .

slope parameters for a linear fit to be evaluated, but is insufficient for much minor variations as shown by Figure 6.1 for low N'' to be determined as well. For such small variations to be detected, errors in the individual oscillator strength would need to be 1% or less, accuracy unattainable by this experiment. No experimental determination of variation of band oscillator strength with rotational number has been attempted before.

6.3 The Present Results

Oscillator strengths and linewidths were obtained for the 3-0 to 14-0 bands, the operating conditions obtainable for the absorption cell allowing these measurements to be made to good accuracy. Results were also obtained for the 2-0 and 15-0 bands, but not to the same accuracy, and some results for the 16-0, 17-0, 18-0 and 1-0 bands were also obtained, though these results should be considered no more than qualitative. The variation in band oscillator strength with rotational number for the 1-0 to 15-0 bands are plotted in Figures 6.5 to 6.19 , and are compared with Allison's theoretical predictions. Each band will be compared with these theoretical predictions and discussed fully later, but the general trend is that Allison's predictions are too low, and in most cases the variation of band oscillator strength with rotational number measured experimentally is more pronounced than predicted.

The oscillator strengths quoted in the tables are those calculated using the final solutions to the curve of growth fitting the experimental equivalent widths. Each pair of equivalent widths usually produce a solution, a_f . That is, using the value of line-broadening parameter a_f the curve of growth of the lines in question pass through the two equivalent widths, W_L , W_u at the right values of pressure. This final value of a_f is then used to extract a $k_p X$, from which the oscillator strength is

calculated. The exceptions to this are the 1-0, 2-0 and 16-0 bands. The oscillator strengths quoted for those bands are all calculated at the same value of α for each line. In the case of the 1-0 band, the value of α chosen is the average of the first two lines in the band. In the case of the 2-0 band, the first four lines had their α-values averaged, and then this average value of α was used to extract a value of k_pX for each line, and this value was then used to calculate oscillator strengths. This procedure tends to reduce random scatter due to different α-value solutions being used to extract k_pX values. In the bands 3-0 to 15-0, the scatter in α-value was not too pronounced, but in the 2-0 band especially, α-value determinations become unreliable at high rotational number.

6.4 Comparison with Previous Experimental Results

Before any comparison can be made between the present work, and that of previous experimenters, the quantity required for comparison, namely mean band oscillator strength $f(v',v'')$, must first be calculated. The results obtained in this work are band oscillator strengths $f(v',v'',N'')$, and are listed in Appendix 11 for all the various rotational lines for which they were measured. The results for each band have been fitted to a straight line of the form given in equation 6.1. A weighted mean band oscillator strength $fv'v''$ can then be calculated from this straight line fit, using the following equation

$$f(v',v'') = \frac{\sum_{N''} f(v',v'',N'')\ \bar{\alpha}(v',N'',T)}{\sum_{N''} \bar{\alpha}(v',N'',T)} \qquad (6.2)$$

where $f(v',v'',N'')$ is the band oscillator strength obtained from equation 6.1 and $\bar{\alpha}(v',N'',T)$ is the total relative population for the N'' rotational line of the v' vibrational band at temperature T (that is

$\bar{\alpha}$ is the sum of the relative populations of the three triplet components). The weighted mean band oscillator strength obtained in this way would then be comparable to that measured by other experimenters using pressure broadening to measure the total absorption area of a whole band, since each line contributes an oscillator strength proportional to its population, which is related to its Boltzmann factor and its associated statistical weight. Use of equation 6.2 to calculate the weighted mean band oscillator strengths gives an answer $f(v',v'')$ identical to the band oscillator strength for the P_{11} line of each band, that is by $N'' = 11$ in equation 6.1.

A comparison of the weighted mean band oscillator strengths of this work with those of previous experimenters, in particular Bethke (1959) Hudson and Mahle (1972) and Ackerman et al (1970) is shown in Figures 6.2 and 6.3 and Table 6.1. The results of other experimenters are also shown in the table, but the above mentioned group, plus the electron impact measurements of Huebner et al (1975) form the basis for comparison. Figure 6.2 shows the results for this weighted mean band oscillator strength to be in fair agreement, for $v' = 2$ to $v' = 8$. For the purpose of clarity, where the oscillator strengths of different experimenters have the same value, or are in very good agreement for some value of v', the plotted points in Figures 6.2 and 6.3 are displaced slightly in the horizontal direction to improve visibility. Figure 6.3 shows the results of this work tend to be slightly higher than most of the other measurements, the difference between the values of this work and those of other investigators being a maximum at $v' = 14$. Values of weighted mean band oscillator strength quoted for the 16-0, 17-0 and 18-0 bands are only approximate, the value actually being an average of the oscillator

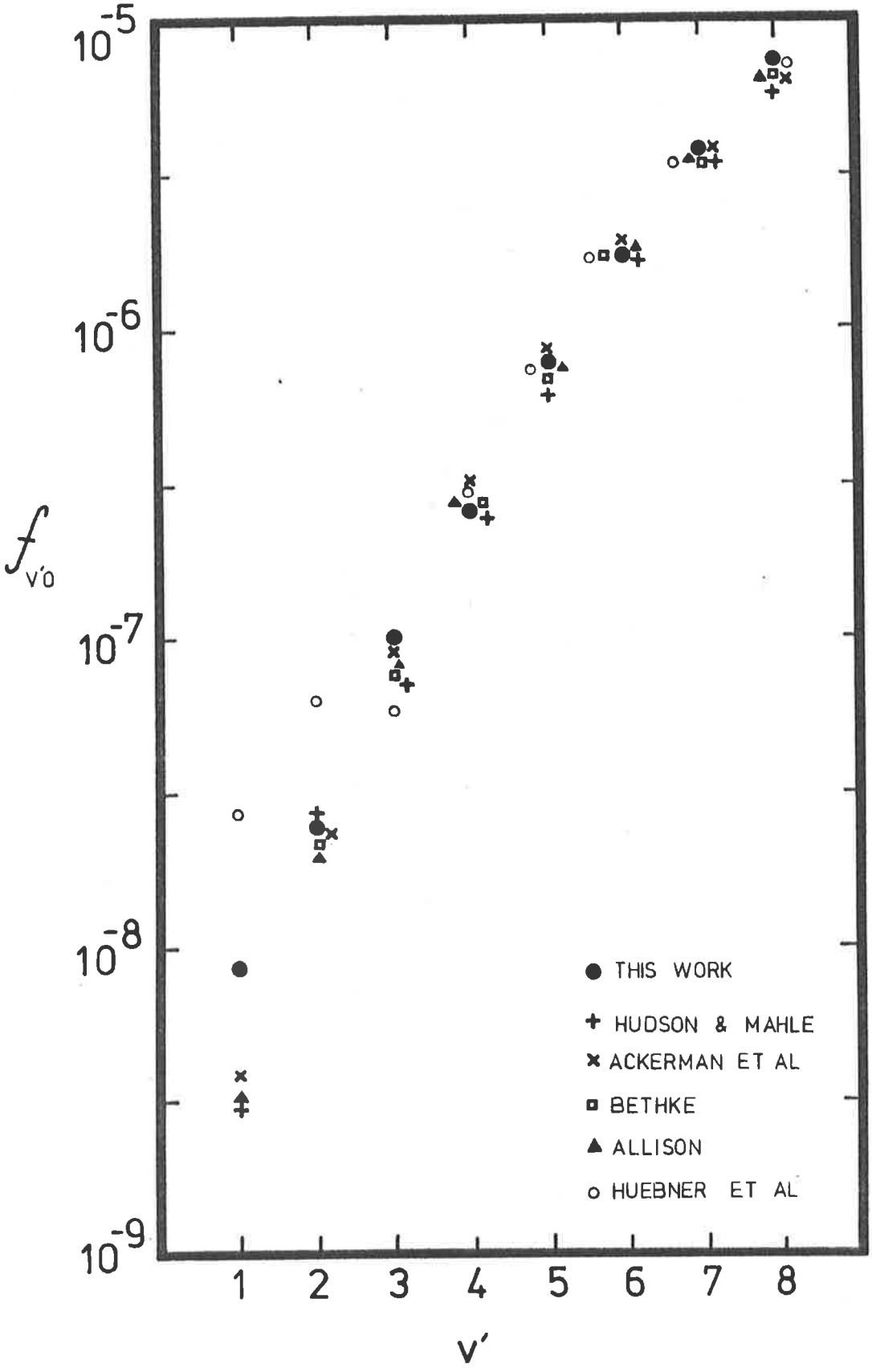

FIG 6.2 A comparison of mean band oscillator strength $f v',v''$ (in this case $f v'o$) for the Schumann-Runge bands 1-0 to 8-0 , for various experimenters listed in Table 6.1.

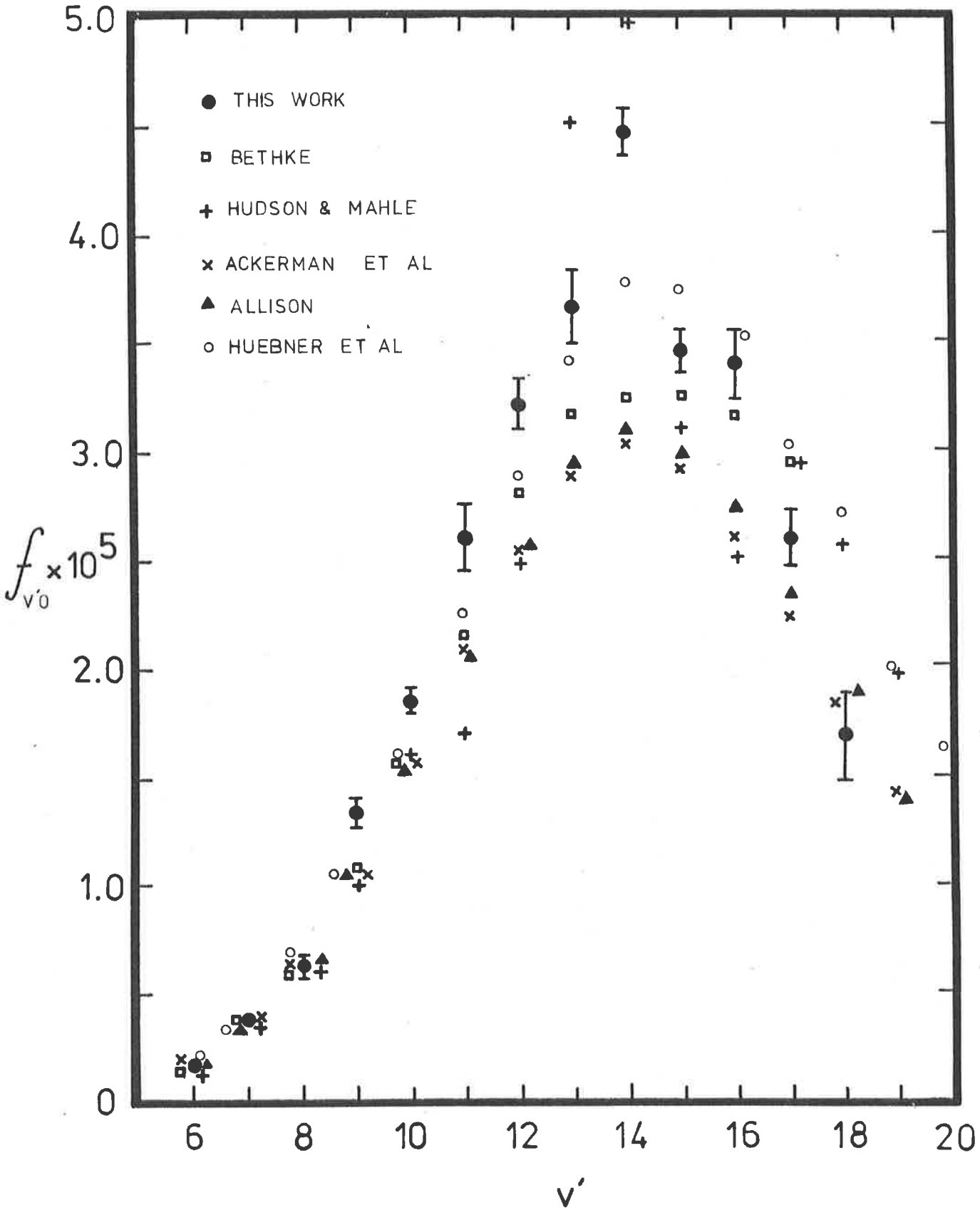

FIG 6.3 A comparison of the mean band oscillator strength $f_{v',v''}$ for the Schumann-Runge bands 6-0 to 19-0 for various experimenters listed in Table 6.1

strengths obtained rather than a weighted mean, there being insufficient points measured for these bands, to realistically calculate a mean band oscillator strength. For the 16-0 band, the band oscillator strength for the P_{11} line, found to be equal to the weighted mean band oscillator strength for the other bands, is quoted. For the 17-0 band, a weighted mean of the three line oscillator strengths is used, while for the 18-0 band, with only a single measurement, the band oscillator strength for the line in question is quoted.

6.5 Comparison with Theoretical Predictions

A comparison of the mean band oscillator strengths of this work with the theoretical predictions of Allison (1975) is made in Table 6.2 and also in Figure 6.3. Between the 7-0 to 16-0 bands, the predictions of Allison are all lower than the results obtained in this work, the maximum difference occurring at $v' = 14$, as for the previous experimental results, upon which Allison's work must be based.

Also shown in Table 6.2 are the $f_0(v')$, the oscillator strengths for $N'' = 0$, for both the P branch and the R branch where possible, calculated from a straight line fit to Allison's values, and also for the results of this work. To make the comparison valid, $f_0(v')$ and $\beta(v')$ values were calculated from Allison's theoretical results, but only theoretical oscillator strengths corresponding to rotational lines which were also used in the calculation of $f_{0_P}(v')$ and $f_{0_R}(v')$ values for this work, were used. In this work, values obtained for $f_{0_P}(v')$ and $f_{0_R}(v')$ are only independent above the 8-0 band, since only for $v'' \geq 8$ can sufficient lines be resolved to use R branch oscillator strengths in a calculation of $f_{0_R}(v')$ and $\beta_R(v')$. In the range 8-0 to 15-0,

Allison predicts

$$f_{o_P}(v') / f_{o_R}(v') = 1.02$$

whereas the results over the same range for this experiment are

$$\frac{f_{o_P}(v')}{f_{o_R}(v')} = 1.06 \pm 0.014$$

The small error in the experimental result arises from counting statistics, but there will be a small additional error because of the assumed linear dependence in equation 6.1.

Allison's predictions for the slope are compared with the results obtained in this work in Table 6.2. The results for the bands 1-0 to 4-0 are subject to large errors, and refinements to the experimental system, and also to the analysis are needed, before further attempts at measurements in this region are performed. From the 5-0 band onwards, however the results obtained for the slope of the oscillator strength with rotational number, β, are sufficiently accurate to allow comparison. In the range 8-0 to 15-0, Allison predicts

$$\beta_R / \beta_P = 1.23$$

whereas the results of this work give

$$\beta_R / \beta_P = 1.03 \pm 0.05$$

That is, the prediction of Allison that the dependence of R branch oscillator strength on rotational number is greater than for the P branch is not verified by this experiment.

Figure 6.4 shows a comparison of the rate of decrease of oscillator strength for this work and for Allison's theoretical predictions, The

	$f_{v'v''}$		f_{0_P}		f_{0_R}
BAND	ALLISON	THIS WORK	ALLISON	THIS WORK	ALLISON
1-0	3.26×10^{-9}	$(8.75 \pm 0.73) \times 10^{-9}$	3.32×10^{-9}	$(8.77 \pm 0.22) \times 10^{-9}$	3.29×10^{-9}
2-0	1.99×10^{-8}	$(2.45 \pm 0.09 \times 10^{-8}$	2.04×10^{-8}	$(2.35 \pm 0.05) \times 10^{-8}$	2.01×10^{-8}
3-0	8.47×10^{-8}	$(1.01 \pm 0.37) \times 10^{-7}$	8.68×10^{-8}	$(1.03 \pm 0.02) \times 10^{-7}$	8.52×10^{-8}
4-0	2.81×10^{-7}	$(2.70 \pm 0.12) \times 10^{-7}$	2.88×10^{-7}	$(2.65 \pm 0.07) \times 10^{-7}$	2.83×10^{-7}
5-0	7.71×10^{-7}	$(7.72 \pm 0.19) \times 10^{-7}$	7.92×10^{-7}	$(7.98 \pm 0.18) \times 10^{-7}$	7.79×10^{-7}
6-0	1.80×10^{-6}	$(1.75 \pm 0.07) \times 10^{-6}$	1.86×10^{-6}	$(1.84 \pm 0.05) \times 10^{-6}$	1.83×10^{-6}
7-0	3.66×10^{-6}	$(3.85 \pm 0.16) \times 10^{-6}$	3.77×10^{-6}	$(4.10 \pm 0.11) \times 10^{-6}$	3.70×10^{-6}
8-0	6.54×10^{-6}	$(7.53 \pm 0.31) \times 10^{-6}$	6.74×10^{-6}	$(8.12 \pm 0.21) \times 10^{-6}$	6.63×10^{-6}
9-0	1.05×10^{-5}	$(1.33 \pm 0.07) \times 10^{-5}$	1.08×10^{-5}	$(1.46 \pm 0.05) \times 10^{-5}$	1.07×10^{-5}
10-0	1.53×10^{-5}	$(1.84 \pm 0.05) \times 10^{-5}$	1.59×10^{-5}	$(1.98 \pm 0.04) \times 10^{-5}$	1.56×10^{-5}
11-0	2.06×10^{-5}	$(2.60 \pm 0.16) \times 10^{-5}$	2.15×10^{-5}	$(2.89 \pm 0.10) \times 10^{-5}$	2.11×10^{-5}
12-0	2.56×10^{-5}	$(3.21 \pm 0.10) \times 10^{-5}$	2.68×10^{-5}	$(3.49 \pm 0.09) \times 10^{-5}$	2.62×10^{-5}
13-0	2.93×10^{-5}	$(3.65 \pm 0.15) \times 10^{-5}$	3.09×10^{-5}	$(4.04 \pm 0.12) \times 10^{-5}$	3.03×10^{-5}
14-0	3.08×10^{-5}	$(4.46 \pm 0.10) \times 10^{-5}$	3.27×10^{-5}	$(4.9[illegible] \pm 0.07) \times 10^{-5}$	3.17×10^{-5}
15-0	2.98×10^{-5}	$(3.45 \pm 0.10) \times 10^{-5}$	3.18×10^{-5}	$(4.81 \pm 0.49) \times 10^{-5}$	3.14×10^{-5}
16-0	2.73×10^{-5}	$(3.40 \pm 0.15) \times 10^{-5}$			
17-0	2.34×10^{-5}	$(2.58 \pm 0.13) \times 10^{-5}$			
18-0	1.89×10^{-5}	$(1.69 \pm 0.19) \times 10^{-5}$			

	f_{0_R}	β_P		β_R	
BAND	THIS WORK	ALLISON	THIS WORK	ALLISON	THIS WORK
1-0		4.68×10^{-13}	$(1.06 \pm 3.9\ ) \times 10^{-13}$	9.56×10^{-13}	
2-0		3.58×10^{-12}	$(-7.89 \pm 3.0\ ) \times 10^{-12}$	5.36×10^{-12}	
3-0		1.67×10^{-11}	$(1.65 \pm 1.1\ ) \times 10^{-11}$	2.27×10^{-11}	
4-0		5.76×10^{-10}	$(-3.68 \pm 3.65) \times 10^{-11}$	8.19×10^{-11}	
5-0		1.70×10^{-10}	$(1.93 \pm 0.08) \times 10^{-10}$	2.29×10^{-10}	
6-0		4.19×10^{-10}	$(6.21 \pm 1.83) \times 10^{-10}$	5.35×10^{-10}	
7-0		8.71×10^{-10}	$(1.94 \pm 0.41) \times 10^{-9}$	1.09×10^{-9}	
8-0	$(8.06 \pm 0.20) \times 10^{-6}$	1.60×10^{-9}	$(4.50 \pm 0.77) \times 10^{-9}$	2.03×10^{-9}	$(4.89 \pm 0.53) \times 10^{-9}$
9-0	$(1.44 \pm 0.06) \times 10^{-5}$	2.70×10^{-9}	$(9.99 \pm 1.67) \times 10^{-9}$	3.49×10^{-9}	$(9.92 \pm 1.91) \times 10^{-9}$
10-0	$1.89 \pm 0.05) \times 10^{-5}$	4.32×10^{-9}	$(1.12 \pm 0.08) \times 10^{-8}$	5.17×10^{-9}	$(1.16 \pm 0.09) \times 10^{-8}$
11-0	$(2.74 \pm 0.10) \times 10^{-5}$	6.72×10^{-9}	$(2.28 \pm 0.41) \times 10^{-8}$	8.31×10^{-9}	$(1.57 \pm 0.34) \times 10^{-8}$
12-0	$(3.44 \pm 0.09) \times 10^{-5}$	9.45×10^{-9}	$(2.11 \pm 0.25) \times 10^{-8}$	1.10×10^{-8}	$(2.38 \pm 0.24) \times 10^{-8}$
13-0	$(3.81 \pm 0.27) \times 10^{-5}$	1.24×10^{-8}	$(2.89 \pm 0.28) \times 10^{-8}$	1.57×10^{-8}	$(2.25 \pm 1.24) \times 10^{-8}$
14-0	$(4.45 \pm 0.06) \times 10^{-5}$	1.48×10^{-8}	$(3.31 \pm 0.17) \times 10^{-8}$	1.66×10^{-8}	$(2.96 \pm 0.14) \times 10^{-8}$
15-0	$(4.27 \pm 1.1\ ) \times 10^{-5}$	1.68×10^{-8}	$(1.04 \pm 0.36) \times 10^{-7}$	2.19×10^{-8}	$(7.75 \pm 0.74) \times 10^{-8}$
16-0					
17-0					
18-0					

TABLE 6.2 A comparison of the theoretical results of Allison for slope parameter β and intercept f_0 with those of this work.

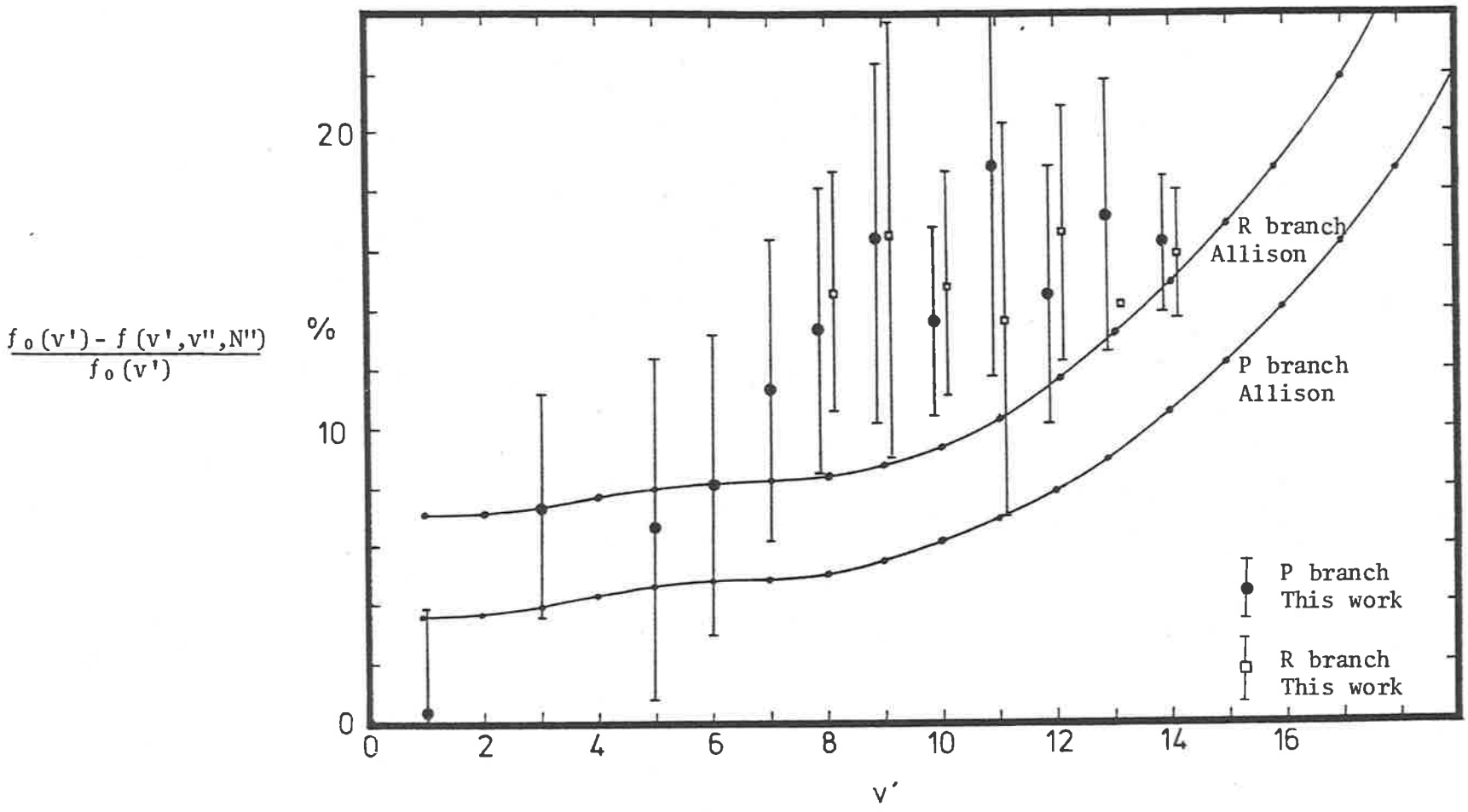

FIG 6.4 A plot of the percentage variation in $\frac{f_0(v') - f(v',v'',N'')}{f_0(v')}$ versus v' for this work compared to the theoretical predictions of Allison.

quantity

$$\frac{f_0(v') - f(v',v'',N'')}{f_0(v')} \qquad (6.3)$$

is calculated for the bands $v' = 1$ to 14, with $N'' = 15$. The experimentally determined results do not confirm Allison's predicted variation. Between $v' = 6$ to $v' = 14$, Allison's predicted results are too low, showing that the slopes assigned to the rotational dependence by Allison are too small (this will be compared for individual bands in the next section). Allison's predicted slopes are represented by the dashed lines in Figures 6.5 to 6.19, while the results of this work are represented by the solid line.

6.6 Discussion

For the purpose of this work, the results will be discussed in sections. The first section consists of the lower bands, comprising the 1-0 to 5-0 bands. The second section comprises the bands from 6-0 to 14-0, and the third and last section describes the 15-0 to 18-0 bands.

6.6.1 The Lower Bands: 1-0 to 5-0

The accuracy of these results improves steadily from the 1-0 through to the 5-0 bands, increasing with increasing band oscillator strength. The band oscillator strength obtained for the 1-0 band is higher by a factor of 2 than that obtained by most of the other experimenters, and this discrepancy is almost certainly due to the weakness of the lines in comparison to the Herzberg continuum in the region of the measurements (discussed in Section 5). The large error is due to the large uncertainty in a-value, which means that the term

$$\left(\frac{\partial k_p X}{\partial a}\right)^2 \delta a^2$$

of equation 5.43 is no longer negligible as it is for most of the other bands (the 2-0 band is the other exception).

Attempts to work out slope parameters β (see equation 6.1) for these low bands were not overly successful. Although values were obtained, the errors were so large (with the exception of the 5-0 band) that the values were almost meaningless. This was basically due to the fact that lines of high rotational number were so difficult to measure for these low bands, either because the strengths were so low, or because of overlap with neighbouring bands, or both, and the omission of these lines makes the slope determination difficult.

The pressure ratio Y decreases for the higher rotational lines in the 1-0 and 2-0 bands, because the limitations of the absorption cell rule out pressures greater than 850 Torr for the high pressure measurement, while the low pressure value must increase due to the weakness of the lines (see Section 5.7). This means that the two results obtained from the measured equivalent widths, f and a are no longer independent. The limiting case would be if only one equivalent width measurement were possible, in which case f and a would be completely dependent. This smaller value of pressure ratio Y means a larger error in the a-value determination. Some idea of the dependence of oscillator strength on a-value can be seen in Figures 6.5 and 6.6 for the 1-0 and 2-0 bands respectively. Oscillator strengths for the various lines are plotted for the final a-value solution for each line, a_f , for the final band average a-value (a = 0.53 for the 1-0 band, and a = 3.8 for the 2-0 band), and for one other a-value.

The band oscillator strengths for the 2-0, 3-0, 4-0 and 5-0 are in reasonable agreement with those of previous experimenters, the results of this work tending to be slightly higher. The 2-0, 4-0 and

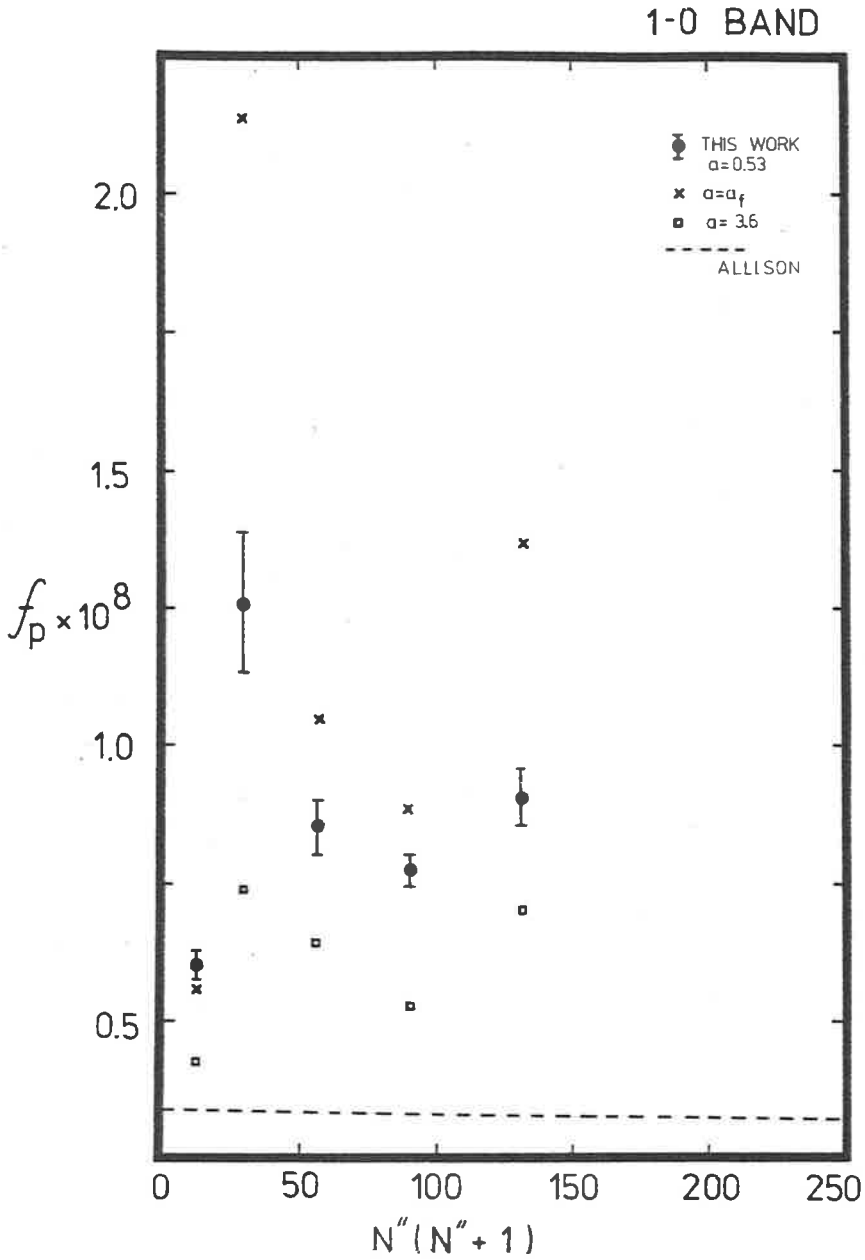

FIG 6.5 Oscillator strengths versus rotational number N" for differing a-values for the 1-0 band.

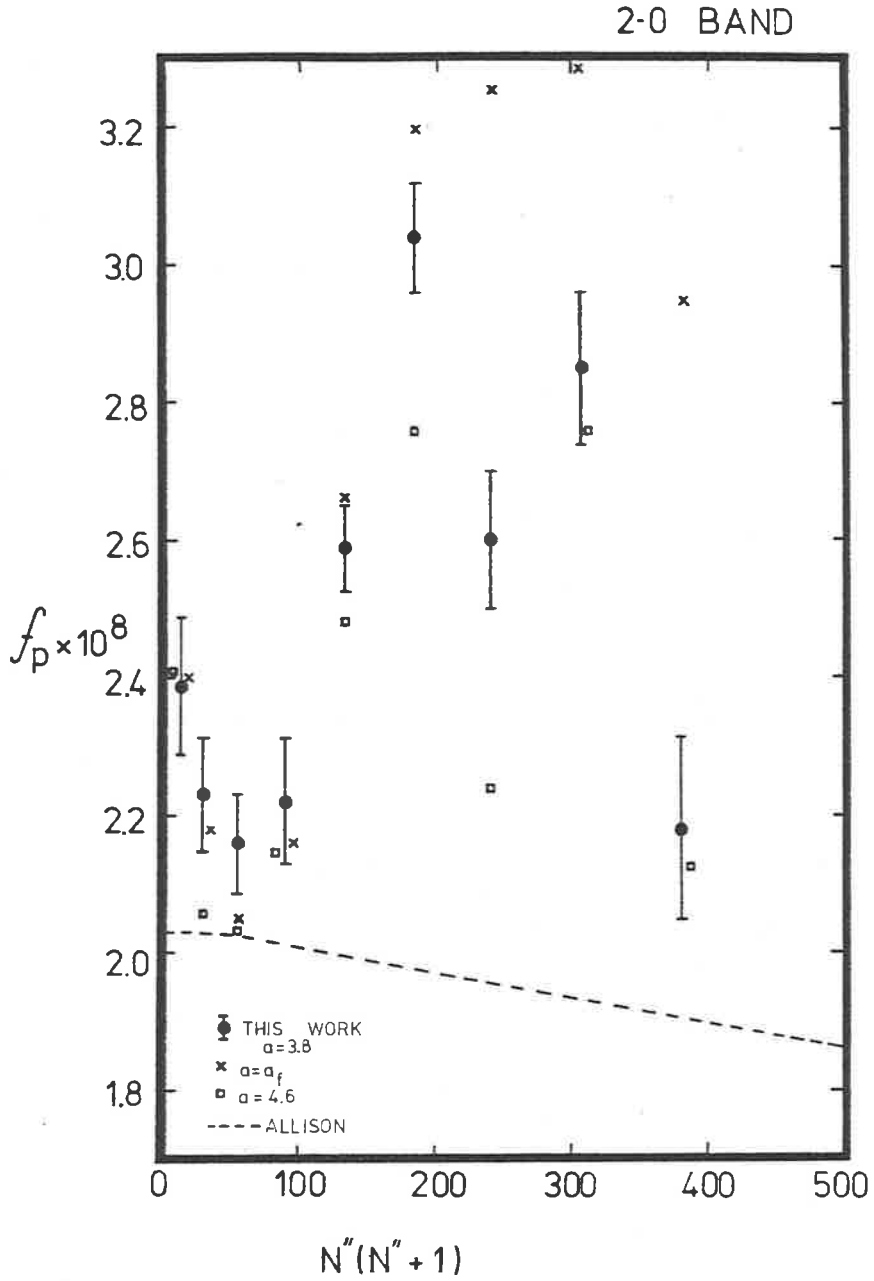

FIG 6.6 Oscillator strengths versus rotational number N" for differing a-values for the 2-0 band.

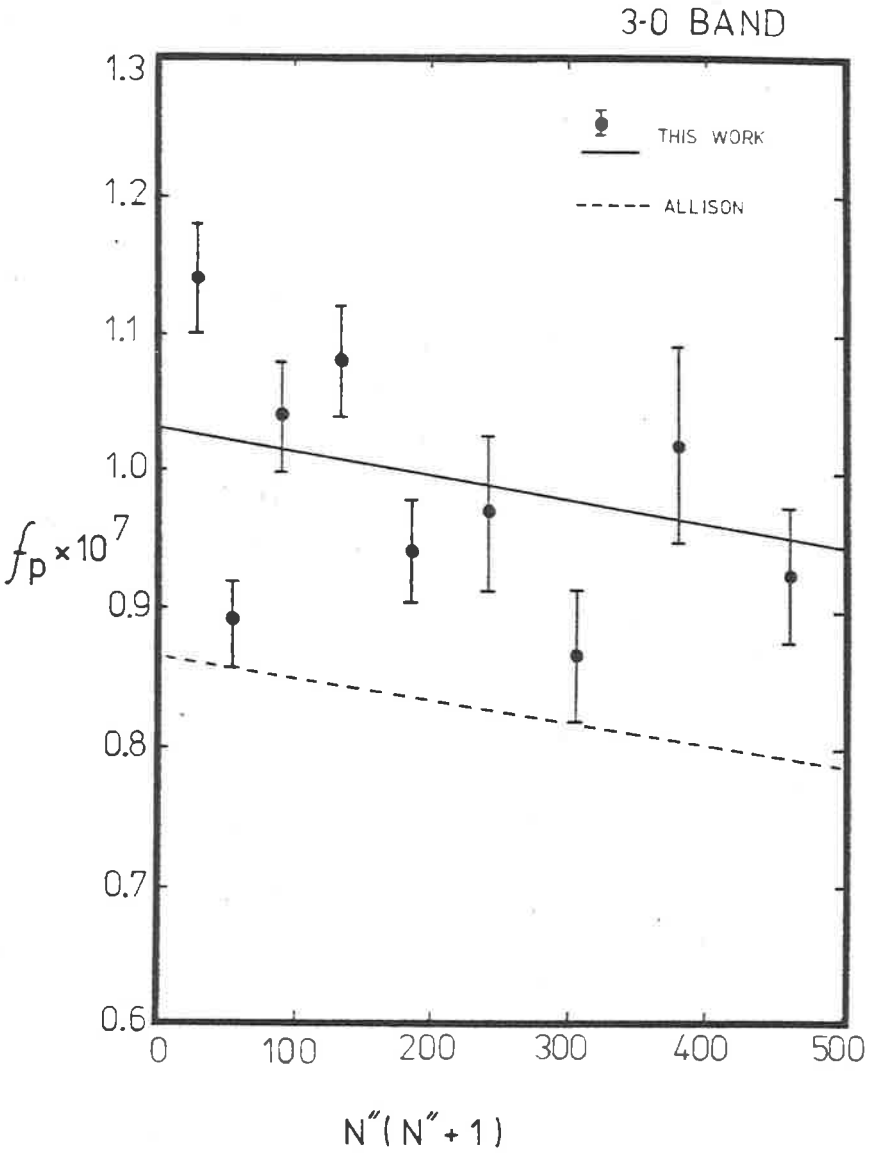

FIG 6.7 Oscillator strengths versus rotational number N'' for the 3-0 band.

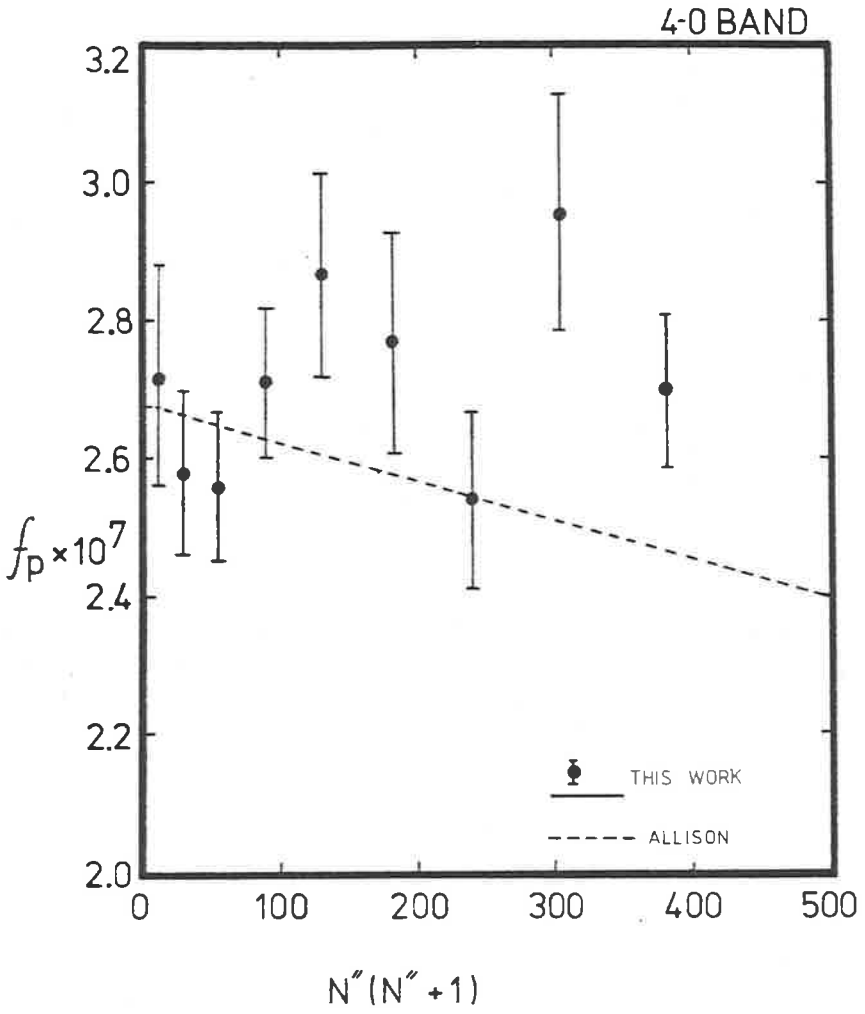

FIG 6.8 Oscillator strengths versus rotational number N'' for the 4-0 band.

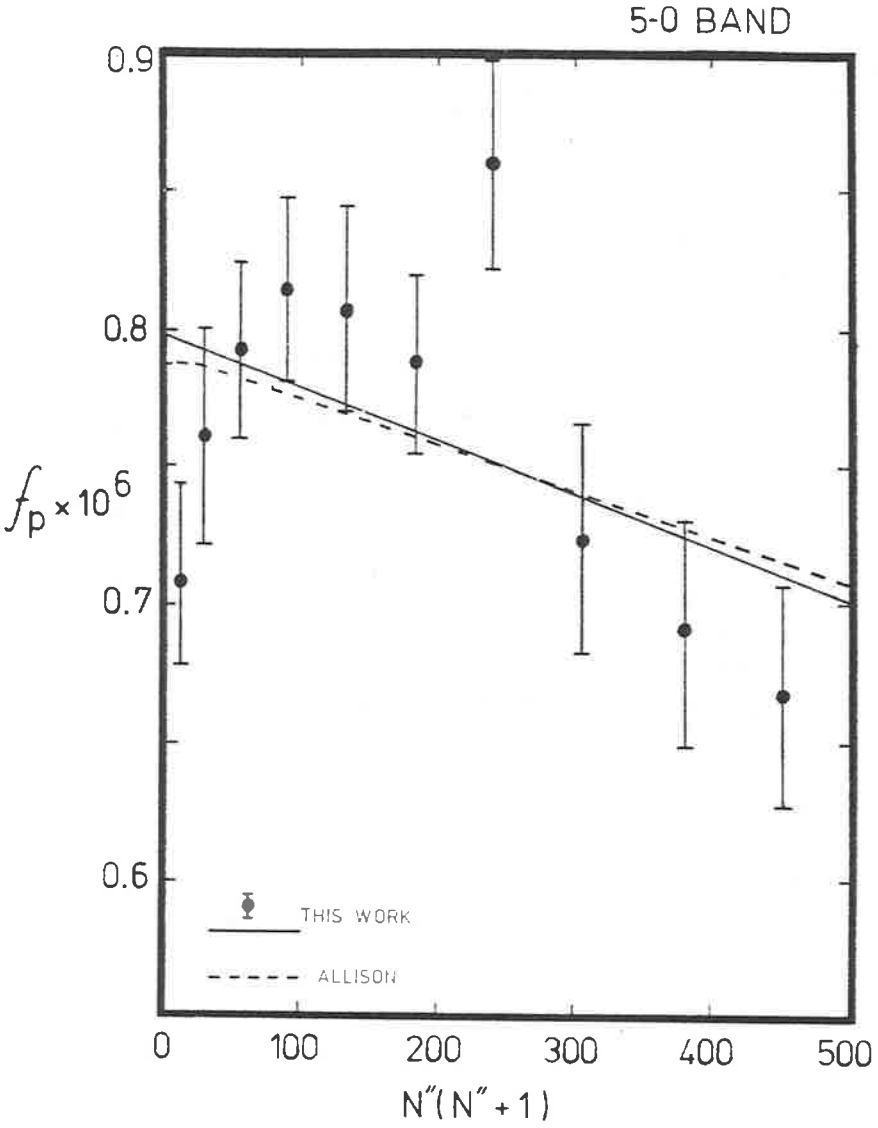

FIG 6.9 Oscillator strengths versus rotational number N'' for the 5-0 band. The determination of the slope parameter β becomes reliable for $v' \geqslant 5$.

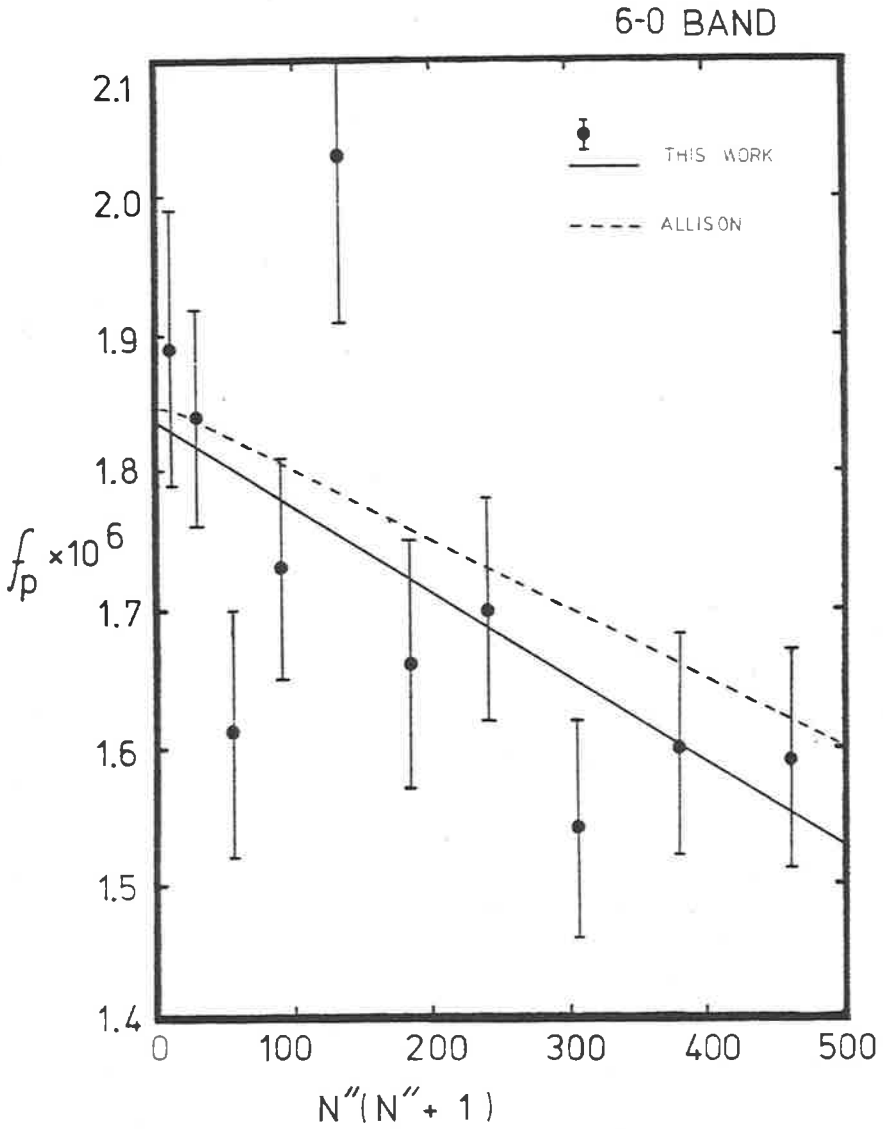

FIG 6.10 Oscillator strengths versus rotational number N'' for the 6-0 band.

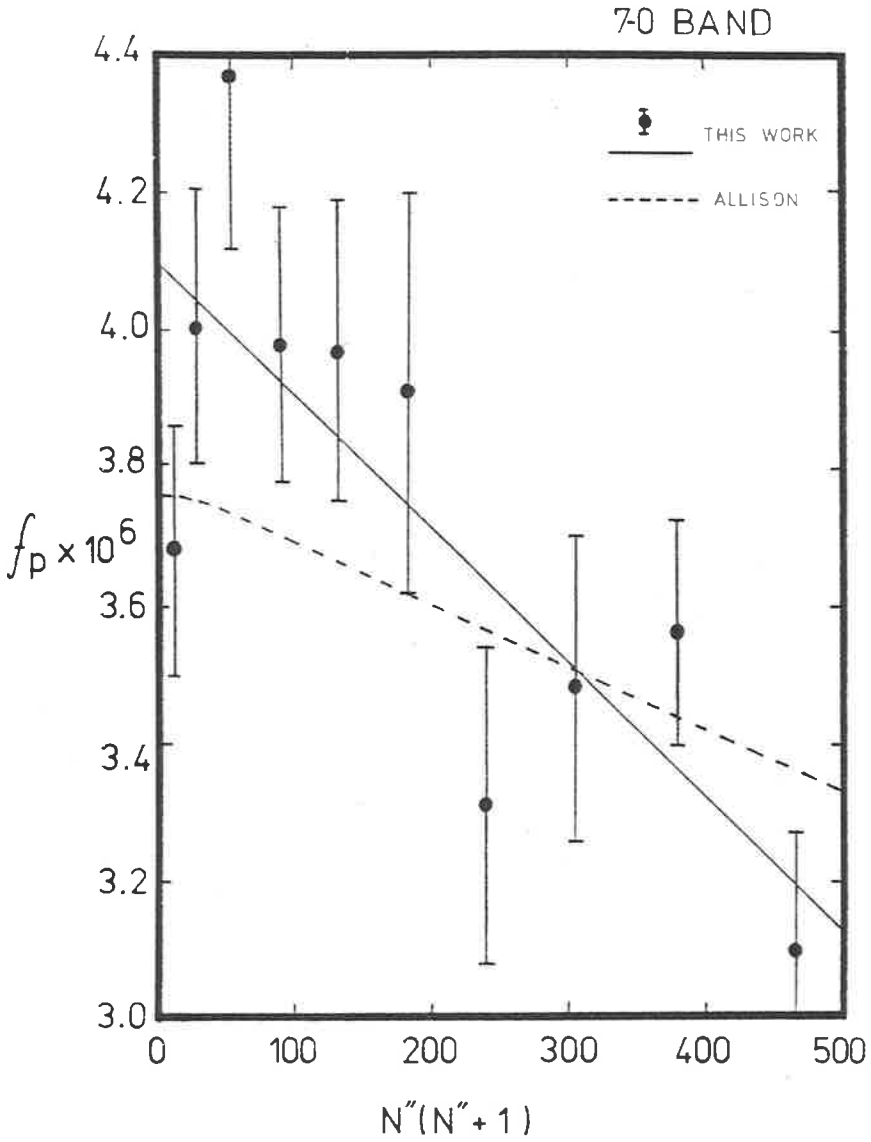

FIG 6.11 Oscillator strengths versus rotational number N'' for the 7-0 band.

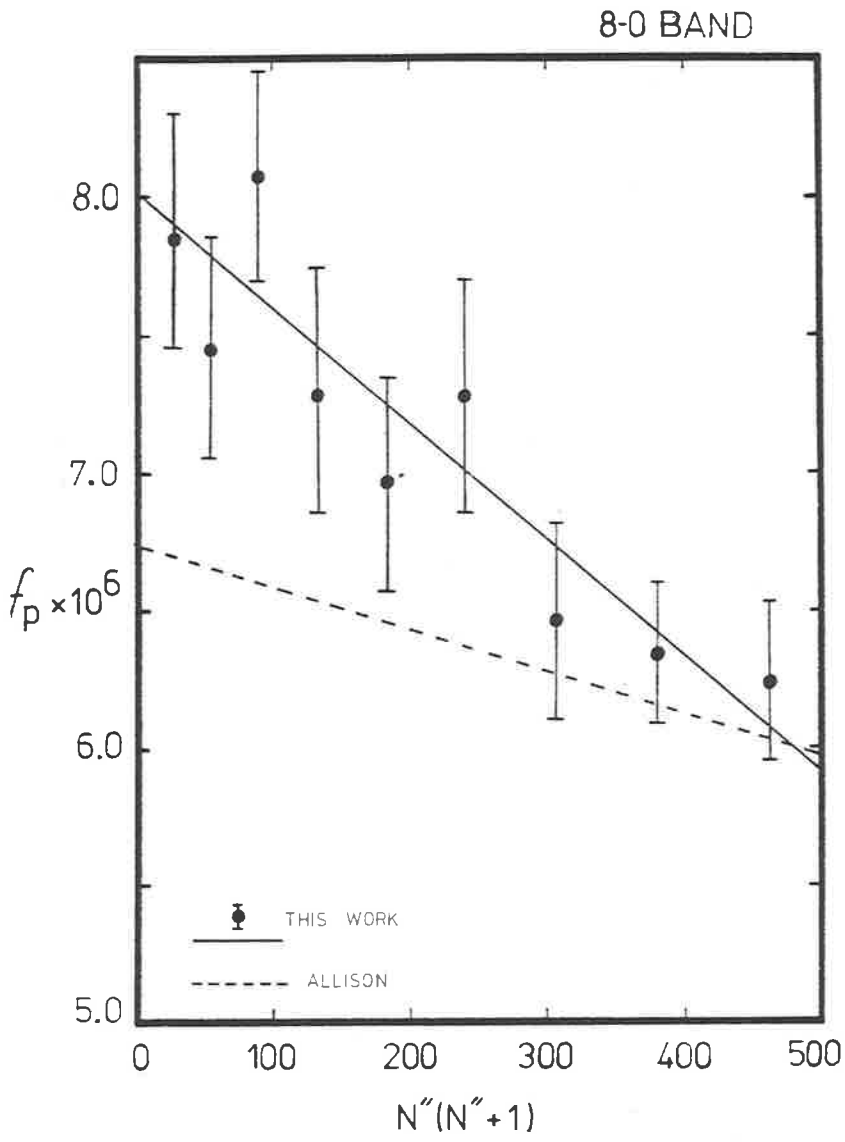

FIG 6.12 Oscillator strengths versus rotational number N'' for the 8-0 band.

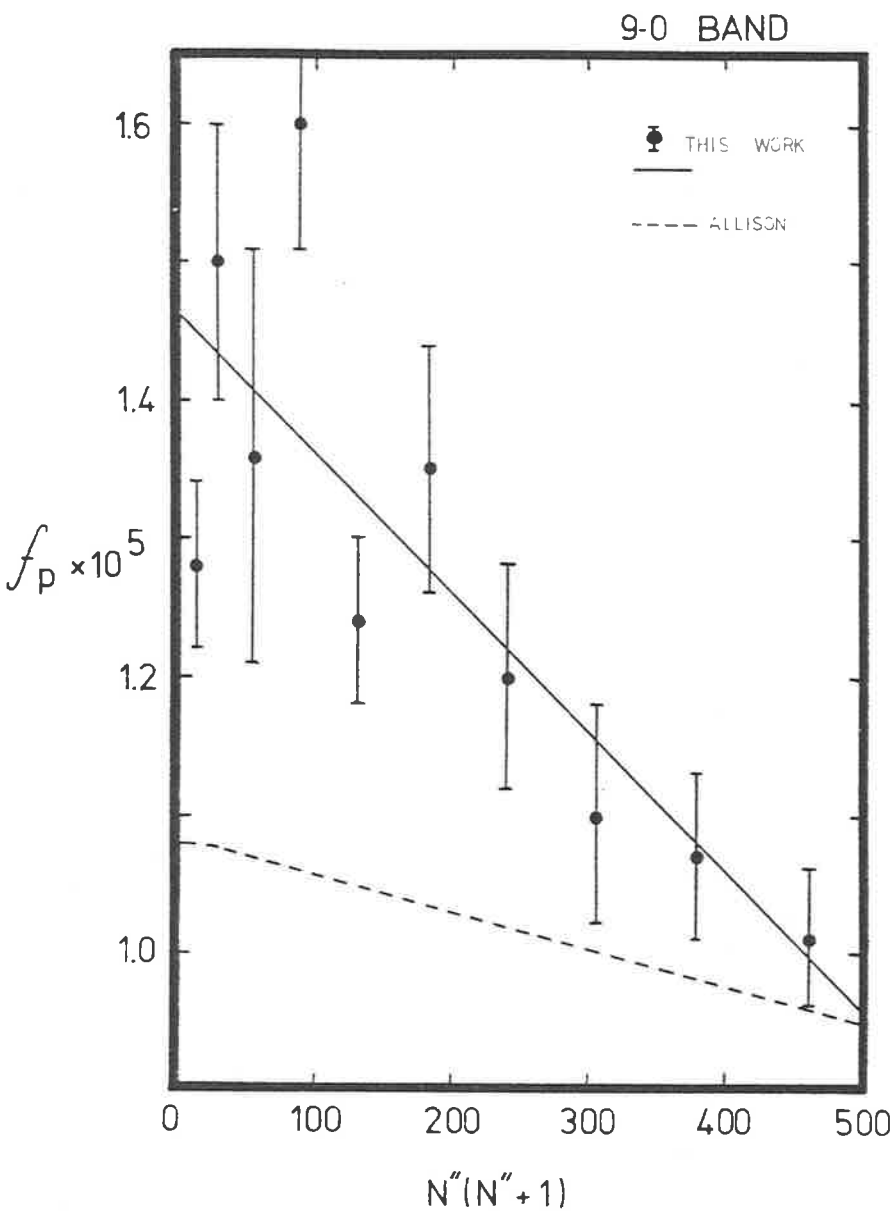

FIG 6.13(a) P-branch oscillator strengths versus rotational number N" for the 9-0 band.

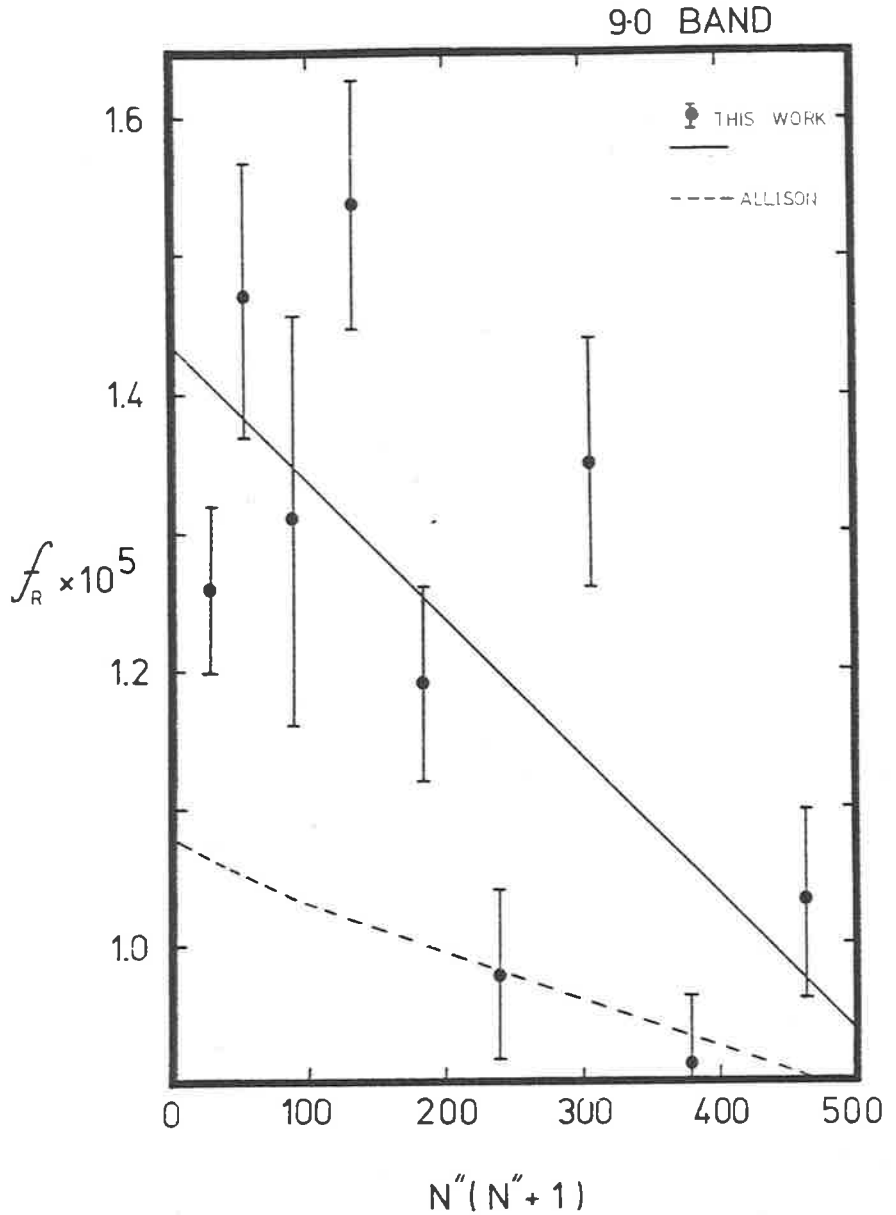

FIG 6.13(b) R-branch oscillator strengths versus rotational number N" for the 9-0 band.

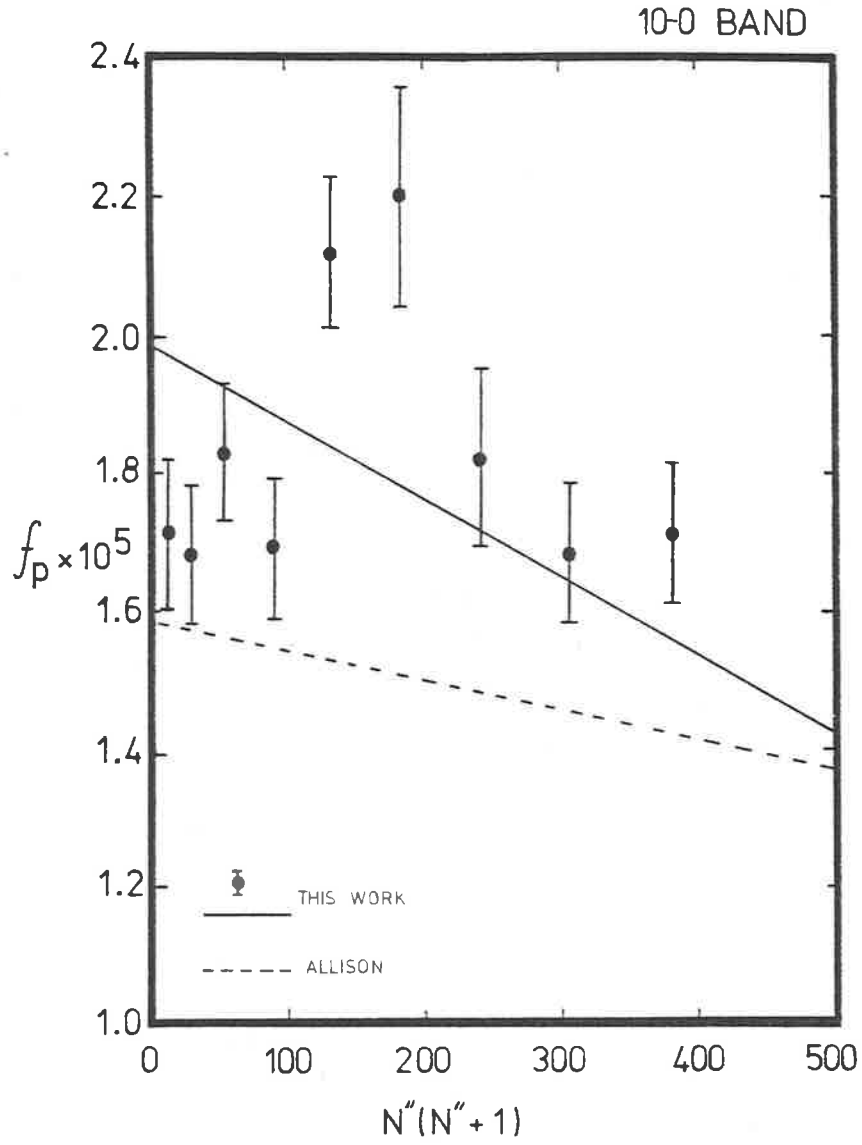

FIG 6.14(a) P-branch oscillator strengths versus rotational number N'' for the 10-0 band.

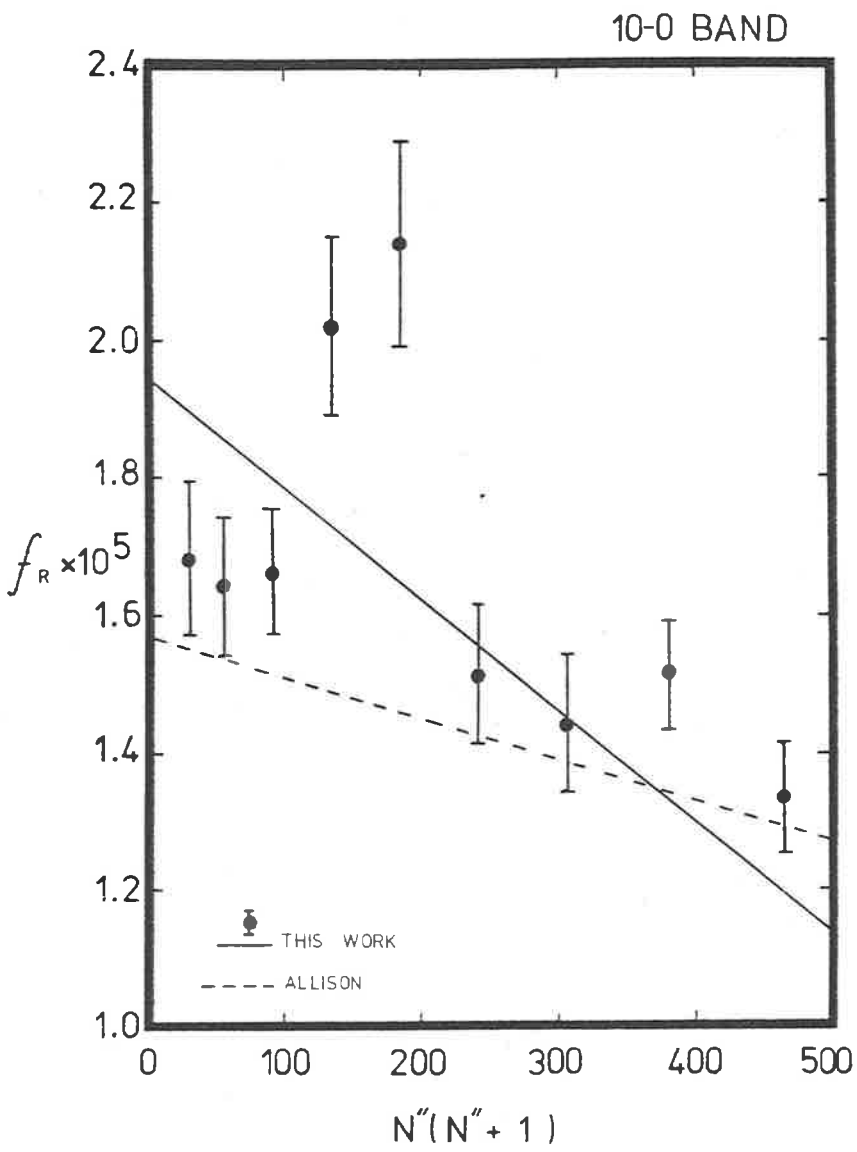

FIG 6.14(b) R-branch oscillator strengths versus rotational number N'' for the 10-0 band.

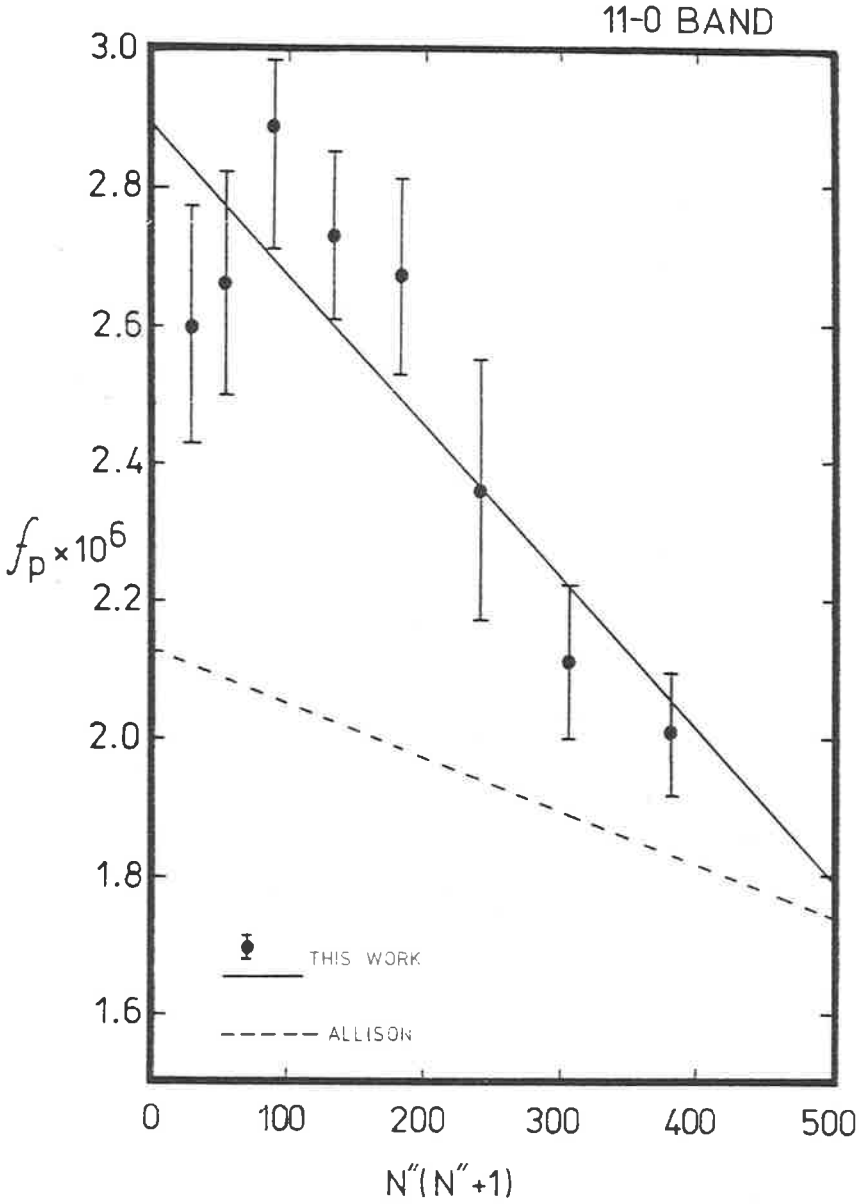

FIG 6.15(a) P-branch oscillator strengths versus rotational number N'' for the 11-0 band.

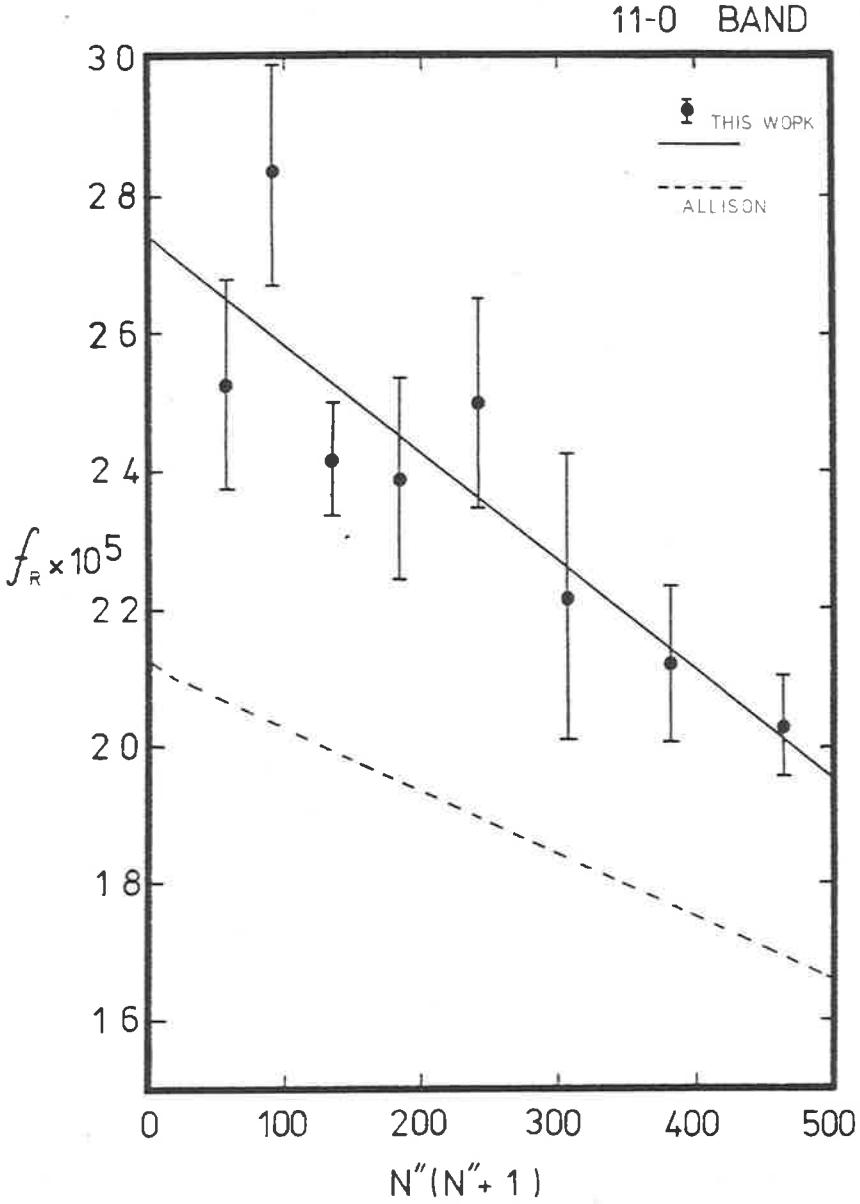

FIG 6.15(b) R-branch oscillator strengths versus rotational number N'' for the 11-0 band.

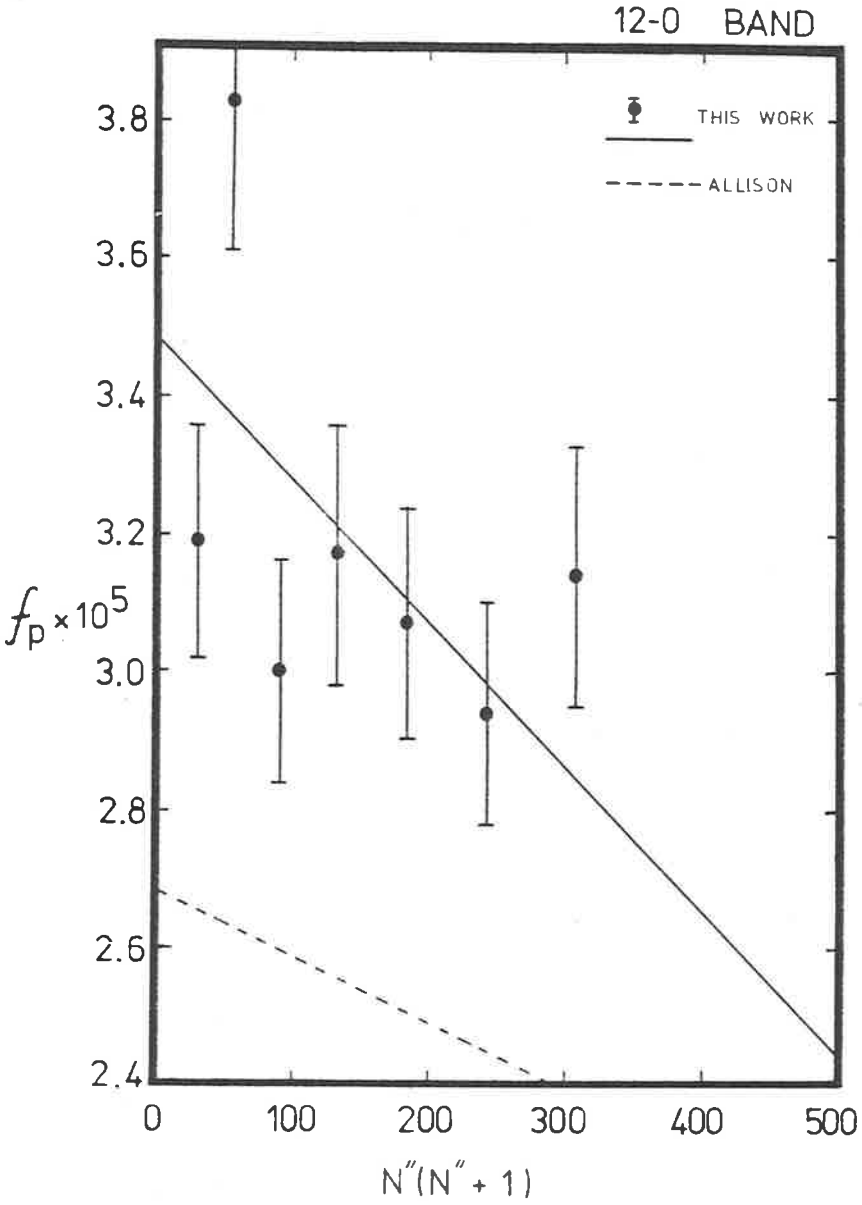

FIG 6.16(a) P-branch oscillator strengths versus rotational number N'' for the 12-0 band.

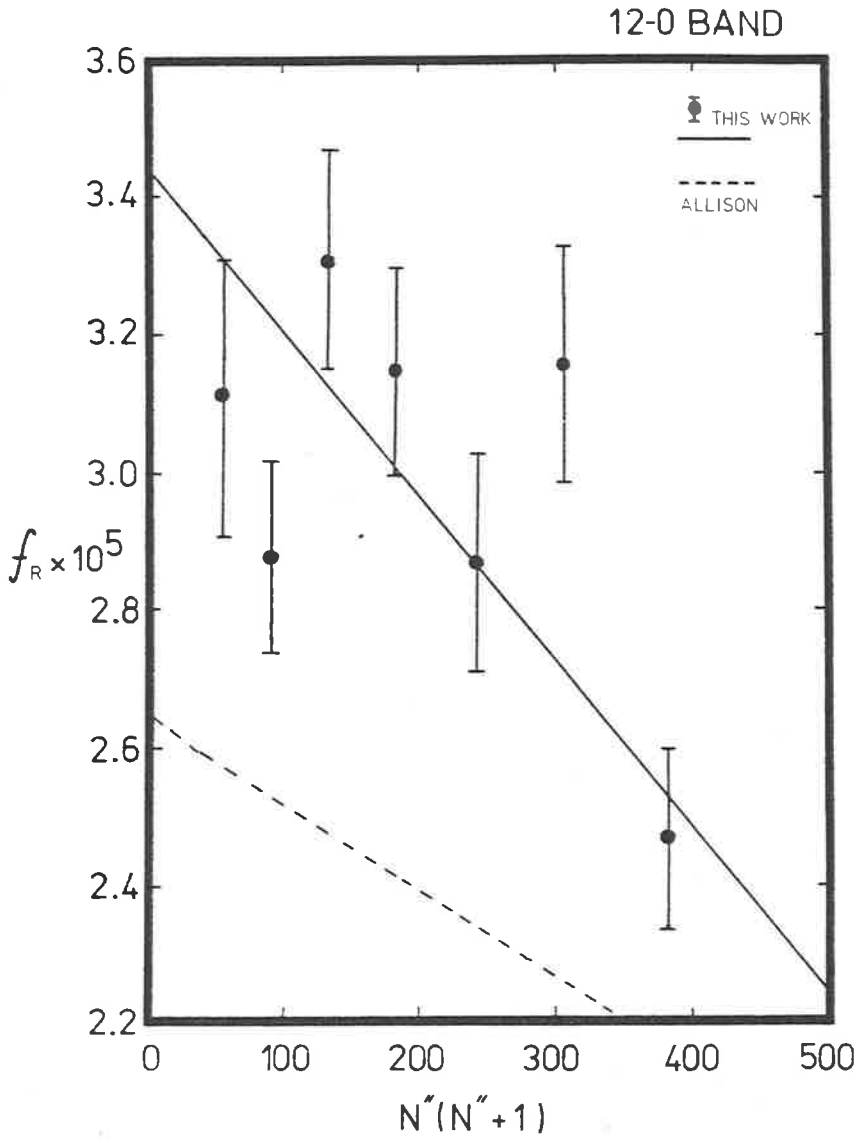

FIG 6.16(b) R-branch oscillator strengths versus rotational number N'' for the 12-0 band.

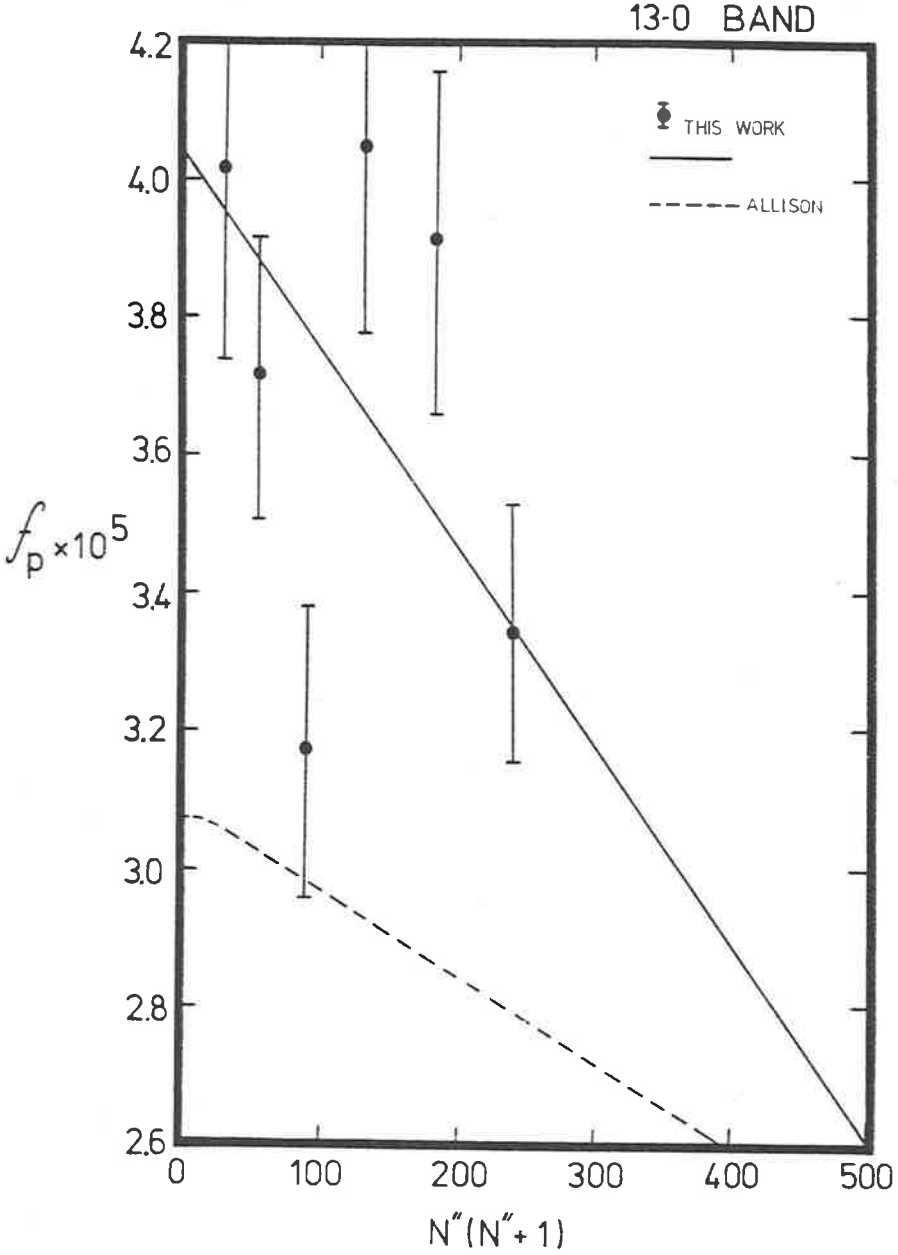

FIG 6.17(a) P-branch oscillator strengths versus rotational number N'' for the 13-0 band.

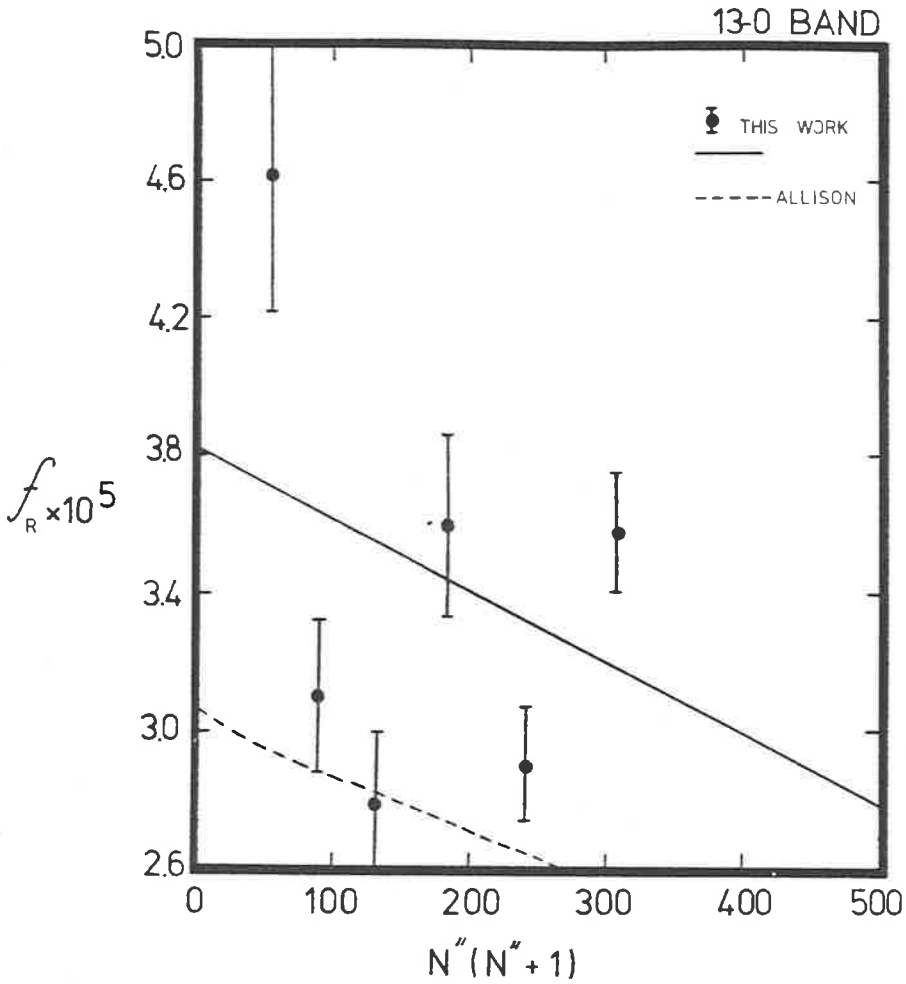

FIG 6.17(b) R-branch oscillator strengths versus rotational number N'' for the 13-0 band.

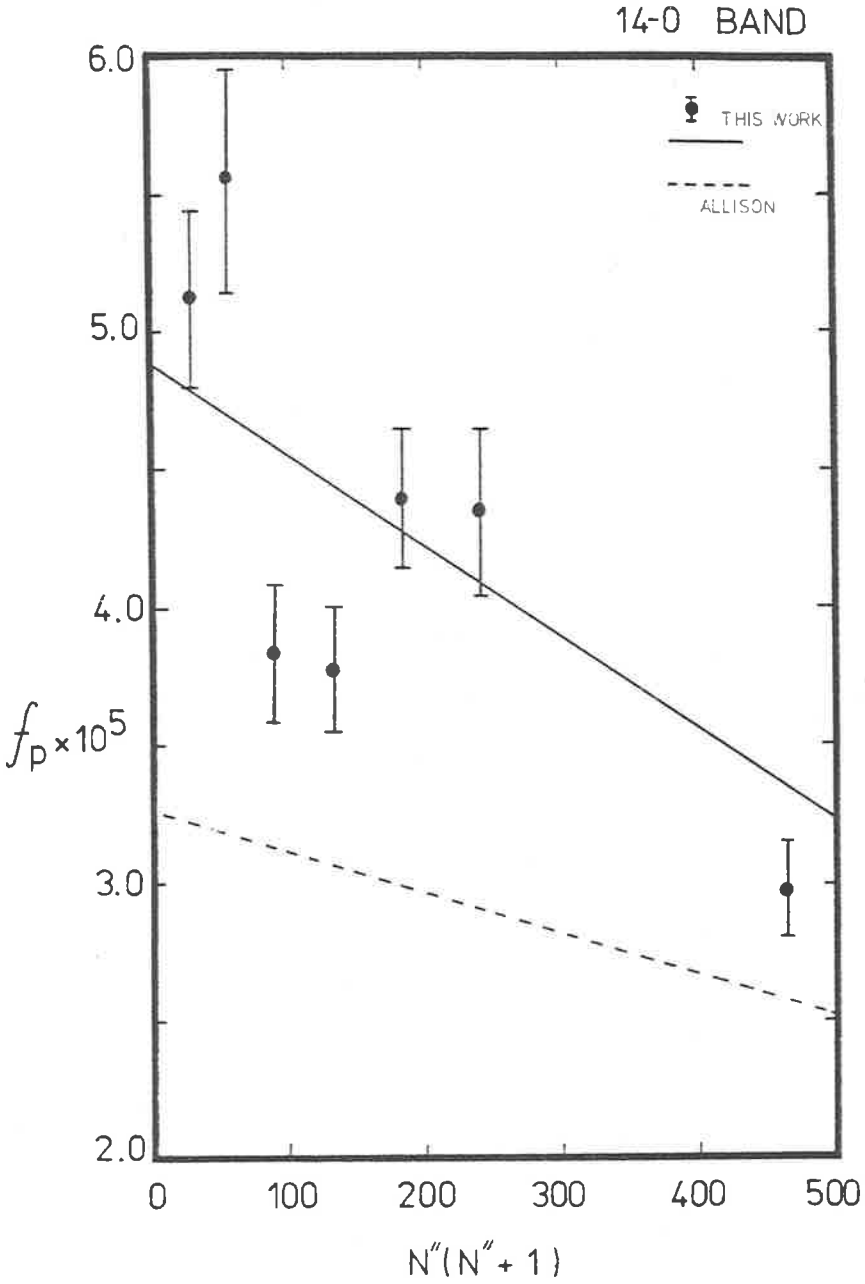

FIG 6.18(a) P-branch oscillator strengths versus rotational number N'' for the 14-0 band.

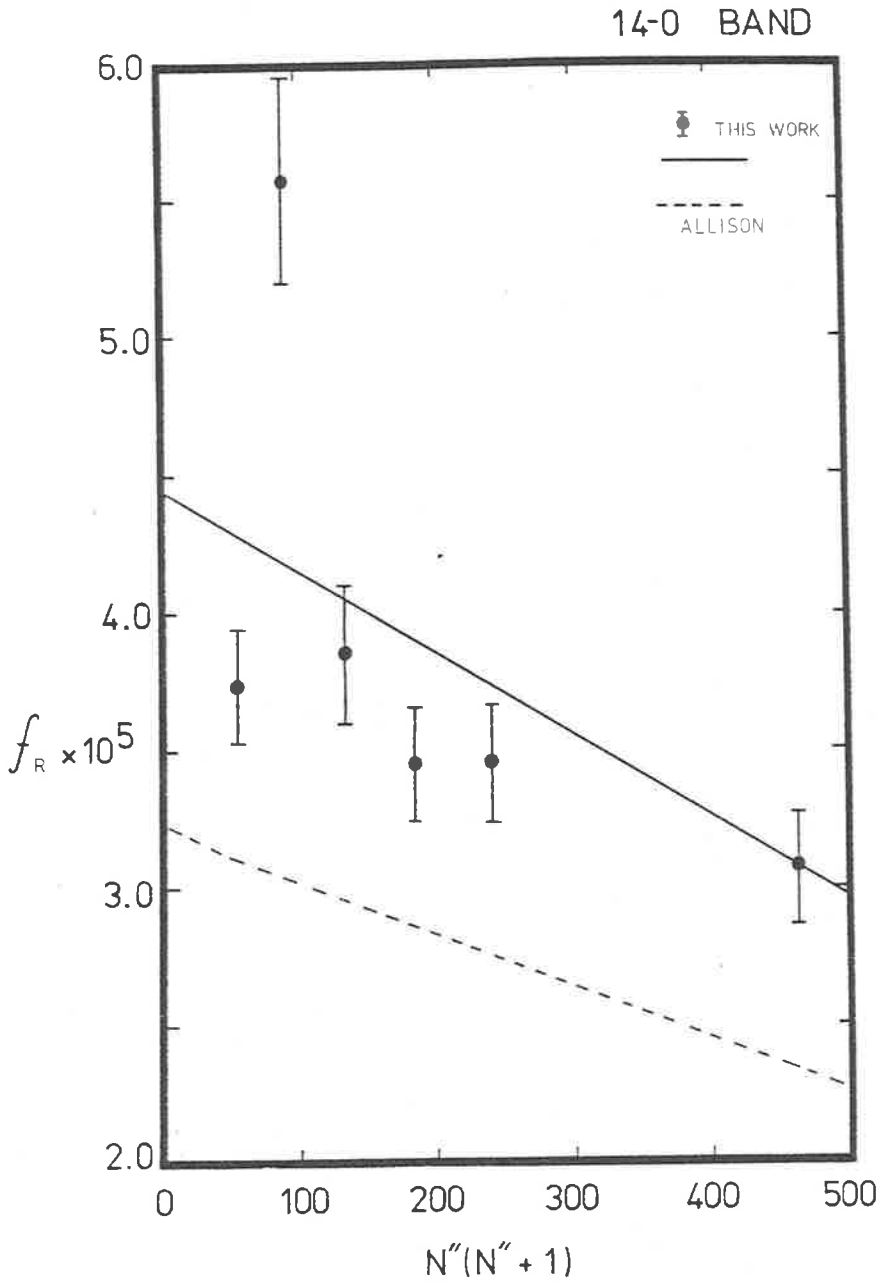

FIG 6.18(b) R-branch oscillator strengths versus rotational number N'' for the 14-0 band.

5-0 bands exhibit the characteristic of having the oscillator strengths for low N'' near the band head, somewhat lower than those of intermediate N'' . That is, oscillator strengths seem to increase with rotational number, attain a maximum, and then decrease with N'' . This observed effect was also noted for the 7-0, 10-0 and 11-0 bands.

No attempt has been made to calculate independent R-branch oscillator strengths for the 1-0 to 5-0 bands, because in each band, only the last few lines visible could be resolved into separate R and P lines. In these cases the ratio of P and R oscillator strengths of Allison were assigned, and the calculations done to give a P branch oscillator strength, although R branch values could just as easily have been calculated instead.

6.6.2 The Middle Region: 6-0 to 14-0 Bands

A comparison of the weighted mean band oscillator strengths of this work with those of the previous experimenters (Figure 6.3 and Table 6.1) shows the present results to be larger over the range 6-0 to 14-0 . There appears to be a gradual increase along the bands in the difference between these results and the previous values, the maximum difference occurring at v' = 14 , which is also the largest value of band oscillator strength.

Comparing these results with those of Bethke (1959), who used a pressure broadening technique, and obtained oscillator strengths from overall integrated band absorption coefficients, shows his results to be consistently lower. The explanation for this may be due to uncertainty introduced in trying to take account of overlap between bands.

Ackerman et al (1970) have assumed linewidths which appear too large at the higher values of v' , and the effect of this is to lower the

value of oscillator strength obtained. Hudson and Mahle used a method examining individual lines at high resolution, and then used an analytical technique similar to that used in the present work. The variability of their results may be due to the dependence of band oscillator strength on N'', the relatively high values they obtained perhaps coming from lines of low N'', and their relatively low values of oscillator strength perhaps coming from lines of high N''. No details of which lines were studied is given by Hudson and Mahle. If this rotational dependence is the correct explanation, then Hudson and Mahle's results may not be inconsistent with those of this work, and tend to support values higher than obtained by other experimenters. The agreement with the low resolution electron impact results of Huebner et al (1975) is slightly better than with the other results near $v' = 13$ and 14.

Figures 6.10 to 6.18 show the present results for oscillator strengths for differing rotational number N''. For $v' \geqslant 8$, the P and R branch lines become separated enough to allow both high and low pressure absorption measurements to be made individually for both branches. This then allows independent measurement of the R branch oscillator strengths and the slopes associated with the rotational dependence. The straight line fit to the individual results of the rotational lines of this work is denoted in Figures 6.10 to 6.18 by the solid lines, and the theoretical predictions of Allison are denoted by the dashed lines. Table 6.2 lists and compares the present results with those of Allison. In almost all cases, the absolute values for the weighted mean band oscillator strengths of this work are higher, while the theoretical predictions of Allison for the rotational dependence of the oscillator strength are found to be too low.

6.6.3 The Upper Bands: 15-0 to 18-0

Above the 15-0 band, perturbations due to curve crossings of the molecular state potential curves in oxygen result in an increase in the complexity of the spectrum, and make the taking of useful measurements difficult. The 15-0, 16-0, 17-0 and 18-0 bands were observed with the target gas at liquid air temperature (82 °K) to reduce spectrum complexity. Due to the curve crossing perturbations, energy levels were shifted, resulting in a shift in wavelength of rotational lines, thus making line identification difficult. The energy level shifts also affect Hönl-London factors, so theoretical line strengths for the perturbed lines cannot be calculated. Therefore, only useful measurements could be made when a rotational line of a given band could be identified, and when it was separated sufficiently from neighbouring lines for these to have little effect on a measured equivalent width. This reduced the number of available lines for these higher bands, and made calculation of a weighted mean band oscillator strength impossible.

Appendix 11 lists the results for the 15-0 to 18-0 bands, and Figure 6.19 shows the variation in oscillator strength with rotational number for the 15-0 band, the only one with sufficient rotational lines visibly measurable. These errors assigned to the slopes of the rotational dependence for the oscillator strength for this band are large because no lines of high N'' could be measured.

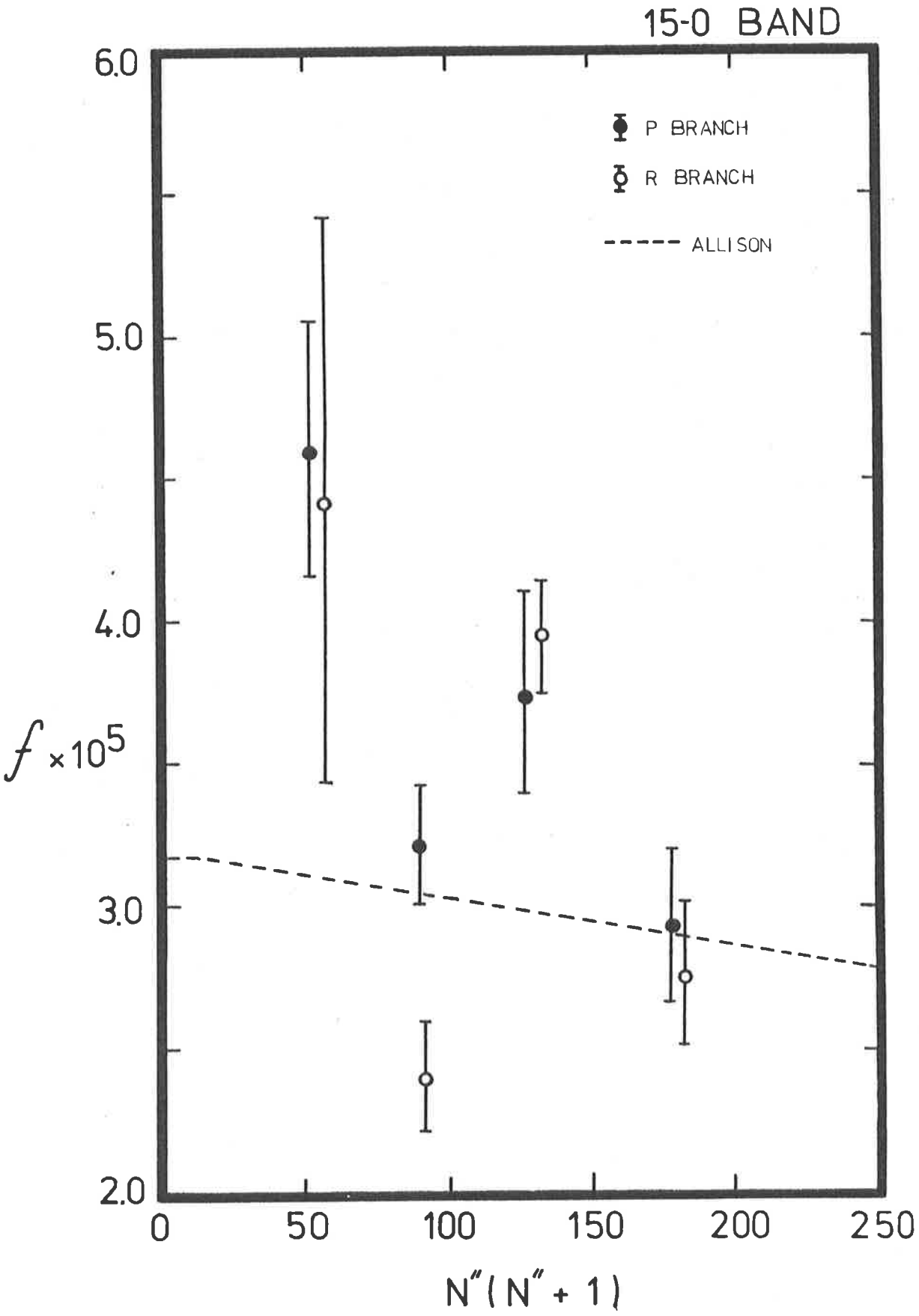

FIG 6.19 Oscillator strengths versus rotational number N'' for the 15-0 band.

6.7 Predissociation and Rotational Linewidths

It was first suggested by Flory(1935) that the rotational lines in the Schumann-Runge bands underwent predissociation broadening. He based this conclusion on the apparent diffuse-ness of rotational lines above the $v' = 2$ level, and on the absence of emission from vibrational levels with $v' > 2$. To account for the predissociation, he postulated that the $^3\pi_u$ state potential curve crossed that of the $^3\Sigma_u^-$ on the outer limb between the $v' = 2$ and $v' = 3$ vibrational levels, the transition $^3\Sigma_u^- \rightarrow {}^3\pi_u$ being an allowed one (see Figure 6.20). Feast (1948) concluded that the experimental evidence was against predissociation but Wilkinson and Mulliken (1956) found some evidence for the 12-0 band being predissociated, since the lines there were observed to be visibly more diffuse than those of the neighbouring 13-0 band. They ruled out the possibility of the $^3\pi_u$ potential curve crossing that of the $^3\Sigma_u^-$ in two places, on the right limb at $v' = 4$, and on the left limb at $v' = 12$ (see Figure 6.21).

Carroll (1958) re-examined some high resolution plates of the Schumann-Runge bands, and obtained a qualitative measure of the line broadening for some of the bands. Even allowing for blending of the triplet components increasing the apparent widths, instrumental broadening, and pressure broadening it was impossible to attribute the large widths in some cases to these factors alone. From close observations of micro-densitometer tracings, Carroll concludes that the 4-0 band is definitely predissociated, more strongly than either the 3-0 or the 5-0 bands, though these too, show broadening. He also concludes that Wilkinson and Mulliken's results must be modified, in that though the 12-0 band is predissociated, the 11-0 band is much more diffuse. Carroll

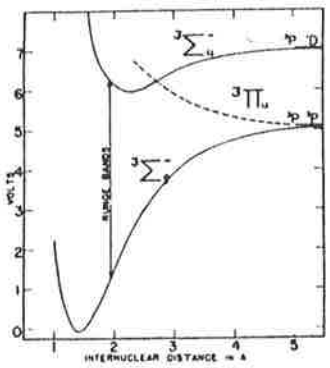

FIG 6.20 The curve crossing of the $^3\pi_u$ state with the $^3\Sigma_u^-$ state originally postulated by Flory to explain predissociation. (Reproduced from Flory (1935))

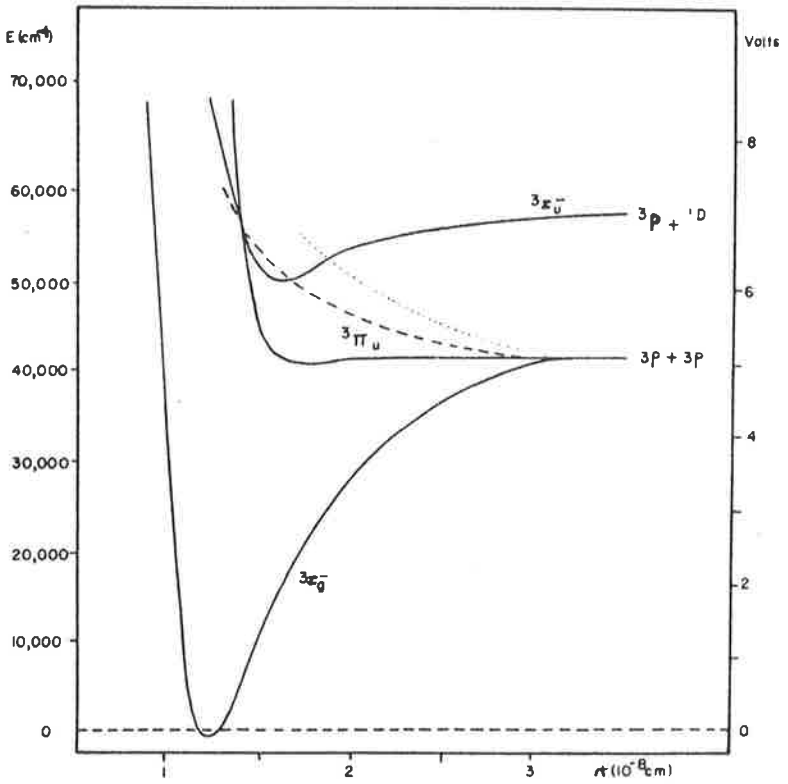

FIG 6.21 The curve crossing suggested by Wilkinson and Mulliken. They conclude the solid line shown crossing the $^3\Sigma_u^-$ state on the left limb is the cause of the predissociation. (Reproduced from Wilkinson and Mulliken (1956))

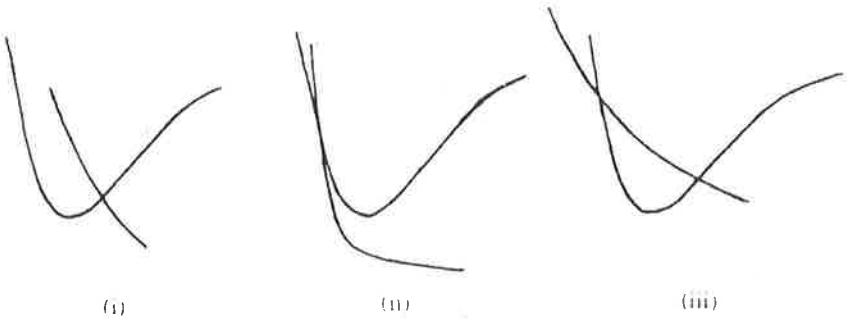

FIG 6.22 The three types of possible curve crossing suggested by Murrell and Taylor (1968) (Reproduced from their paper).

lists the bands with associated broadening as follows. The 11-0 band is more diffuse than the 12-0 ; the 10-0 is more diffuse than the 12-0 but less than 11-0 ; the 9-0 is slightly diffuse, approximately the same as the 12-0 ; the 8-0 is more diffuse than 9-0 ; but less than the 4-0 . There seem to be two maxima in the broadening process, one at 4-0, and the other at 11-0 . Carroll is undecided as to whether this implies two predissociations, and thus two curve crossings, or whether it can be explained by one crossing point at $v' = 4$, with the subsidiary maximum at $v' = 11$ and the minimum at $v' = 9$ corresponding to varying overlap integrals between the $^3\pi_u$, $^3\Sigma_u^-$ states which are obtained using the Franck-Condon principle. If two predissociations are present, Carroll suggests that one of the other repulsive states, perhaps the $^1\pi_u$, $^5\Sigma_u^-$ or $^5\pi_u$ could be the cause, crossing the curve near $v' = 11$. He suggests the most likely possibility is that of one potential curve crossing point, on the inner limb of the $^3\Sigma_u^-$, as suggested by Wilkinson and Mulliken, but with v' changed from $v' = 12$ to $v' = 4$. Murrell and Taylor (1968) showed that predissociation probabilities could be explained by a single crossing at $v' = 4$, with several subsidiary maxima above this. They give an expression for the repulsive curve, and discuss the different possible types of crossings. Their calculations show that the $^3\Sigma_u^- - {}^3\pi_u$ crossing in O_2 is of the type (i) in Figure 6.22.

Hudson and Carter (1969) confirmed the predissociation of the $B^3\Sigma_u^-$ state for $v' = 3$ to $v' = 17$. They noted a definite increase in line width of the 3-0 band compared to the 2-0 band, but did not rule out the possibility of predissociation in the 2-0 band. They suggested the intersection of the $^3\pi_u$ and $B^3\Sigma_u^-$ states could be between $v' = 2$ and $v' = 3$ rather than between $v' = 3$ and $v' = 4$.

Ackerman and Biaume (1970) as well as measuring line positions, also observed apparent line half-widths appearing on the spectra, and their results are compared with the predictions of Murrell and Taylor in Figure 6.23. Ackerman, Biaume and Kockarts (1970) obtained line-width values, and these are listed in Table 6.1 for comparison with later experimenters. They conclude that the line shapes and widths in the Schumann-Runge bands can only be explained by predissociation. Schaeffer and Miller (1971) perform some theoretical calculations, and conclude that the $^3\pi_u$ state crosses the $^3\Sigma_u^-$ state on the inner limb, and that the $^1\pi_u$ crosses too low to be the second state in question. They do not rule out the possibility that the $^5\pi_u$ or $^5\Sigma_u^-$ states may cross near $v' = 4$.

The most complete papers on predissociation in the Schumann-Runge bands of O_2 are those by Julienne and Krauss (1975) and Julienne (1976). Julienne and Krauss deduced the position of the dominant repulsive curve by a deperturbation of the level shift in the second vibrational difference. Their use of ab initio results combined with information contained in available experimental data, allowed them to calculate level shifts and linewidths for each repulsive state. They stated that the level shift provides better contact between theory and experiment than linewidths, which were not available to enough accuracy. They decided that the dominant state in the predissociation was the $^5\pi_u$ state, although the $^1\pi_u$ and $^3\pi_u$ states contribute slightly as well. Their predictions of linewidths agreed well with experimental data for $v' = 2$ to $v' = 4$, and for $v' \geqslant 12$ (since the spin splitting of the rotational lines is resolvable here), but agreement for $v' = 5$ to $v' = 11$ was poor. Their results are shown in Figure 6.25. Also shown in Figure 6.24 are the deduced crossing points for the potential curves. They conclude the levels $v' = 0$ and $v' = 1$,

ACKERMAN AND BIAUME

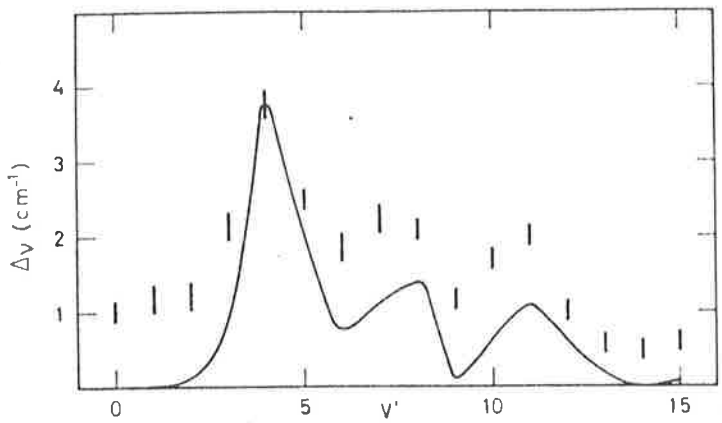

Apparent line half-width $\Delta\nu$ (cm^{-1}) versus vibrational quantum number (v') of the upper state: (----), the theoretical values given by Murrell and Taylor (*13*), normalized at $v' = 4$

FIG 6.23 The linewidth measurements of Ackerman and Biaume (1970) compared to the theoretical predictions of Murrell and Taylor (1968). (Reproduced from Ackerman and Biaume (1970))

JULIENNE AND KRAUSS

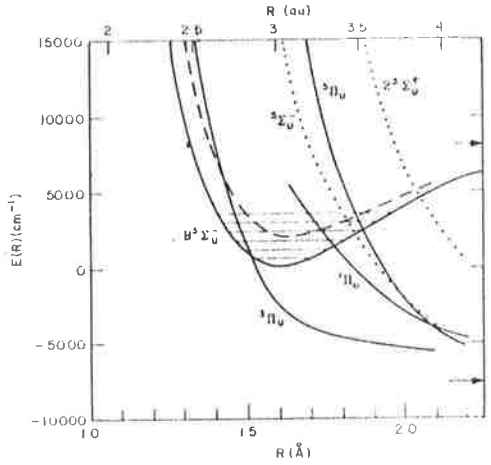

FIG 6.24 Curve crossings deduced by Julienne and Krauss (1975) to explain the predissociation linewidths. The results of the present work basically support the above scheme.

(Reproduced from Julienne and Krauss (1975))

and to a lesser extent $v' = 2$ are predissociated by the $^1\pi_u$ state, but that the dominating predissociation of the $^5\pi_u$ state causes the linewidths to rise rapidly for $v' = 2$ to 4 . Here, their theory and experiment agree well. The levels $v' = 12$ to 16 also give good agreement between theory and experiment, showing that the $^5\pi_u$ state predissociation is substantially correct. The $^1\pi_u$ and $^3\pi_u$ states also contribute to the linewidths above $v' \geqslant 12$, the $^3\pi_u$ state being more important.

$^3\Sigma_u^- - {}^3\pi_u$ coupling should produce different widths for the three different triplet components. The lack of agreement between the theoretical and experimental linewidths for $v' = 5$ to $v' = 11$ resulted in a theoretical paper by Julienne (1976). He took account of the interaction of the $2^3\Sigma_u^+$ state, which contributes to the widths of $v' \geqslant 6$ levels. Julienne also examined whether it was possible for the line-shapes to be non-Lorentzian, and concluded that slight departures could occur for low J lines ($J \leqslant 3$) near band origins, but that P and R triplets could adequately be represented by non-interfering Lorentzian profiles. The variation of width with J-value only affects the F_1 and F_3 levels, and is strongest for the low J values, and also depends upon which states are interacting. He concludes that the J-variation is quite complex, since there are several sources of possible variation. Each of the four states $^5\pi_u$, $^3\Sigma_u^+$, $^3\pi_u$ and $^1\pi_u$ contribute to the width, and the total width is simply the sum of the various contributions. Julienne's results are also plotted in Figure 6.25.

6.8 The Present Results

The results of the present work confirm that the rotational lines in the Schumann-Runge bands are predissociation broadened. The maximum of

TABLE 6.3

Band	Ackerman & Biaume	Hudson & Mahle	Ackerman *et al*	Julienne & Krauss	Julienne	This Work
0-0	1-0	0.001	1.00	0.1	0.06	-
1-0	1.2	0.002	1.10	0.39	0.45	0.07 ± 0.006*
2-0	1.2	0.34	1.20	0.25	0.27	0.50 ± 0.013
3-0	2.15	1.25	2.20	1.26	1.30	1.12 ± 0.03
4-0	3.8	3.30	3.70	3.00	2.93	2.95 ± 0.10
5-0	2.5	2.20	2.30	1.19	1.33	1.87 ± 0.05
6-0	1.85	1.70	1.90	1.12	1.80	1.57 ± 0.04
7-0	2.2	2.25	2.20	0.74	1.90	1.51 ± 0.04
8-0	2.1	2.21	2.00	1.26	1.59	1.28 ± 0.02
9-0	1.2	0.72	1.10	0.32	0.89	0.55 ± 0.013
10-0	1.7	0.34	1.70	0.49	0.67	0.58 ± 0.012
11-0	2.0	1.80	1.70	0.88	1.30	0.77 ± 0.016
12-0	1.0	0.48	1.00	0.49	0.70	0.54 ± 0.014
13-0	0.55	0.08	0.60	0.14	0.20	0.10 ± 0.003
14-0	0.5	0.06	0.50	0.07	0.20	0.068 ± 0.003
15-0	0.6	0.20	0.50	0.13	0.29	0.13 ± 0.004
16-0		0.25	0.50	0.18	0.29	0.14 ± 0.014
17-0		0.40	0.50			0.42 ± 0.06
18-0		0.40	0.50			0.20 ± 0.043
19-0		0.40	0.50			
20-0						

A Comparison of the previous experimental results for rotational linewidths with those of this work.

* The error quoted is a statistical error. A more realistic error would be ± 0.05. (see Section 5.8)

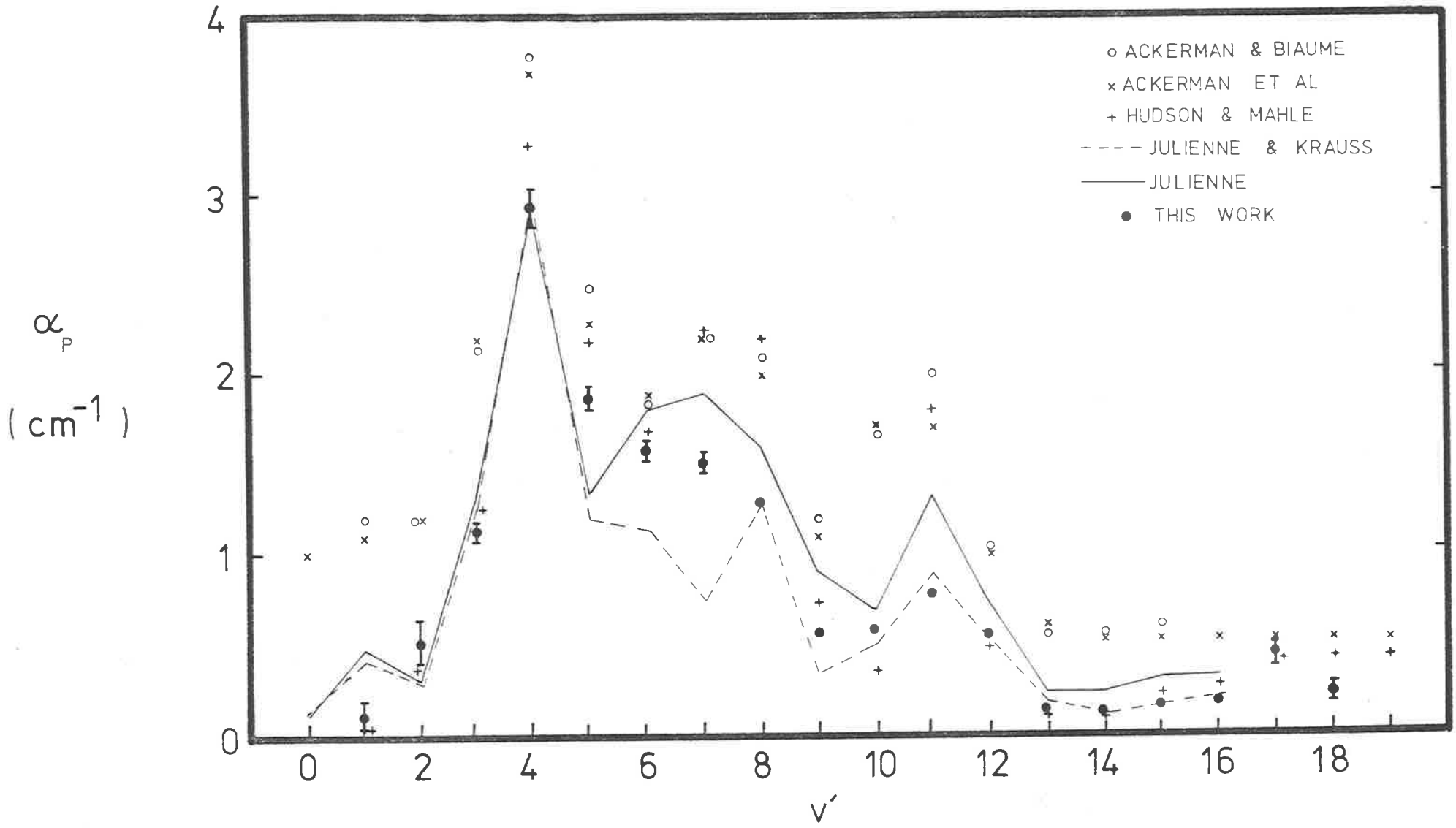

FIG 6.25 Predissociation linewidths in cm^{-1} versus vibrational number for the 1-0 to 18-0 bands of this work, compared to those of previous experimenters, and to theoretical predictions.

this predissociation broadening occurs at $v' = 4$ with a subsidiary maximum at $v' = 11$, and a minimum at $v' = 9$. Some predissociation may occur for the 1-0 band, the non-Doppler component of the linewidth being comparable to the pressure-broadened width, thus making an exact evaluation of the width due to only predissociation very difficult. For all bands above the 1-0, predissociation definitely occurs, though in varying amounts. The individual linewidth results are listed in Appendix 11, while the band average linewidths are listed in Table 6.3.

Variations in predissociation linewidths along a vibrational band occurred, but the variation was less than the error in most cases, so no attempt has been made to plot the variation in line-width with rotational number.

6.9 Comparison with Previous Experimental Work

The present results are compared with the results given by Ackerman and Biaume (1970), Hudson and Mahle (1972) and Ackerman et al (1970) in Table 6.3 and Figure 6.25. The results of this work are consistently less than those obtained by the other experimenters, and are more closely in agreement with those of Hudson and Mahle in the range 1-0 to 18-0 than with those of Ackerman et al (1970) or Ackerman and Biaume (the exception being the 7-0, 8-0 and 11-0 bands). The reason for this appears to be that Ackerman and Biaume have listed apparent half-widths, and have thus not taken any effects due to instrument resolution and triplet splitting into account. Similarly, Ackerman et al have obtained linewidths which are based on those obtained previously by Ackerman and Biaume (1970), but which have been modified by comparison with absorption coefficients measured at the wavelengths of narrow silicon emission lines. Their results obtained in this way are not markedly different from

those of Ackerman and Biaume (1970). Failure to take instrument resolution into account may explain why the linewidths so obtained are too large in comparison to both Hudson and Mahle's results, and the results of the present work, and why the apparent linewidths obtained for the 14-0 to 18-0 bands are all 0.5 cm , a width comparable to the instrument resolution.

6.10 Comparison with Theoretical Predictions

The theoretical predictions of Julienne and Krauss (1975) and the more recent work of Julienne (1976) are compared with the present results in Figure 6.25. Overall agreement in the range 1-0 to 18-0 is quite good for both theoretical works in comparison to the present results, the positions of maxima and minima in linewidths corresponding closely. Agreement with Julienne and Krauss is closer over the range 8-0 to 16-0, while agreement with Julienne is better over the range 5-0 to 7-0 . The two theoretical works differ because the interaction of the $^3\Sigma_u^+$ state with the $B^3\Sigma_u^-$ state is taken into account in the latter work. This has meant an increase in the theoretically predicted widths in the range 5-0 to 11-0 , the region where the discrepancy between the previous theoretical papers was largest.

The present result for the 1-0 band linewidth due to predissociation is very uncertain, but both the previous experimental measurements of Ackerman et al and the theoretical predictions of Julienne appear to be too large. The value obtained by Hudson and Mahle for the 1-0 linewidth is quite low, as is that of the present work.

6.11 Conclusions

The theoretical predictions of Julienne and Krauss (1975) and Julienne (1976) based on the deperturbation of the second vibrational differences appear to be basically correct. The addition of the $2^3\Sigma_u^+$ interaction had improved agreement between the present experimental results and the theoretical predictions in the range 5-0 to 7-0 , but has made the agreement worse in the range 8-0 to 16-0 , by increasing the theoretically predicted widths there slightly. So the predictions of Julienne and Krauss are correct, and although some of the $2^3\Sigma_u^+ - B^3\Sigma_u^-$ interaction discussed must be added in, a better agreement could be obtained if the interaction was weaker than predicted by Julienne.

The good agreement between this work and the predictions of Julienne and Krauss suggests that their analysis is correct, and that the curve crossings of the various molecular state shown in Figure 6.24 are fairly accurate. The exception may be that the intersection point of the $^3\pi_u$ state on the left-hand side of the $^3\Sigma_g^-$ state be moved upwards to a position above the 1st vibrational level, in order to reduce the predissociation there.

CHAPTER 7

RESULTS — LYMAN-α REGION

7.1 Measurement of Experimental Quantities

The measurement of temperature, wavelength and pressure for the O_2 Lyman-α absorption coefficients was identical to the procedure for the Schumann-Runge bands described in Chapter 5 (Section 5.1). One major difference between the experimental cases was the much greater care required to purify the oxygen before entry into the absorption cell for the Lyman-α work. Because the cross-section of water vapour at Lyman-α is so high compared to that for molecular oxygen (1.4×10^{-17} cm^2 as compared to 10^{-20} cm^2 for oxygen), even a small amount of water vapour impurity will greatly affect the results. For this reason, additional vapour traps were used. The medical grade oxygen was first passed through two test tubes containing drying agents, and then through two test tubes immersed in a cold slush mixture of carbon tetra-chloride and chloroform, to condense out the water vapour impurity. The absorption cell was also pumped continuously, when not in use, to remove impurities adhering to the walls. Any exposure to the air for maintenance purposes meant a few days continuous pumping of the cell to clean off surface impurities.

The Lyman-α line emitted by the laboratory discharge source consists of a doublet, due to self absorption by hydrogen removing the central core of the emission line. The wavelengths of the peaks and minimum are known to a high degree of accuracy, and the wavelength calibration was checked against the minimum in the Lyman-α line at 1215.67Å. The absolute errors for the wavelengths quoted in this chapter are less than 0.06Å.

The pressures used for the measurements varied between 0.2 and 30 Torr, giving pressure errors of approximately 1% or less. Since the cross-section is a smoothly varying one, the scan procedures used in the

case of the Schumann-Runge bands were not used here. The chosen wavelength was selected, the pressure stabilized at the desired value, and a number of measurements of transmission τ were made, again using

$$\tau = \gamma/\gamma_o$$

where γ is the monitor detector signal ratio at the pressure of the measurement, and γ_o is the signal ratio at zero pressure. We have

$$\tau = \gamma/\gamma_o = \exp\left(-\frac{P}{760} kx \frac{273}{T}\right)$$

or $$k = \ell n\,(\gamma/\gamma_o)\,\frac{1}{x}\,\frac{760}{P}\,\frac{T}{273} = \ell n\,(\gamma/\gamma_o)\,1/X$$

where k is the absorption coefficient, x is the actual path length, P is the pressure in torr. T is the temperature in $^\circ K$, and X is the path length normalised to S.T.P. The measurement of transmission τ at various values of pressure allowed the calculation of the pressure dependence of the cross-section. Transmission measurements were repeated at wavelength intervals of 0.2Å, and also at temperatures of $294^\circ K$ and $82^\circ K$ using respectively room temperature, a dry ice-methanol slush and liquid air in the cell coolant jacket.

7.2 The Statistical Error in Transmission

The error in the absorption coefficient is related to the error in transmission, $\delta\tau$, and can be expressed as

$$(\delta k)^2 = \left(\frac{\partial k}{\partial X}\right)^2 \delta X^2 + \left(\frac{\partial k}{\partial \tau}\right)^2 \delta\tau^2 \qquad (7.1)$$

where δk is the error in the absorption coefficient, δX is the error in the path length, and $\frac{\partial k}{\partial X}$ and $\frac{\partial k}{\partial \tau}$ are the rates of change of absorption coefficient k with path length and transmission respectively. Equation 7.1 becomes

$$(\delta k)^2 = (\ell n\ \tau)^2 \left(\frac{\delta X}{X}\right)^2 + \left(\frac{1}{X}\right)^2 \left(\frac{\delta\tau}{\tau}\right)^2 \qquad (7.2)$$

and, since $\frac{\delta X}{X}$ is very small, this term can be neglected. The above equation can be written as

$$\delta k = \frac{1}{X} \frac{\delta\tau}{\tau} \qquad (7.3)$$

where $\frac{\delta\tau}{\tau} = \sqrt{\frac{1 + \gamma_o}{M_o\ \gamma_o} + \frac{1 + \gamma}{M\gamma}}$

is obtained from equation 5.17. The relative error $\frac{\delta k}{k}$ can be written as

$$\left|\frac{\delta k}{k}\right| = \frac{1}{X} \sqrt{\frac{1 + \gamma_o}{M_o\ \gamma_o} + \frac{1 + \gamma}{M\gamma}} \cdot \frac{X}{\ell n\tau} \qquad (7.4)$$

Setting $M = M_o$, that is putting the number of counts used for γ and γ_o equal to each other, equation 7.4 becomes

$$\left|\frac{\delta k}{k}\right| = \left|\frac{1}{\sqrt{M_o}} \sqrt{2 + \left(\frac{1 + \tau}{\gamma_o \tau}\right)} \cdot \frac{1}{\ell n\tau}\right|. \qquad (7.5)$$

A plot of the above is shown in Figure 7.1 for fixed M_o for various values of γ_o as τ is varied. The minimum error in the value of

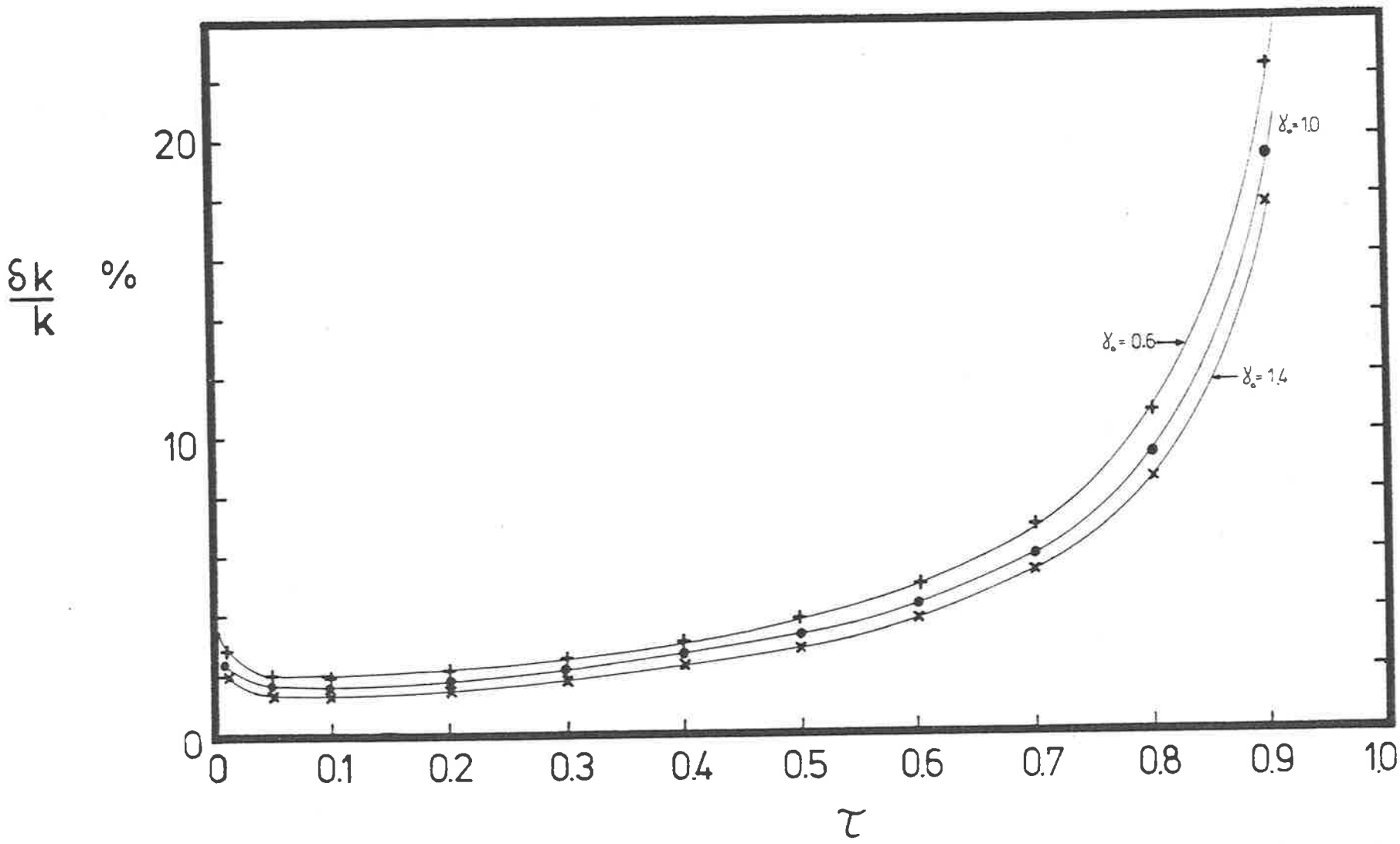

FIG. 7.1 A plot of the relative error in absorption coefficient $\delta k/k$ versus transmission τ for three different values of γ_0 .

absorption coefficient k for fixed counting time and fixed γ_o occurs for transmission values near $\tau = 0.1$. This meant the experiment would have achieved optimum performance if this condition could have been met. It was not always possible however, due to the fixed cell-length, and the limitations of the Baratron gauge used for the experiment restricting the pressure to 30 torr or below. Most of the measurements carried out were done with transmission values of close to 0.5 , and the error does not vary markedly for values of τ below this.

7.3 The Previous Experimental Work

The absorption coefficient of molecular oxygen at Lyman-α is important for two main reasons. Since Lyman-α is one of the most intense emission lines in the solar spectrum, it has an important role to play in dissociation processes in the atmosphere, in particular the dissociation of molecular oxygen in the height range 75-105 km, to form atomic oxygen. Accurate measurements of the absorption coefficient are therefore necessary to determine to what height significant amounts of Lyman-α radiation will penetrate. Many measurements of the molecular oxygen density in the atmosphere have been made by observing the absorption of solar Lyman-α as it passes down through the atmosphere. A discrepancy between these measurements and those made by other techniques indicated that the laboratory derived absorption coefficients were in error, and it was in an attempt to resolve these discrepancies that the present measurements were taken.

The first laboratory measurements of the absorption cross-section of molecular oxygen at Lyman-α were made by Watanabe (1958) and Metzger and Cook (1963), and they obtained 0.27 and 0.28 cm^{-1} respectively at $\lambda = 1215.7$Å. Watanabe obtained a number of other values at nearby wave-

lengths, and his results are in good agreement with the present work. Watanabe also obtained a measure of the pressure dependence of the absorption coefficient at Lyman-α. Ogawa (1968) obtained values of the absorption coefficient at 0.2Å intervals near 1215.7Å , and attempted to measure the pressure dependence of the coefficient, but due to the low pressures used in his experiment was unable to find a measurable pressure dependence. However, the more recent results of Dose et al (1975) and Ogawa and Yamawaki (1970) confirm the pressure dependence of the absorption coefficient. These laboratory measurements have been used to analyse the extinction of Lyman-α radiation in the atmosphere.

Early rocket measurements, such as those of Carver et al (1964), were all analysed by assuming a constant cross-section for molecular oxygen, in particular the one obtained by Watanabe of 1.0×10^{-20} cm^{-2} (0.27 cm^{-1}). Hall (1972) showed that the variation in the molecular oxygen cross-section over the width of the Lyman-α line, which coincides with a deep minimum in the cross-section (see Figure 7.2), has a significant effect on the analysis of results of the rocket observations. Using the measurements of Ogawa (1968), he showed that there is some "hardening" of the radiation as it passes through the atmosphere, the lower wavelength limb being absorbed more strongly than the right limb, and consequently the effective absorption coefficient will be height dependent. Smith and Miller (1974) came to the conclusion that the laboratory derived absorption cross-section for molecular oxygen was either in error, or did not apply to atmospheric measurements because of a marked temperature dependence. They based this conclusion on the fact that the molecular oxygen densities derived from the Lyman-α extinction method were in disagreement with those made using three other independent techniques; grenades, falling sphere and Pitot tube, while these three methods were in agreement.

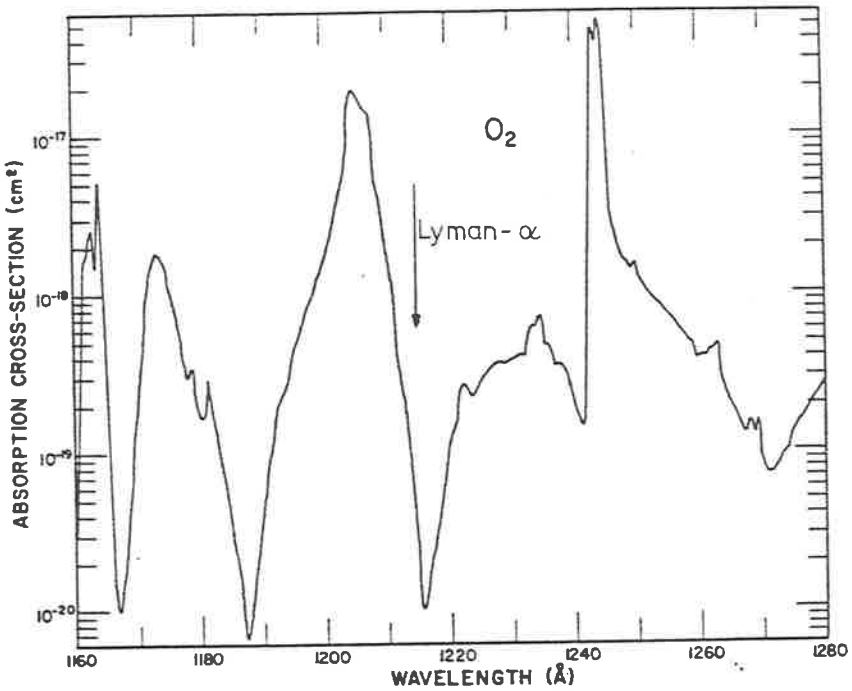

Fig 7.2 A plot of the absorption coefficient of O_2 versus wavelength, showing the deep minimum near Lyman-α (1215.7Å).

(reproduced from Watanabe 1958)

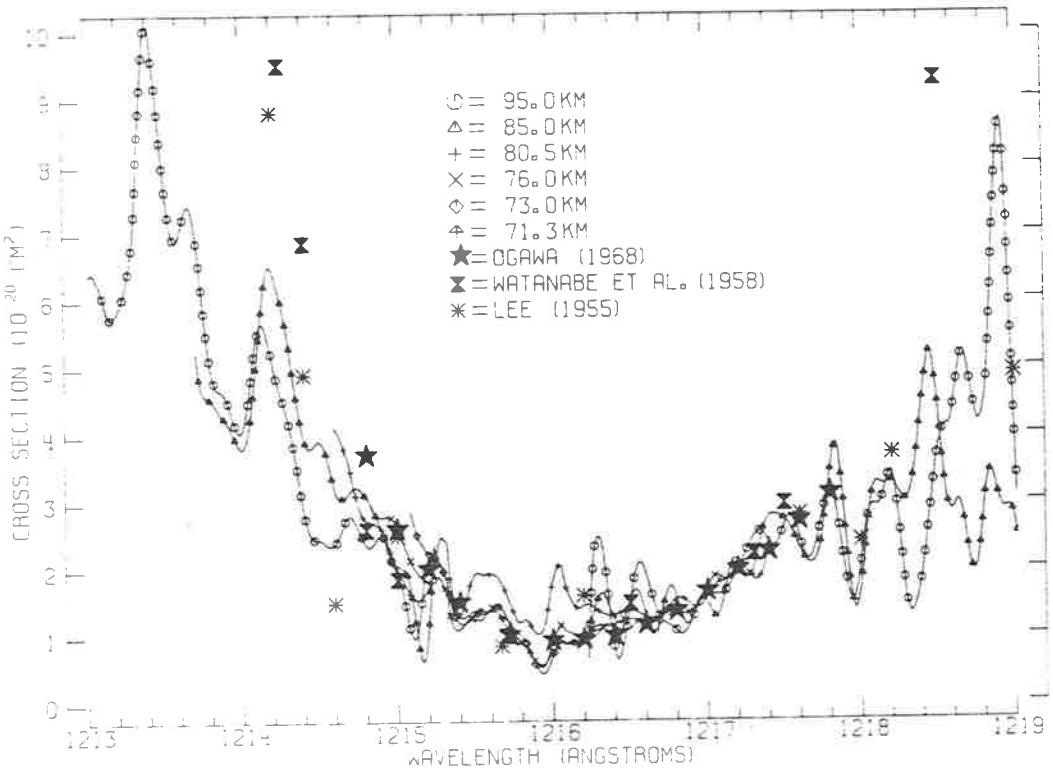

Fig 7.3 Cross-section measurements for O_2 near Lyman-α obtained by Prinz and Brueckner (1975), compared with Ogawa (1968), Watanabe (1958) and Lee (1955).

(reproduced from Prinz and Brueckner 1975)

Thrane and Johannessen (1974), with their measurements of the Lyman-α extinction in the Arctic mesosphere, also came to the conclusion that the laboratory derived measurements were inapplicable to atmospheric results. Weeks (1975) ascribed the major uncertainties in the extinction results to uncertainty in the behaviour of the O_2 cross-section with temperature, and to over-estimates of the densities due to absorption by nitric oxide and water vapour. Later work by Prinz and Brueckner (1977) obtained cross-section versus wavelength measurements from rocket observations, and had values agreeing well with Ogawa in the wavelength range 1215 - 1217.8Å , but they also had better agreement with the values of Watanabe on the short wavelength side of Lyman-α down to λ = 1214.4Å (see Figure 7.3).

7.4 Results and Discussion

7.4.1 Pressure Dependence

Watanabe (1958) and Ogawa and Yamawaki (1970) had obtained values for the pressure dependence of the cross-section of molecular oxygen at Lyman-α at high pressures (20-500 Torr) of about $+ 2 \times 10^{-23}$ cm^2/ torr. Values of this order would explain why Ogawa (1968) found no noticeable effect of pressure dependence in the pressure range he used for his experiment (1.2 - 6.3 torr), the differences being too slight to show through his experimental error. The present measurements, taken at room temperature, over the pressure range 5-30 torr, and at wavelengths of 1215.63Å and 1215.72Å corresponding to the peaks of the Lyman-α line emitted by the discharge lamp used in these experiments, are plotted in Figure 7.4. As shown in Table 7.1, these results are in satisfactory agreement with those of previous investigators, although their measurements were done at higher pressure. This indicates that the linear dependence of cross-section on pressure extends down to pressures of about 5 torr. The error bars on the points plotted decrease because a large part of the error for each point is a pressure error, which decreases as the pressure increases. There is no reason to believe that the pressure dependence is a strong function of wavelength near 1216Å, and the pressure dependence shown in Figure 7.4 has been used to correct all the measured room temperature cross-sections to zero pressure. Since 30 Torr was the maximum pressure used, these corrections were never more than 5%, and over most of the range were less than 2%. The uncertainties in making a correction to zero pressure make a negligible contribution to the overall error. There is a small absolute error of approximately 2% due to uncertainties in the

TABLE 7.1

PRESSURE DEPENDENCE OF MOLECULAR OXYGEN PHOTO-ABSORPTION CROSS SECTIONS NEAR LYMAN-α.

Investigator	$\frac{d\sigma}{dP}$ x10^{23} (cm^2/torr)	Wavelength (Å)	Pressure Range (torr)
This work	2.14 ± 0.33	1215.72	5 - 30
This work	2.15 ± 0.37	1215.63	5 - 30
Ogawa and Yamawaki [1970]	1.60 1.56	1215.72 1215.63	10 - 200 10 - 200
Dose et al. [1975]	2.5 ± 1.5 3.0 ± 0.8	1215.73 1215.70	
Watanabe et al. [1958]	1.9	1215.7	20 - 500
Shardanand [1967]	1.7	1215.7	25 - 400

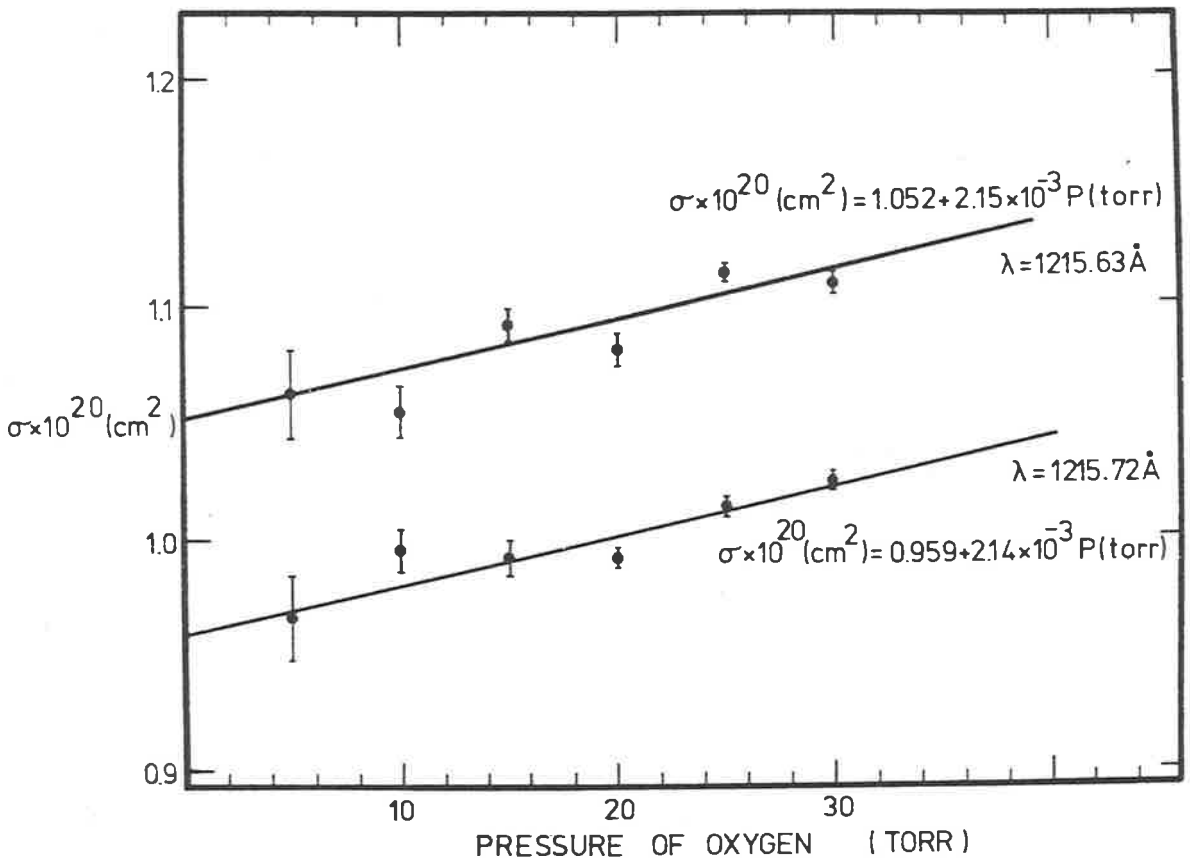

Fig 7.4 Pressure dependence of room temperature molecular oxygen photoabsorption cross-sections measured at 1215.63 and 1215.72Å.

measurement of cell temperature, cell length and pressure. Random error in the results is due predominantly to counting statistics of 1-3%.

7.4.2 Temperature Dependence

Room temperature cross-sections measured in this work are displayed in Figure 7.5 versus wavelength at 0.2A intervals, and the values are given in Table 7.2. The previous measurements of Watanabe (1958), Ogawa (1968) and Dose et al (1975) are also shown in Figure 7.5, and as can be seen, all the results are in good agreement near the minimum in the absorption cross-section at 1216.0Å . At shorter wavelengths, the present results lie significantly below those of Ogawa, and the measurements of Watanabe, though more widely separated, are in better agreement with the present ones. The present results also lie below those of Ogawa on the long wavelength side of the minimum, and the results of Dose et al (1975) above 1218Å have been calculated from their analytical curve, and are also above those of this work.

Figure 7.6 shows the variation of the absorption cross-sections with temperature in the wavelength range 1214.0 to 1218.6Å . Each set of points represents a variation with wavelength at one of the experimental temperatures 294 °K, 195 °K or 82 °K. The temperature dependence is significant, and varies with wavelength, the greatest dependence being on the long wavelength side of the minimum, which includes high-order rotational lines (J=25 to 33) of the $\alpha\,{}^1\Sigma_u^+ - X\,{}^3\Sigma_g^-$ band of molecular oxygen [Ogawa and Yamawaki (1969), Alberti et al (1967) and Dose et al (1957)]. The minimum of the absorption cross-section at 294 °K is at 1216.0Å, but has shifted to 1216.4Å at 82 °K, while at the same time decreasing to 60% of its room temperature value. The Lyman-α profile

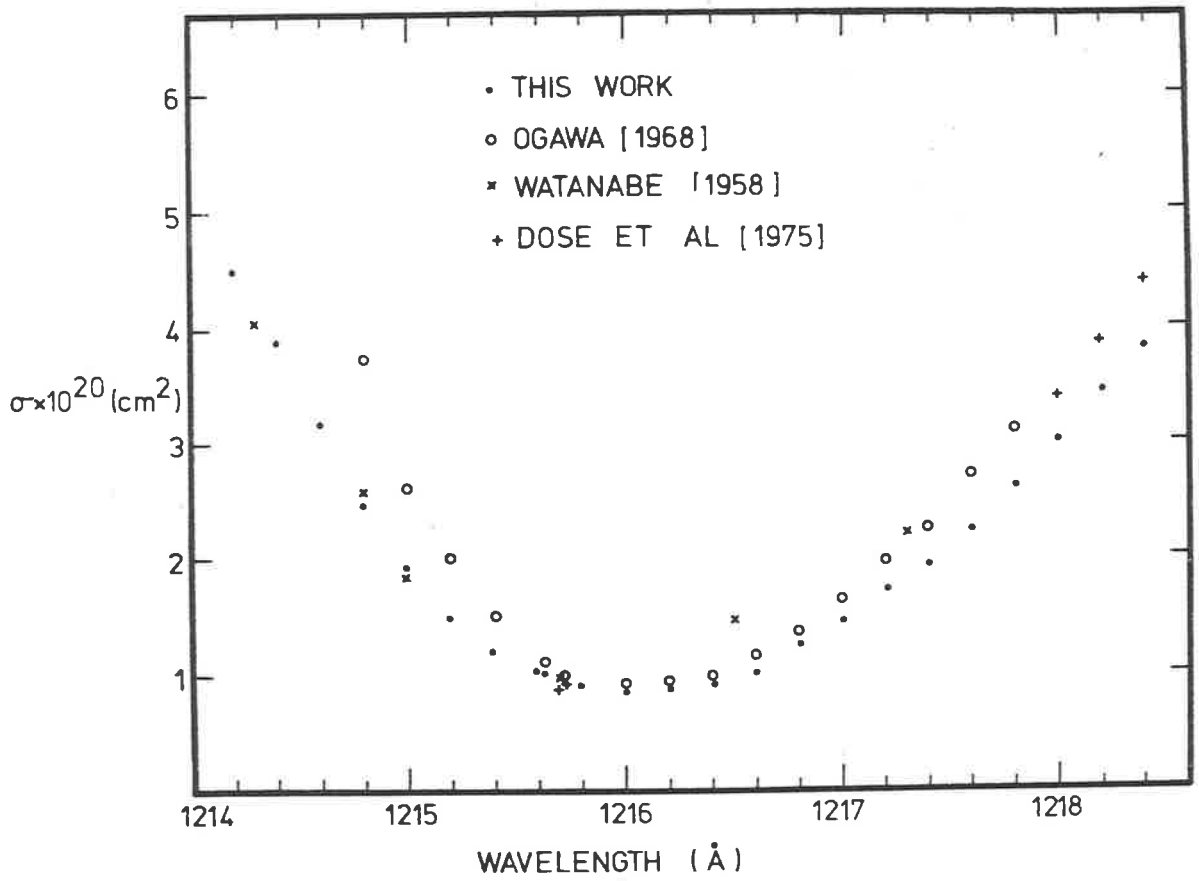

Fig 7.5 Comparison of the present room temperature results with other measurements of the molecular oxygen photoabsorption cross-section in the Lyman-α window region.

TABLE 7.2

MEASURED MOLECULAR OXYGEN PHOTOABSORPTION COEFFICIENTS AS A FUNCTION OF TEMPERATURE AND WAVELENGTH NEAR LYMAN-α.

The errors listed are statistical errors; there is an additional error of ± 2% in the absolute calibration arising from uncertainties in pressure, temperature and cell length.

Wavelength (Å)	$\sigma x10^{20}$ (cm^2), T=294°K	$\sigma x10^{20}$ (cm^2), T=195°K	$\sigma x10^{20}$ (cm^2), T=82°K
1214.0	5.58 ± 0.11	5.69 ± 0.15	5.50 ± 0.15
1214.2	4.50 ± 0.11	4.57 ± 0.15	4.76 ± 0.11
1214.4	3.90 ± 0.11	3.83 ± 0.07	3.64 ± 0.07
1214.6	3.19 ± 0.07	3.27 ± 0.07	3.23 ± 0.07
1214.8	2.49 ± 0.04	2.60 ± 0.07	2.53 ± 0.07
1215.0	1.96 ± 0.03	2.08 ± 0.07	1.82 ± 0.04
1215.2	1.50 ± 0.04	1.42 ± 0.05	1.35 ± 0.03
1215.4	1.22 ± 0.02	1.25 ± 0.03	1.06 ± 0.03
1215.6	1.06 ± 0.02	0.92 ± 0.03	0.90 ± 0.03
1215.63	1.052± 0.011		
1215.72	0.959± 0.007		
1215.8	0.933± 0.015	0.78 ± 0.04	0.73 ± 0.03
1216.0	0.877± 0.007	0.66 ± 0.03	0.67 ± 0.02
1216.2	0.900± 0.015	0.68 ± 0.04	0.56 ± 0.03
1216.4	0.929± 0.015	0.79 ± 0.03	0.53 ± 0.03
1216.6	1.02 ± 0.02	0.77 ± 0.05	0.60 ± 0.03
1216.8	1.28 ± 0.02	0.96 ± 0.04	0.67 ± 0.03
1217.0	1.46 ± 0.02	1.08 ± 0.05	0.82 ± 0.03
1217.2	1.74 ± 0.02	1.37 ± 0.04	0.96 ± 0.04
1217.4	1.94 ± 0.05	1.64 ± 0.06	1.17 ± 0.07
1217.6	2.24 ± 0.04	1.90 ± 0.05	1.43 ± 0.07
1217.8	2.62 ± 0.05	2.20 ± 0.06	1.51 ± 0.07
1218.0	3.03 ± 0.02	2.44 ± 0.10	1.90 ± 0.04
1218.2	3.46 ± 0.11	2.83 ± 0.11	2.38 ± 0.05
1218.4	3.83 ± 0.11	3.16 ± 0.07	2.79 ± 0.07
1218.6	4.35 ± 0.07	3.72 ± 0.07	3.31 ± 0.07

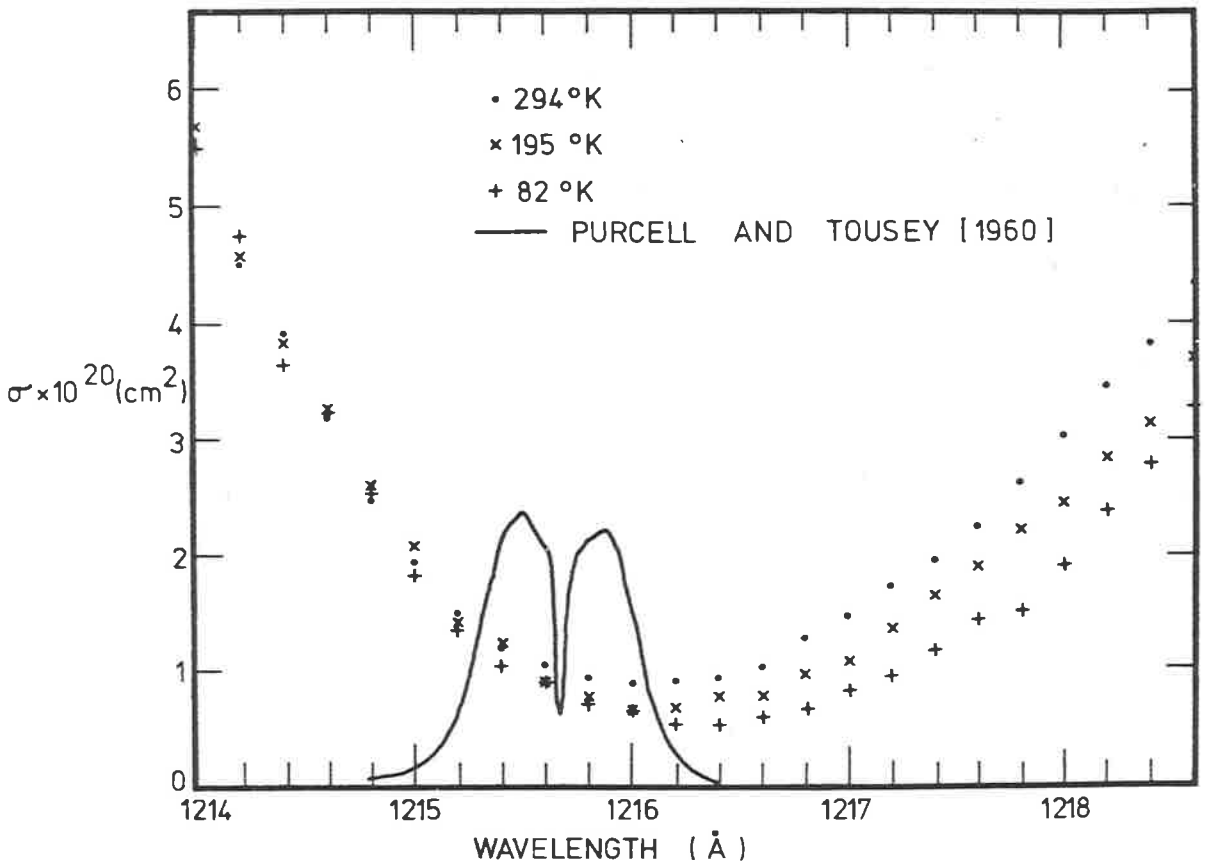

Fig 7.6 Molecular oxygen photoabsorption cross-sections near Lyman-α as functions of wavelength and temperature. The solar Lyman-α profile observed by Purcell and Tousey (1960) is also shown.

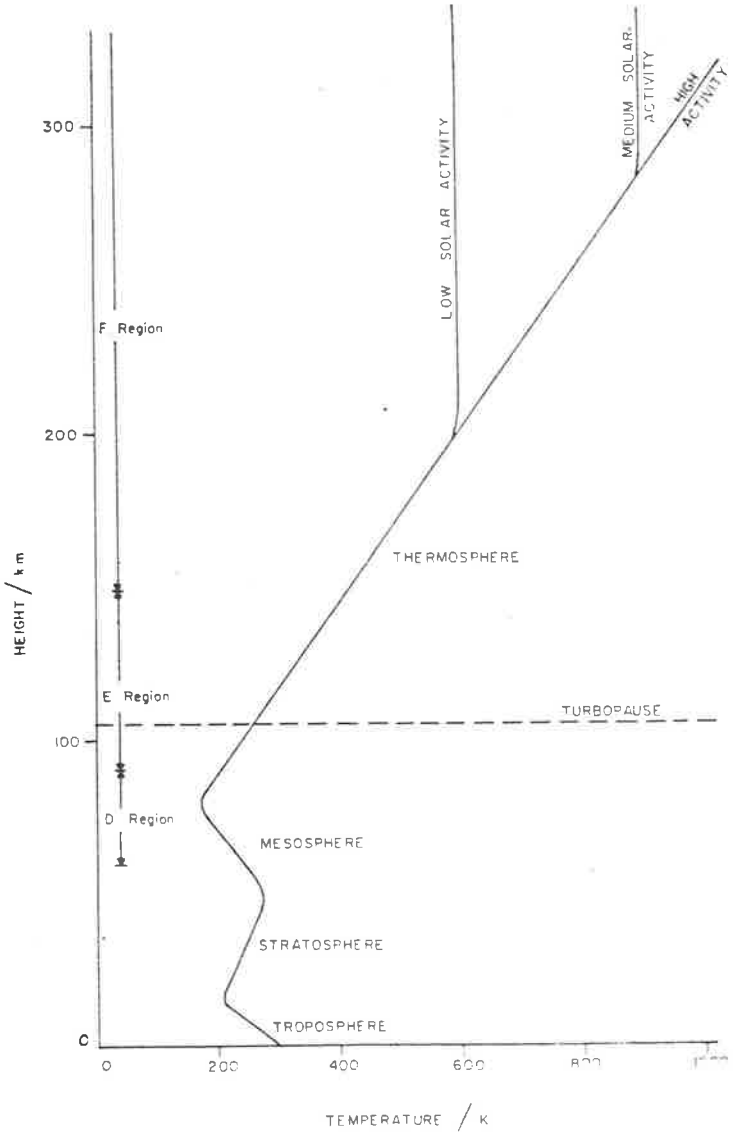

Fig 7.7(a) A plot of altitude versus temperature for the atmosphere.

(reproduced from Beer 1976)

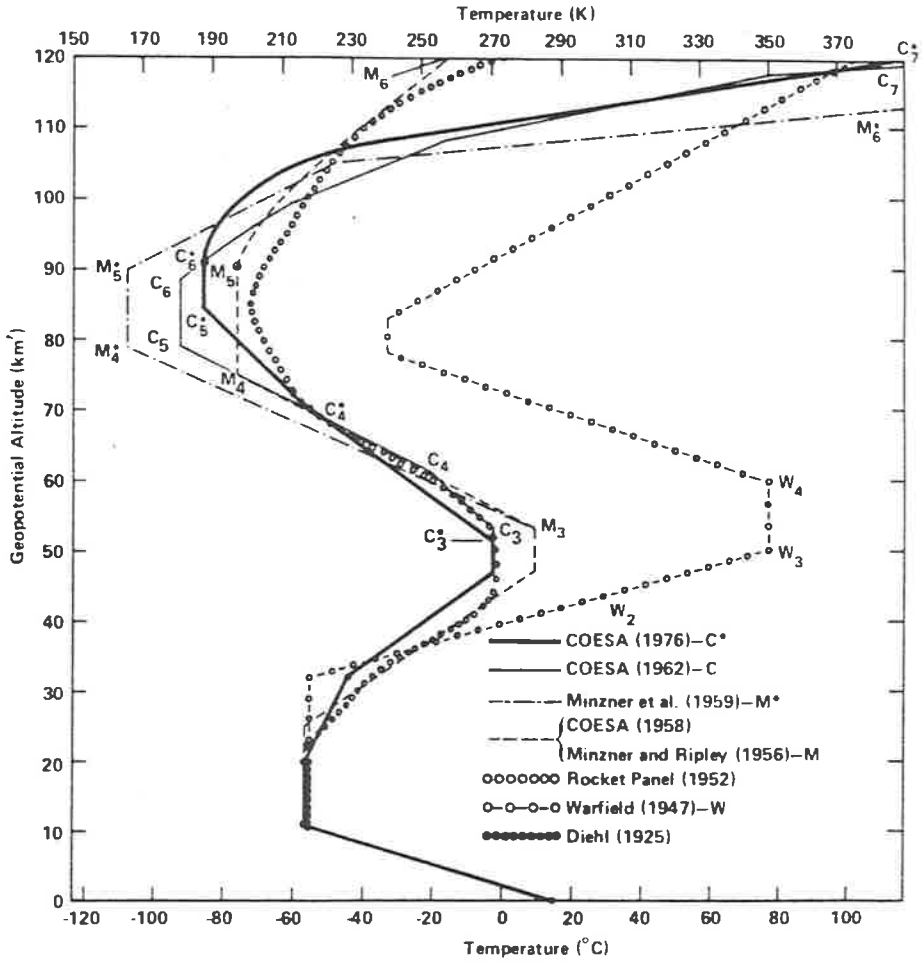

Fig 7.7(b) A plot of altitude versus temperature for the atmosphere below 120 km.

(reproduced from Minzner 1977)

in Figure 7.5 is based on the work of Purcell and Tousey (1960).

7.5 Absorption of Solar Lyman-α Radiation in the Atmosphere

Figure 7.5 clearly shows that the molecular oxygen absorption cross-section varies significantly over the width of the Lyman-α profile. The exact amount of this variation will depend upon the temperature. The temperature of the atmosphere varies with height (see Figure 7.7), so laboratory measurements at room temperature can be expected to yield incorrect results, when applied to the atmosphere. The following calculation illustrates the importance of taking the temperature dependence into account, for example, the case of a rocket probe carrying a Lyman-α detector. Some assumptions necessary for the calculation are that the detector has a flat response over the width of the Lyman-α line, that the detector has a negligible response to radiation of other wavelengths (not always a safe assumption), and that absorption by other species in the wavelength region is either negligible or correctable [Carver (1964), Hall (1972)]. Provided the solar zenith angle is not too large ($\chi \leqslant 75^\circ$), then the attenuation of the solar flux J over a height interval d is given by $\exp(- \bar{\sigma} n d \sec \chi)$ where $\bar{\sigma}$ is the effective absorption cross-section and n is the molecular oxygen number density. A knowledge of the detector current allows n at altitude z to be determined as follows

$$n(z) = \frac{1}{\sigma(z) \sec \chi} \frac{1}{J} \frac{dJ}{dz} \qquad (7.6)$$

The effective absorption cross-section at altitude z is given by

$$\bar{\sigma}(z) = \frac{\int \sigma(\lambda)\, \phi\, (\lambda, z)\, d\lambda}{\int \phi(\lambda, z)\, d\lambda} \qquad (7.7)$$

where $\sigma(\lambda)$ is the oxygen absorption cross-section at wavelength λ ,

ϕ (λ,z) is the Lyman-α flux at altitude z, and the integration extends over the full width of the Lyman-α line. If $N(z)$ is the total column density of oxygen molecules above altitude z, then

$$\phi\ (\lambda,\ z) \ = \ \phi\ (\lambda,\ \infty) \ \ \exp[\ -N(z)\ \sigma\ (\lambda)\ ] \qquad (7.8)$$

where $\phi\ (\lambda,\ \infty)$ is the solar flux at Lyman-α incident on the atmosphere. It should be noted that the shape of the Lyman-α line, $\phi\ (\lambda,\ z)$, changes as the radiation penetrates to lower altitudes z (the radiation "hardens") owing to the variation of $\sigma(\lambda)$ over the width of the line. $\bar{\sigma}(z)$ has been evaluated from (7.7) using the cross-section measurements of Table 7.2. The results are expressed versus the extinction $j(z)$, of the integrated Lyman-α flux, in the atmosphere, where

$$j(z) \ = \ \frac{J(z)}{J(\infty)} \ = \ \frac{\int \phi(\lambda,\ z)\ d\lambda}{\int \phi(\lambda,\infty)\ d\lambda} \qquad (7.9)$$

Figure 7.8 and Table 7.3 show effective molecular photoabsorption cross-sections $\bar{\sigma}(z)$ calculated as functions of the integrated Lyman-α extinction $j(z)$. These effective cross-sections have been calculated for atmospheric temperatures of 82, 195 and 294 °K, together with the solar Lyman-α profile of Purcell and Tousey (1960). To show that the calculated effective cross-sections are not very sensitive to the Lyman-α line profile used, the results using Quessette's profile (1970) are compared, and can be seen to be not very different from that of Purcell and Tousey (Figure 7.8). Also shown for comparison, is the effective molecular oxygen cross-section calculated using the Ogawa (1968) cross-section values, and these are identical to those derived by Hall (1972). Figure 7.8 shows the present results lead to effective cross-sections differing significantly from those based on Ogawa's room temperature measurements.

TABLE 7.3

EFFECTIVE MOLECULAR OXYGEN PHOTOABSORPTION CROSS SECTIONS $\overline{\sigma}(z)$ CALCULATED AS FUNCTIONS OF THE INTEGRATED LYMAN-α EXTINCTION j(z), FOR VARIOUS TEMPERATURES AND SOLAR LYMAN-α PROFILES.

j(z)	$\overline{\sigma}(z) \times 10^{20}$ (cm^2)			
	Solar Ly-α profile: *Purcell and Tousey* [1960]			*Quessette* [1970]
	T = 294°K	T = 195°K	T = 82°K	T = 195°K
1	1.10	0.99	0.91	1.04
0.9	1.09	0.98	0.91	1.02
0.8	1.08	0.96	0.90	1.00
0.7	1.08	0.95	0.89	0.99
0.6	1.07	0.94	0.88	0.97
0.5	1.06	0.93	0.87	0.95
0.4	1.06	0.91	0.85	0.92
0.3	1.05	0.89	0.84	0.90
0.2	1.03	0.86	0.82	0.86
0.1	1.01	0.83	0.79	0.82
0.05	1.00	0.80	0.77	0.79
0.01	0.97	0.76	0.72	0.74
0.001	0.95	0.72	0.69	0.71
0	0.88	0.66	0.53	0.66

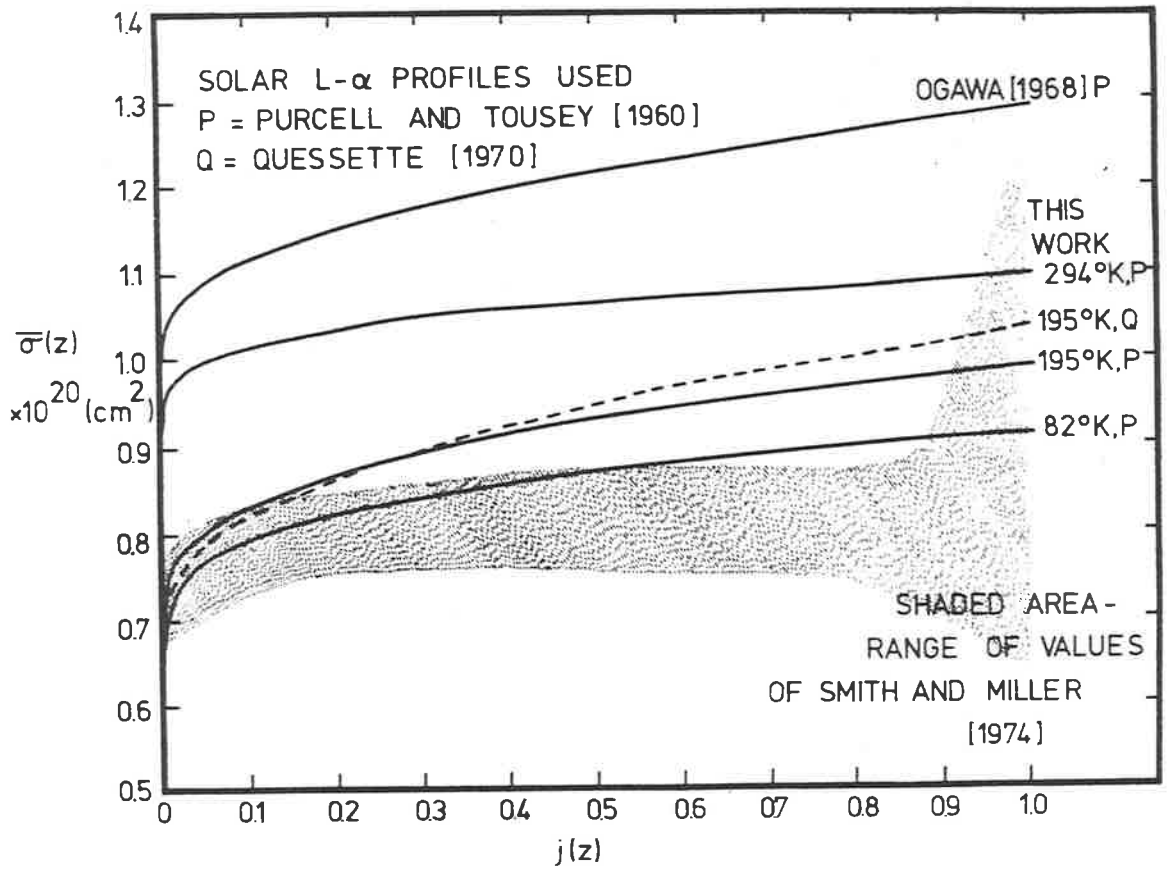

Fig 7.8 Effective molecular oxygen photoabsorption cross-section for the integrated solar Lyman-α line as functions of the integrated Lyman-α extinction. Effective cross-sections calculated by using the cross-sections measured by Ogawa (1968) are also shown for comparison.

The empirical effective cross-sections deduced by Smith and Miller (1974) in their attempt to bring their atmospheric molecular oxygen concentrations derived from the Lyman-α extinction measurements into agreement with those obtained using the other three techniques are also shown in Figure 7.7. The agreement between their range of values (the shaded area) and the effective cross-section derived using the present results and a temperature of 195 °K is quite reasonable, and is definitely better than between this work at 294 °K and Smith and Miller, or Ogawa's room temperature measurements, and Smith and Miller.

7.6 Conclusion

The conclusion to be drawn from these results is that the assumption of Smith and Miller that room temperature absorption cross-sections are inappropriate for application to atmospheric transmission problems is basically correct, since it resolves almost all of the discrepancy between the molecular oxygen densities derived by different methods. It is essential to take account of temperature and wavelength dependence of the molecular oxygen absorption cross-section if satisfactory oxygen densities are to be deduced from the Lyman-α extinction measurements by rockets in the atmosphere. The marked effect of temperature on the long wavelength side of the Lyman-α window seems to be due to the rotational lines known to be there, the populations of states of high rotational number depending critically upon temperature. Rotational lines of the $\alpha^1\Sigma_u^+ - X^3\Sigma_g^-$ system exist at wavelengths near Lyman-α, and while none were observed by this experiment below 1218Å, some of the lines above 1220Å were observed, due to their larger strengths. The rotational number varies between 21 and 33 between 1218Å and 1214Å, and so a temperature change would be expected to have a significant effect, since

levels with such high rotational numbers would be sparsely populated, and therefore subject to large variations with temperature. The variation in absorption cross-section with temperature decreased with decreasing wavelength, and this could be explained by a decrease in population of rotational levels as the temperature decreased.

CHAPTER 8

Application of the Results

8.1 Theoretical Absorption Models

Attempts to build theoretical models of absorption of incident solar radiation at different heights in the atmosphere in different wavelength regions require a knowledge of the real absorption behaviour of the gases under discussion. This is especially difficult for band structure, where the fine structure of the bands is not directly resolvable by the present measuring instruments, as is the case with the Schumann-Runge bands. The present results provide the most accurate measurements of parameters required in an analysis of transmission of light through these bands, and as such provide the 'real' absorptions and transmissions to which all simplified or approximate absorption models should tend.

Theoretical absorption models are basically necessary because of the breakdown of Beer's Law, due to structure present in the absorption coefficient over the wavelength range of interest (discussed more fully in Chapter 3). In order for Beer's Law to be valid over the range of the Schumann-Runge bands, a very narrow wavelength interval would be required, and therefore at least 10,000 data points are necessary at any given temperature to adequately describe these bands. To simplify the calculations, various band models have been devised. Some of the band models in Goody (1964) for the calculation of transmission in the infra-red region are useful, in that they provide a simple expression for the calculation of absorption or transmission as a function of the column density or optical depth.

Brinkman (1971), and Turco (1975) have calculated atmospheric photodissociation rates using the absorption cross-section measurements of Blake et al (1966) as well as the square root law associated with the absorption by the wings of a Lorentzian line. Blake et al (1966) showed that Beer's Law was not valid for the Schumann-Runge bands for wavelength intervals of 1 to 2Å , but that a square root law of the form

$$T = \exp(- C \sqrt{N}) \qquad (8.1)$$

where T is the transmission, and N is the number density of the absorbing species is a valid approximation.

Fang et al (1974) produced opacity distribution functions for various wavenumber ranges, with different sets of coefficients for different temperatures. Their method requires the numerical integration of the functions to obtain the transmission through an oxygen column. Several models have used constructions of detailed absorption cross-sections for the Schumann-Runge band region. The cross-section at any wavelength is computed by using the molecular constants to sum the contributions at that wavelength from all nearby absorption lines. A contribution due to the underlying continuum must also be added in. Using a resolution of 0.5 cm^{-1} , Kockarts (1971) has calculated photodissociation rates by integrating a theoretical cross-section.

Hudson and Mahle (1972) have calculated average transmissions for wavelength intervals between successive $v' - 0$ band heads. Kockarts (1976) has computed coefficients for the mean transmission as a function of absorber thickness for intervals covering a whole band, 500 cm^{-1} , and 10Å . The transmission for each interval is directly

described by a function with eight coefficients. Blake (1978) modified the random band model, and expresses the transmission versus optical path or number density as a function of $\beta = \bar{\delta}/2\pi d$, the ratio of line spacing to linewidth, and $X = \bar{S}/\bar{\delta}$, the mean line strength to average line spacing. That is, $\bar{T}$, the mean transmission is

$$\bar{T} = \exp\left(\frac{-XN}{\sqrt{1+BXN}}\right) \qquad (8.2)$$

and for $\beta << 1$ the above expression tends to Beer's Law, and for β large, it tends to equation 8.1.

In order to apply any of the theoretical models to the problems associated with the atmosphere, such as photodissociation rates of various molecular species or transmission of radiation versus height in the atmosphere, knowledge of the number densities of the numerous atmospheric gases is required. Chapter 7 has dealt with the problem of determination of O_2 number density by using Lyman-α absorption measurements. Most of the more recent models take some account of the temperature profile of the atmosphere for their calculations. Use of the models to give photodissociation rates, allows calculations on atmospheric photochemistry to be performed (see Blake and Carver (1977)).

8.2 Atmospheric Evolution : A Statement of the Problem

Knowledge of the photodissociation rates and photochemistry of the present atmosphere allows improved models of past atmospheres to be devised. It is generally accepted that the present atmosphere is a secondary atmosphere, and the earth's primary atmosphere consisting of the gases hydrogen, helium, neon, argon 36, krypton and xenon was completely lost. This is inferred from the deficiency of all these gaseous elements on earth relative to the cosmic abundances of these same elements. The

question of how the earth went from a state of no atmosphere to one consisting of nitrogen and oxygen is still very much under investigation.

The atmosphere and oceans were produced by discharge of volcanic gases over a long period of time. Amounts of various compounds and vapours produced by efflux from volcanoes have been measured from Hawaiian volcano eruptions. It is found that oxygen in its free state does not exist in volcanic gases. Leaving aside the problem of the growth of nitrogen in the earth's atmosphere, which is not as simple as the 1-38% amount present in volcanic effluent might suggest, we will concentrate on the growth in the amount of oxygen in the atmosphere. The transition from this primitive (anoxygenic) reducing atmosphere of volcanic gases to the present oxidizing atmosphere should be derivable from predictable sources and known reactions and with a definite timetable.

The origin of the oxygen in the atmosphere has been suggested as due to the photodissociation of water vapour by ultraviolet radiation. Berkner and Marshall (1965) were amongst the first to look into this problem.

The photodissociation of water vapour to produce oxygen is limited by the very oxygen it produces. This was first pointed out by Urey (1959), and is due to the shielding effect of the oxygen produced. That is, although incident radiation may at first dissociate the water vapour, once enough oxygen is produced it absorbs the radiation and no more water vapour is dissociated to form oxygen. The oxygen concentration possible by this method is therefore limited. Oxygen is distributed exponentially above the surface, while water vapour falls to very low concentrations above the base of the stratosphere due to the stratospheric cold trap. That is, the content of water vapour in the atmosphere is

limited to regions below the super-cooling temperature limit, -40 °C , which occurs at a height of approximately 10 kilometres. The content of water vapour above this diminishes rapidly and the stratospheric cold trap prevents significant convective circulation upwards above 10 kms. This means that the oxygen produced is mostly above the water vapour and thus can more effectively shield it.

Berkner and Marshall thus reach the conclusion that a concentration of oxygen in the primitive atmosphere greater than 10^{-3} P.A.L.* would be impossible due to the "Urey self-regulating effect". As well as this, strong photodissociation of O_2 and production of O and O_3 , which are very reactive, close to the surface where they will react quickly to form surface oxides, giving a large loss rate further reduces the O_2 level. Therefore water vapour dissociation cannot explain the oxygen level of the present atmosphere and was a minor factor in the past.

Berkner and Marshall then ask the question of whether it is possible for dissociation of water vapour to have supplied all the oxygen required to oxidize the surface layers of the earth. They draw the conclusion that the oxides of the crust could have been produced by active species of oxygen dissociated photochemically from H_2O in an oxygen atmosphere less than 10^{-3} of the present atmospheric level.

8.2.1 Photosynthesis

Berkner and Marshall then put forward the argument that oxygen in the atmosphere is due to photosynthesis. Photosynthesis seems to have begun about 2.7 billion years ago, and would be a feasible method of producing the large amounts of oxygen required, and of maintaining the oxygen balance. To give some idea of the rate at which oxygen can be produced by photosynthesis, the replacement times of various gases are as follows. Carbon dioxide is totally consumed and replaced in 300-400 years,

* Present Atmospheric Level.

oxygen in a little over 2000 years, and the entire waters of the ocean are passed through the biological process in about 2 million years. So photosynthesis can very quickly supply oxygen to the system.

Berkner and Marshall conclude that the oxygen density in the past atmosphere has been steadily rising, there being two sharp increases, called by them the first and second critical levels. These critical levels coincide with the Cambrian period, and the Upper Silurian period of geological time. The increase in oxygen density at these times was apparently due to the increase in the amount of space available for life, the oceans supposedly becoming a shielded habitat during the Cambrian period, and the land safe from damaging ultraviolet light during the Upper Silurian period.

A serious correction which must be applied, and one that has been overlooked by Berkner and Marshall is the dependence of the effective absorption coefficient on path length. This correction is very important for the Schumann-Runge bands, the individual rotational lines of which are much narrower than the instrumental resolution. These lines have natural (Lorentz) widths, and can be considered as purely Lorentzian when investigated with an instrumental resolution of about 2Å , as was the case with the results used by Berkner and Marshall. Under such conditions the "effective absorption coefficient" for a single line varies very nearly as the inverse square root of the number density N (equation 8.1). Blake et al (1966) have shown that in the vicinity of 1800Å the absorption coefficients within the Schumann-Runge bands obey the simple square root scaling law for a single line.

Brinkman (1969) does a calculation using the incident solar flux and calculates transmissions and absorptions versus wavelength. Since nearly every absorption by H_2O below 2000Å results in dissociation,

the curve for H_2O can be taken as the photodissociation rate. Appreciable water vapour dissociation occurs over a wide altitude range, and about half is produced by photons in the narrow wavelength range 1775-1830Å . CO_2 absorption occurs somewhat lower in the atmosphere and at longer wavelengths. Ozone absorbs most strongly at the longest wavelengths and quite low in the atmosphere.

Only the wavelength range 1750-2000Å has been considered because radiation of longer wavelengths does not dissociate water vapour and radiation of shorter wavelengths is absorbed by atomic and molecular oxygen and nitrogen before it can reach the H_2O . Even the intense Lyman-α line of the sun cannot penetrate into the atmosphere far enough, and is appreciably absorbed above 80 kilometres. To neglect the contribution to dissociation of Lyman-α will be to slightly underestimate the O_2 production rate by this method.

Brinkman concludes that the level of oxygen in the past may have reached an appreciable fraction of the present amount in the absence of biological activity, and quotes a value of O_2 density greater than 0.27 P.A.L. (present atmosphere level) over 99% of geologic time.

Two things which could have very major effects on the validity of the result are that the H_2O mixing ratio in the past may have been different, and the escape efficiency of hydrogen from the atmosphere is unknown. There is a net production of oxygen from H_2O only if the hydrogen can be removed. The mixing ratio could have been less than now if the "cold trap" temperature at the tropopause were lower.

As for the escape of hydrogen, the problem is largely unsolved. Knowledge of H_2O_2 , HO_2 and other such species is very poor, and the

reaction rates and mechanisms of the dissociation problem are complex. Brinkmann can only say that the possibility that a large fraction of the liberated H atoms survive long enough to escape cannot be ruled out. The escape rate is proportional to hydrogen density at the critical level (which occurs at about 500 kms. in the earth's atmosphere). The temperature at the critical level changes appreciably during the day. Clarification of the problem awaits reliable measurements of the hydrogen atom density.

Brinkmann concludes by saying that the calculations of Berkner and Marshall are in error because (1) they assume the photodissociation of H_2O becomes inefficient as an oxygen producing mechanism when the fraction of photons absorbed by O_2 becomes larger than the fraction absorbed by H_2O , and (2) they have not allowed for the path length dependence of the oxygen absorption coefficient.

8.2.2 The Problem of Hydrogen Loss

The present view of the problem of oxygen evolution is that neither Berkner and Marshall, nor Brinkmann are totally correct. While Brinkmann's work is an improvement on that of Berkner and Marshall, it too has its inconsistencies, the most obvious being that of the hydrogen escape factor. Brinkmann assumed that half of the hydrogen produced by the dissociation of water vapour escapes from the earth's atmosphere. This estimate is much too high, as it does not take into account the recombination of the hydrogen with other reactive species e.g.

$$H + OH \longrightarrow H_2O^* \qquad \text{or} \quad H_2 + O \longrightarrow H + OH \ .$$

Other reactions are also possible. It is only when hydrogen escapes from the atmosphere, and is therefore removed from the system, that there can

be a net production of oxygen. To escape from the atmosphere, most of the hydrogen must diffuse from a height of 30 kms, where it is formed to a height of about 500 kms, near the exobase from which it can escape. This diffusion process allows many opportunities to recombine and react with other species. Once the hydrogen reaches the critical level (the level where the mean free path equals the scale height) in the exosphere, escape is possible. A better estimate of the escape factor might be 1/10th or less.

Molecules or atoms can escape from the earth's atmosphere if their velocity component vertical to the earth's surface is greater than the escape velocity. Usually, atmospheric molecules collide with other molecules before they can escape. It is only in the exosphere where the collision frequency is low and the mean free path long that the possibility of escape becomes appreciable. The rate of loss of the species is determined by the velocity distribution, which is basically Maxwellian. Brinkmann (1971) proposed a modification to the Maxwellian distribution due to the depletion of the high energy tail, that is due to depletion of the faster atoms and the finite time required for collisions to replace the high energy component. He proposed the escape flux be multiplied by a factor of 0.73 to allow for the depletion. Most of the factors required in the calculation of the escape flux are well known, but two are difficult to determine. The number density of the escaping atoms at the exobase, and the temperature of the gas at the exobase are these critical quantities. The temperature term is very important since it occurs in the calculations as an exponential term. The exobase temperature is very variable, the range of possible values being 600 $^{\circ}$K - 2500 $^{\circ}$K . An average temperature of 1500 $^{\circ}$K is usually assumed.

Values of the escape flux have been obtained from observations of Lyman-α dayglow (Maier and Mange (1973)). Tinsley (1969) puts an upper limit on the hydrogen escape flux, an order of magnitude lower than that assigned by Brinkmann (1969). He (Tinsley) calculates that enough hydrogen could have been lost to give an amount of oxygen equivalent to 75% of the present atmosphere, in agreement with a calculation by Hunter and Strobel (1974) and Hunton (1973) who calculate a loss of hydrogen sufficient to give an amount of O_2 half that at present in the atmosphere.

Meadows (1972) reviews the stability of the earth's atmosphere, and compares the atmospheres of the Earth, Venus and Mars. He concludes that a consistent model of their evolution can be obtained on the basis of degassing from the solid planet. Ratner and Walker (1972) use a simple photochemical model to evaluate ozone densities in atmospheres similar to the present one, but containing less oxygen. They conclude that very little atmospheric oxygen (10^{-3} PAL) is required to produce a biologically effective ozone screen. Blake and Carver (1977) obtain results in agreement with Ratner and Walker.

The present view is therefore that while Berkner and Marshall's values are too low, Brinkmann's value is too high, and an intermediate value would be the most likely. Before the theories can be accepted with confidence, a number of quantities such as the hydrogen escape rate, accurate number densities of present atmospheric molecular species and better estimates of the amount of free oxygen in past atmospheres (from oxide layers of ancient rocks) are required.

8.3 Suggestions for Future Work

The present experimental system has enabled measurements of good accuracy to be made for oscillator strengths and linewidths in the Schumann-Runge bands of oxygen for the range of bands 3-0 to 15-0. In order to measure these quantities for the 0-0 to 2-0 bands, a much longer absorption cell is required, to circumvent the problem of pressure broadening encountered in this work. If the pressure in the present experimental system could be increased to 10 atmospheres or more, then enough absorption would take place to allow reliable measurements in these low bands, but the pressure broadened width would generally exceed the predicted predissociation width, and would thus effectively mask the required values. An increase in the length of the cell used would allow measurements to be made in a pressure range where pressure broadening was relatively unimportant.

A longer cell would also enable measurements of the Herzberg continuum to be made, and the effects of pressure and temperature on the absorption cross-section could be studied. Knowledge of these effects would give some insight into the mechanism responsible for the absorption (and allow a determination of whether O_4 dimers actually exist).

A shorter cell would enable pressure measurements to be made in the most sensitive region of the present pressure gauge, and thus allow more accurage measurements of oscillator strengths and linewidths for the bands 16-0 to 20-0 . Revised Hönl-London factors and splitting parameters must first be computed due to the perturbations in these bands, to enable the present programme to analyse the results.

A shorter cell would also allow measurements of the O_2 Schumann-Runge continuum cross-section, and the temperature dependence of these cross-sections. It is also proposed to investigate the oxygen absorption coefficients at various transmission windows between Lyman-α and the Schumann-Runge continuum, and to make high resolution studies of the structure in this region.

APPENDIX 1

The Independence of Equivalent Width with respect to Resolution

The equivalent width of an absorption line is given by

$$W = \int A(\lambda)\, d\lambda$$

where $A(\lambda)$ is the actual absorption at wavelength λ. The observed absorption at wavelength λ, $C(\lambda)$ is given by the convolution of $A(\lambda)$ with the instrument resolution function $g(\lambda)$, that is by

$$C(\lambda) = \frac{\int g(\lambda - \lambda')I(\lambda')A(\lambda')d\lambda'}{\int g(\lambda - \lambda')I(\lambda')d\lambda'} \qquad (1)$$

where $I(\lambda)$ is the intensity of the incident light at wavelength λ. If $I(\lambda)$ is a continuum, and therefore independent of wavelength, then equation 1 reduces to

$$C(\lambda) = \int g(\lambda - \lambda')A(\lambda')d\lambda'$$

The apparent observed equivalent width W' is given by

$$W' = \int C(\lambda)d\lambda$$

or

$$W' = \int \left(\int g(\lambda - \lambda')A(\lambda')\, d\lambda' \right) d\lambda \qquad (2)$$

Since it is true that

$$\int g(\lambda - \lambda')d\lambda = \int g(\lambda - \lambda')d\lambda' = 1.0$$

equation 2 reduces to

$$W' = \int A(\lambda')d\lambda' \int g(\lambda - \lambda')d\lambda$$

which reduces further to

$$W' = \int A(\lambda')d\lambda' = W$$

irrespective of $g(\lambda - \lambda')$.

APPENDIX 2

The Integrated Absorption Coefficient Under a Doppler Line

The area beneath the Doppler line shown below can be calculated as follows. The line profile is given by

$$k(\lambda) = k_p \exp\left(- \left(\frac{\lambda - \lambda_o}{\alpha_D} \right)^2 4\ln 2 \right) \qquad (3.7)$$

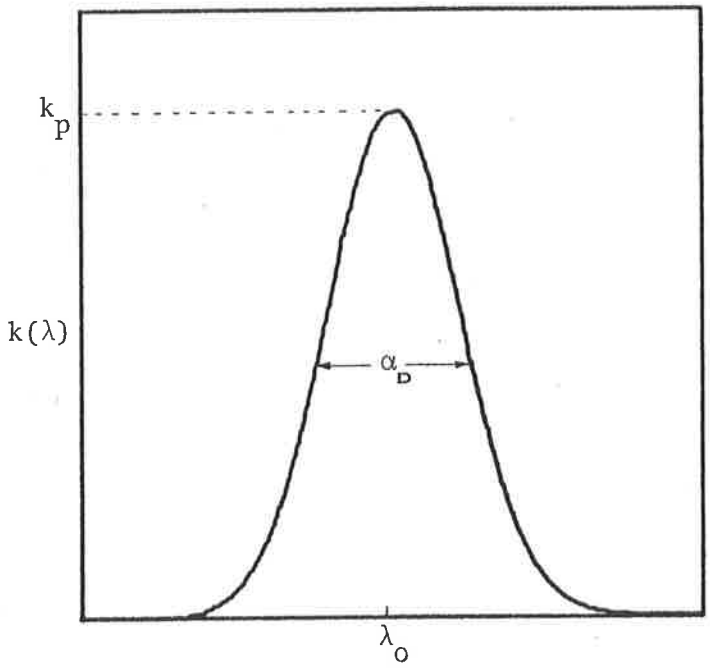

where $k(\lambda)$ is $k_p/2$ when $\lambda - \lambda_o = \alpha_D/2$, and α_D is the full width at half maximum. The error function erf(x), gives the relation

$$\int_{-\infty}^{\infty} e^{-t^2} dt = \sqrt{\pi} \qquad (5.34)$$

and putting $\frac{4\ln 2}{\alpha_D^2}(\lambda - \lambda_o)^2 = t^2$ into equation 5.34, it follows that

$$\int k(\lambda) d\lambda = k_p \int_{-\infty}^{\infty} \exp\left(- 4\ln 2 \left(\frac{\lambda - \lambda_o}{\alpha_D} \right)^2 \right) d\lambda$$

(the term $\int k(\lambda) d\lambda$ has been used repeatedly in the text as a convenient and simple way to describe a term which, if written in full, would be

$$\int_{-\infty}^{\infty} k(\lambda - \lambda_o) d(\lambda - \lambda_o) \quad) \; .$$

Now $\frac{4\ln 2}{\alpha_D^2}(\lambda - \lambda_o)^2 = t^2$ reduces to $\sqrt{\frac{4\ln 2}{\alpha_D^2}} = \frac{t}{(\lambda - \lambda_o)}$ and

differentiating both sides with respect to λ and t gives $d\lambda = \frac{dt}{\sqrt{4\ln 2/\alpha_D^2}}$

so $$\int_{-\infty}^{\infty} k_p \exp\left(-4\ln 2\left(\frac{\lambda - \lambda_o}{\alpha_D}\right)^2\right) d\lambda = \int_{-\infty}^{\infty} k_p \sqrt{\frac{\alpha_D^2}{4\ln 2}}\, e^{-t^2} dt$$

or $$\int k(\lambda)d\lambda = \frac{k_p\, \alpha_D \sqrt{\pi}}{2\sqrt{\ln 2}}$$ (using equation 5.34).

APPENDIX 3

The Integrated Absorption Coefficient Under a Lorentz Line

The area beneath the Lorentz line shown below can be calculated as follows. The line profile is given by

$$k(\lambda) = k_p \frac{1}{1 + \left(\frac{\lambda - \lambda_o}{\alpha_N/2} \right)^2} \qquad (3.8)$$

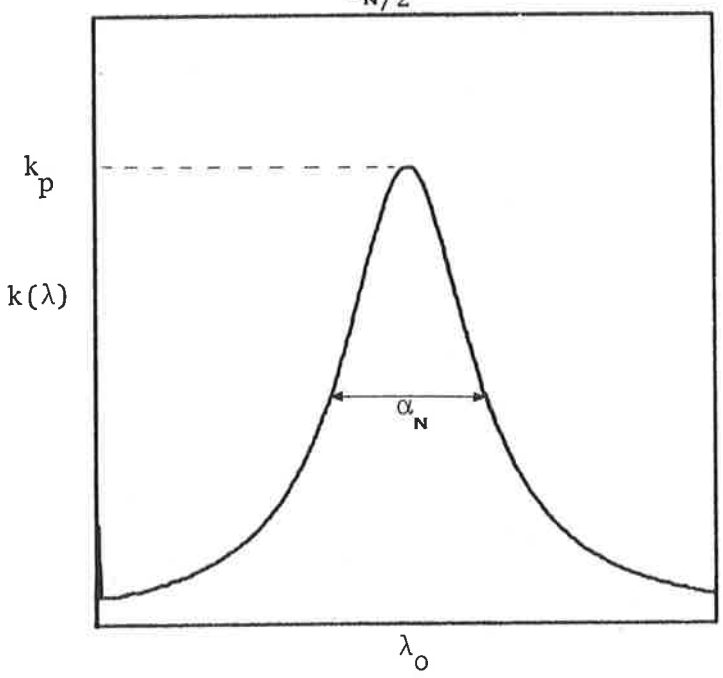

where $\lambda - \lambda_o = \alpha_N/2$ sets $k(\lambda) = k_p/2$, and α_N is full width at half maximum. A well known integral is

$$\int_{-\infty}^{\infty} \frac{1}{1 + x^2} dx = \arctan x \Big]_{-\infty}^{\infty} = \pi$$

and using the substitution $x^2 = \left(\frac{\lambda - \lambda_o}{\alpha_N/2} \right)^2$ and $\frac{\alpha_N}{2} dx = d\lambda$ (obtained by differentiating $x^2 = \left(\frac{\lambda - \lambda_o}{\alpha_N/2} \right)^2$), in equation 3.8, and integrating we get

$$\int_{-\infty}^{\infty} k_p \frac{1}{1 + \left(\frac{\lambda - \lambda_o}{\alpha_N/2} \right)^2} d\lambda = \int_{-\infty}^{\infty} k_p \frac{1}{1 + x^2} \frac{\alpha_N}{2} dx$$

$$\int k(\lambda) d\lambda = k_p \frac{\alpha_N}{2} \pi$$

APPENDIX 4

The Voigt Profile

The Voigt profile, given by equation 3.32 is

$$k(\lambda) = k_o \frac{a}{\pi} \int_{-\infty}^{\infty} \frac{\exp(-x^2)}{a^2 + (v-x)^2} dx$$

where $v = 2\left(\frac{\lambda - \lambda_0}{\alpha_N}\right)\sqrt{\ln 2}$, and represents the true line profile of an absorption line undergoing a Doppler broadening and a Lorentz broadening simultaneously. It has the disadvantage that each point on the line profile requires an integration to obtain the profile value. To speed up computing time, the second approximation of Whiting (1968) is used. Tables of the Voigt profile are given by Posener (1959), and a comparison of the Voigt profile k_v and that of Whiting is shown in Figure 1.

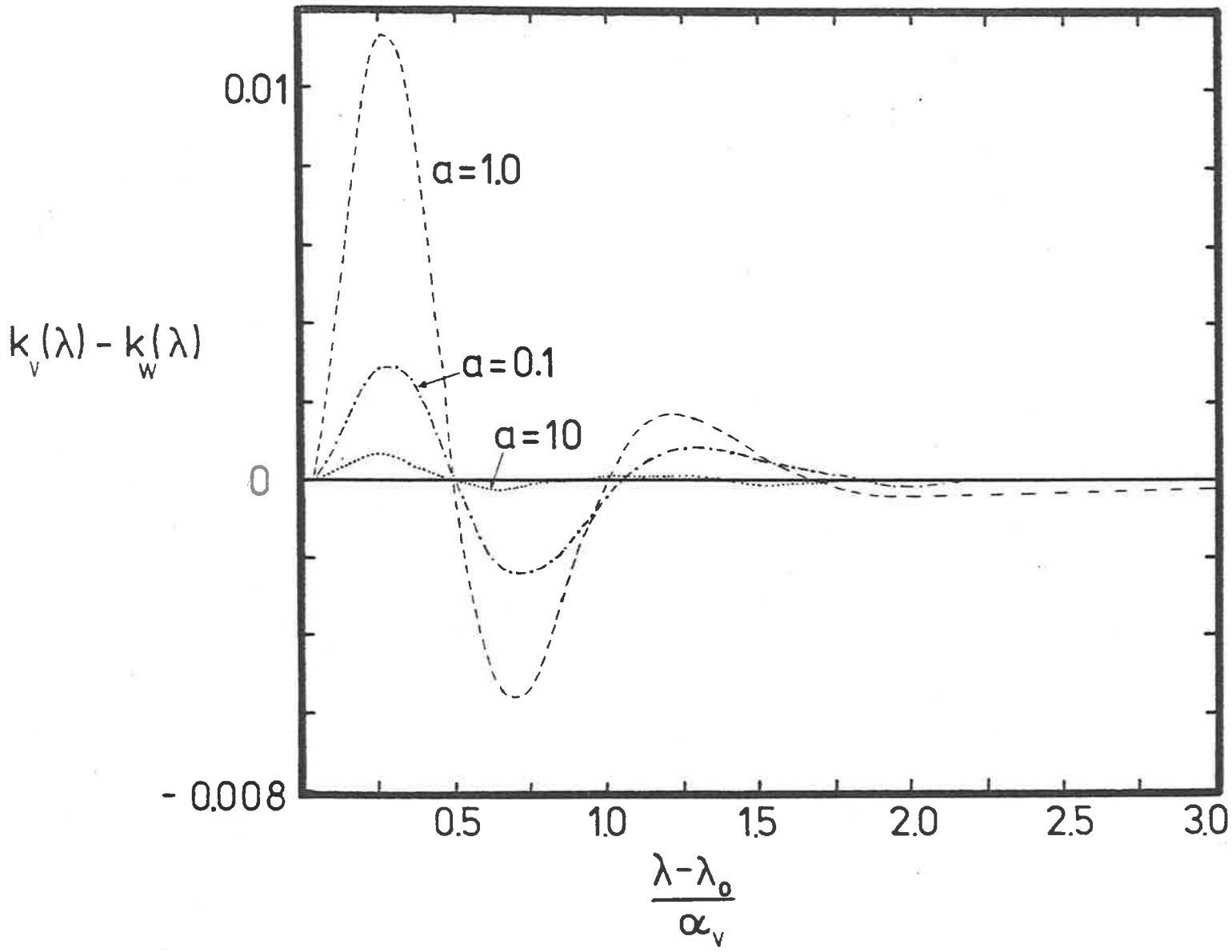

FIG 1 A plot of the difference between the Voigt line profile k_v and the line profile given by Whiting's second approximation as a function of distance from the line centre for three different a-values.

APPENDIX 5

Whiting's 2nd Approximation to the Voigt Profile

In considering line profiles, Whiting's 2nd approximation to the Voigt profile can be seen to consist of a weighted combination of Doppler and Lorentz profiles with the addition of a correction term, which improves accuracy in comparison to the 1st approximation markedly. The general applicability of Whiting's 2nd approximation, and the low errors involved in its use, make it a very useful tool in the calculation of absorption coefficient line profiles. Its associated errors are plotted in Figures 1 - 4 .

The basic line shape is given by

$$(1 - \frac{\alpha_L}{\alpha_V}) \exp(- 2.772(\frac{\lambda - \lambda_O}{\alpha_V})^2) + \frac{\alpha_L}{\alpha_V} \frac{1}{1 + 4(\frac{\lambda - \lambda_O}{\alpha_V})^2)}$$

and this reduces to the Doppler case for $\alpha_L = 0$ and to the Lorentz case for $\alpha_L = \alpha_V$. The correction term

$$0.016(\frac{\alpha_L}{\alpha_V})(1 - \frac{\alpha_L}{\alpha_V}) (\exp(- 0.4(\frac{\lambda - \lambda_O}{\alpha_V})^{2.25} - \frac{10}{10 + (\frac{\lambda - \lambda_O}{\alpha_V})^{2.25}})$$

follows the difference between the Voigt profile and the 1st approximation of Whiting, and its inclusion reduces errors by a factor of about 10. The expression for k_p is

$$k_p = \frac{\int k(\lambda)\, d\lambda}{\alpha_V(1.065 + 0.447 \frac{\alpha_L}{\alpha_V} + 0.058(\frac{\alpha_L}{\alpha_V})^2)}$$

and is used to correct the area. For a pure Doppler line of width $\alpha_D = 1.0$

$$\int k(\lambda)\, d\lambda = k_p \alpha_D \sqrt{\pi} / 2\sqrt{\ln 2} = 1.065 \quad \text{if} \quad k_p = 1.0$$

For a Lorentz line

$$\int k(\lambda)\, d\lambda = k_p \frac{\alpha_D \pi}{2} = 1.5708 \quad \text{if} \quad \alpha_L = 1.0 \text{ and } k_p = 1.0 .$$

If any meaningful treatment of absorption and curves of growth is to be made, then all lines compared must have the same area, so the function

$$1.065 + 0.447 \frac{\alpha_L}{\alpha_V} + 0.058 \left(\frac{\alpha_L}{\alpha_V} \right)^2$$

is used. It is basically a polynomial fitted to the area beneath an absorption line, and for $\alpha_L = 0$, the Doppler case, takes the value 1.065, while for $\alpha_L = \alpha_V$, the Lorentz case, takes the value $\pi/2 = 1.5708$ (see Figure 6). The approximation to the Voigt profile can also be written as a function of a, using the relations

$$a = \frac{\alpha_L}{\alpha_D} \sqrt{\ln 2}$$

$$\beta = 1 + \left(1 + \frac{4 \ln 2}{a^2} \right)^{\frac{1}{2}}$$

$$\frac{\alpha_L}{\alpha_V} = 2/\beta$$

That is, the approximation can be written as

$$k(\lambda) = k_p (1 - 2/\beta) \exp\left(-2.772 \frac{\varepsilon^2}{a^2 \beta^2} \right) + 2/\beta \left(\frac{1}{1 + 4 \left(\frac{\varepsilon^2}{a^2 \beta^2} \right)} \right) + E$$

where E is the correction term, and $\frac{\lambda - \lambda_0}{\alpha_V} = \frac{\varepsilon}{a\beta}$.

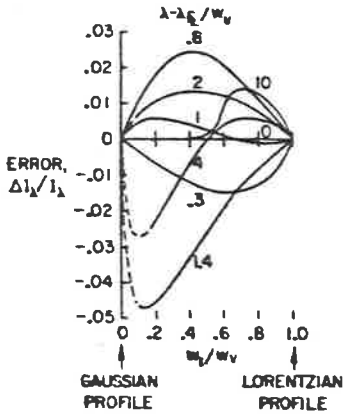

Accuracy of second approximation to Voigt profile.

FIG 1 (Reproduced from Whiting (1968))

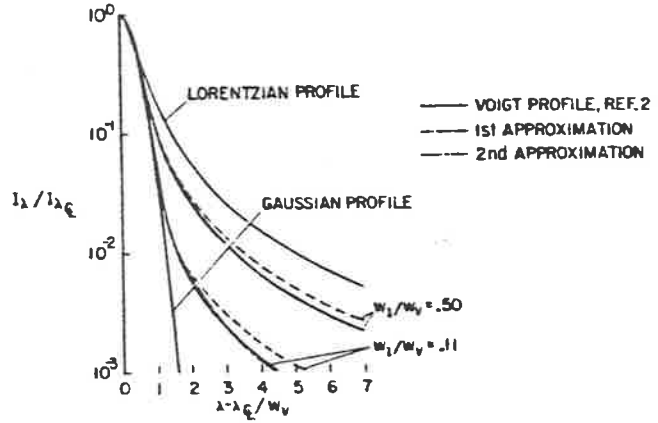

Comparison of first and second approximations to exact Voigt profile from Ref. 2.

FIG 2 (Reproduced from Whiting (1968))

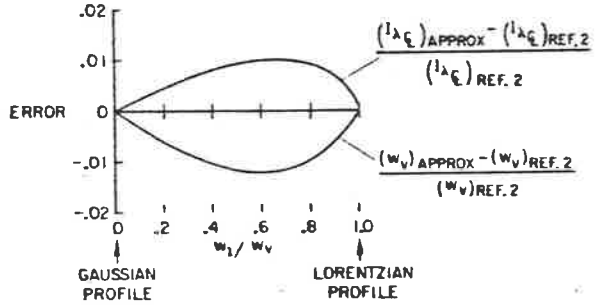

Accuracy of approximations for line width at half-height and intensity at line center.

FIG 3 (Reproduced from Whiting (1968))

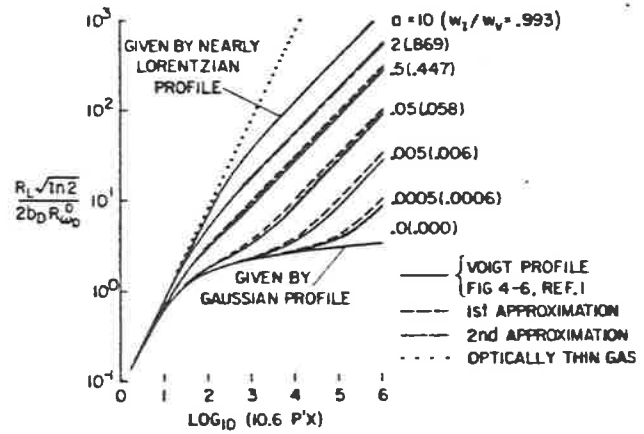

Comparison of curves-of-growth computed from first and second approximations with those computed from exact Voigt profile. (Notation from Ref. 1.)

FIG 4 (Reproduced from Whiting (1968))

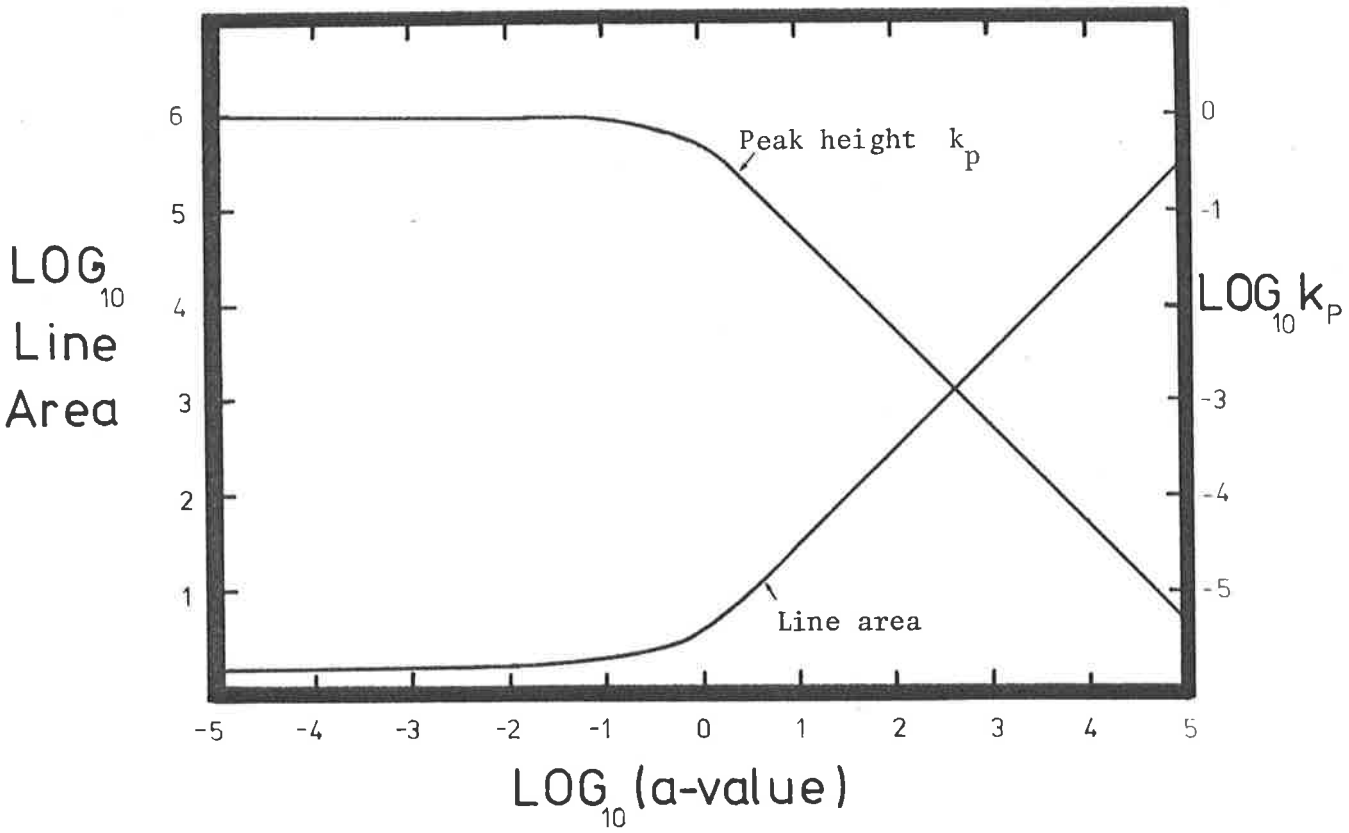

FIG 5 A plot of the area beneath a line given by the 2nd approximation of Whiting versus α-value for constant peak height k_p, and a plot of peak height versus α-value for constant ^{p} area.

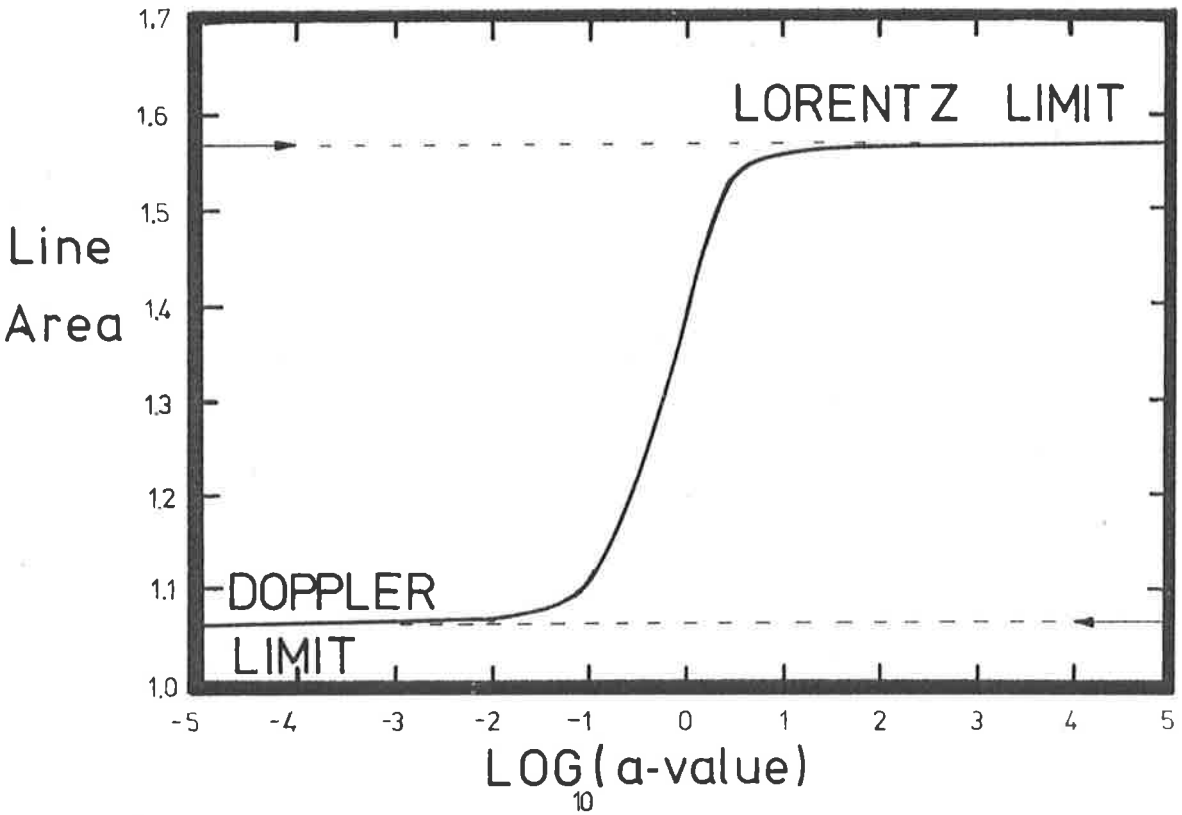

FIG 6 A plot of the area beneath a line versus α-value for Whiting's 2nd approximation.

APPENDIX 6

The Linear Region of the Curve of Growth

The curves of growth for all lines, irrespective of line profile, all have a linear region. The linear region occurs where the equivalent width W of an absorption line follows a straight line of slope 1 for all optical depths $k_p X < 0.1$.

The expression for equivalent width W can be written as

$$W = \int (1 - \exp(- k_p X \, k(\lambda))) \, d\lambda \, .$$

If the term $k_p X$ is small (usually less than 0.1, since $k(\lambda)$ usually takes values between 0 and 1), then the approximation

$$\exp(-t) = 1 - t \qquad \text{for } t \text{ small,}$$

holds to a high degree of accuracy. The equivalent width W can then be written as

$$W \approx \int k_p X \; k(\lambda) \, d\lambda \approx k_p X \int k(\lambda) \, d\lambda \, .$$

Since $\int k(\lambda) \, d\lambda$ is constant for all lines, then

$$W \propto k_p X$$

that is, the equivalent width is proportional to optical depth.

APPENDIX 7

Equivalent Width Versus Scan Range

The ideal value of equivalent width W is obtained when the scan range is infinite, and has the property that W is independent of resolution (see Appendix 1). However, in the Schumann-Runge bands, it is quite usual to have a scan range of between 5 and 10 times the line half-width. The effect this has depends upon the type of line being examined, and how much Doppler component it contains. The more Doppler-like the line, the less effect a narrow scan range has on the equivalent width (see Figure 1).

The effect of instrument resolution is always taken into account during results computation, so the equivalent widths measured experimentally should compare with those generated theoretically. The effect due to scan range will only become important if the scan function is left out altogether, and the differences plotted below are then a measure of the error this will introduce. For Doppler-like lines, the effect is minimal, but for Lorentz-like lines, it can be significant. Reasonable results, approximating the true equivalent width would still be obtained to 10% accuracy in most cases.

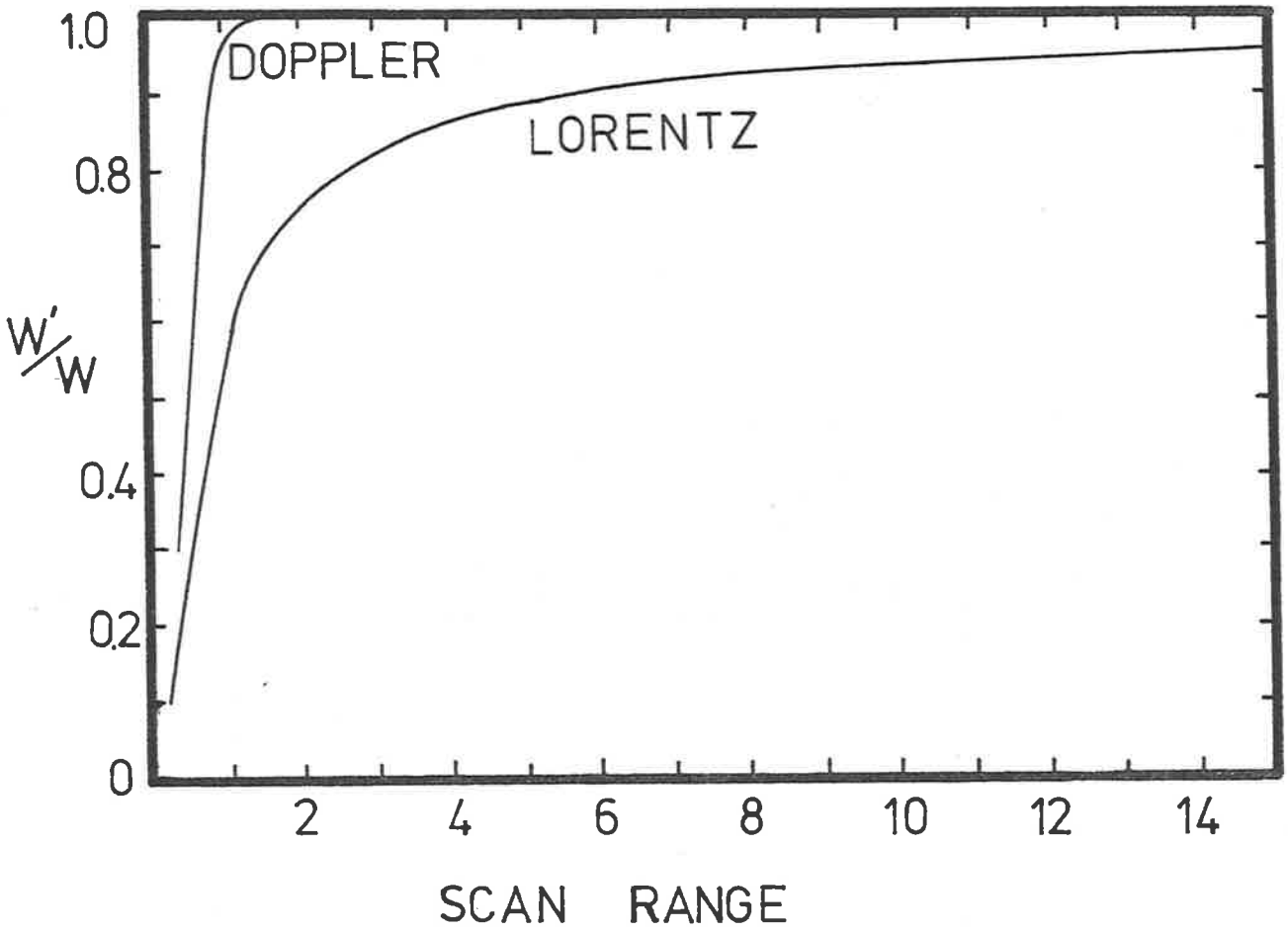

FIG 1. A plot of the ratio of the measured equivalent width to total real equivalent width versus scan range in units of half-width α_D (or α_N). The total real equivalent width W is that obtained for infinite scan range.

APPENDIX 8

Curve of Growth Study

The behaviour of curves of growth for various α-values as the optical depth k_pX varies is shown in Figures 3.10 and 3.11. These Figures both show the linear increase in equivalent width with k_pX for low k_pX, where all the curves of growth for different α-values are almost coincident, and they show the departures from the linear once k_pX becomes appreciable. Lines with any amount of Lorentz component, no matter how small will eventually follow an increase of the form

$$W \propto \sqrt{k_pX}$$

which is due entirely to the Lorentzian wings of the line.

Studies were also made in the growth of equivalent width for fixed scan range. In certain circumstances, it was possible for the curve of growth of one α-value, say α, to lie below that of another α-value, say α_2, where $\alpha_1 > \alpha_2$. In the ideal case, of infinite scan range, this would have been impossible. It also means that it is possible to obtain two solutions to the α-value iteration, usually separated by many orders of magnitude. Only one of the solutions will be a correct one, and it will be apparent in most cases which solution is the answer. None of the scans done in this work produced two solutions, although one or two did not produce answers due to two solutions being available, and to the iteration procedure oscillating between them.

A sketch of $\log_{10}$ equivalent width versus $\log_{10}$ α-value is shown in Figure 1. For any one value of equivalent width, there are two solutions of α at a given k_pX. The equivalent width begins to fall off with α-value for a fixed k_pX, for a fixed scan range, again, something

not expected from the ideal, infinite scan range case.

This leads to the possibility of optimizing the experiment. It should now be possible to predict a value of k_pX for which $\frac{\partial W}{\partial a}$ would be a maximum, in order to determine the correct a-value to the greatest accuracy. This corresponds to the tangent to the curves of Figure 1 being as far from horizontal as possible. When the experiment was first done, calculations of this sort were impossible, due to the long computing time of the programme, but by the end of the project, refinements of this type were possible, due to the improved computer programmes. This allows more accurate results to be obtained in shorter counting times.

The expression $W \approx \sqrt{k_pX}$ for k_pX large can be obtained as follows. The equivalent width W is given by

$$W = \int \left(1 - \exp\left[- k_pX \frac{1}{\left(\frac{\lambda - \lambda_0}{\alpha_N/2}\right)^2 + 1} \right]\right) d(\lambda - \lambda_0)$$

Use of the substitutions

$$y = \frac{k_pX}{z}$$

and

$$\tan(\theta/2) = \frac{\lambda - \lambda_0}{\alpha_N/2}$$

gives

$$W = \int \{ 1 - \exp[- (y + y\cos\theta)]\} \frac{\alpha_N}{2} d(\tan\theta/2)$$

and this reduces to (Penner 1969 , Page 43)

$$W \approx \alpha_N \sqrt{k_pX\,\pi} \quad .$$

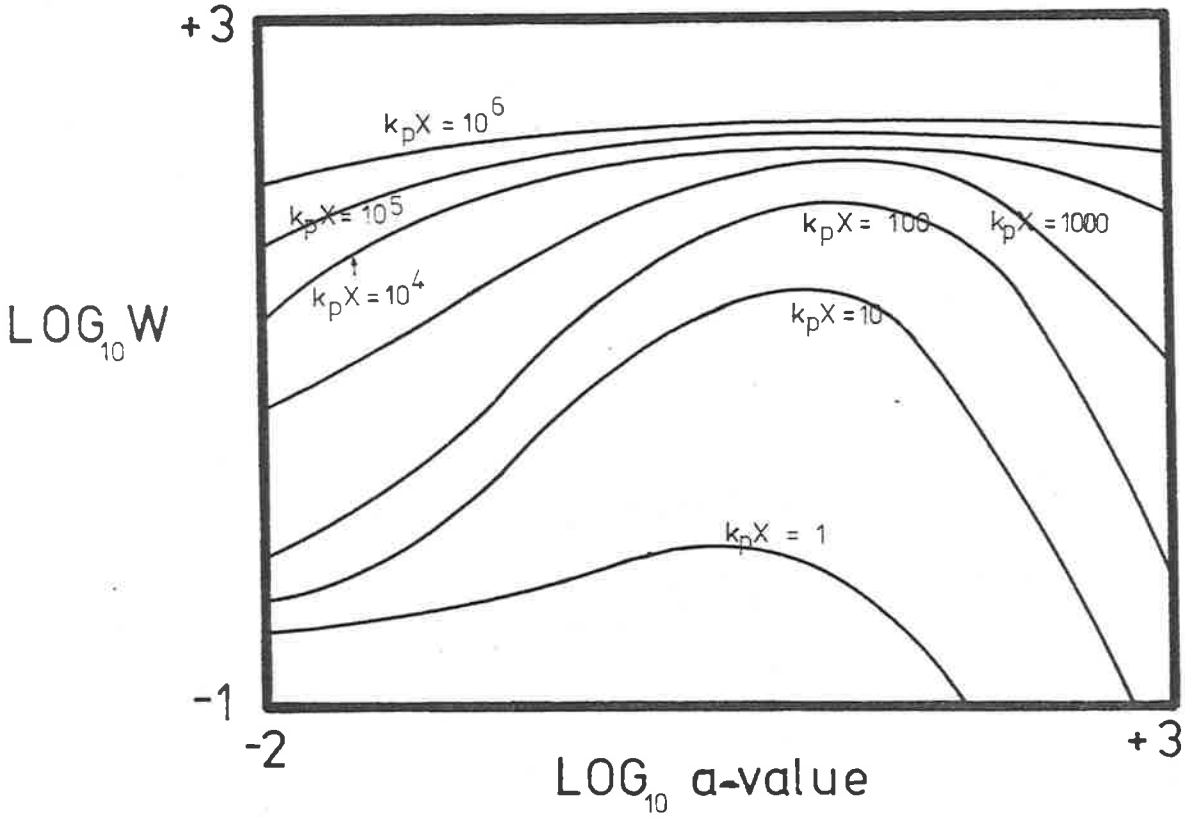

FIG 1. A log-log plot of equivalent width versus a-value for fixed values of k_pX. The curve for $k_pX = 10^6$ is virtually flat because for such a large value of k_pX, the equivalent width is simply the completely absorbed rectangle corresponding to the scan range for almost all values of a.

APPENDIX 9

The Error Function

The error function is defined as

$$\text{erf } x = \frac{2}{\sqrt{\pi}} \int_0^x e^{-t^2} dt \qquad (5.34)$$

and basically consists of the area beneath the Gaussian or Doppler function from the centre at $t = 0$ to a position at $t = x$ (see Figure 1). A list of the values of the error function can be found in "Handbook of Mathematical Functions" by Abramowitz and Segun. A plot of

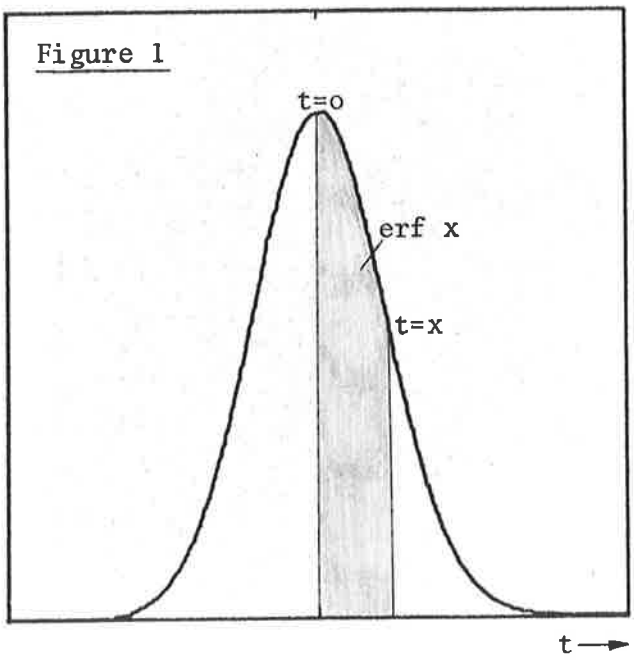

the values is shown above in Figure 2 .

The error function has been used in this work because of its relation to the Gaussian or Doppler function. The alternate convolution method of Section 5.6.2 makes extensive use of the error function. Since no error function is directly available for use in a computer programme, an approximation listed in Abramowitz and Segun (1968) was used. This consisted of

$$\text{erf } x = 1 - \frac{1}{(1 + a_1 x + a_2 x^2 + \ldots . a_6 x^6)^{16}} + \varepsilon(x)$$

where $|\varepsilon(x)| \leqslant 3 \times 10^{-7}$, sufficient accuracy for this work.

The constants are

$a_1 = .0705230784$ $\quad$ $a_2 = .0422820123$

$a_3 = .0092705272$ $\quad$ $a_4 = .0001520143$

$a_5 = .0002765672$ $\quad$ $a_6 = .0000430638$

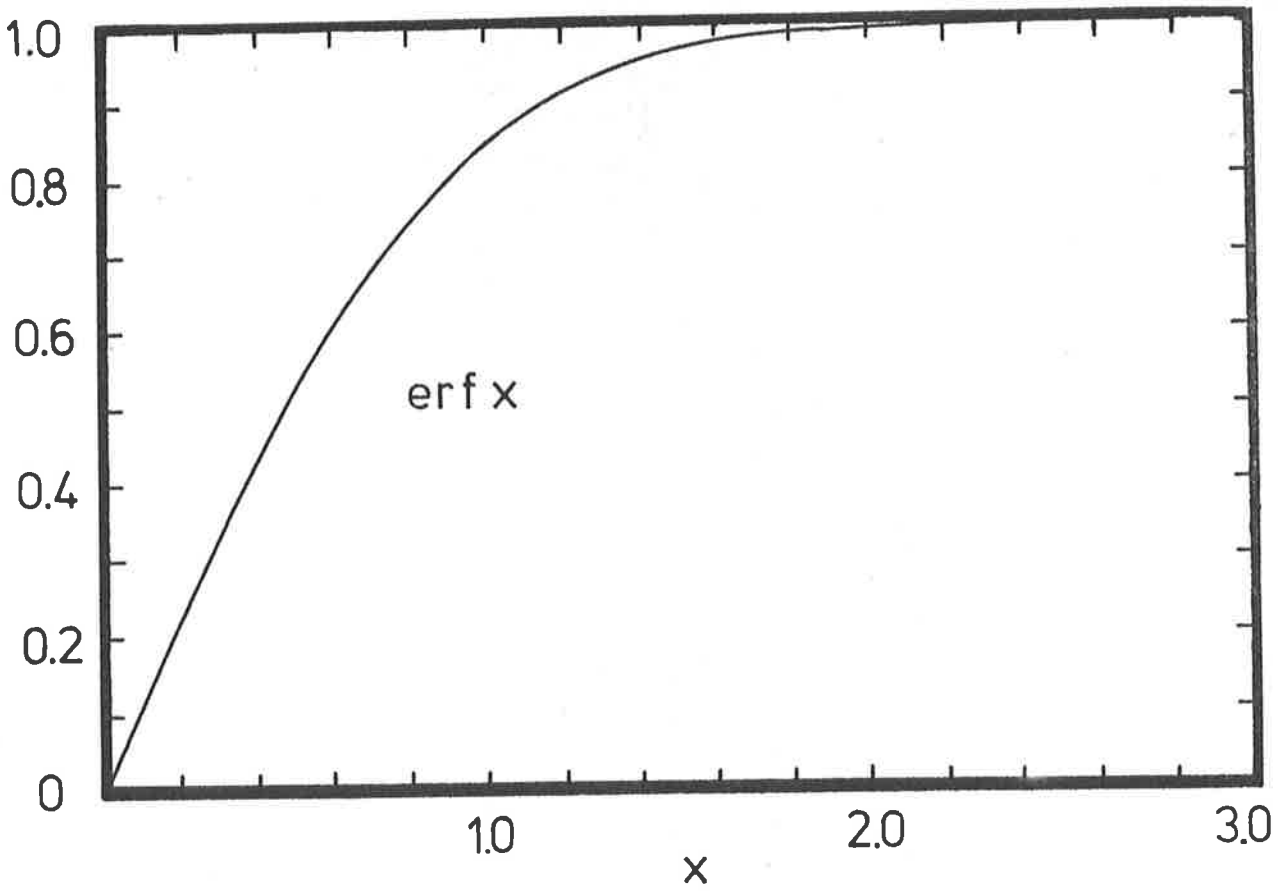

FIG 2 A plot of erf x for the range $0 \leqslant x \leqslant 3$.

APPENDIX 10

The Relation between Oscillator Strength and $k_p X$

A well known equation relating oscillator strength to the integrated area beneath a line profile, $\int k(\lambda)d\lambda$ is Thorne (1974)

$$f = \frac{4\ \varepsilon_0\ m\ c^2}{\alpha_J\ Ne^2\ \lambda^2} \int k(\lambda)d\lambda \qquad (5.38)$$

This work, where most discussions use wavelength, adopts the form $\int k(\lambda)d\lambda$, whereas most books use $\int k(\nu)d\nu$ where $\nu = \frac{c}{\lambda}$.

The two integrals are related by

$$\frac{\int k(\lambda)d\lambda}{\lambda} = \frac{\int k(\nu)d\nu}{\nu} = \frac{\int k(\omega)d\omega}{\omega}$$

where $\omega = 1/\lambda$. The integrated line area is defined as

$$\int k(\lambda)d\lambda = k_p \sqrt{\pi}\ \alpha_e$$

where $\alpha_e = \frac{\lambda}{c}\sqrt{\frac{2K_B T}{M}}$ is the $\frac{1}{e}$ Doppler width.

The ideal gas equation $PV = N K_B T$ gives

$$\frac{P}{K_B T} = \frac{N}{V} = N$$ where N is the number of molecules per volume.

Use of equation 3.16 and $N = P/K_B T$ in equation 5.38 gives

$$f = \frac{4\ \varepsilon_0\ mc^2\ K_B T\ k_P\ \sqrt{\pi}}{\alpha J\ Pe^2\ \lambda^2} \frac{\lambda}{c}\sqrt{\frac{2K_B T}{M}}$$

which reduces further to

$$f = \frac{4\sqrt{2\pi}\ \varepsilon_0\ mc\ K_B^{3/2}}{e^2\ \sqrt{M}} \frac{k_p X\ T^{3/2}}{\alpha_J\ P(MKS)\ \lambda(MKS)\ \ell(MKS)}$$

For convenience, since the pressure measurements are made in non-MKS units, as are the wavelength and temperature, the above equation can be converted to

$$f_L = 1.577 \times 10^{-3} \frac{k_p X \; T^{3/2}}{\alpha_J \; P(\mu) \; \lambda(\text{Å}) \; \ell(\text{cms})}$$

by using $\frac{1}{P(\text{MKS})} = \frac{760000}{101300 \; P(\mu)}$, $\frac{1}{\lambda(\text{MKS})} = \frac{10^{-10}}{\lambda(\text{Å})}$

and $\frac{1}{\ell(\text{MKS})} = \frac{10^2}{\ell(\text{cms})}$

Use of equation 2.20 then gives the final relation

$$f = 1.577 \times 10^{-3} \frac{k_p X \; T^{3/2}}{P(\mu) \; \lambda(\text{Å}) \; \ell(\text{cms}) \; \alpha_J \delta_J}$$

where $f_L = f(v', v'', n'', J'')$ is the line oscillator strength, and f is the equivalent band oscillator strength for the Jth rotational line.

APPENDIX 11

The results listed in this Appendix are for all the individual lines observed, and show a-value (at a temperature specified), predissociation width and associated equivalent band oscillator strengths. The a-value and linewidth are related by

$$\alpha_V = a\,\alpha_D \,/\sqrt{\ln 2}\;\left[\,1 + \left(\frac{1 + 4\ln 2}{a^2}\right)^{\frac{1}{2}}\right] \qquad (3.37)$$

and $\alpha_P = \alpha_V - \alpha_D$

where α_P is the predissociation width, α_V is the total linewidth and α_D is the Doppler width (at the specified temperature).

Band	Line	Oscillator Strength	α-value (294° K)	Predissociation Width
1-0	R_5P_3	6.01 ± 0.19	0.49 ± 0.07	0.06 ± 0.014**
	R_7P_5	12.6 ± 1.2	0.41 ± 0.10	0.05 ± 0.013**
	R_9P_7	8.63 ± 0.47	0.69 ± 0.09	0.09 ± 0.012**
	$R_{11}P_9$	7.55 ± 0.24	-	-
	$R_{13}P_{11}$	9.01 ± 0.49	-	-
2-0	R_5P_3	2.39 ± 0.10	3.70 ± 0.26	0.48 ± 0.034
	R_7P_5	2.23 ± 0.08	3.74 ± 0.12	0.49 ± 0.02
	R_9P_7	2.16 ± 0.07	5.18 ± 0.42	0.68 ± 0.06
	$R_{11}P_9$	2.22 ± 0.09	3.59 ± 0.24	0.47 ± 0.03
	$R_{13}P_{11}$	2.59 ± 0.06	3.58 ± 0.10	0.47 ± 0.01
	$R_{15}P_{13}$	3.04 ± 0.08	2.84 ± 0.14*	0.37 ± 0.02*
	$R_{17}P_{15}$	2.60 ± 0.10	1.46 ± 0.11*	0.19 ± 0.01*
	$R_{19}P_{17}$	2.85 ± 0.11	2.68 ± 0.28*	0.35 ± 0.04*
	$R_{21}P_{19}$	2.18 ± 0.13	1.15 ± 0.08*	0.15 ± 0.01*
3-0	R_7P_5	11.4 ± 0.40	6.66 ± 0.38	0.89 ± 0.05
	R_9P_7	8.91 ± 0.29	10.42 ± 0.62	1.39 ± 0.08
	$R_{11}P_9$	10.4 ± 0.40	9.86 ± 0.61	1.31 ± 0.08
	$R_{13}P_{11}$	10.8 ± 0.40	8.59 ± 0.48	1.14 ± 0.06
	$R_{15}P_{13}$	9.41 ± 0.37	10.8 ± 0.99	1.44 ± 0.13
	$R_{17}P_{15}$	9.70 ± 0.56	15.1 ± 1.45	2.00 ± 0.20
	$R_{19}P_{17}$	8.68 ± 0.44	8.77 ± 1.58	1.16 ± 0.21
	$R_{21}P_{19}$	11.2 ± 0.07	5.62 ± 0.93	0.75 ± 0.12
	$R_{23}P_{21}$	9.72 ± 0.49	8.30 ± 2.0	1.10 ± 0.27

** Total non-Doppler component - includes pressure broadening

* These α-values discarded because pressure factor too small

Band	Line	Oscillator Strength	α-value (294° K)	Predissociation Width
4-0	R_5P_3	$(2.72 \pm 0.16) \times 10^{-7}$	18.4 ± 2.48	2.48 ± 0.33
	R_7P_5	$2.58 \pm 0.12 \times 10^{-7}$	19.3 ± 1.67	2.61 ± 0.23
	R_9P_7	2.56 ± 0.11 "	26.4 ± 3.69	3.56 ± 0.50
	$R_{11}P_9$	2.71 ± 0.11 "	30.4 ± 5.00	4.10 ± 1.89
	$R_{13}P_{11}$	2.87 ± 0.15 "	17.1 ± 1.51	2.30 ± 0.20
	$R_{15}P_{13}$	2.77 ± 0.16 "	26.8 ± 1.43	3.61 ± 0.19
	$R_{17}P_{15}$	2.54 ± 0.13 "	25.6 ± 2.16	3.45 ± 0.30
	$R_{19}P_{17}$	2.96 ± 0.17 "	28.9 ± 12.0	3.88 ± 1.61
	$R_{21}P_{19}$	2.70 ± 0.11 "	-	-
			(297° K)	
5-0	R_5P_3	$(7.08 \pm 0.33) \times 10^{-7}$	-	-
	R_7P_5	7.61 ± 0.39 "	12.9 ± 0.9	1.77 ± 0.12
	R_pP_7	7.93 ± 0.32 "	9.57 ± 0.87	1.31 ± 0.12
	$R_{11}P_9$	8.15 ± 0.33	18.9 ± 1.15	2.60 ± 0.16
	$R_{13}P_{11}$	8.07 ± 0.37	13.9 ± 1.50	1.91 ± 0.21
	$R_{15}P_{13}$	7.88 ± 0.34	17.4 ± 1.58	2.38 ± 0.22
	$R_{17}P_{15}$	8.61 ± 0.38	12.6 ± 0.83	1.73 ± 0.11
	$R_{19}P_{17}$	7.23 ± 0.42	21.5 ± 1.94	2.93 ± 0.27
	$R_{21}P_{19}$	6.91 ± 0.41	17.2 ± 2.73	2.34 ± 0.37
	$R_{23}P_{21}$	6.67 ± 0.40	13.1 ± 2.0	1.79 ± 0.27

Band	Line	Oscillator Strength	a-value (297° K)	Predissociation Width
6-0	R_5P_3	$(1.89 \pm 0.10) \times 10^{-6}$	9.26 ± 0.62	1.28 ± 0.09
	R_7P_5	1.84 ± 0.08 "	8.79 ± 0.60	1.22 ± 0.08
	R_9P_7	1.61 ± 0.09 "	10.8 ± 0.99	1.50 ± 0.14
	$R_{11}P_9$	1.73 ± 0.08 "	13.6 ± 0.93	1.89 ± 0.13
	$R_{13}P_{11}$	2.03 ± 0.12 "	8.98 ± 1.33	1.24 ± 0.18
	$R_{15}P_{13}$	1.66 ± 0.09 "	10.8 ± 1.15	1.50 ± 0.16
	$R_{17}P_{15}$	1.70 ± 0.08 "	13.8 ± 0.79	1.91 ± 0.11
	$R_{19}P_{17}$	1.54 ± 0.08 "	14.1 ± 0.92	1.95 ± 0.13
	$R_{21}P_{19}$	1.60 ± 0.08	18.0 ± 1.70	2.48 ± 0.23
	$R_{23}P_{21}$	1.59 ± 0.08	18.5 ± 1.60	2.54 ± 0.22
7-0	R_5P_3	$(3.68 \pm 0.18) \times 10^{-6}$	-	-
	R_7P_5	4.02 ± 0.20 "	10.0 ± 0.58	1.40 ± 0.08
	R_9P_7	4.37 ± 0.25 "	9.06 ± 0.54	1.27 ± 0.08
	$R_{11}P_9$	3.98 ± 0.20 "	10.4 ± 0.57	1.45 ± 0.08
	$R_{13}P_{11}$	3.97 ± 0.22 "	11.8 ± 0.72	1.65 ± 0.10
	$R_{15}P_{13}$	3.91 ± 0.29 "	13.8 ± 0.90	1.93 ± 0.13
	$R_{17}P_{15}$	3.31 ± 0.23	13.7 ± 0.90	1.91 ± 0.13
	$R_{19}P_{17}$	3.48 ± 0.22 "	11.4 ± 1.43	1.60 ± 0.20
	$R_{21}P_{19}$	3.56 ± 0.16 "	10.5 ± 0.82	1.46 ± 0.11
	$R_{23}P_{21}$	3.10 ± 0.17 "	-	-

Band	Line	Oscillator Strength	a-value (297° K)	Predissociation Width
8-0	R_5P_3	$(8.60 \pm 0.46) \times 10^{-6}$	6.30 ± 0.42	0.89 ± 0.06
	R_7P_5	7.85 ± 0.40 "	6.81 ± 0.39	0.96 ± 0.06
	R_9P_7	7.45 ± 0.39 "	9.92 ± 0.50	1.40 ± 0.07
	$R_{11}P_9$	8.08 ± 0.38 "	8.99 ± 0.46	1.27 ± 0.06
	$R_{13}P_{11}$	7.29 ± 0.45 "	9.74 ± 0.47	1.37 ± 0.07
	$R_{15}P_{13}$	6.96 ± 0.38 "	10.3 ± 0.50	1.45 ± 0.07
	$R_{17}P_{15}$	7.28 ± 0.42 "	9.97 ± 0.50	1.40 ± 0.07
	$R_{19}P_{17}$	6.47 ± 0.35 "	11.5 ± 0.60	1.61 ± 0.08
	P_{19}	6.68 ± 0.27 "	12.0 ± 1.06	1.69 ± 0.15
	R_{21}	5.29 ± 0.33 "	17.8 ± 3.38	2.49 ± 0.48
	P_{21}	6.06 ± 0.31 "	-	-
	R_{23}	5.77 ± 0.38 "	-	-
9-0	R_5P_3	$(12.8 \pm 0.60) \times 10^{-6}$	-	-
	R_7P_5	15.0 ± 1.00 "	$3.15 \pm .22$	0.45 ± 0.03
	R_9P_7	13.6 ± 1.50 "	-	-
	$R_{11}P_9$	16.0 ± 0.90 "	3.09 ± 0.17	0.44 ± 0.02
	P_{11}	12.4 ± 0.60 "	5.44 ± 0.45	0.77 ± 0.08
	R_{13}	11.9 ± 0.70 "	5.73 ± 0.44	0.82 ± 0.06
	P_{13}	13.5 ± 0.90 "	3.49 ± 0.32	0.50 ± 0.04
	R_{15}	9.76 ± 0.60 "	4.42 ± 0.34	0.63 ± 0.05
	P_{15}	12.0 ± 0.80 "	5.61 ± 0.38	0.80 ± 0.05
	R_{17}	13.5 ± 0.90 "	2.93 ± 0.32	0.42 ± 0.05
	P_{17}	11.0 ± 0.80 "	5.12 ± 0.90	073 ± 0.13
	R_{19}	9.12 ± 0.50 "	5.99 ± 0.87	0.85 ± 0.12
	P_{19}	10.7 ± 0.60 "	5.98 ± 0.59	0.85 ± 0.08
	R_{21}	10.3 ± 0.70 "	5.47 ± 0.63	0.78 ± 0.09
	P_{21}	10.1 ± 0.50 "	4.63 ± 0.37	0.66 ± 0.05

Band	Line	Oscillator Strengths	α-value (297° K)	Predissociation Width (cm^{-1})
10-0	R_5P_3	$(1.71 \pm 0.11) \times 10^{-5}$	-	-
	R_7P_5	1.68 ± 0.10 "	-	-
	P_7	1.83 ± 0.10 "	5.21 ± 0.41	0.75 ± 0.06
	R_9	1.66 ± 0.09 "	5.27 ± 0.39	0.76 ± 0.06
	P_9	1.69 ± 0.10 "	5.86 ± 0.68	0.84 ± 0.10
	R_{11}	2.02 ± 013 "	4.74 ± 0.37	0.68 ± 0.05
	P_{11}	2.12 ± 0.11 "	5.32 ± 0.39	0.76 ± 0.06
	R_{13}	2.14 ± 0.15 "	2.40 ± 0.23	0.34 ± 0.03
	P_{13}	2.20 ± 0.16 "	3.18 ± 0.23	0.46 ± 0.03
	R_{15}	1.51 ± 0.10 "	4.41 ± 0.37	0.63 ± 0.05
	P_{15}	1.82 ± 0.13 "	4.77 ± 0.58	0.68 ± 0.08
	R_{17}	1.44 ± 0.10 "	3.20 ± 0.45	0.46 ± 0.06
	P_{17}	1.68 ± 0.10 "	4.92 ± 0.41	0.70 ± 0.06
	R_{19}	1.51 ± 0.08 "	2.92 ± 0.24	0.42 ± 0.03
	P_{19}	1.71 ± 0.10 "	4.98 ± 0.49	0.71 ± 0.07
	R_{21}	1.33 ± 0.08 "	5.93 ± 0.56	0.85 ± 0.08
	P_{21}	1.45 ± 0.09 "	-	-
	R_{25}	0.95 ± 0.06 "	-	-
	R_{29}	0.90 ± 0.05 "	-	-
	P_{31}	0.70 ± 0.05 "	-	-

Band	Line	Oscillator Strength	α-value (297° K)	Predissociation Width (cm^{-1})
11-0	R_7P_5	(2.60 ± 0.17) x 10^{-5}	6.30 ± 0.78	0.91 ± 0.11
	P_7	2.66 ± 0.16 "	4.06 ± 0.37	0.59 ± 0.05
	R_9	2.84 ± 0.17 "	3.64 ± 0.22	0.53 ± 0.03
	P_9	2.89 ± 0.18 "	5.69 ± 0.48	0.82 ± 0.07
	R_{11}	2.42 ± 0.08 "	6.55 ± 0.42	0.95 ± 0.06
	P_{11}	2.73 ± 0.12 "	7.63 ± 1.00	1.10 ± 0.14
	R_{13}	2.39 ± 0.15 "	6.78 ± 0.45	0.98 ± 0.07
	P_{13}	2.67 ± 0.14 "	6.61 ± 0.30	0.95 ± 0.04
	R_{15}	2.50 ± 0.15 "	6.70 ± 0.45	0.97 ± 0.07
	P_{15}	2.36 ± 0.19 "	5.95 ± 0.55	0.86 ± 0.08
	R_{17}	2.22 ± 0.21 "	5.16 ± 0.56	0.74 ± 0.08
	P_{17}	2.11 ± 0.11 "	8.66 ± 0.70	1.25 ± 0.10
	R_{19}	2.12 ± 0.11 "	5.88 ± 0.78	0.85 ± 0.11
	P_{19}	2.01 ± 0.09 "	7.62 ± 0.60	1.10 ± 0.09
	R_{21}	2.03 ± 0.07 "	4.23 ± 0.30	0.61 ± 0.04
	P_{25}	1.40 ± 0.08 "	-	-

Band	Line	Oscillator Strength	a-value (297° K)	Predissociation Width (cm^{-1})
12-0	P_5	$(3.19 \pm 0.17) \times 10^{-5}$	-	-
	R_7	3.12 ± 0.19 "		
	P_7	3.83 ± 0.22 "	3.28 ± 0.26	0.48 ± 0.04
	R_9	2.88 ± 0.14 "	3.70 ± 0.27	0.54 ± 0.04
	P_9	3.00 ± 0.16 "	4.28 ± 0.35	0.62 ± 0.05
	R_{11}	3.31 ± 0.16 "	2.52 ± 0.23	0.37 ± 0.03
	P_{11}	3.17 ± 0.19 "	4.00 ± 0.31	0.58 ± 0.05
	R_{13}	3.15 ± 0.15 "	4.38 ± 0.39	0.64 ± 0.06
	P_{13}	3.07 ± 0.17 "	4.34 ± 0.36	0.63 ± 0.05
	R_{15}	2.87 ± 0.16 "	4.13 ± 0.38	0.60 ± 0.06
	P_{15}	2.94 ± 0.16 "	4.56 ± 0.46	0.66 ± 0.07
	R_{17}	3.16 ± 0.17 "	5.10 ± 1.26	0.74 ± 0.18
	P_{17}	3.14 ± 0.19 "	3.98 ± 0.30	0.58 ± 0.04
	R_{19}	2.47 ± 0.13 "	4.50 ± 0.55	0.65 ± 0.08
	R_{25}	1.70 ± 0.08 "	-	-
	P_{25}	2.03 ± 0.10 "	-	-
13-0	P_5	$(4.02 \pm 0.24) \times 10^{-5}$	0.66 ± 0.06	0.10 ± 0.009
	R_7	4.62 ± 0.40 "	0.50 ± 0.05	0.07 ± 0.007
	P_7	3.72 ± 0.21 "	0.91 ± 0.11	0.13 ± 0.016
	R_9	3.10 ± 0.21 "	1.00 ± 0.12	0.15 ± 0.018
	P_9	3.17 ± 0.21 "	1.13 ± 0.14	0.16 ± 0.020
	R_{11}	2.79 ± 0.21 "	1.23 ± 0.15	0.18 ± 0.022
	P_{11}	4.05 ± 0.27 "	0.78 ± 0.12	0.11 ± 0.018
	R_{13}	3.60 ± 0.25 "	0.94 ± 0.10	0.14 ± 0.015
	P_{13}	3.91 ± 0.25 "	0.61 ± 0.05	0.09 ± 0.007
	R_{15}	2.90 ± 0.17 "	1.64 ± 0.28	0.24 ± 0.041
	P_{15}	3.34 ± 0.19 "	1.05 ± 0.08	0.15 ± 0.012
	R_{17}	3.58 ± 0.17 "	1.13 ± 0.08	0.16 ± 0.012
	P_{25}	2.06 ± 0.11 "	-	-

Band	Line	Oscillator Strength	α-value (297° K)	Predissociation Width (cm^{-1})
14-0	P_5	$(5.14 \pm 0.33) \times 10^{-5}$	-	-
	R_7	3.74 ± 0.20 "	0.90 ± 0.11	0.13 ± 0.016
	P_7	5.57 ± 0.42 "	0.43 ± 0.04	0.06 ± 0.006
	R_9	5.58 ± 0.38 "	0.37 ± 0.05	0.05 ± 0.007
	P_9	3.84 ± 0.25 "	0.95 ± 0.10	0.14 ± 0.015
	R_{11}	3.85 ± 0.25 "	0.65 ± 0.10	0.10 ± 0.015
	P_{11}	3.78 ± 0.22 "	1.00 ± 0.10	0.15 ± 0.015
	R_{13}	3.45 ± 0.20 "	0.81 ± 0.09	0.12 ± 0.013
	P_{13}	4.40 ± 0.25 "	0.22 ± 0.05	0.03 ± 0.007
	R_{15}	3.46 ± 0.22 "	0.48 ± 0.05	0.07 ± 0.007
	P_{15}	4.36 ± 0.29 "	0.44 ± 0.06	0.06 ± 0.009
	R_{21}	3.07 ± 0.19 "	-	-
	P_{21}	2.97 ± 0.18 "	-	-
	R_{27}	2.33 ± 0.17 "	-	-
	P_{27}	2.66 ± 0.18 "	-	
			(82° K)	
15-0	R_7	$(4.42 \pm 1.00) \times 10^{-5}$	1.62 ± 0.16	0.13 ± 0.012
	P_7	4.60 ± 0.44 "	1.62 ± 0.13	0.13 ± 0.010
	R_9	2.40 ± 0.18 "	3.46 ± 0.49	0.27 ± 0.038
	P_9	3.22 ± 0.21 "	3.36 ± 0.26	0.26 ± 0.020
	R_{11}	5.52 ± 0.42 "	2.50 ± 0.19	0.19 ± 0.015
	P_{11}	3.74 ± 0.75 "	1.12 ± 0.09	0.09 ± 0.007
	R_{13}	2.76 ± 0.25 "	1.71 ± 0.16	0.13 ± 0.012
	P_{11}	2.93 ± 0.26 "	-	-
	R_{11}	3.47 ± 0.23 "	0.96 ± 0.10**	0.14 ± 0.015

** Done at Room Temperature

Band	Line	Oscillator Strength	a-value (82° K)	Predissociation Width (cm^{-1})
16-0	P_7	$(5.60 \pm 0.56) \times 10^{-5}$	-	-
	R_9	3.45 ± 0.45 "	0.78 ± 0.10	0.11 ± 0.015
	R_{11}	3.56 ± 0.33 "	-	-
	P_{11}	3.43 ± 0.30 "	1.99 ± 0.24	0.29 ± 0.035
17-0	R_7	$(2.88 \pm 0.20) \times 10^{-5}$	3.07 ± 0.65	0.45 ± 0.10
	R_9	2.37 ± 0.17 "	2.76 ± 0.47	0.41 ± 0.07
	P_9	2.31 ± 0.21 "	-	-
18-0	R_7P_7	$(1.69 \pm 0.19) \times 10^{-5}$	1.35 ± 0.29	0.20 ± 0.043

Appendix 12

Computer Programme Listing

```
      PROGRAM FNL294 (INPUT,OUTPUT)
      DIMENSION XA(820),YN(820),ER(220),YW(820),YE(820),X(820),SM(820)
      DIMENSION IRAY(6),WE(2),W(10),AP(10),F(10),WW(2),P(2),AA(6),XX(6)
      DIMENSION ALA(20),ABL(20),ASFF(20),IJKA(20,2),NV(2)
      DATA IRAY/6*(-0)/
      IRAY(4)=0
      CALL SYSTEMC(115,IRAY)
      CALL MODERR(0)
     **************    VARIABLE SECTION ************
      READ 770,N,NK,JK,AF,XSS
  770 FORMAT(I2,8X,I3,7X,I2,8X,F8,2X,F8)
      READ 754,NV(1),NV(2),NL,NU
  754 FORMAT(2(I4),2(I2))
      READ 760,WE(1),WE(2)
  760 FORMAT(F8,2X,F8)
  750 FORMAT(4(F8,2X))
      READ 750,(ALA(I),I=1,N)
      READ 750,(ABL(I),I=1,N)
      READ 750,(ASFF(I),I=1,N)
      READ 499,IJKA(1,1),IJKA(1,2)
  499 FORMAT(I4,6X,I4)
        IF(N.EQ.1)970,971
  971 CONTINUE
      DO 751 LMN=1,2
      DO 752 I=2,N
      ALP=(ABL(1)-ABL(I))*1000/XSS
      IJKA(I,LMN)=IJKA(1,LMN)-INT(ALP)
  752 CONTINUE
  751 CONTINUE
  970 CONTINUE
       AP(1)=ALA(NL)   $   AP(2)=ALA(NL)/2.0
       BF=2.1628E-3
      F(1)=0.1
      LMN=1
      PRINT 566,WE(1),WE(2)
  566 FORMAT(10X,6HWE(1)=,E10.4,5X,6HWE(2)=,E10.4)
      PRINT 700,(ALA(I),I=1,N)
  700 FORMAT(10X,9(F8.3,3X))
      PRINT 701,(ABL(I),I=1,N)
  701 FORMAT(10X,9(F8.2,2X))
      PRINT 702,(ASFF(I),I=1,N)
  702 FORMAT(10X,9(F8.5,2X))
      PRINT 703,(IJKA(I,1),I=1,N)
  703 FORMAT(5X,9(I4,3X))
      PRINT 704,(IJKA(I,2),I=1,N)
  704 FORMAT(5X,9(I4,3X))
      PRINT 567,NV(1),NV(2),NL,NU
  567 FORMAT(4(I4,2X))
     **************    VARIABLE SECTION ************
         GEH=36.0
      XS=XSS/GEH
  SCAN FUNCTION CALCULATION -  ER IS THE ERROR FUNCTION FOR THE S_ITS
  SM IS THE MATRIX  IN WHICH THE SCAN FUNCTION OF THE MONCHROMATOR IS ST
   56 CONTINUE
      IF(LMN.EQ.1)30,31
   30 NN=NV(1)   $   GO TO 34
   31 NN=NV(2)
   34 CONTINUE
      DO 50 I=1,NN
  NAM=I $ XA(I)=AM
   50 CONTINUE
  NNKK=NK-1 $ NJ=NN-NKK $ NJJ=2*NK $ NKN=NN-NK-NKK $ NJN=NKN+1
      CALL ERFS(ER,XS,NK)
      NKK=NK-1 $ NJ=NN-NKK $ NJJ=2*NK $ NKN=NN-NK-NKK $ NJN=NKN+1
      DO 2 I=1,NK
      II=I-1 $ N1=NK-II $ SM(I)=(1-ER(N1))/2.0
    2 CONTINUE
      DO 3 I=1,NKK
      N2=I+NK $ III=I+1 $ SM(N2)=(1+ER(III))/2.0
    3 CONTINUE
      DO 4 I=NJJ,NKN
      SM(I)=1.0
    4 CONTINUE
      DO 6 I=1,NK
      II=I-1 $ NJL=NKN+I $ NK2=NK-II $ SM(NJL)=(1+ER(NK2))/2.0
    6 CONTINUE
      II=I-1 $ NJL=NKN+I $ NK2=NK-II $ SM(NJL)=(1+ER(NK2))/2.0
      DO 8 I=1,NKK
      N3=NJ+I $ IJ=I+1 $ SM(N3)=(1-ER(IJ))/2.0
    8 CONTINUE
  THIS SECTION CALCCULATES THE LINESHAPES  FOR THE SCAN
  YN IS THE MATRIX OF THE TOTAL ABSORPTION COEFFICIENT CALCULATED USING
  WHITING≠S SECOND APPROXIMATION
```

```
 40 CONTINUE
    DO 5 I=1,NN
    YN(I)=0
  5 CONTINUE
    DO 22 M=1,N
    A=ALA(M) $ BL=ABL(M) $ SFF=ASFF(M) $ IJK=IJKA(M,LMN)
 23 CONTINUE
    GFF=.69315 $ BD=BL*BF $ GF=.832555 $ CD=XSS*2.0*GF/BD
    XC=XSS
    AG=A*A $ BT=1.0+4.0*ALOG(2.0)/AG $ B=1.0+SQRT(BT) $ AB=A*B
      BB=B*B $ BA=2.0/B
     BB=B*B $ BA=2.0/B $ ABC=1.77334132/(A*B*(1.065+0.894/B+0.232/BB))
    I=1
 20 CONTINUE
    II=IJK-I
    ATI=II $ CI=ABS(ATI) $ EA=CI*CD $ EAA=EA*EA $ Z=EAA/AB/AB
    ZZ=-2.772589*Z $ TA=(1.0-BA)*EXP(ZZ) $  TB=BA*(1.0/(1.0+4.0*Z))
    ZA=(EA/AB)**2.25 $ ZB=-0.4*ZA
    TC=0.016*(1-BA)*BA*(EXP(ZB)-10/(10+ZA)) $ TF=TA+TB+TC
    ATF=ABC*TF*SFF $ AAC=YN(I) $ YN(I)=ATF+AAC
        I=I+1
    IF(I.GT.NN)21,20
 21 CONTINUE
 22 CONTINUE
    CALL SIMPS(YN,XC,YGST,NN)
    PRINT 555,YGST
555 FORMAT(10X,6HYGST=   ,F10.4)
     A=ALA(NL)
ITERATION FOR P≠X     VALUES FOR P≠X ARE STORED IN MATRIX F
P≠X VALUES ARE CHANGED UNTIL  THE VALUES OF EQUIVALENT WIDTH STORED IN
MATRIX W AGREE WITH THE EXPERIMENTAL VALUE IN WE(1)
    IF(LMN.EQ.1)80,81
 80 CONTINUE
    J=2
    PRINT 615,A
615 FORMAT(5X,F10.4,5X,18H P≠X ITERATION          )
 72 CONTINUE

    DO 70 I=1,NN
    JJ=J-1 $ AK=F(JJ) $ XK=-YN(I)*AK $  YW(I)=EXP(XK)
 70 CONTINUE
    DO 10 I=1,NN
    YE(I)=1.0-YW(I)
 10 CONTINUE
    DO 7 I=1,NN
    YW(I)=YE(I)*SM(I)
  7 CONTINUE
    CALL SIMPS(YW,XC,WST,NN)
    GGST=WST $ SL=ALOG10(GGST) $ JJJ=J-1 $ SJ=F(JJJ)
    SJL=ALOG10(SJ)
     PRINT 14,A,JJJ,SJ,GGST
    W(JJ)=GGST $ WAB=WE(1)-W(JJ) $ WBA=ABS(WAB)
    IF(WBA.LT.1E-2)96,85
 85 IF(J.GT.JK)86,87
 87 IF(J.EQ.2)83,84
 83 F(J)=WE(1)/W(1)*F(1)  $  J=J+1  $  GO TO 72
 84 CONTINUE
    JL=J-2 $ FJA=W(JL)-WE(1) $ FAJ=W(JL)-W(JJ) $ FPA=F(JL)-F(JJ)
    F(J)=F(JL)-FJA/FAJ*FPA
    IF(F(J).LT.0)183,184
183 F(J)=F(JJ)/2.0
184 J=J+1 $ GO TO 72
 86 CONTINUE
    P(1)=F(JJ) $ WW(1)=W(JJ) $ LMN=2 $ J=2 $ GO TO 56
ITERATION FOR A-VALUE      P≠X VALUE IS GIVEN IN P(2)
 A-VALUES ARE STORED IN MATRIX AP     THE FIRST ONE IS GUESSED AND THE
SECOND VALUE IS TAKEN AT HALF OF THE FIRST TO GIVE TWO ITERATIVE POINT
 A-VALUES ARE STORED IN MATRIX AP     THE FIRST ONE IS GUESSED AND THE
 WHEN A VALUE OF A HAS BEEN FOUND THE  ITERATION FOR P≠X IS DONE AGAIN
 81 CONTINUE
    P(2)=P(1)*AF
 92 CONTINUE
    DO 90 I=1,NN
    JJ=J-1 $ AK=P(2) $ XK=-YN(I)*AK $ YW(I)=EXP(XK)
 90 CONTINUE
    DO 110 I=1,NN
    YE(I)=1.0-YW(I)
110 CONTINUE
    DO 107 I=1,NN
    YW(I)=YE(I)*SM(I)
107 CONTINUE
    CALL SIMPS(YW,XC,WST,NN)
    GGST=WST $ JJ=J-1 $ SL=ALOG10(GGST) $ JJJ=J-1 $ SJ=P(2)
    SJL=ALOG10(SJ)
    PRINT 16,JJ,A,SJ,GGST
 16 FORMAT(10X,I4,2X,4H A= ,E10.4,4X,5HP≠X= ,E10.4,4X,4H W= ,E10.4)
```

```
      W(JJ)=GGST $ WAB=WE(2)-W(JJ) $ WBA=ABS(WAB)
      IF(WBA.LT.0.5)96,95
   95 IF(J.GT.JK)96,97
   97 IF(J.EQ.2)93,94
   93 DO 11 I=NL,NU
    ****** THIS IS A VARIABLE PROGRAM STEP   SHOULD BE CHANGED WITH EACH
      ALA(I)=ALA(I)/2.0
    ****** THIS IS A VARIABLE PROGRAM STEP   SHOULD BE CHANGED WITH EACH
   11 CONTINUE
      PRINT 614,A,P(2)
  614 FORMAT(5X,F10.4,5X,F10.4,5X,20H A VALUE ITERATION       )
      J=J+1 $ GO TO 40
   94 CONTINUE
      JL=J-2 $ AWJ=W(JL)-WE(2) $ AWL=W(JL)-W(JJ) $ APW=AP(JL)-AP(JJ)
      IF(AWL.EQ.0)96,76
   76 CONTINUE
      AP(J)=AP(JL)-AWJ/AWL*APW
      APJ=AP(J)
      IF(APJ.LT.0)78,79
   78 AP(J)=AP(JJ)
   79 CONTINUE
      DO 12 I=NL,NU
      ALA(I)=AP(J)
   12 CONTINUE
      J=J+1  $  JJ=J-1 $ GO TO 40
   96 CONTINUE
      WW(2)=W(JJ) $ LMN=1 $ AP(1)=A $ AP(2)=A/2.0
      IF(J.EQ.2)99,98
   98 CONTINUE
      PRINT 126
  126 FORMAT(10X,4H126    )
      GO TO 56
   99 CONTINUE
      P1=P(1) $ P2=P(2) $ WW1=WW(1) $ WW2=WW(2)
      PRINT 100,P1,P2,WW1,WW2,A
  100 FORMAT(10X,4H 100,5(E10.4,5X))
       PRINT 800,A,CD,B,AB,ABC
  800 FORMAT(10X,3HA= ,E10.4,5X,4HCD= ,E10.4,5X,3HB=,E10.4,5X,4HAB= ,
     2,E10.4,5X,5HABC=,E10.4)
   15 FORMAT(1H0,20X,20H* CURVE OF GROWTH *      ,5X,2HA=,E10.4,5X,3HCD=,
     1 E10.4)
   14 FORMAT(5X,3HA= ,F10.4,5X,I4,5X,5HP#X= ,F10.4,5X,3HW= ,F10.4)
        CALL QIKPLT(XA,YW,NN,1,14H*WAVE LENGTH*    ,14H*INTENSITY*      )
   44 CONTINUE
   55 CONTINUE
  200 CONTINUE
      STOP          $  END
      SUBROUTINE SIMPS(X,XCD,GST,NN)
      DIMENSION X(820)
    ****** THIS IS A VARIABLE PROGRAM STEP   SHOULD BE CHANGED WITH EACH
  THE SIMPSON#S RULE SUBPROGRAM    EXCHANGES MATRICES  WITH  X AND INTEG
    USING STEP SIZE TRANSFERRED  THRU XCD AND NUMBER OF STEPS  NN
    ANSWER  GIVEN IN GST
      NNN=NN $ CC=1.0/3.0*XCD $ ST=0 $ I=1
   61 IF(I.EQ.NNN)62,63
   63 IF(I.EQ.1)64,65
   64 CONTINUE
      S=X(I) $ ST=ST+S $ I=I+1 $ GO TO 61
   65 VI=I $ VV=VI/2 $ II=INT(VV) $ VA=VV-II
      IF(VA.EQ.0)66,67
   66 CONTINUE
      S=X(I) $ ST=ST+4*S $ I=I+1 $ GO TO 61
   67 CONTINUE
      S=X(I) $ ST=ST+2*S $ I=I+1 $ GO TO 61
   62 CONTINUE
      S=X(I) $ ST=ST+S $ ST=ST*CC $ GST=ST
      RETURN
      END
      SUBROUTINE ERFS(ERR,XS,NK)
      DIMENSION ERR(720),AA(6),XX(6)
    ****** THIS IS A VARIABLE PROGRAM STEP   SHOULD BE CHANGED WITH EACH
   THE ERROR FUNCTION SUBPROGRAM      USES THE GAUSSIAN SLIT FUNCTION OF
  THE MONOCHROMATOR TO CALCULATE ERROR FUNCTION VALUES FOR THE SCAN FUNC
      AA(1)=.0705230784 $ AA(2)=.0422820123 $ AA(3)=.0092705272
      AA(4)=.0001520143 $ AA(5)=.0002765672 $ AA(6)=.0000430638
      DO 170 I=1,NK
      II=I-1 $ AI=II $ XI=AI*XS
      XX(1)=XI $ XX(2)=XI*XI % XX(3)=XX(2)*XI
      XX(4)=XX(2)*XX(2) $ XX(5)=XX(4)*XI $ XX(6)=XX(3)*XX(3)
      XAA=1.0
       DO172 J=1,6
      XAA=XAA+AA(J)*XX(J)
  172 CONTINUE
      X1=XAA*XAA $ X2=X1*X1 $ X3=X2*X2 $ X4=X3*X3 $ XB=1.0/X4
      ERR(I)=1.0-XB
  170 CONTINUE
      RETURN
      END
```

BIBLIOGRAPHY

Abramowitz, M. & Segun, I.A. "Handbook of Mathematical Functions" Dover Publications, New York (1968)

Ackerman, N., Biaume, F. & Nicolet, M. "Absorption in the spectral range of the Schumann-Runge bands" Can. J. Chem. Vol. 41 P 1834-1840

Ackerman, M. & Biaume, F. "Structure of the Schumann-Runge Bands from the 0-0 to the 13-0 Band" J. Mol. Spelt. 35 73-82 (1970)

Ackerman, M., Biaume, F. & Kockarts, G. "Absorption Cross-Sections of the Schumann-Runge Bands of Molecular Oxygen" Planet. Space. Sci. Vol. 18, p 1639-1651, (1970)

Alberti, F., Ashby, R.A. & Douglas, A.E. "Absorption Spectra of O_2 in the $a'\Delta_g$, $b'\Sigma_g^+$ and $X^3\Sigma_g^-$ States" Can. J. of Phys. Vol. 46, p 337-342, (1968)

Allison, A.C. (Private Communication) (1975)

Allison, A.C., Dalgarno, A. & Pasachoff, N.W. "Absorption of Vibrationally Excited Molecular Oxygen in the Schumann-Runge Continuum" Planet. Space Sci. Vol. 19, p 1463-1473, (1971)

Armstrong, B.H. "Spectrum Line Profiles : The Voigt Function" J. Quant, Spectrosc. Radiat. Transfer, Vol. 7, p 61-88, (1967)

Beer, T. "The Aerospace Environment" Wykeham Publications (London) Ltd. (1976)

Bergeman, T.H. & Wofsy, S.C. "The Fine Structure of O_2 $(B^3\Sigma_u^-)$" Chem. Phys. Lett. Vol. 15, No. 1, p 104-107, (1972)

Berkner, L.V. & Marshall, L.C. "On the Origin and Rise of Oxygen Concentration in the Earth's Atmosphere" J. of the Atmos. Sci. Vol. 22, No. 3, p 225-261, (1965)

Bethke, G.W. "Oscillator Strengths in the Far Ultraviolet. II. Oxygen Schumann-Runge Bands" J. Chem. Phys. Vol. 31, No. 3, p 669-673, (1956)

Blake, A.J., Carver. J.H., & Haddad, G.N. "Photoabsorption Cross Sections of Molecular Oxygen between 1250Å and 2350Å" J.Q.S.R.T. Vol. 6, p 451-459, (1966)

Blake, A.J. & Carver, J.H. "The Evolutionary Role of Atmospheric Ozone" J. of the Atmos. Sci. Vol. 34, No. 5, p 720-728, (1977)

Blake, A.J. "An Atmospheric Absorption Model for the Schumann-Runge Bands of Oxygen" (In Press)

Breene (Jr) R.G. "Oscillator Strengths in certain air Molecule Systems - I. The O_2 Schumann-Runge System" J.Q.S.R.T. Vol. 11, p 37-41, (1970)

Brinkmann, R.T. "Dissociation of Water Vapour and Evolution of Oxygen in the Terrestrial Atmosphere" J.G.R. Vol. 74, No. 23, p 5355-5368, (1969)

Brinkmann, R.T. "Photochemistry and the Escape Efficiency of Terrestrial Hydrogen" Fiocco (Ed) Mesospheric Models and Related Experiments, p 82-102, (1971)

Brix, P. & Herzberg, G. "Fine Structure of the Schumann-Runge Band near the Convergence Limit and the Dissociation Energy of the Oxygen Molecule" Can. J. Phys. Vol. 32, p 110-135, (1951)

Buenker, R.J., Peyerimhoff, S.D. & Peric, M. "Ab Initio Vibrational Analysis of the Schumann-Runge Bands and the Neighbouring Absorption Region of Molecular Oxygen" Chem. Phys. Lett., Vol. 42, p 383-389, (1976)

Carroll, P.K. "Predissociation in the Schumann-Runge Band of Oxygen" Astrophys. Journ. 129, p 794-800.

Carver, J.H., Mitchell, P., Murray, E.L. & Hunt, B.G. "Molecular Oxygen Density and Lyman-α Absorption in the Upper Atmosphere" J.G.R., Vol. 69, No. 17, p 3755-3756, (1964)

Carver, J.H. "The Origin of Atmospheric Oxygen" Search, Vol. 5, No. 4, p 130-135, (1974)

Carver, J.H. "The Atmospheric Density of Molecular Oxygen" I.Q.S.Y. Data Review, Space Research : 4, Vol. 6, Paper 16.

Carver, J.H., Gies, H.P.F., Hobbs, T.I., Lewis, B.R. and McCoy, D.G. "Temperature Dependence of the Molecular Oxygen Photoabsorption Cross-Section near the H Lyman-α Line" J. Geophys. Res. Vol. 82, No. 13, p. 1955-1959, (1977)

Carver, J.H., Haddad, G.N., Hobbs, T.I., Lewis, B.R. and McCoy, D.G. "Vacuum Ultraviolet 6m Monochromator" Applied Optics, Vol. 17, p. 420-429, (1978)

Creek, D.M. & Nicholls, R.W. "A Comprehensive Re-analysis of the $O_2(B^3\Sigma_u^- - X^3\Sigma_g^-)$ Schumann-Runge Band System" Proc. R. Soc. London. A. 341, p 517-536, (1975)

Curry, J. & Herzberg, G. "Uber de ultravioletten Absorptionsbanden des Sauerstoffs (Schumann-Runge-Banden)" Annal. der Physik, Vol. 5, No. 19, p 800-807, (1934)

Dawson, L.H. & Hulbert, E.O. "The Absorption of Ultraviolet and visible Light by Water" J. Opt. Soc. Am. Vol. 24, p 175-77, (1934)

Ditchburn, R.W. & Heddle, D.W.D. "Absorption cross-sections in the Vacuum Ultraviolet. " The Schumann-Runge Bands of Oxygen (2000 - 1750Å)" Proc. Roy. Soc. (London) A. 220 - No. 6, p 509-521.

Ditchburn, R.W. & Young, P.A. "The Absorption of Molecular Oxygen between 1850 and 2500Å" J. of Atmos & Terrest. Phys. Vol. 24, p 127-139, (1962)

Dose, V., Schmocker, U. & Sele, G. "Photoabsorption Coefficient of Molecular Oxygen in the Vicinity of the Hydrogen Lyman-α Line" Z. Physik. A. Vol. 274, p. 1-8 (1975)

Fang, T.M., Wofsy, S.C. & Dalgarno, A. "Density Distribution Functions and Absorption in the Schumann-Runge Bands of Molecular Oxygen" Planet. Space Sci. Vol. 27, No. 2, p. 511-519, (1974)

Farmer, A.J.D., Fabian, W., Lewis, B.R., Lokan , K.H. & Haddad, G.N. "Experimental Oscillator Strengths for the Schumann-Runge Band System in Oxygen" J.Q.S.R.T., Vol. 8, p. 1739-1746 (1968)

Feast, M.W. "On the Schumann-Runge O_2 Bands emitted at Atmospheric Pressure" Proc. Phys. Soc. Vol. 62, Part 2-A p. 114-121, (1949)

Finn, G.D. & Mugglestone, D. "Tables of the Line Broadening Function H(a, ν)" Mon. Not. R. Ast. Soc. Vol. 129, No. 2, p. 221-235 (1965)

Flory, P.J. "Predissociation of the Oxygen Molecule" J. Chem. Phys. Vol. 4, p. 23-27, (1936)

Goldstein, R. & Mastrup, F.N. "Absorption Coefficients of He O_2 Schumann-Runge Continuum from 1270Å-1745Å using a New Continuum Source" J. Opt. Soc. Am. Vol. 56, No. 6, p. 765-769, (1966)

Granath, L.P. "The Absorption of Ultraviolet Light by Oxygen, Water Vapour and Quartz" Phys. Rev. Vol. 34, p. 1045-1048, (1929)

Goody, R.M. "Atmospheric Radiation" Oxford University Press. (1964)

Hall, J.E. "Atmospheric pressure, density and scale height calculated from H Lyman-α Absorption allowing for the variation in cross-section with wavelength" J. of Atmos & Terrest. Phys. Vol. 34, p. 1337-1348, (1972)

Halmann, M. "Isotope Effects on Franck-Condon Factors. VI. Pressure-Broadened Absorption Intensities of the Schumann-Runge Bands of $^{16}O_2$ and $^{18}O_2$" J. Chem. Phys. Vol. 44, No. 6, p. 2406-2408, (1966)

Hasson, V., Hebert, G.R. & Nicholls, R.W. "Measured Transition Probabilities for bands of the Schumann-Runge ($B^3\Sigma_u^- - X^3\Sigma_g^-$) band system of Molecular Oxygen" J. Phys. B. - Mol. Phys. Vol. 3, p. 1188-1191, (1970)

van der Held, E.F.H. (in Utrecht) "Intensität und natürliche Breite von Spektrallinien" Zeitschrift für Physik. Bd. 70, p. 508-515, (1931)

Herzberg, G. "Spectra of Diatomic Molecules" van Nostrand. (1950)

Holland, H.D. "The History of Ocean Water and its effect on the Chemistry of the Atmosphere" N.A.S. Symposium, Vol. 53, p. 1173-1183, (1965)

Hudson, R.D., Carter, V.L. & Breig, E.L. "Predissociation in the Schumann-Runge Band System of O_2 : Laboratory Measurements and Atmospheric Effects" J. Geophys. Res. Space Phys. Vol. 74, No. 16, p. 4079-88, (1969)

Hudson, R.D., Carter, V.L. & Stein, J.A. "An Investigation of the Effect of Temperature on the Schumann-Runge Absorption Continuum of Oxygen, 1580 - 1950Å" J. Geophys. Res. Vol. 72, No. 9, p. 2295-2298, (1966)

Hudson, R.D. "Critical Review of Ultraviolet Photoabsorption Cross Sections for Molecules of Astrophysical and Aeronomic Interest" Revs. of Geophys. & Space Phys., Vol. 9, No. 2, p. 305-407, (1971)

Hudson, R.D. & Carter, V.L. "Absorption of Oxygen at Elevated Temperatures (300-900 °K) in the Schumann-Runge System" J. Opt. Soc. Am., Vol. 58, p. 1621-1629, (1968)

Hudson, R.D. & Carter, V.L. "Predissociation in N_2 and O_2" Can. J. Chem., Vol. 47, p. 1840-1845, (1969)

Hudson, R.D. & Mahle, S.H. "Photodissociation Rates of Molecular Oxygen in the Mesosphere and Lower Thermosphere" J. Geophys. Res., Vol. 77, No. 16, P. 2902-2904, (1972)

Huebner, R.H., Celotta , R.J., Mielczarek & Kuyatt, C.E. "Apparent oscillator strengths for Molecular Oxygen derived from electron energy-loss Measurements" J. Chem. Phys., Vol. 63, No. 1, p. 241-248, (1975)

Huffman, R.E. "Absorption cross-sections of atmospheric gases for use in aeronomy" Can. J. Chem., Vol. 47, p. 1823-1824, (1969)

van de Hulst, H.C. & Reesink, J.J.M. "Line Breadths and Voigt Profiles" Ap. J. Phys., Vol. 137, p.1302 - (1963)

Hunten, D.M. "The Escape of Light Gases from Planetary Atmospheres" Journ. of Atmos. Sciences. Vol. 30, No. 8, p. 1481-1494, (1973)

Hunten, D.M. & Strobel, D.F. "Production and Escape of Terrestrial Hydrogen" Journ. of Atmos. Sciences. Vol. 31, No. 2, p. 305 - 317, (1974)

Jansson, P.A. & Korb, C.L. "A Table of the Equivalent Widths of Isolated Lines with Combined Doppler and Collision Broadened Profiles" J.Q.S.R.T. Vol. 8, p. 1399-1409, (1968)

Jarmain, W.R. "Franck-Condon Factors from Klein-Dunham Potentials for the V" = 0 Progression of the Schumann-Runge System of O_2" Can. J. Phys. Vol. 41, p. 1926-1929, (1963)

Jarmain, W.R. & Nicholls, R.W. "A Theoretical Study of the v'-0,1,2 progressions of Bands and adjoining Photodissociation Continua of the O_2 Herzberg I System" Proc. Phys. Soc. Vol. 90, p. 545-553, (1967)

Johns, J.W.C. & Lepard, D.W. "Calculation of Rotation-Electronic Energies and Relative Transition Intensities in Diatomic Molecules" J. Mol. Spect. Vol. 55, p. 374-406, (1975)

Julienne, P.S. & Krauss, M. "Predissociation of the Schumann-Runge Bands of O_2" J. Mol. Spectr., Vol. 56, p. 270-308, (1975)

Julienne, P.S. " $^3\Sigma_u^- - {}^3\Sigma_u^+$ Coupling in the O_2 $B^3\Sigma_u^-$ predissociation" J. Mol. Spectr., Vol. 63, p 60-79. (1976)

Kavanagh, R.W. & Penner, S.A. "Nomogram for the Evolution of Blackbody Radiancy and of Peak and Total Intensities for Spectral Lines with Lorentz Countour" J. Opt. Soc. Am., Vol. 43, No. 5, p. 383-389, (1953)

Kavanagh, R.W., Björnerud, E.K. & Penner, S.S. "Nomogram for the Evaluation of Blackbody Radiancy and of Peak and Total Intensities for Spectral Lines with Doppler Countour" J. Opt. Soc. Am., Vol. 43, No. 5, p. 380-384, (1953)

Kielkopf, J.F. "New Approximation to the Voigt Function with applications to Spectral-Line Profile Analysis" J. Opt. Soc. Am., Vol. 63, No. 8, p. 987-995, (1973)

Kockarts, G. "Penetration of Solar Radiation in the Schumann-Runge Bands of Molecular Oxygen" Book Title: "Mesospheric Models and Related Experiments" Fiocco (Ed) p. 160-176, (1971)

Kopfermann, H. & Ladenburg, R. (in Berlin-Dahlem) "Untersuchungen über die Anomole Dispersion angeregter Gase. V. Teil. Negative Dispersion in angeregtem Neon" Neits f. Physik. Vol. 65, p. 167-188, (1930)

Knauss, H.D. & Ballard, S.S. "Rotational Structure of the Schumann-Runge Bands of Oxygen in the Vacuum Region" Phys. Reviews. Vol. 48, P. 796-799, (1935)

Ladenburg, R. & Reiche, F. "Selektive Absorption" Annln. Phys. Vol. 42, p. 181-209, (1911)

Lawrence, G.M. & McEwan, M.J. "Production of O('S) from Photodissociation of O_2" J. Geophys. Res. Vol. 78, No. 34, p. 8314-8319, (1973)

Lee, P. "Photodissociation and Photoionization of Oxygen (O_2) as Inferred from Measured Absorption Coefficients" J. Opt. Soc. Am. Vol. 45, No. 9, p. 703-709, (1955)

Lewis, B.R., Carver, J.H., Hobbs, T.I., McCoy, D.G. and Gies, H.P.F. "Experimentally Determined Oscillator Strengths and Linewidths for the Schumann-Runge Band System of Molecular Oxygen - I. The 6-0 - 14-0 Bands" J. Quant, Spectrosc. Radiat. Transf. Vol. 20, No. 2, p. 191-203, (1978)

Lewis, B.R., Carver, J.H., Hobbs, T.I., McCoy, D.G. and Gies, H.P.F. "Experimentally Determined Oscillator Strengths and Linewidths for the Schumann-Runge Band System of Molecular Oxygen - II The 2-0 - 5-0 Bands. (In Press)

Meadows, A.J. "The Atmospheres of the Earth and the Terrestrial Planets : Their Origin and Evolution" Physics Reports (Section C of Phys. Letters). Vol. 5, No. 4, p. 197-236, (1972)

Metzger, P.M. & Cook, G.R. "A Re-Investigation of the Absorption Cross-Sections of Molecular Oxygen in the 1050-1800Å Region" J.Q.S.R.T. Vol. 4, p. 107-116, (1964)

Minzner, R.A. "The 1976 Standard Atmosphere and its Relationship to Earlier Standards" Revs. of Geophys. & Space Phys., Vol. 15, No. 3, (1977)

Mitchell, A.C.G. & Zemansky, M.W. "Resonance Radiation and Excited Atoms" Cambridge Univ. Press (1934)

Murrell, J.N., & Taylor, J.M. "Predissociation in diatomic spectra with special reference to the Schumann-Runge Bands of O_2" Molecular Physics, Vol. 16, No. 6, p. 609-621, (1969)

Nicolet, M. "Stratospheric Ozone : An Introduction to its Study" Revs. of Geophys. & Space Phys., Vol. 13, No. 5, p. 593-635, (1975)

Nielsen, J. Rud., Thornton, V. & Dale, E. Brock. "The Absorption Laws for Gases in the Infra-Red" Reviews of Modern Physics. Vol. 16, Nos 3 & 4, p. 307-324, (1944)

Ogawa, M. & Yamawaki, K.R. "Absorption Coefficients of O_2 at the Lyman-α Line and of other O_2 Transmission Windows" Applied Optics, Vol. 9, No. 7, p. 1709-1711, (1970)

Ogawa, M. "Absorption Coefficients of O_2 at the Lyman-α Line and its Vicinity" J.G.R. (Space Physics) Vol. 73, No. 21, p. 6759-6763, (1968)

Ogawa, M. & Yamawaki, K.R. "Forbidden Absorption Bands of O_2 in the Argon Continuum Region" Can. J. Phys. Vol. 47, p. 1805-1811, (1969)

Olivero, J.J. & Longbothum, R.L. "Empirical Fits to the Voigt Line Width : A Brief Review" J.Q.S.R.T. Vol. 17, p. 233-236, (1977)

Pauling, L. and Wilson, E.B. "Introduction to Quantum Mechanics" McGraw Hill (1935)

Penner, S.S. "Quantitative Molecular Spectroscopy and Gas Emmissivities" Addison-Wesley (1959)

Penner, S.S. & Kavanagh, R.W. "Radiation from Isolated Spectral Lines with Combined Doppler and Lorentz Broadening" Journ. Opt. Soc. Am. Vol. 43, No. 5, p. 385, (1953)

Plass, G.N. & Fivel, D.I. "Influence of Doppler Effect and Damping on Line Absorption Coefficient and Atmospheric Radiation Transfer" Astrophys. J. Vol. 117, p. 225 - (1953)

Posener, D.W. "The Shape of Spectral Lines : Tables of the Voigt Profile $\frac{a}{\pi}\int_{-\infty}^{\infty}\frac{e^{-y^2}\,dy}{a^2+(v-y)^2}$ Aust. J. Phys. Vol. 12, p. 184-196, (1959)

Prinz, D.K. & Brueckner, G.E. "Observations of the O_2 Column Density between 120 and 70 km and Absorption Cross Section in the Vicinity of the H Lyman-α" J.G.R. Vol. 82, No. 10, p. 1481-1486, (1977)

Purcell, J.D. & Tousey, R. "The Profile of Solar Hydrogen Lyman-α" J.G.R. Vol. 65, No. 1, p. 370-372, (1960)

Quessette, J.A. "On the Measurement of Molecular Oxygen Concentration by Absorption Spectroscopy" J.G.R. (Space Phys) Vol. 75, No. 4, p. 839-844, (1970)

Raff, R.A. & Meaburn, G.M. "Photochemical Reaction Mechanisms for Production of Organic Compounds in a Primitive Earth Atmosphere" Nature, Vol. 221, p. 459-460, (1969)

Ratner, M.I. & Walker, J.C.G. "Atmospheric Ozone and the History of Life" Journ. Atmos. Sciences. Vol. 29, No. 5, p. 803-808, (1972)

Rubey, W.W. "Geologic History of Sea Water" Bulletin of the Geologic Soc. of Am. Vol. 62, p. 1111-1148, (1951)

Samson, J.A.R. "Techniques of Vacuum Ultraviolet Spectroscopy" John Wiley & Sons, (New York) (1967)

Schaefer III H.F., & Miller, W.H. "Curve Crossing of the $B^3\Sigma_u^-$ and $^3\pi_u$ States of O_2 and its Relation to Predissociation in the Schumann-Runge Bands" J. Chem. Phys., Vol. 55, No. 8, p. 4107-4115, (1971)

Shardanand & Prasad Rao, A.D. "Collision Induced Absorption of O_2 in the Herzberg Continuum" J.Q.S.R.T. Vol. 17, p. 433-439, (1977)

Shardanand "Absorption Cross Sections of O_2 and O_4 between 2000 and 2800Å" Phys. Rev. Vol. 186, No. 1, p. 5-9 (1969)

Smith, L.G. & Miller, K.L. "The Measurement of O_2 Number Density by Absorption of Lyman-α" J.G.R. Vol. 79, No. 13, p. 1965-1968, (1974)

Tatum, J.B. & Watson, J.K.G. "Rotational Line Strengths in $^3\Sigma^{\pm} - {}^3\Sigma^{\pm}$ Transitions with Intermediate Coupling" Can. J. Phys. Vol. 49, p. 2694-2703, (1971)

Tatum, J.B. "Hönl-London Factors for $^3\Sigma^{\pm} - {}^3\Sigma^{\pm}$ Transitions" Can. J. Phys. Vol. 44, p. 2944-2946, (1966)

Tatum, J.B. "The Interpretation of Intensities in Diatomic Molecular Spectra" Astrophys. Journal, Supplement Series, Vol. 14, p. 21-56, (1967)

Thompson, B.A., Harteck, P. & Reeves, R.R. (Jnr) "Ultraviolet Absorption Coefficients of CO_2, CO, O_2, H_2O, N_2O, NH_2, NO, SO_2 and CH_4 between 1850 and 4000Å" J.G.R. Vol. 68, No. 24, p. 6431-6436, (1963)

Thorne, A.P. "Spectrophysics" Chapman J. Hall, London (1974)

Thrane, E.V. & Johannessen, A. "A Measurement of the Extinction of Solar Hydrogen Lyman-α radiation in the Summer Arctic Mesosphere" Jourm. Atmos. Terres. Phys. Vol. 37, p. 655-667, (1975)

Turco, R.P. "Photodissociation Rates in the Atmosphere below 100 km" Geophysical Surveys 2 p. 153-192, (1975)

Veseth, L. & Lofthus, A. "Fine Structure and Centrifugal Distortion in the Electronic and Microwave Spectra of O_2 and SO_2" Mol. Phys. Vol. 27, No. 2, p. 511-519, (1974)

Watanabe, K., Inn, E.C.Y. & Zelikoff, M. "Absorption Coefficients of Oxygen in the Vacuum Ultraviolet" J. Chem. Phys. p. 1026-1030, (1935)

Weeks, L.H. "Determination of O_2 Density from Lyman-α Ion Chambers" J.G.R. Vol. 80, No. 25, p. 3655-3660, (1975)

Weissler, G.L. & Lee, P.O. "Absorption Coefficients of Oxygen in the Vacuum Ultraviolet" JJ. Opt. Soc. Am. Vol. 42, No. 3, p. 200-203, (1952)

Wilkinson, A.G. & Mulliken, R.S. "Dissociation Processes in Oxygen above 1750Å" Astrophys. Journ. No. 125, p. 595-600, (1957)

Yamada, H.Y. "Total Radiances and Equivalent Widths of Isolated Lines with Combined Doppler and Collision Broadened Profiles" J. Quant. Spectrosc. Radiat. Transfer, Vol. 8, p. 1463-1473, (1968)

Young, C. "Calculation of the Absorption Coefficient for Lines with Combined Doppler and Lorentz Broadening" J. Quant. Spectrosc. Radiat. Transfer. Vol. 5, p. 549-552, (1965)